THE SENSITIVITY OF CONVECTION TO BOUNDARY LAYER PARAMETERIZATION IN HURRICANES HARVEY AND IRMA 2017

by

Dylan R. Card

A Dissertation

Submitted to the University at Albany, State University of New York

in Partial Fulfillment of

the Requirements for the Degree of

Doctor of Philosophy

College of Arts and Sciences

Department of Atmospheric and Environmental Sciences

2020

ABSTRACT

Tropical cyclones (TCs) pose a significant threat to life and property, and exhibit many severe weather hazards as they make landfall, such as storm surge, strong winds, flooding rains, and tornadoes. TC convection is associated with nearly all of these hazards, which can extend hundreds of kilometers inland; thus, understanding the characteristics and organization of convective cells is important to mitigating risk. Observational studies have noted that TC convection tends to organize downshear and that rotating thunderstorms tend to occur in the downshear-right quadrant of the TC. Modeling studies have also shown that convective cells tend to form upshear right and mature as the traverse cyclonically around the TC. Rotating thunderstorms in TCs are strongly influenced by the low-level helicity and convective available potential energy (CAPE), which have been highlighted in numerous modeling and observational studies. The distribution and magnitude of low-level helicity and CAPE can be strongly influenced by planetary boundary layer (PBL) parameterizations in numerical weather prediction, motivating this research.

High-resolution Weather Research and Forecasting (WRF) simulations of hurricanes Harvey and Irma (2017) will investigate the role of boundary layer parameterizations in determining the structure and distribution of rotating and non-rotating convection in TCs. Specifically, this dissertation focuses on the YSU, MYNN3, and ACM2 PBLs, as these schemes represent the three major types of PBL schemes in numerical models. The spatial distribution of rotating and non-rotating cells in the simulations were consistent with past literature, while the temporal distribution aligned well with the observed tornado reports in Harvey and Irma, but not with the previously documented diurnal cycle of tornadoes in

TCs. The rotating cells were generally located closer to both the TC center and the coastline compared to the non-rotating cells. The differences between the rotating and non-rotating cell locations and structure show that rotating cells are more representative of mature TC principal rainband cells, while non-rotating cells are less mature and closer to the start of the principal rainband. Reflectivity observations of rotating and non-rotating cells from mobile Doppler radar during the landfall of Harvey are in large agreement with the reflectivity structures present in the rotating and non-rotating cell composites from the simulations. Tropical cyclone tornado surrogates are a useful tool to partition convective cells within TCs that are likely to produce tornadoes and those that do not in model simulations.

The simulations also show many differences in the convective environment between the investigated PBL schemes, specifically the 0–3-km updraft helicity, low-level relative humidity, and low-level CAPE. The key mechanisms that result in the differences in the convective environments were the depth and magnitude of the vertical eddy diffusivity (mixing), which was influenced by stability in the YSU and ACM2 simulations. Compared to the observations of numerous TCs in past literature, the MYNN3 simulations of both Harvey and Irma showed the best 500 m wind speed and eddy diffusivity relationship. The vertical profiles of temperature and dew point temperature in the simulations of hurricanes Harvey and Irma verify best in the areas of the TC with high moisture content compared to observed vertical profiles; however, almost every profile within the TC precipitation exhibited a cold bias near the surface in each PBL scheme. Temperature cold biases near the surface are problematic for PBL schemes that utilize K-profile parameterization (KPP), such as the YSU and ACM2 parameterizations that are very sensitive to the near surface stability. The results of the simulations of hurricanes Harvey and Irma suggest that non-local and hybrid PBL schemes, which utilize aspects of KPP closure, should be used with caution in the TC environment.

ACKNOWLEDGMENTS

I began my higher education as an undergrad studying atmospheric science at the University at Albany (UAlbany) in August 2011. Since then I have had the great opportunity to take on leadership roles and become part of the Great Dane Family. First, I would like to acknowledge those that have made large impact on my overall time at UAlbany. I would like to acknowledge all of the administrators I have had the pleasure of working with on the many committees I have served on at the University at Albany during my graduate career. This includes the members of the University Auxiliary Services board (UAS), including the leadership of UAS, the Sustainability Committee, The UAlbany Strategic Planning Committee, the Graduate Academic Council (GAC), and the many members of the University Faculty Senate, amongst many other committees I have had the pleasure of serving on. Each of these committees and the interactions they allowed me to have with various leaders across the university helped shape my understanding and gain viewpoints from a wide verity of disciplines as I advocated for the graduate students at UAlbany. I would also like to acknowledge the time I have spent working with the Sustainability Office since my second semester of my Sophomore year of undergrad, particularly with the various staff in the office as well as the director Mary Ellen Mallia, who has been a great mentor and friend over the past 10 years. My time working in the Sustainability Office helped me to expand my goals and move on to take on further leadership roles at the University.

My advisors and committee members also provided formative advice and feedback that shaped my graduate school research and for that I am very thankful. I am extremely pleased with my selection to pursue both my Masters and PhD under Dr. Kristen Corbosiero who has been an amazing advisor and mentor throughout my graduate career. I would like to acknowledge Kristen, she has truly helped me to become a better scientist. I would also like to acknowledge Dr. Brian Tang who I have worked with as part of the tropical cyclone research group and as the second reader on my Masters work. Brian has always provided helpful and thoughtful feedback and is always a friendly face to see around the department. I would also like to acknowledge the other two members of my committee Dr. Rob Fovell and Dr. Ryan Torn who have always been there to answer questions and provide helpful feedback both on my research and career.

The Department of Atmospheric and Environmental Science at UAlbany has been my home for the past 10 years and I have very fond memories of my time here. There are so many friendly and helpful staff members in the department. I would like to acknowledge the main office staff including Chaina Porter and Carolyn DeLuise for all they do to help the department. I would also like to acknowledge Kevin Tyle for his tireless work keeping the computing resources up and running in the department. Kevin has always been there to answer any computing question I have had over my many years in the department from the days I first started using python to today. I would also like to thank Annette Audi and Barbara Zampella for all the administrative work they do to ensure we can go to conferences and share our research with the rest of the academic community.

I have also meet many wonderful students during the time in the department who I am glad to call my friends. I will not name them all here as the list would be longer than the dissertation, but I would like to acknowledge their support. I want to highlight some of the fun times I have had with friends during my time at UAlbany. I have enjoyed many game nights, hikes, dinners, Apple and Wine Festivals, office lunches, coffee breaks, and wine o'clock. My friends at UAlbany have also been there to bounce complex ideas off from and engage in academic discussion, I not only consider them my friends but also my colleagues.

Last, but certainly not least, I would like to thank my family and my boyfriend Adam. They have always been huge supporters in me reaching from my academic and professional goals. I would like to acknowledge my family for always being there for me and encouraging me to pursue my academic and professional goals. I would like to acknowledge Adam for always being there to support me whenever there was a setback in the research or for any other reason. I am very thankful to have a supportive family and supportive boyfriend who have all been there every step of the way along my academic career and into the future.

CONTENTS

APPENDICES

LIST OF TABLES

LIST OF FIGURES

1. Introduction

1.1 Motivation

Tropical cyclones (TCs) pose a significant threat to life and property for those living near the coast, exhibiting many different types of severe weather hazards as they make landfall, such as storm surge, strong winds, flooding rains, and tornadoes. Convection in tropical cyclones can contribute to a variety of these hazards. From 1995 to 2016, rotating convection in tropical cyclones directly resulted in 1296 confirmed tornadoes in the United States, accounting for 10–25% of all tornado activity in the coastal states from Louisiana to Maryland (Edwards 2012). Tropical cyclone tornadoes also make up a large amount of the yearly tornado activity in Japan and China (Bai et al. 2019). Roughly 60% of landfalling tropical cyclones in the United States produce at least one tornado and the threat for such tornadoes can persist for up to five days after landfall (McCaul 1991). The risk for these tornadoes can extend 200–500 km from the tropical cyclone center to inland areas typically spared from strong winds and storm surge. The tornadoes associated with tropical cyclones are typically weak with only 14% rated F/EF2 or higher (Schultz and Cecil 2009). Each tropical cyclone also has large variability in the amount of tornadoes reported. Some storms, such as Hurricane Ivan (2004), produce upwards of 118 tornado reports (Edwards 2010), while others result in no tornado reports although sharing similar intensities and landfall locations. The total number of tornadoes reported in tropical cyclones is shown in Figure 1.1. The weak and numerous tornadoes in tropical cyclones present a unique operational challenge to forecasters and decision makers as awareness may be relatively low compared to the other threats present in landfalling tropical cyclones (Weiss 1987; McCaul 1991).

The National Weather Service (NWS) preforms service assessments to evaluate forecast performance following significant weather events such as hurricanes, floods, and impactful winter storms. Their assessment of Hurricane Irene (2011) discussed tornado warning false alarm rates of nearly 88%. It was also found that the high false alarm rates of tropical cyclone tornado warnings damaged the credibility of the NWS (NWS 2012), taking away from other tropical cyclone risks. Martinaitis (2017) found a similar problem when looking at tropical cyclone landfalls from 2008 to 2013 in the United States that produced at least one confirmed tornado and in which at least 10 tornado warnings were issued. Martinaitis (2017) found that of the 1397 tornado warnings issued during the 12 tropical cyclones examined, only 198 tornado warnings verified, leading to an appalling false alarm rate of nearly 86% (Fig. 1.2). In comparison, the national false alarm rate for tornado warnings in the United States has ranged from 80% in 1998 to 69% in 2016 (Fig. 1.3), which includes tropical cyclone tornado warnings. Brotzge et al. (2011) found that the false alarm rate for non-tropical cyclone tornado warnings from 2000 to 2004 was about 70%. Thus, tornado prediction in tropical cyclones remains difficult.

The understanding of tropical cyclone tornadoes has increased by using tropical cyclone tornado surrogates in numerical weather prediction models. Carroll-Smith et al. (2019) showed that thresholds of updraft helicity could be used in simulations of Hurricane Ivan to identify where tornado reports may occur. Although tropical cyclone tornado surrogates can be useful to predict tropical cyclone tornadoes, the thresholds used vary based on the grid spacing of the model and may be sensitive to the choice of model parameterizations. The latter of which motivates the current work.

1.2 Rotating convective cells in tropical cyclones

Hurricane Danny (1985) was one of the first hurricane supercell environments to be studied comprehensibly because of the 20 long-track supercells and 22 tornado reports it spawned (McCaul 1987). McCaul (1987) noted that not only was veering of the low-level wind important, but so were dry air intrusions, which acted to increase convective instability. McCaul (1991) continued this research by creating a climatology of buoyancy and shear in hurricane-spawned tornado environments using all available sounding data near reported tornado cases in the United States from 1948–1986. For the first time, it was documented that the distributions of buoyancy and shear in hurricanes had significant differences from quadrant to quadrant with respect to north, the direction of the large-scale vertical wind shear, and storm motion. The 0–3-km shear and helicity within the right-front quadrant was the most favorable for producing rotating convection and, in fact, these variables are very well correlated with the observed tornado frequency maximum in the right-front quadrant with respect to motion (McCaul 1991).

Edwards (2012) reviewed the climatology, distributions, and environments of tropical cyclone tornadoes. In this review paper, the synoptic, tropical cyclone, and meso-β scales were examined to summarize what influences tropical cyclone tornado and supercell potential on each scale. On the synoptic scale, the predominant driver of tropical cyclone convective (both rotating and non-rotating) development is the enhancement of vertical shear (McCaul 1991; Corbosiero and Molinari 2003; Molinari and Vollaro 2010). This increase in shear is generally attributed to the midlatitude westerlies and baroclinc boundaries associated with troughs that recurve tropical cyclones. Consistent with Edwards (2012), Verbout et al. (2007) found that tropical cyclones with relatively high tornado counts were accompanied by larger 500-hPa geopotential height anomalies and stronger height gradients, suggesting interactions with the midlatitudes.

Convection at the tropical cyclone scale is predominantly driven by the distributions of buoyancy and shear. Operational experience indicates that it is common for rotating convection to develop offshore and move inland (Baker et al. 2009). Some rotating convection weakens as it moves onto the more thermodynamically stable land as low-level (0–3-km) convective available potential energy (CAPE) is about 35% less (Baker et al. 2009). Zhang et al. (2017) showed the CAPE in simulations of landfalling hurricanes was strongly affected by the vertical mixing in the planetary boundary layer (PBL) scheme. Convective cells also increase mesocyclone intensity and undergo tornadogensis due to the increased helicity from friction (Edwards 2012). On the meso-β (convective) scale, tropical cyclone supercells have been observed to be smaller in vertical and horizontal extent compared to midlatitude supercells (McCaul and Weisman 1996). Eastin and Link (2009) found supercells in Hurricane Ivan (2004) were typically 5–7 km in diameter, compared to non-tropical cyclone supercells which typically encompass a larger range of 3–12 km in diameter.

On the mesoscale, low-level, baroclinic, convergent boundaries and dry air intrusions can potentially influence the intensity and spatial distribution of tropical cyclone supercells (Edwards and Pietrycha 2006). Dry air ingested into the midlevels has a strong influence on convective structures in tropical cyclones as it can enhance CAPE (McCaul 1987; Vescio et al. 1996; Curtis 2004). Spatially, dry slots can lead to the formation of baroclinic boundaries due to differential heating within the tropical cyclone envelope. Relatively cloud-free areas between tropical cyclone rainbands can support a few degrees Celsius of diabatic surface heating (Card 2019). This surface heating can substantially magnify CAPE and yield baroclinic boundaries that may contribute to supercell maintenance (Edwards 2012). Edwards and Pietrycha (2006) argued that most landfalling tropical cyclones are not homogenized with equal tornado potential everywhere, and that boundaries and dry air intrusions may play a role in the clustering of tornadoes. Indeed, tropical cyclone tornado outbreak cases tend to have pronounced relative humidity gradients from 700–500 hPa at the outer edge of the moist tropical cyclone envelope (Curtis 2004)

Of tropical cyclones from 1948 to 2019, Hurricane Ivan (2004) holds the record for the number of confirmed tropical cyclone tornadoes at 118 (McCaul 1991; Schultz and Cecil 2009). Baker et al. (2009) looked at the environmental ingredients for the development of supercells and tornadoes in Hurricane Ivan via airborne and land-based observations. The azimuthal location of the tornadoes in Hurricane Ivan could be explained by significant 0–1-km shear (7.4 $\frac{m}{s}$) and low lifting condensation level (LCL) heights (415 m) in the right-front quadrant with respect to storm motion. Motivated by an apparent increase in individual convective cell rotation as convection made landfall, Baker et al. (2009) further investigated the differences in the convective environments between the ocean and land. They found that the land soundings had very similar total-column CAPE to the ocean soundings; however, the low-level (0–3-km) CAPE was 35% less over the land. McCaul and Weisman (1996, 2001) suggested that updraft strength and vorticity were both enhanced when buoyancy is concentrated in the low-levels, suggesting convection is more likely to form over the ocean. The other appreciable difference between the land and ocean environments in Baker et al. (2009) was that the 0–1-km storm relative helicity (SRH) was 50% greater over land, due to frictional effects.

Although not observed in Hurricane Ivan, some researchers have suggested that changes in surface wind speeds as large as 8–10 $\frac{m}{s}$ could occur across horizontal distances of 10 km at land–ocean interfaces (Powell and Houston 1998). Gentry (1983) showed that there is an increase in low-level helicity because of the increase in friction between the land–ocean interface acting to enhance low-level vertical shear. As a result, individual convective cells making landfall tend to increase updraft rotation and intensity due to the enhanced low-level shear (Baker et al. 2009), even though there was lower CAPE over land.

Eastin and Link (2009) used the same collection of airborne and land-based observations as Baker et al. (2009), and concluded that the offshore environment was conducive for supercell formation. In the examination of the individual rotating convective cells, mesocyclonic updrafts extended from the boundary layer up to 6–8 km and were 5–7 km in diameter. The production of the updraft likely results from a combination of convergence, thermal instability, and perturbation pressure gradients, which help to produce mesocyclones by tilting and stretching environmental vorticity (Eastin and Link 2009).

These observational studies of Hurricane Ivan (2004) led to high-resolution, real-data simulations to document the structure of potentially tornadic supercells embedded within tropical cyclone rainbands. Carroll-Smith et al. (2019) produced one such simulation at 3- and 1-km grid spacing. In an attempt to verify the tropical cyclone tornadoes associated with Hurricane Ivan (2004), percentile values of maximum updraft helicity and simulated radar reflectivity were used to identify tropical cyclone tornado surrogates and compare those surrogates to observed tornado reports. The surrogates with the 99.9^{th} (99.95^{th}) percentile of maximum updraft helicity in the 3-km (1-km) domain provided the most favorable results capturing the distribution of tropical cyclone tornadoes compared to observations. These high updraft helicity percentiles suggest that supercells with strong mesocyclones are more likely to produce tornado reports in tropical cyclones. Thus, updraft helicity and simulated radar reflectivity can be successfully used as tropical cyclone tornado surrogates (Carroll-Smith et al. 2019).

The Storm Prediction Center (SPC) has shown that 2017 was the fourth most active year for tornado reports in tropical cyclones behind 2008 (third), 2005 (second), and 2004 (first). The two largest tornado producers of the 2017 tropical cyclone season were Hurricane Harvey and Hurricane Irma. Figures 1.4 and 1.5 (left) show the locations of tornado reports during these two storms. The diurnal distribution of tornado reports in Harvey peaks between 0400–1000 UTC and between 1700–2300 UTC in Irma (Figs. 1.4 and 1.5, right).

Card (2019) used a similar analysis technique to Carroll-Smith et al. (2019) to diagnose rotating convection in both hurricanes Harvey and Irma (2017) using the National Center for Atmospheric Research (NCAR) 10-member ensemble. In Card (2019), the number of identified rotating storms outnumbered the identified non-rotating storms by a factor of two to three in both Harvey and Irma (2017). With respect to storm motion and north, the distributions of rotating and non-rotating convection are very similar (Figs. 1.6 and 1.7). There is a strong relationship between shear and storm motion near the U.S. coasts because tropical cyclones are typically recurving. As shown in Corbosiero and Molinari (2003), shear is the dominant factor in the distribution of convection in tropical cyclones. Most of the rotating storms occur directly downshear, while most of the non-rotating storms occur in the upshear-right quadrant in both the NCAR ensemble and in observations (Figs. 1.6 and 1.7).

In summary, the common environmental characteristics of rotating convection in tropical cyclones are: 1) high 0–3-km helicity, 2) high 0–3-km CAPE, 3) low LCL heights, 4) relatively dry air at midlevels, and 5) low-level boundaries (such as a convergence axis or baroclinic zone) (Novlan and Gray 1974; McCaul 1991; Curtis 2004; Edwards and Pietrycha 2006; Eastin and Link 2009). To generalize these important characteristics, tornadic rotating convection is sensitive to the location and magnitude of baroclinic and convergent boundaries as well as momentum, heat, and moisture distributions in the low levels, which can all be influenced by the choice of PBL schemes in numerical models. These factors will be explored in greater depth in the next sections.

1.3 Tropical cyclone boundaries

Tropical cyclones do not have equal supercell potential everywhere as they tend to cluster near boundaries. There are two major types of boundaries that have been documented in observations of landfalling tropical cyclones. The first is areas of convergence of the low-level wind due to frictional differences between the ocean and land (Baker et al. 2009; Green et al. 2011). The second is baroclinic boundaries due to variations in temperature and moisture (Edwards and Pietrycha 2006). Convergent boundaries tend to enhance shear, while baroclinic boundaries can influence the distribution of CAPE as well as shear. Edwards and Pietrycha (2006) suggests four distinct classes of boundaries, with different distributions of shear and CAPE that may influence tropical cyclone supercell and tornado potential. The first type of boundary is the buoyancy-limiting case, such that there are supportive vertical shear profiles on both sides, but sufficient CAPE only on one side of a boundary. The second is the shear-limiting case, such that there is supportive CAPE on both sides, but favorable shear on one side of the boundary. The third is the overlapping case, where there is supportive CAPE on one side and supportive vertical shear on the other side of a boundary. The last class is the null group, which would have no apparent organization of shear and CAPE. These four distinct classes of boundaries can affect the organization of convection in tropical cyclones.

The coastline acts as a boundary as the land-ocean frictional differences drives strong convergence near the coast. This friction can have a large impact on the low-level winds in tropical cyclones. Powell and Houston (1998) suggested that changes in surface wind speed from ocean to land may be as large as 8–10 $\frac{m}{s}$ across horizontal distances of about 10 km. The winds around a tropical cyclone in the boundary layer can be approximated as in surface wind balance, which is a balance between the pressure gradient force (PGF), the centrifugal force ($\frac{mv^2}{r}$), the Coriolis force ($2\Omega * v * sin(latitude)$), and friction. From surface wind balance, deceleration of the wind also has impacts on the wind direction. In the BL, as the wind decelerates due to friction, it is deflected towards the center of the tropical cyclone as the centrifugal force is a function of the square of the velocity (v^2); thus, it becomes smaller faster than the Coriolis force which is only a function of velocity (v). In observations of Hurricane Ivan (2004), Baker et al. (2009) showed near surface wind speed changes from ocean to land of 2–4 $\frac{m}{s}$, which is not as large as what was proposed in Powell and Houston (1998). Baker et al. (2009) reported that it seemed plausible that rapidly moving supercells could experience drastically different low-level wind profiles within spans of a few kilometers in tropical cyclones during landfall. The change in wind speed and direction due to friction results in increased low-level shear (increased helicity), which climatological studies suggest is often associated with more frequent tornadoes (Markowski et al. 2003) and stronger mesocyclones (Baker et al. 2009) in both the midlatitudes and landfalling tropical cyclones.

The formation of baroclinic boundaries can happen through a variety of processes in the tropical cyclone envelope. Vescio et al. (1996) first noted that midlevel dry air intrusions have the potential to substantially alter the thermodynamic structure, which can influence tornado outbreaks and generate baroclinic boundaries in the tropical cyclone environment. Dry air intrusions into the tropical cyclone can result in local warming and, therefore, baroclinic boundaries (Edwards and Pietrycha 2006). Curtis (2004) found that tropical cyclones associated with tornado outbreaks exhibited three noteworthy environmental details. Tropical cyclones with tornado outbreaks had: lower LCLs, more moisture from the surface to

900 hPa, and more dry air above 700 hPa, which is indicative of dry air intrusions, than the tropical cyclones that did not produce tornado outbreaks or the null cases. The lower LCL height is consistent with both the buoyancy-limiting case from Edwards and Pietrycha (2006) and the findings from Rasmussen and Blanchard (1998) who noted that the LCL height for soundings associated with tornadoes were significantly lower than for soundings associated with only supercells or even non-supercells across the United States. The resulting temperature and moisture differences caused by midlevel dry air intrusion create baroclinic boundaries that can act as a catalyst for tornado outbreaks in tropical cyclones (Curtis 2004).

Baroclinic boundaries have been documented in both observations and in model simulations (Green et al. 2011; Edwards and Pietrycha 2006; Card 2019) of tropical cyclones. Dry slots can lead to the formation of baroclinic boundaries due to differential surface heating within the tropical cyclone rainband region (Edwards and Pietrycha 2006). Relatively cloud-free areas between rainbands can support a few degrees Celsius of surface heating (Card 2019). The asymmetric surface warming can act to locally magnify CAPE and contribute to supercell maintenance (Edwards 2012).

Boundaries like those due to frictional differences between land and ocean surfaces, and baroclinic gradients caused by gradients in temperature and/or moisture, can help convection develop and mature near the coast during tropical cyclone landfall. Dry air intrusions can also act to increase convective instability, invigorating convection, and helping develop rotating convection in localized areas.

As previously mentioned, PBL parameterizations in numerical model simulations can affect the tropical cyclone environment, particularly in the low levels and can possibly affect the identification of tropical cyclone tornado surrogates. With respect to boundaries, the PBL parameterization can influence the low-level baroclinic and convergent boundaries. Various types of planetary boundary layer schemes will be explored in greater depth in the next section.

1.4 Structure and types of planetary boundary layer (PBL) schemes

The PBL is customarily divided into three layers, the surface layer (constant-flux layer), the mixed layer, and the free atmosphere (Kepert 2012). In reality, there is no distinct division between these layers, though the surface layer typically occupies the lowest tenth of the boundary layer. In the WRF model, the surface layer is governed by the surface layer scheme and the mixed layer is governed by the PBL scheme. Because there is no distinct division between these two layers, the PBL scheme must satisfy physics both in the surface and mixed layers depending on the depth of the surface layer in the model. This also allows for mixing into the free atmosphere. A simple schematic of the structure of the atmospheric boundary layer is presented in Figure 1.8. The PBL scheme parameterizes the vertical turbulent fluxes of heat, moisture, and momentum because the grid spacing of most numerical weather prediction (NWP) models is too coarse to resolve the spatial and temporal scales of turbulence. The theoretical foundation of PBL parameterization can be represented by two major components: the order of the turbulence closure and if the mixing uses local or non-local closure (Stull 1988; Stensrud 2007).

The order of closure relates to the equations for turbulence modeling. These equations always contain more unknown terms than known terms; therefore closure of these turbulence equations requires relating the unknown terms to the known terms (Cohen et al. 2015). For example, one-and-a-half-closure schemes predict second-order turbulent kinetic energy (TKE) by estimating second-moments for some variables and first-moments for others. Typically, diagnosis of the second-moment terms involves relating the variance of some variables to their covariances (Stensrud 2007; Coniglio et al. 2013).

The mixing in PBL schemes is parameterized as local or non-local (or sometimes a hybrid of the two). Specifically, these mixing types drive the depth over which the known variables of the turbulence equations can affect a given model level. Local closure schemes allow for interaction between only adjacent model levels. Non-local closure schemes allow for multiple vertical levels in the PBL to interact with each other. Overall, local PBL schemes can be prone to limiting the depth of the PBL by resolving localized stability maxima that are not representative of the state of mixing in the PBL (Stensrud 2007). Vertical mixing in the PBL is primarily driven by large eddies that are typically unaffected by local variations in static stability (Cohen et al. 2015). Generally, non-local closure schemes represent the depth of the PBL better than local closure schemes. In some circumstances, however, the use of higher-order closure can improve the accuracy of local closure schemes (Mellor and Yamada 1982; Nakanishi and Niino 2009; Coniglio et al. 2013).

Uncertainty of the atmospheric state variables in the PBL can have a large impact on the predicted weather phenomena in NWP (Jankov et al. 2005; Stensrud 2007; Nielsen-Gammon et al. 2010), including tropical cyclones. Bu et al. (2017) has shown that PBL parameterization affects the size of modeled tropical cyclones, particularly that the vertical mixing of water vapor in the boundary layer acts to influence the storm size by modulating convective activity in the outer core.

In depth descriptions of the non-local, local, and hybrid PBL schemes will be presented in the following subsections. Each subsection will introduce the type and mechanisms of the PBL scheme, and present advantages and disadvantages for the use of each scheme in numerical models.

1.4.1 Yonsei University (YSU) PBL

The Yonsei University (YSU) PBL (Hong et al. 2006) parameterization is a first-order closure non-local PBL scheme. This scheme allows for mixing between all the model levels in the boundary layer. The YSU scheme uses a parabolic K-profile parameterization (KPP) in unstable mixed layers and impose an empirical eddy diffusivity profile in the PBL (Hong and Lim 2006). In KPP schemes, the PBL depth plays a crucial role as it can directly influence mixing depth and the magnitude, and height, of maximum heating (Kepert 2012). In this scheme, model drag is modified based on the sub-grid variance in terrain elevation and also resolves local variability (Lorente-Plazas et al. 2016). The YSU scheme also uses an explicit term to represent entrainment at the top of the PBL (Banks et al. 2016).

The YSU PBL scheme use KPP to determine the height of the PBL by a critical Richardson number (CRN). This CRN is determined based on the stability in the low levels of the model, as well as if the grid point is over land or water. When the virtual temperature at the surface is warmer than the virtual temperature at the first model level the boundary layer is considered unstable and the PBL height is determined based on a CRN of zero. When the virtual temperature at the surface is colder than the virtual temperature at the first model level the boundary layer is considered stable and the PBL height is determined based on a CRN greater than zero. The Hong (2010) stable boundary layer revision to KPP PBL schemes over water eliminates the countergradient term. This change lets the mechanical mixing terms dominate, meaning the wind speed modulates the CRN such that higher wind speeds result in a lower CRN. If land areas satisfy the conditions for the stable boundary layer revision the CRN is set to 0.25. In the YSU scheme, the explicit entrainment at the top of the PBL acts to modify the PBL height over time through mixing above the PBL irrespective of the local stability. KPP schemes in general place the PBL height in the lowest inversion layer (Hong 2010). The largest revisions from Hong and Lim (2006) to Hong (2010) include the computation of PBL height using a CRN greater than 0 and the parabolic profile of the eddy diffusivity coefficients with height.

The choice of a particular CRN to determine the depth of the PBL in the YSU scheme has major impacts on the eddy mixing, which can directly influence tropical cyclone size through more vertical diffusion of state variables in the boundary layer (Bu et al. 2017). In model simulations of Tropical Cyclone Phailin (2013), the YSU PBL scheme showed slightly stronger inflow and convergence within the boundary layer; however, the presence of outward moving air parcels just above the boundary layer resulted in a general spin-down of the tropical cyclone (Rai and Pattnaik 2018).

The advantages of the YSU scheme are that it can accurately simulate deep vertical mixing in buoyancy-driven PBLs and shallower mixing in strong wind environments (Hong and Lim 2006). The YSU scheme tends to overdeepen the PBL in deep convective environments, which often results in too much dry air near the surface (Coniglio et al. 2013). In the YSU PBL scheme, the day-time convective boundary layer tends to over mix, producing conditions that are too warm and dry in the PBL (Bright and Mullen 2002; Kain et al. 2005; Hill and Lackmann 2009; Hu et al. 2010). In the observed soundings and convective allowing model simulations of Coniglio et al. (2013), the YSU PBL scheme produced temperature and moisture profiles that had significantly less bias then the other PBL schemes tested. These biases in temperature and moisture profiles result in the mixed-layer CAPE being under predicted by the YSU scheme when the observed mixed-layer CAPE is relatively large (Coniglio et al. 2013). In assessment of PBL parameterizations over southern Italy, Tyagi et al. (2018) found that the YSU scheme preformed the best amongst all other first-order closure schemes. The YSU scheme was able to increase the thermally-induced mixing that allowed for earlier development of the PBL compared to the ACM2 and other first-order schemes (Tyagi et al. 2018). García-Díez et al. (2013) showed that the diurnal, seasonal, and geographical sensitivities of PBL schemes over Europe showed cold biases in surface temperatures throughout the summer both in precipitating and clear sky situations. Gunwani and Mohan (2017) echoed the results of García-Díez et al. (2013) for regions over India. Specifically, the local PBL schemes tended to produce the strongest cold temperature biases compared to non-local schemes like the YSU (García-Díez et al. 2013; Cohen et al. 2017). This is attributed to the ability of non-local PBL schemes to promote relatively deeper PBLs compared to local schemes (García-Díez et al. 2013).

1.4.2 Mellor–Yamada–Nakanishi–Niino (MYNN) turbulence closure PBL

The MYNN3 (Mellor-Yamada-Nakanishi-Niino Level 3; Nakanishi and Niino 2009) and MYNN2 (Nakanishi and Niino 2006) schemes share many similar characteristics and are both turbulent kinetic energy (TKE) schemes (Banks et al. 2016). The major difference is with the closure type of these individual schemes, where MYNN3 uses second-order closure and the MYNN2 uses one-and-a-half-order closure. The MYNN2 scheme is tuned to a collection of large-eddy simulations (instead of observational datasets) to overcome some of the biases associated with other local PBL Mellor-Yamada schemes (Coniglio et al. 2013). The MYNN3 scheme is second order and, thus, predicts the TKE and other second moment terms instead of relying on approximations and tuning like lower-order schemes. Both schemes predict TKE, but the MYNN3 scheme also includes variances of potential temperature, moisture, and their covariances. Dzebre and Adaramola (2020) found that when examining boundary layer winds over coastal Ghana, the MYNN3 PBL scheme had the best prediction skill score of the ten PBL schemes tested across all major seasons, with the MYNN2 scheme being the third best. The high performance of the two local MYNN schemes suggested that turbulent eddies generated by thermal turbulence over the site in Ghana were typically small and localized, which would be best resolved by local closure schemes (Warner 2010). As discussed above, higher-order closure typically leads to greater accuracy in local PBL schemes, henceforth, this discussion of TKE PBL schemes will continue with the MYNN3 scheme.

In the MYNN3 scheme, the PBL height is determined by where the TKE falls below a critical value ($1.0 * 10^{-6}\frac{m^2}{s^2}$). Unlike non-local schemes, the PBL height in local schemes is a diagnostic variable and does not impact further calculations in the PBL scheme. MYNN3 uses a second-order closure scheme and can do well at simulating mixed layers and stable boundary layers; however, it has difficulty capturing deep vertical mixing (Nakanishi and Niino 2006). Thus, the advantage of the MYNN3 scheme is that it can depict stable boundary layers well. Yet, this advantage can also cause the MYNN3 scheme to not account fully for deep vertical mixing associated with large eddies, which results in weaker updrafts than observed (Nakanishi and Niino 2006). Not accounting for deep vertical mixing is a common problem associated with all local PBL schemes. Past literature suggests that the MYNN3 tends to more accurately predict wind speeds in a variety of situations and locations compared to many non-local PBL schemes (Misaki et al. 2019; Dzebre and Adaramola 2020).

Local PBL schemes tended to produce the strongest cold temperature biases compared to non-local or hybrid PBL schemes like the ACM2 (García-Díez et al. 2013; Cohen et al. 2017).

1.4.3 Asymmetric convective model version 2 (ACM2) PBL

The ACM2 is a hybrid PBL scheme, allowing for a combination of local and non-local mixing in the boundary layer, incorporating concepts from both TKE and KPP closure schemes (Pleim 2007a) depending on the stability. ACM2 combines the original non-local ACM with an eddy diffusion such that this scheme uses first-order closure for upward fluxes (much like a non-local PBL schemes would) and downward fluxes extend from each layer to each immediately underlying layer (much like local PBL schemes). The ACM2 scheme utilizes a CRN of 0.25 in both the unstable and stable boundary layer. Similar to other KPP schemes (e.g., the YSU), the ACM2 scheme tries to place the PBL height in the lowest inversion layer. The calculation of PBL height in stable conditions is identical for the YSU and ACM2 schemes, while in unstable conditions the ACM2 scheme the PBL height is calculated from the top of the unstable layer. For stable and neutral stability, the ACM2 scheme uses pure eddy diffusion (local mixing), as the non-local mixing is only appropriate for convective conditions where the size of the eddies typically exceeds the vertical grid spacing (Pleim 2007a). The amount of local versus non-local mixing is determined by the magnitude of the stability. Unique to the ACM2 scheme is that eddy diffusivity is required for all stability conditions in and above the boundary layer. Above the PBL, the eddy diffusivity is based on local wind shear and stability, while within the boundary layer the eddy diffusivity is defined similarly to the YSU scheme (Hong et al. 2006; Pleim 2007a) as a parabolic profile of the eddy diffusivity coefficients with height.

The advantage of the ACM2 scheme is that the local and non-local mixing rates are defined in terms of the bulk characteristics of the PBL (Pleim 2007a). One advantage of the ACM2 scheme is that it can depict the vertical profiles of potential temperature and velocity in the PBL with greater accuracy than solely local or non-local schemes (Pleim

2007a). Further validation of the ACM2 scheme has shown that it is able to support the PBL heights typically seen in afternoon wind profiler data and radar (Pleim 2007b). Like the YSU scheme, the ACM2 scheme also tends to overdeepen the PBL in deep convective environments (Coniglio et al. 2013). Very similar findings to these advantages and disadvantages were seen in Xie et al. (2012), where the choice of PBL scheme can result in sizable differences in the vertical profiles of temperature, moisture, and momentum in the boundary layer. García-Díez et al. (2013) also showed that the ACM2 produced cold biases over Europe in surface temperatures throughout the summer both in precipitating and clear sky situations, with Gunwani and Mohan (2017) echoing the results of García-Díez et al. (2013) for regions over India. As noted in the discussion of the MYNN3 PBL scheme, local PBL schemes tend to have stronger cold biases compared to non-local (YSU) and hybrid (ACM2) PBL schemes. Again, this is attributed to the ability of non-local PBL schemes to promote relatively deeper PBLs compared to local schemes (García-Díez et al. 2013).

Cruz and Narisma (2016) examined the rainfall sensitivity to PBL and microphysics parameterizations for Typhoon Ketsana in the Philippines. Cruz and Narisma (2016) tested the YSU, Mellor-Yamada-Janjic (MYJ), and ACM2 PBL schemes as well as the Goddard, Purdue Lin, and Weather Research and Forecasting (WRF) single moment class 6 (WSM6) microphysics schemes. The WRF model simulations showed that the ACM2 PBL scheme with the WSM6 microphysics scheme produced the most skillful forecast capturing the heavy rainfall in terms of its spatial distribution, amount, and timing.

1.5 Summary of science objectives

To help further understand tropical cyclone tornadoes, Carroll-Smith et al. (2019) used tropical cyclone tornado surrogates in high-resolution model simulations of Hurricane Ivan, noting that further research should work to understand how model parameterizations, such as PBL schemes, might impact convection. This dissertation will investigate the convective environments of rotating convection, and the three-dimensional structure of convection in the rainbands of tropical cyclones, with emphasis being drawn to the differences in the environments across the PBL schemes and the mechanisms within the PBL schemes that cause these differences.

The first goal will be to discuss the spatial and temporal distribution of rotating and non-rotating convection in modeled tropical cyclones Harvey and Irma (2017), as well as their convective environments. I expect to find the distribution of both the identified rotating and non-rotating cells to be very similar to the past work, i.e. being maximized downshear and in the northeast quadrants of hurricanes Harvey and Irma (McCaul 1993; Schultz and Cecil 2009; Edwards et al. 2012; Edwards 2012). I hypothesize that rotating cells will more frequently occur over land since numerous observational studies have shown that convective cells tend to start rotating as they approach the coast (Baker et al. 2009; Eastin and Link 2009), making the coastline an important feature for rotating cells in tropical cyclones. In a temporal sense, the distribution of rotating cells in past literature suggests a peak in tropical cyclone tornado activity in the early-mid afternoon (McCaul 1991; Schultz and Cecil 2009; Edwards 2012). It is expected that the peak in rotating cell activity in hurricanes Harvey and Irma will align best with the observed peak in tornado reports (Figs. 1.4 and 1.5) at 0400–1000 UTC for Harvey and 1700–2300 UTC for Irma. Some questions to answer as a part of this first goal include: Do the spatial and temporal distribution of rotating convection align with previous studies of tornadoes in tropical cyclones? What effect does the coastline have on convective cells and convective cell types?

As outlined previously, many aspects of the low-level environment are important for tropical cyclone tornadoes (Novlan and Gray 1974; McCaul 1991; Curtis 2004; Edwards and Pietrycha 2006; Eastin and Link 2009), all of which can be influenced by the mechanisms within the PBL schemes, specifically the manner in which the schemes define the PBL depth and vertical eddy mixing. It is hypothesized that the sub-grid scale mixing in the boundary layer in each PBL scheme results in differences in the convective environments including the 0–3-km helicity, low-level relative humidity, and low-level CAPE as these have been shown to be important to tropical cyclone supercell development as discussed in the previous sections. It is expected that the 0–3-km helicity (vertical shear) will be higher over the land compared to the ocean, with this low-level helicity being important in the development of rotating convection in tropical cyclones (McCaul and Weisman 1996). It is also expected that the PBL scheme with the largest vertical mixing will have the largest low-level CAPE (Zhang et al. 2017). Some additional questions to answer in this first goal include: What are the differences in the convective environments that are affected by the choice of PBL scheme? How do the modeled rotating and non-rotating cells differ in structure from one another? What is the typical structure of the modeled rotating and non-rotating convective cells, both over the land and over the ocean?

The second goal will be to discuss the mechanisms of the PBL schemes and how they result in the differences seen in the simulations of tropical cyclones Harvey and Irma (2017). This dissertation will investigate differences in the PBL and inflow layer heights, as well as transport of moisture, heat, and momentum in the boundary layer. Mixing in the boundary layer acts to vertically transport moisture, heat, and momentum. The MYNN3 PBL scheme will likely underestimate the depth of this vertical mixing (Cohen et al. 2017), leading to higher moisture in the boundary layer and drier air aloft compared to the YSU and ACM2 PBL schemes. Moisture is a key component influencing the distribution of CAPE. Abundant low-level moisture and heat with dry air in the midlevels increases the CAPE in the tropical cyclone environment. In the MYNN3 PBL scheme, it is likely that the abundant moisture and heat in the boundary layer will lead to higher values of CAPE. Specifically, the depth of the vertical mixing of the boundary layer will affect the amount of moist air fluxed out of the boundary layer and into the midlevels impacting the distribution of CAPE (Zhang et al. 2017), such that the PBL scheme with the most vertical mixing should have the highest values of CAPE. The lack of depth of the vertical mixing in the MYNN3 simulation will also reduce 0–3-km helicity compared to the YSU and ACM2 PBL schemes, as deep mixing will result in homogenized winds in the low-levels, reducing the low-level helicity. In this section the questions to be answered are: Why does the PBL height differ between land and ocean identified cells? How do the differences in PBL height affect the vertical eddy mixing? What mechanisms of the PBL schemes contribute to the differences seen in the environment, in terms of mixing of heat, moisture, and momentum?

Lastly, this dissertation will discuss the verification of the PBL simulations using radiosonde and dropsonde observations from hurricanes Harvey and Irma (2017). The observations and model vertical profiles are hypothesized to show that the YSU and ACM2 simulations will have the warmest temperatures in the PBL (García-Díez et al. 2013; Cohen et al. 2017). Although not explicitly shown in tropical cyclones, past literature such as Hariprasad et al. (2014) and Banks et al. (2016) suggest it is likely that the model simulations will show a cold bias in the low levels. Misaki et al. (2019) and Dzebre and Adaramola (2020) suggest that the MYNN3 simulation will more accurately predict the wind speeds compared to non-local PBL schemes (YSU and ACM2). Some questions to answer from this final section include: Which PBL schemes preform best in different locations around the storms compared to observations? Should any PBL scheme be avoided in simulations of landfalling tropical cyclones?

Additionally, observations from a mobile Doppler radar during the landfall of Hurricane Harvey will analyze the depth of the inflow and compare those to the results of Alford et al. (2020), who examined the hurricane boundary layer during the landfall of Hurricane Irene (2011). The mobile Doppler radar will also allow for the comparison of observed reflectivity structures to the modeled vertical profiles of the rotating and non-rotating cells. The depth of the inflow level, thermodynamic profiles, and momentum in the boundary layer will be investigated to determine which aspects of the PBL are preforming realistically with respect to observations.

Zhang et al. (2011c) ascertained that the inflow depth represents the top of the hurricane boundary layer better than the thermodynamic boundary layer depth and that methods to identify the depth of the boundary layer using a CRN may not produce the correct pattern of behavior of the PBL; as such, in this thesis the results will focus on the inflow depth. Alford et al. (2020) showed the boundary layer flow in observations of Hurricane Irene (2011) was different between the land and over the ocean. The inflow depth across the coast is expected to change across the coastline as observed in Hurricane Irene (Alford et al. 2020), while the inflow depth is expected to be consistent over the land. It was noted previously that the PBL heights in both the Irma and Harvey simulations differed drastically between the land and ocean, such that it is also expected that the depth of the tropical cyclone inflow (a good measure for the actual depth of the PBL; Zhang et al. (2011c)) will differ between the land and ocean. In particular, it is expected that the YSU and ACM2 simulations of both Harvey and Irma will show the deepest inflow depths. It is expected that the simulations of Harvey and Irma will align well with the dropsonde observations of Zhang et al. (2011c). The caveat being that the results of Zhang et al. (2011c) looked at dropsondes of oceanic tropical cyclones, but this research is looking at landfalling tropical cyclones with a mix of land and ocean points creating the azimuthal averages. The final questions to be answered by this section include: How do inflow depths in observations from soundings, dropsondes, mobile radar, and past literature (Zhang et al. 2011c) compare to the model simulations? How does the reflectivity cross sections from rotating and non-rotating cells observed by the mobile Doppler radar compare to the model rotating and non-rotating cell composites?

1.6 Figures

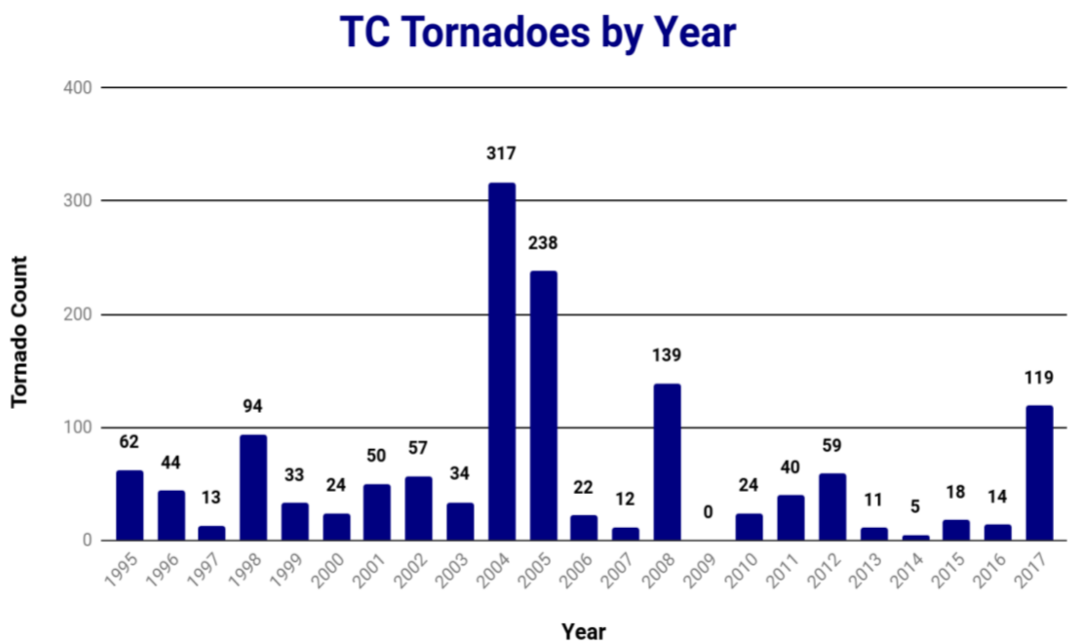

Figure 1.1: Tropical cyclone tornado counts 1995–2017 from the tropical cyclone tornado (TCTOR) database (Edwards 2010).

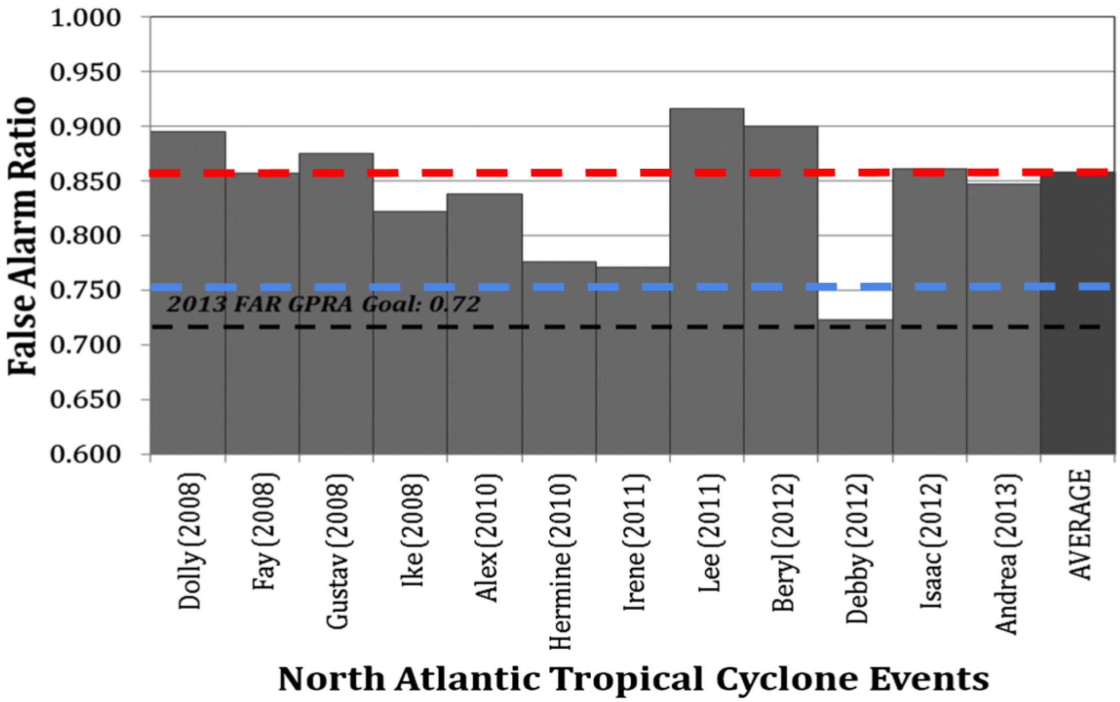

Figure 1.2: Tropical cyclone tornado warning false alarm ratio (FAR) for North Atlantic tropical cyclones adapted from Martinaitis (2017). 2008–2013 tropical cyclone FAR average (red, dashed), 2008–2013 national FAR average (blue, dashed), and 2013 Government Performance and Results Act (GPRA) FAR requirement (black, dashed).

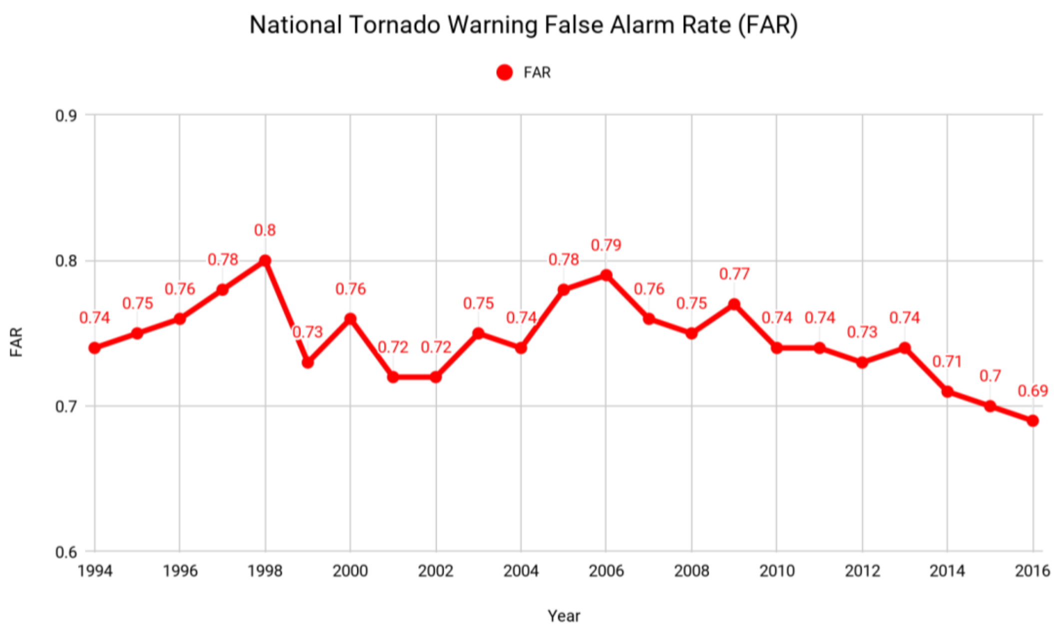

Figure 1.3: National tornado warning false alarm ratio (FAR) for the United States from the Storm Prediction Center (SPC) 1994–2016.

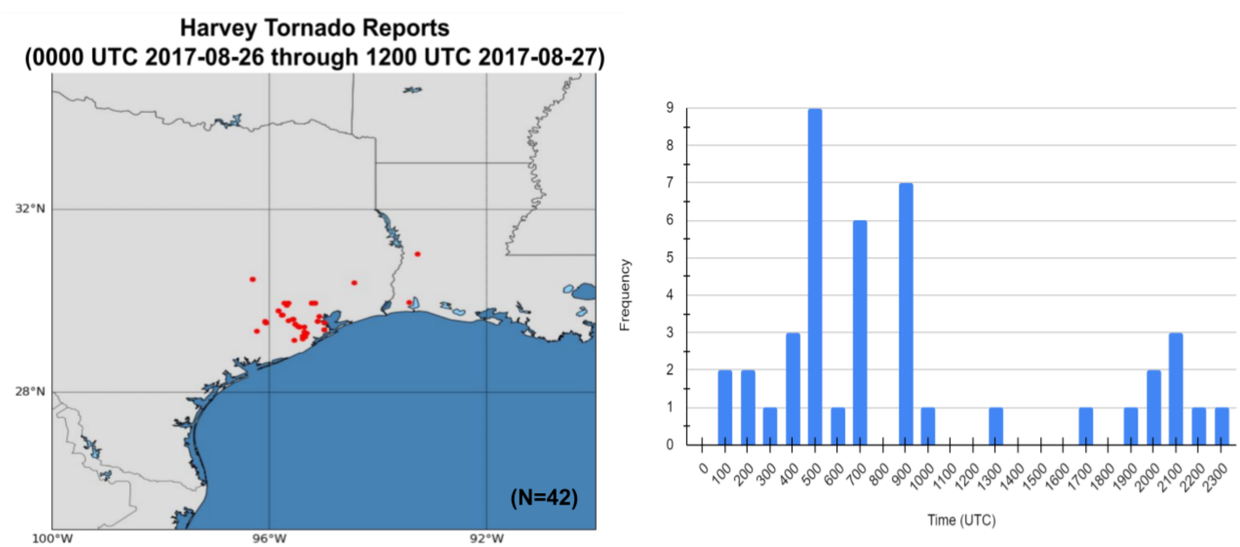

Figure 1.4: Storm Prediction Center (SPC) tornado reports (red, left) and the diurnal distribution of tornado reports (right) for 0000 UTC 26 August through 1200 UTC 27 August.

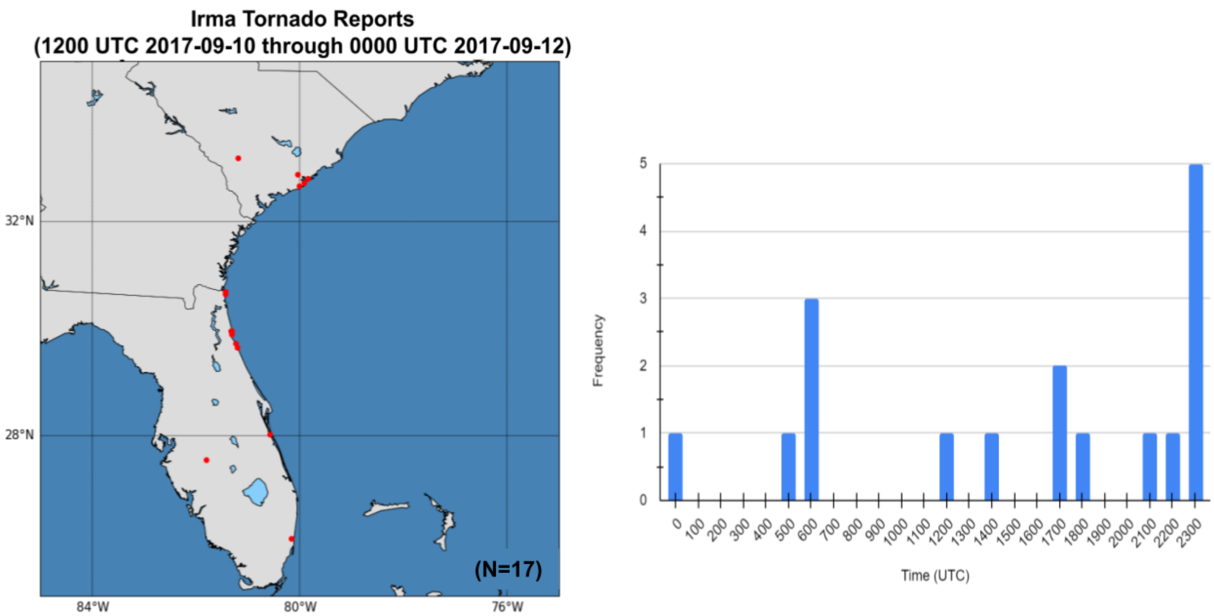

Figure 1.5: Storm Prediction Center (SPC) tornado reports (red, left) and the diurnal distribution of tornado reports (right) for 1200 UTC 10 September through 0000 UTC 12 September.

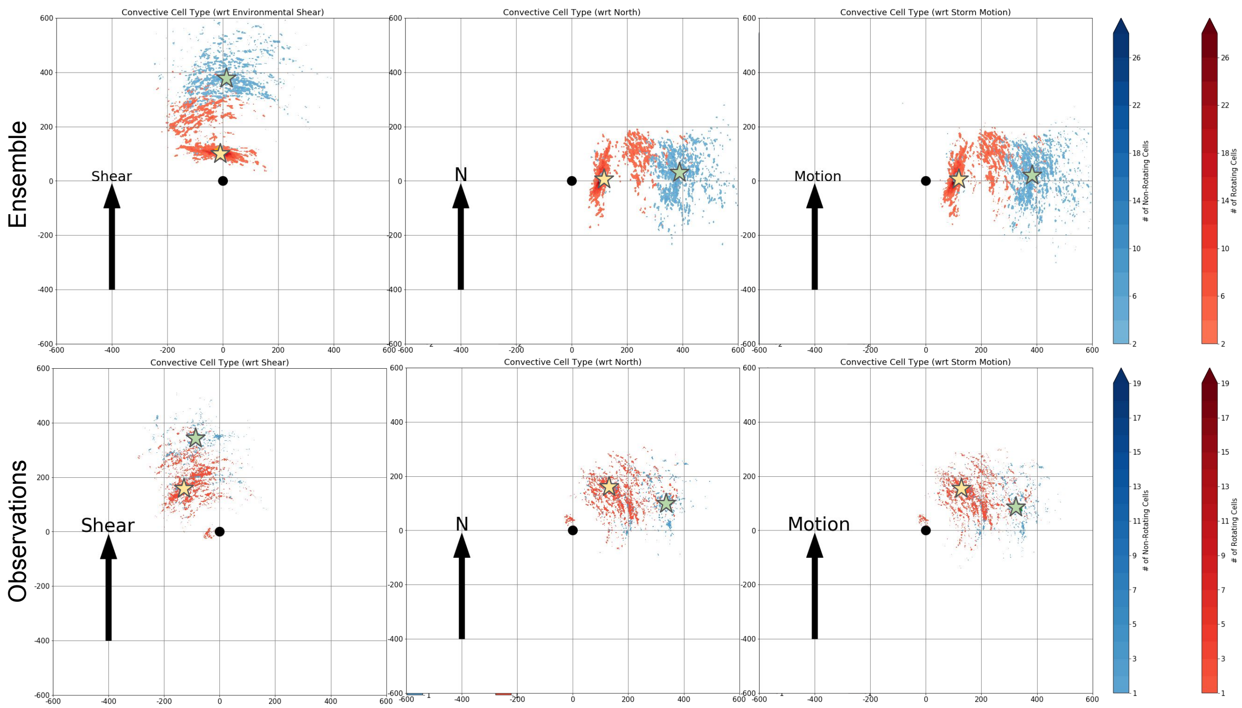

Figure 1.6: Distribution of rotating (red) and non-rotating (blue) cells in the NCAR ensemble initialized at 0000 UTC 26 August (top) and observations (bottom) with respect to vertical shear, north, and storm motion from 0000 UTC 26 August through 1200 UTC 27 August 2017. Center of mass of the rotating cells (yellow star) and non-rotating cells (green star). From Card (2019).

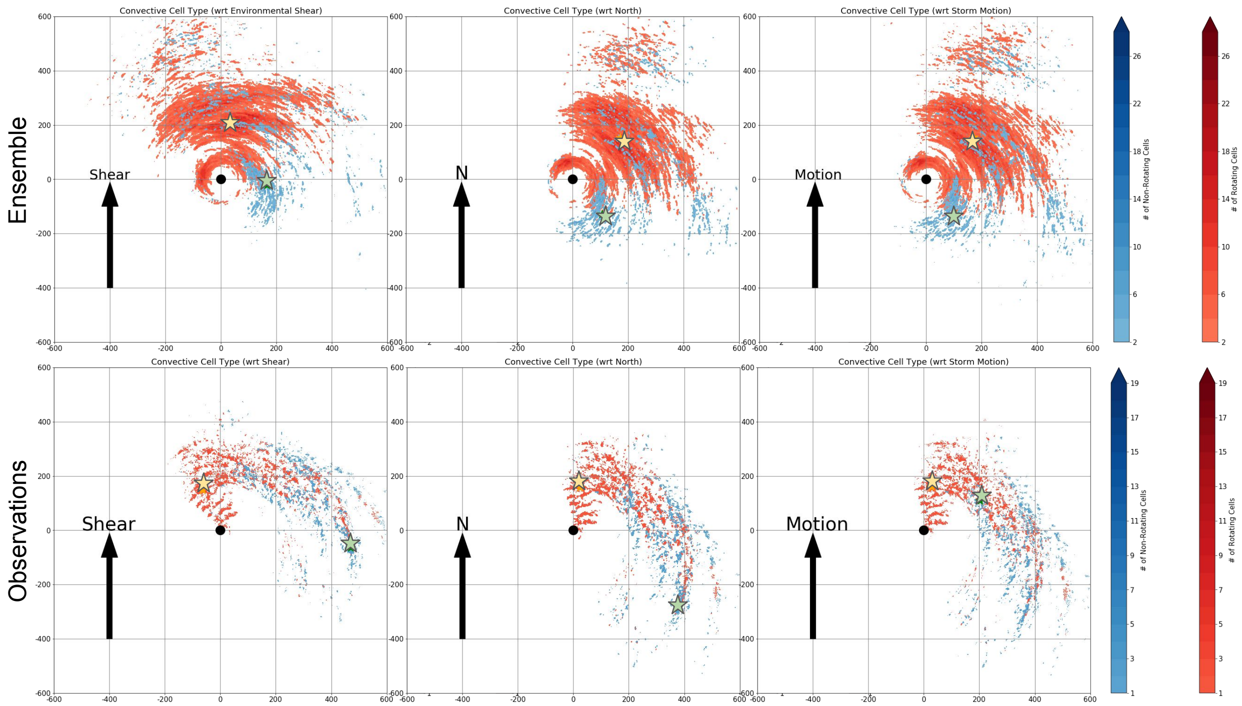

Figure 1.7: Same as Figure 1.6, but for Hurricane Irma (2017) from 1200 UTC 10 September through 0000 UTC 12 September 2017. The NCAR ensemble was initialized at 0000 UTC 10 September. From Card (2019).

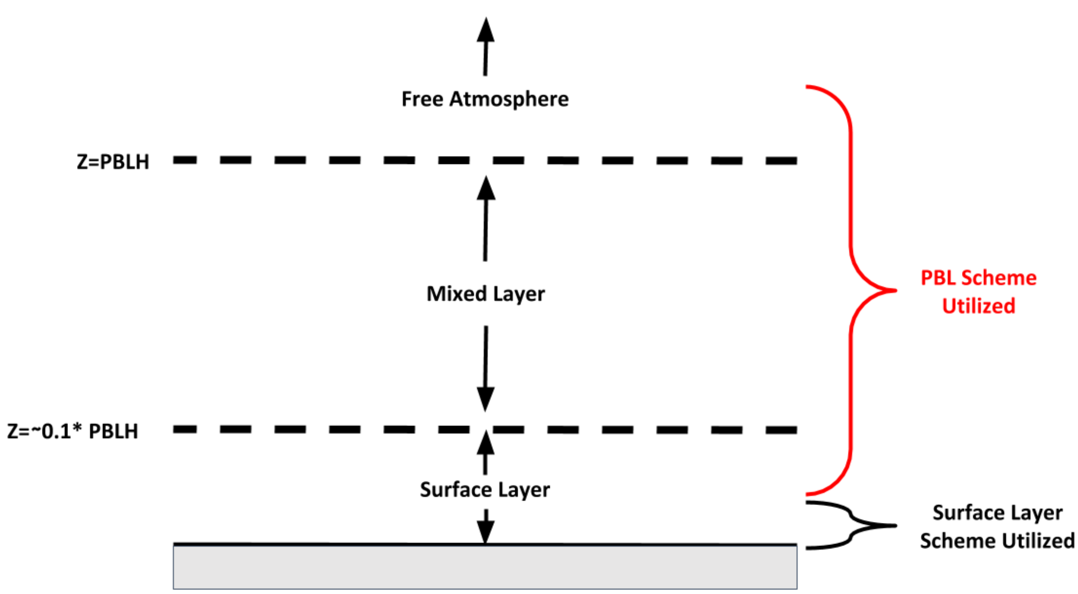

Figure 1.8: Schematic depicting the structure of the atmospheric boundary layer and the corresponding parts of the numerical weather model. Adapted from Kepert (2012).

2. Data and methodology

2.1 Weather Research and Forecasting model (WRF)

The Advanced Research WRF version 4.1 will be used in both the static and vortex-following nest configurations to run simulations of both hurricanes Harvey and Irma (2017). To efficiently use computing resources, an adaptive time step will also be utilized in all simulations. Each storm will be simulated in two separate steps, a 9-km run and then a separate 3-km run with a 1-km vortex following nest.

First, a 9-km horizontal grid spacing simulation (Domain 1) will be used to provide the initial and boundary conditions to the higher-resolution, and vortex-following, nests in the second set of simulations [Figs. 2.1a (350 X 300 gridpoints) and 2.2a (300 X 350 gridpoints)]. Domain 1 is run from 0000 UTC 24 August through 1200 UTC 27 August for Hurricane Harvey (2017) and 1200 UTC 8 September through 0000 UTC 12 September for Hurricane Irma (2017). These times allow 24 h for the model to spin up prior to using it as initial and boundary conditions for the second set of simulations. The fifth generation of European Centre for Medium-Range Weather Forecasts (ECMWF) atmospheric reanalysis (ERA5) (Copernicus Climate Change Service (C3S) 2019) is used for the initial and boundary conditions for the 9-km domain at three-hourly intervals. To help the simulation develop the storms' intensity and convection faster, the cumulus parameterization scheme New Tiedtke (Zhang et al. 2011a) was used. For consistency, the 9-km domain is run in multiple configurations covering all the PBL parameterizations to be tested in the second set of simulations. All of the 9-km simulations have a 10-hPa model top with 50 vertical levels.

The 3-km static domain (Domain 2) in the second set of simulations used the 9-km simulation as initial and boundary conditions [Figs. 2.1b (750 X 600 gridpoints) and 2.2b (600 X 750 gridpoints)]; however, this means that there is a one-way interaction between the 9-km and 3-km domains. The 1-km vortex following domain (Domain 3) is nested within Domain 2 [Figs. 2.1b and 2.2b (901 X 901 gridpoints)]. Convective processes are explicitly resolved in the 3-km and 1-km domains, therefore no convective parameterization was used. Both Domain 2 and 3 have a 50-hPa model top with 50 vertical levels, in part to slightly decrease the the average vertical grid spacing. In each of these simulations, the PBL scheme was the only parameterizations varied. Domains 2 and 3 were run from 0000 UTC 25 August through 1200 UTC 27 August for Hurricane Harvey (2017) and 1200 UTC 9 September through 0000 UTC 12 September for Hurricane Irma (2017). This timing will provide a 24-h adjustment period from model start to the analysis times.

The WRF model configuration was set following previous tropical cyclone studies (Gentry and Lackmann 2010; Sun and Barros 2012, 2014; Lackmann 2015; Carroll-Smith 2018). All three domains for each simulation used: the updated Rapid Radiative Transfer Model (RRTMG; Iacono et al. 2008) longwave and shortwave radiation schemes; the revised National Center for Atmospheric Research (NCAR) fifth-generation Mesoscale Model (MM5) Monin-Obukhov (Jiménez et al. 2012) surface layer parameterization; the Noah land surface model (Chen and Dudhia 2001); and, WRF double moment 6-class microphysics scheme (WDM6; Lim and Hong 2010). To improve the tropical cyclone surface fluxes the "isftcflx" option is activated such that Donelan (Donelan et al. 2004) and Garratt (Garratt 1977) formulations are used to calculate the surface moist enthalpy and momentum exchange coefficients in the surface layer (Lackmann 2015). Individual model parameterizations for each domain are located in Table 2.1.

2.2 Simulations of hurricanes Harvey and Irma (2017)

Figure 2.3a shows that the track of Hurricane Harvey (2017) in the 9-km simulation was very similar to the observed track in the Atlantic Best Track (Landsea and Franklin 2013) from 0000 UTC 24 August through 1200 UTC 27 August. Early in the 9-km simulation, the track of Harvey is slightly too far south between 0600 UTC 24 August and 0000 UTC

25 August. As a result, the 1-km simulations, shown in Figure 2.3b, are initialized slightly too far south and continue on a track south of that observed in the Best Track. The 1-km simulations penetrated similar distances inland compared to observations before beginning to turn back out to sea.

Figure 2.4a shows that the 9-km WRF simulation of Hurricane Harvey was initialized at a similar intensity to the observed Harvey, but remained much weaker than observed in the Atlantic Best Track from 0300 UTC 24 August through 1200 UTC 26 August. There is a divergence of the model simulations at 0000 UTC 25 August where the model simulation using the MYNN3 PBL scheme does not strengthen as rapidly as the other simulations. The most intense run is the model simulation using the YSU PBL parameterization, reaching a minimum sea level pressure of 965 hPa compared to the observed minimum sea level pressure of 942 hPa. Figure 2.4b shows that the 1-km WRF simulations were initialized at a weaker intensity than what was observed in the Best Track. The 1-km simulation using the MYNN3 PBL scheme also showed a weaker intensity compared to the other simulations over the first 24 h of the simulation.

Figure 2.5a shows that the track of Hurricane Irma (2017) in the 9-km simulation was very similar to the observed track in the Atlantic Best Track from 1200 UTC 8 September through 0000 UTC 12 September. The one major difference between the simulated and observed tracks is that the storm is slightly closer to Cuba from 0000 UTC 9 September through 0000 UTC 10 September in the model runs. Like the 9-km simulations, the 1-km simulations, shown in Figure 2.5b, produce very similar tracks to the Best Track along the entire analysis time. The simulated storms start off slightly closer to Cuba and turn northwards more quickly than in the observed track.

Figure 2.6a shows that the 9-km WRF simulation of Hurricane Irma was initialized and remained much weaker than the observed intensity from the Atlantic Best Track. This discrepancy in the intensity is not surprising since coarse resolution models such as the ERA5 (0.25° X 0.25°), which was used to initialize the 9-km WRF simulations, had a minimum sea level pressure at 1200 UTC 8 September of about 960 hPa. Although the simulations of Hurricane Harvey did better with respect to intensity than the Hurricane Irma simulations, this is most likely due to the fact that Hurricane Harvey was much weaker in observations at the start of the simulation compared to Hurricane Irma. The 9-km WRF simulations have Hurricane Irma maintaining intensity between 955 and 970 hPa before beginning to weaken after 0000 UTC 11 September. It is seen again that the weakest simulation uses the MYNN3 PBL scheme (Fig. 2.6a). Figure 2.6b shows that the 1-km simulations of Hurricane Irma were stronger than the 9-km simulations, reaching intensities between 965 and 945 hPa before weakening after 0000 UTC 11 September. The 1-km simulation did not become as intense as the observations from the Best Track. Like the 9-km simulation, the MYNN3 scheme 1-km simulation produced a less intense storm.

As a proxy for tropical cyclone size, the area of the tropical storm force winds (34 kt) at 10 m above mean sea level (MSL) in the model simulations and the area of the 34 kt wind from the Atlantic Best Track observations is shown in Figure 2.7. In the first 24 hours of the simulations for both hurricanes Harvey and Irma, the MYNN3 PBL simulations have the smallest area of tropical storm force winds. The YSU and ACM2 PBL simulations show fairly similar areas of tropical storm force winds across all times. Recall, Bu et al. (2017) showed that PBL parameterization can affect the size of tropical cyclones in models through modulating the vertical mixing of water vapor in the boundary layer which modulates convective activity in the outer core. In both Harvey and Irma, the area of 34 kt winds is larger in the observed storms compared to the simulated storms at all times, but the shapes of the curves are similar. The larger area of the 34 kt winds in observations can be contributed to the stronger storm. Recall, that the observed storm from the Atlantic Best Track was much stronger than the model simulations, which results in the larger are of 34 kt winds in the observations (Figs. 2.4 and 2.6).

2.3 Sensitivity tests

Sensitivity tests of two aspects of the model setup were investigated in order to ensure that the results were not unintentionally altered by choices in model methodology. First is the sensitivity of the one-way nest between the 9- and 3-km domains and second is the sensitivity of the simulations to the 50-hPa model top in the 3- and 1-km simulations. These tests were done by examining the differences between the 50-hPa model top simulation described in the methodology above and a new simulation with 10-hPa model top, and in a three-nest configuration of 9, 3, and 1 km of Hurricane Irma (2017). Both of these simulations utilize the WRF single moment 6-class (WSM6) microphysics scheme and the YSU PBL scheme. Figure 2.8a compares the intensity in terms of minimum sea level pressure of both simulations to observations. The 10-hPa model top simulation is weaker than both the 50-hPa model top simulations and the observations. Figure 2.8b shows the tracks of the two simulations compared to observations. We can see that the 10-hPa model top simulation has a track that is closer to the observed track of Hurricane Irma, although not by a large amount (∼30 km). The change in model methodology did not provide any large differences in terms of intensity and track.

Since the 9-km simulation does not receive feedback from the 3-km domain, discontinuities could occur between the model dynamics and the linear tendencies at the boundaries, which could result in an accumulation of mass, and therefore temperature anomalies, within a few grid points of the boundary (Torn et al. 2006). The outflow jet is the best place to look for such anomalies as the outflow in the 3-km domain may be drastically different to the outflow of the storm in the 9-km simulation. The issues would present as warm or cold temperature anomalies within a few grid points of the edge of the 3-km boundary and could be advected throughout the model domain. Figure 2.9 shows the 250-hPa temperature anomalies (from the 3-km domain mean) and wind for the 50-hPa model top (top) and the 10-hPa model top (bottom) simulations from 1200 UTC 9 September to 1200 UTC 10 September focused on the eastern half of the 3-km domain (which is where the outflow is located). Comparing the temperature anomalies between the two simulations, we see little in the way of difference at any of the presented times near the eastern 3-km boundary. The lack of large temperature anomalies in the outflow layer seems to suggest that the model dynamics of the 3-km domain and the linear tendencies provided by the 9-km domain are not discontinuous.

The 9-km simulations use a 10-hPa model top, whereas the 3- and 1-km simulations use a 50-hPa model top. The benefit of using a 50-hPa model top in the 3- and 1-km domains is to slightly decrease the average vertical grid spacing without altering the number of vertical levels; however, using a 50-hPa model top may be too low, which would act to limit deep convection as the damping layer below the 50-hPa model top could interfere with the tropical cyclone. Both the 10-hPa and 50-hPa model simulations use a w-Rayleigh damping layer extending 5 km below the model top. Figure 2.10 shows north–south vertical cross sections of reflectivity and temperature, as well as radial and tangential winds in the 1-km domain of a simulation with a 50-hPa model top (Figs. 2.10a and 2.10b) and with a 10-hPa model top (Figs. 2.10c and 2.10d). The beginning of the damping layer in both cross sections is denoted with a purple line. The simulation with the 50-hPa model top is 20 km in height with the damping layer beginning at 15 km. The simulation with the 10-hPa model top is 28 km in height with the damping layer beginning at 23 km. In both simulations, the beginning of the isothermal layer (tropopause) is located at 15 km, with the stratosphere beginning at around 18 km. In both simulations, the rainband convection at outer radii reaches very similar depths (∼9 km). The convection in the eyewall also reaches similar depths in both simulations (∼15 km).

In these sensitivity experiments, alteration to the domain methodology and the change from a 50- to 10-hPa model top did not produce appreciable differences in the modeled tropical cyclones in terms of depth of the convection, production of rainbands, location of features in the upper atmosphere (such as tropopause and the beginning of the stratosphere), intensity, or track. The findings of the model top sensitivity experiment are consistent with

Fovell and Su (2007) and Fovell et al. (2009) that tested the impacts of cloud microphysics on hurricane track in idealized experiments and also looked at how the depth of the domain impacted their experiments. Both Fovell and Su (2007) and Fovell et al. (2009) noted that increasing the domain depth from 50 to 1 hPa was not found to materially influence the storm structure or motion, independent of which microphysics scheme was used.

2.4 Tables and figures

Table 2.1: Select WRF version 4.1 model settings and parameterizations.

WRF Model Parameterizations:	**9-km Simulation (Domain 1)**	**3-km Simulation (Domain 2)**	**1-km Simulation (Domain 3)**	
Grid spacing	9 km	3 km	1 km	
Vertical levels (Model top)	50 (10 hPa)	50 (50 hPa)	50 (50 hPa)	
Vortex following (Level)	--	--	Yes (500 hPa)	
Long- and shortwave radiation parameterization	RRTMG	RRTMG	RRTMG	(Iacono et al. 2008)
Land surface model	Noah	Noah	Noah	(Chen and Dudhia 2001)
Surface layer physics	Revised MM5 Monin-Obukhov scheme	Revised MM5 Monin-Obukhov scheme	Revised MM5 Monin-Obukhov scheme	(Jimenez et al. 2012)
Other physics	TC surface fluxes	TC surface fluxes	TC surface fluxes	Donelan Cd + Garratt Ck (Lackmann 2015)
Cumulus parameterization	Tiedtke	--	--	(Zhang et. al 2011)
Microphysics	WDM6	WDM6	WDM6	(Lim and Hong 2010)
Planetary boundary layer	YSU, MYNN3, ACM2	YSU, MYNN3, ACM2	YSU, MYNN3, ACM2	(Hong et al. 2006), (Nakanishi and Niino 2006), (Pleim 2007a,b)

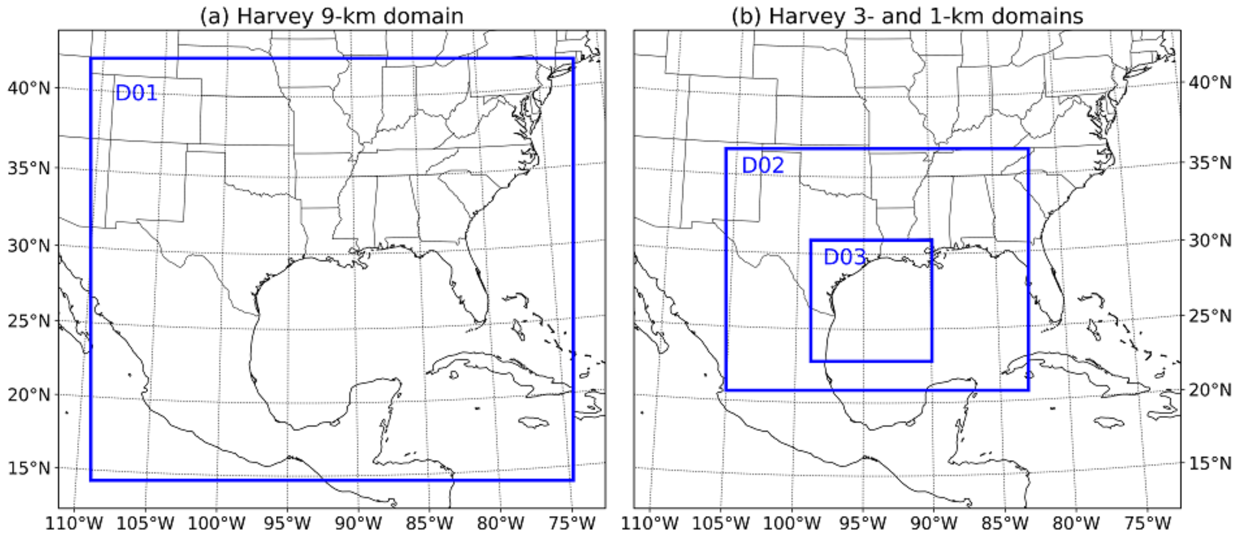

Figure 2.1: The WRF domains for Hurricane Harvey (2017): a) 9-km domain (D01, 350 X 300 gridpoints) and b) 3-km static domain (D02, 750 X 600 gridpoints) with 1-km vortex following domain (D03, 901 X 901 gridpoints).

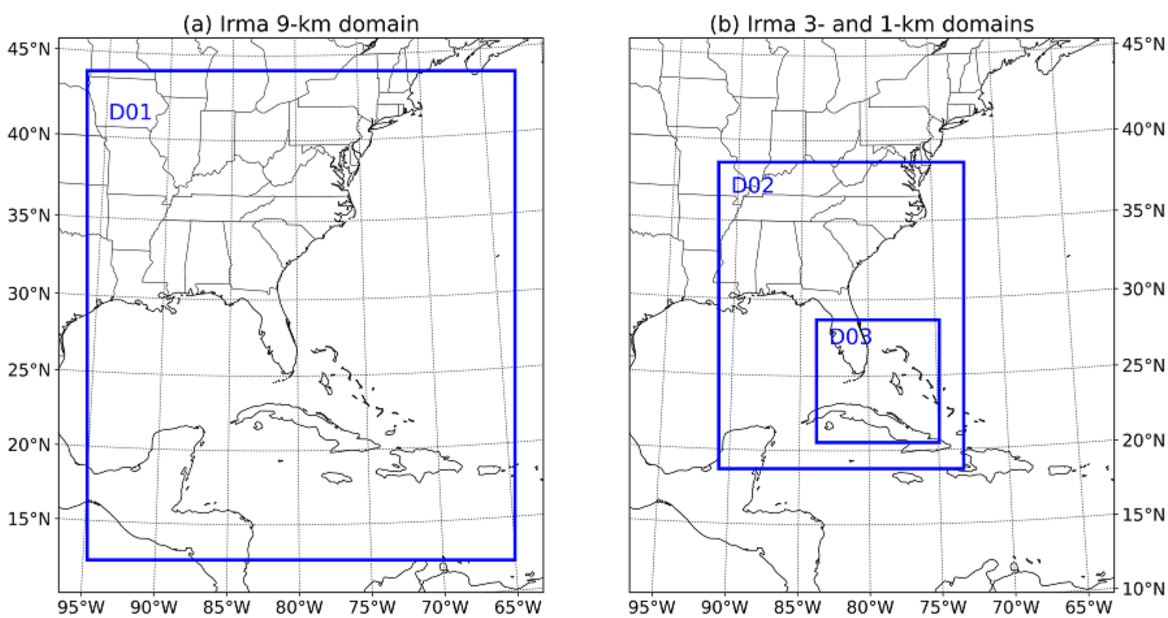

Figure 2.2: The WRF domains for Hurricane Irma (2017): a) 9-km domain (D01, 300 X 350 gridpoints) and b) 3-km static domain (D02, 600 X 750 gridpoints) with 1-km vortex following domain (D03, 901 X 901 gridpoints).

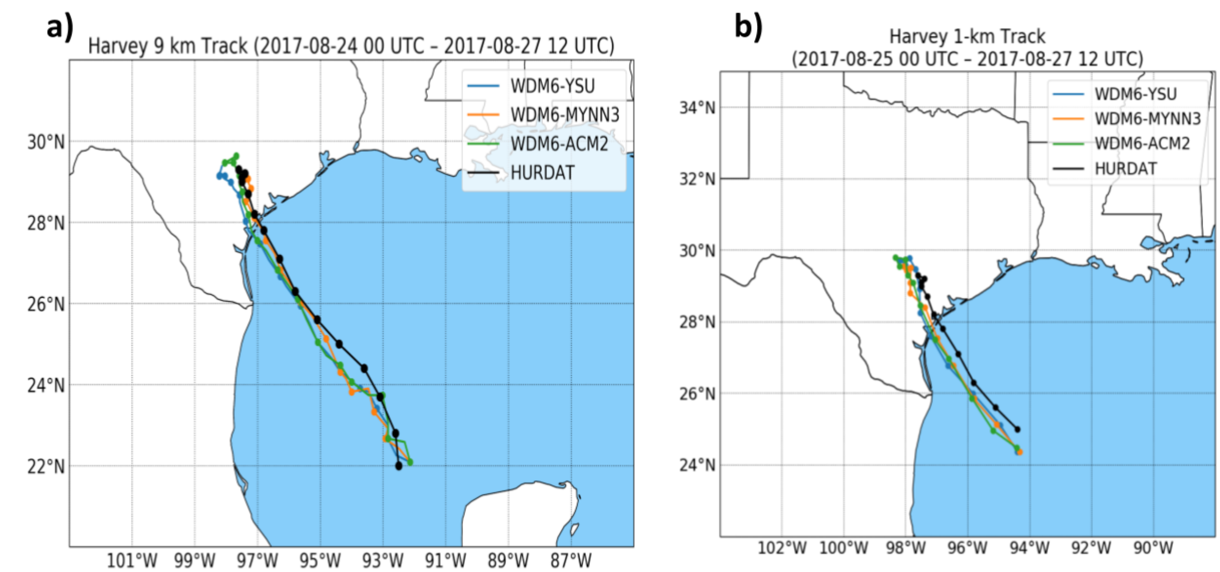

Figure 2.3: Tropical cyclone tracks using minimum mean sea level pressure for the a) 9-km WRF simulation initialized at 0000 UTC 24 August and b) 1-km WRF simulation initialized at 0000 UTC 25 August, compared to the Atlantic Best Track of Hurricane Harvey (2017) every 6 h.

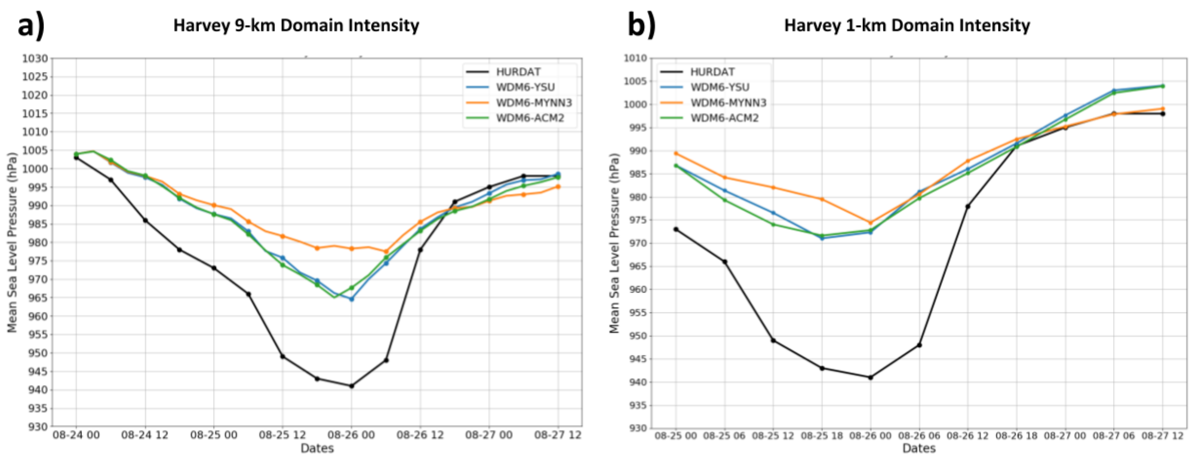

Figure 2.4: Intensity, in terms of minimum mean sea level pressure (hPa), for the a) 9-km WRF simulation initialized at 0000 UTC 24 August and b) 1-km WRF simulation initialized at 0000 UTC 25 August, compared to the Atlantic Best Track of Hurricane Harvey (2017) every 6 h.

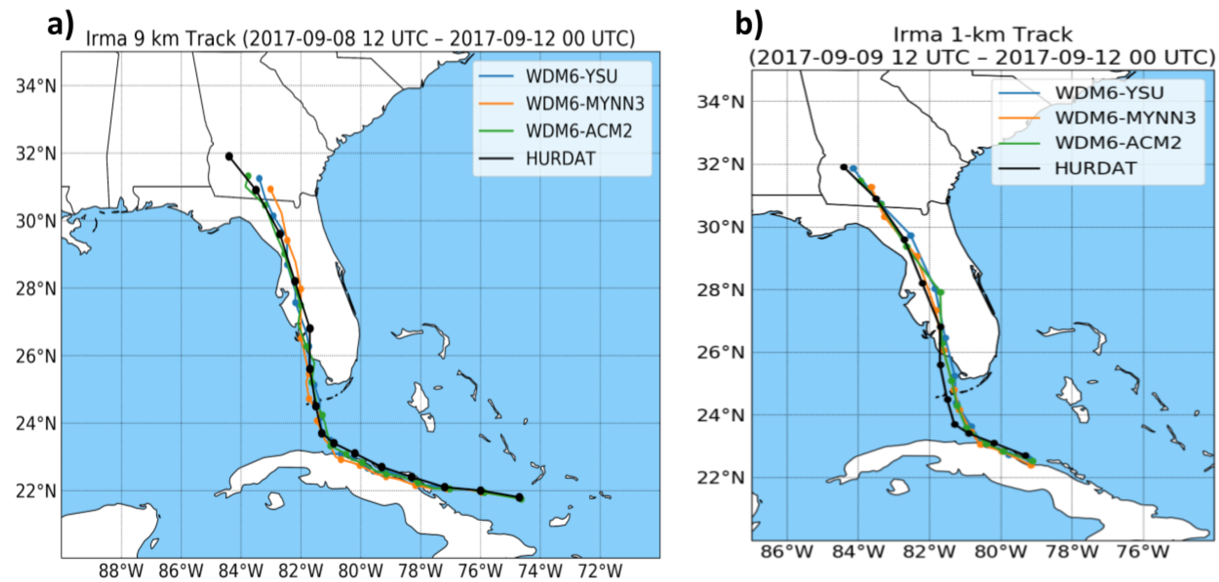

Figure 2.5: Tropical cyclone tracks using minimum mean sea level pressure for the a) 9-km WRF simulation initialized at 1200 UTC 8 September and b) 1-km WRF simulation initialized at 1200 UTC 9 September, compared to the Atlantic Best Track of Hurricane Irma (2017) every 6 h.

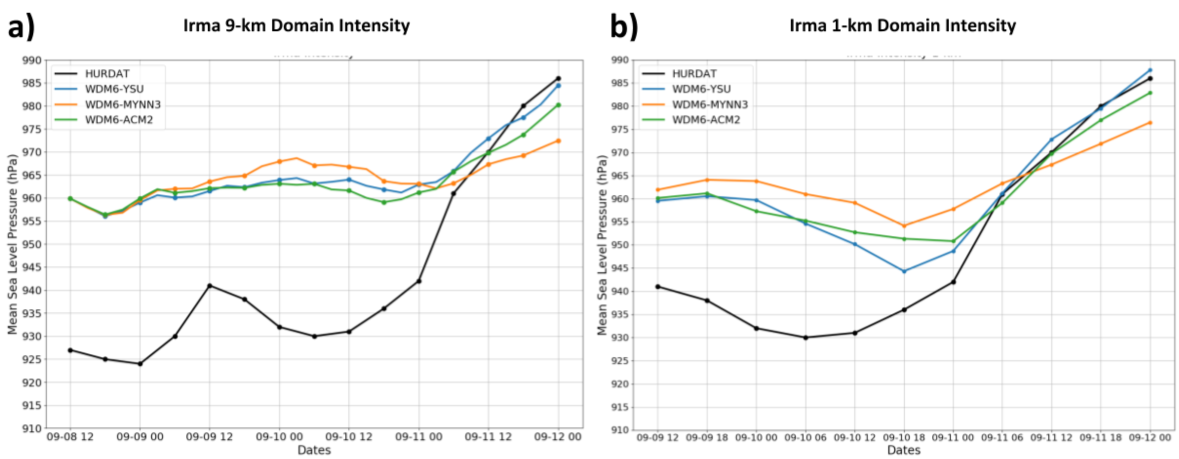

Figure 2.6: Intensity, in terms of minimum mean sea level pressure (hPa), from the a) 9-km WRF simulation initialized at 1200 UTC 8 September and b) 1-km WRF simulation initialized at 1200 UTC 9 September, compared to the Atlantic Best Track of Hurricane Irma (2017) every 6 h.

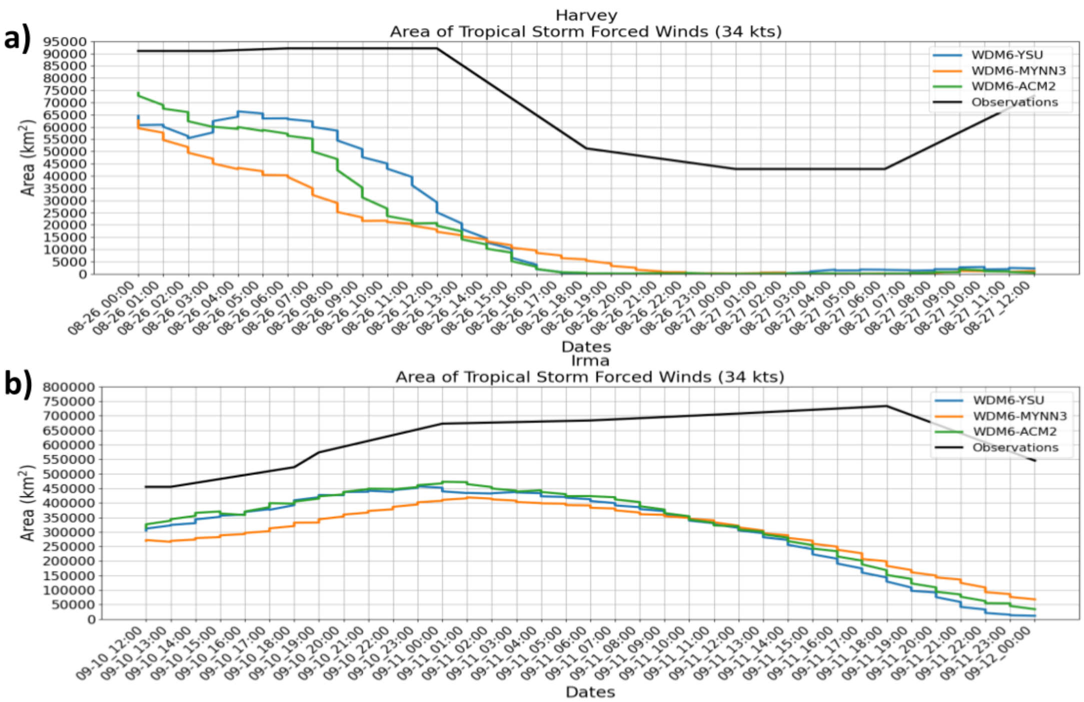

Figure 2.7: Tropical cyclone size in terms of area of tropical storm force winds (34 kt) for a) Hurricane Harvey (2017) and b) Hurricane Irma (2017).

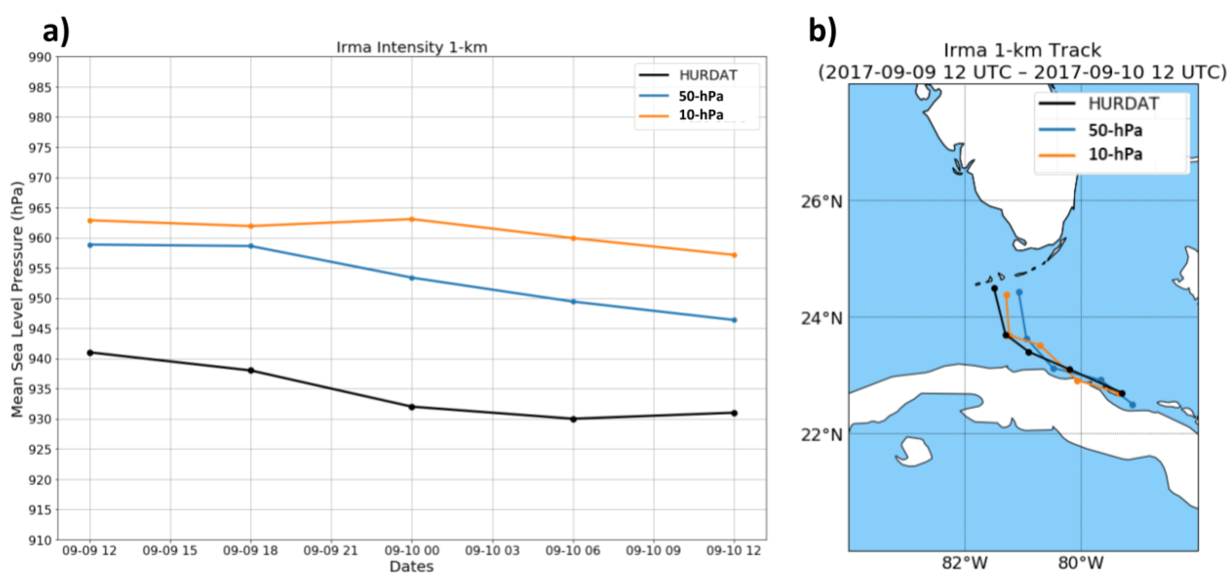

Figure 2.8: Sensitivity test simulations of Hurricane Irma (2017): a) intensity, in terms of minimum mean sea level pressure (hPa), and b) track compared to the Atlantic Best Track of Hurricane Irma (2017) every 6 h.

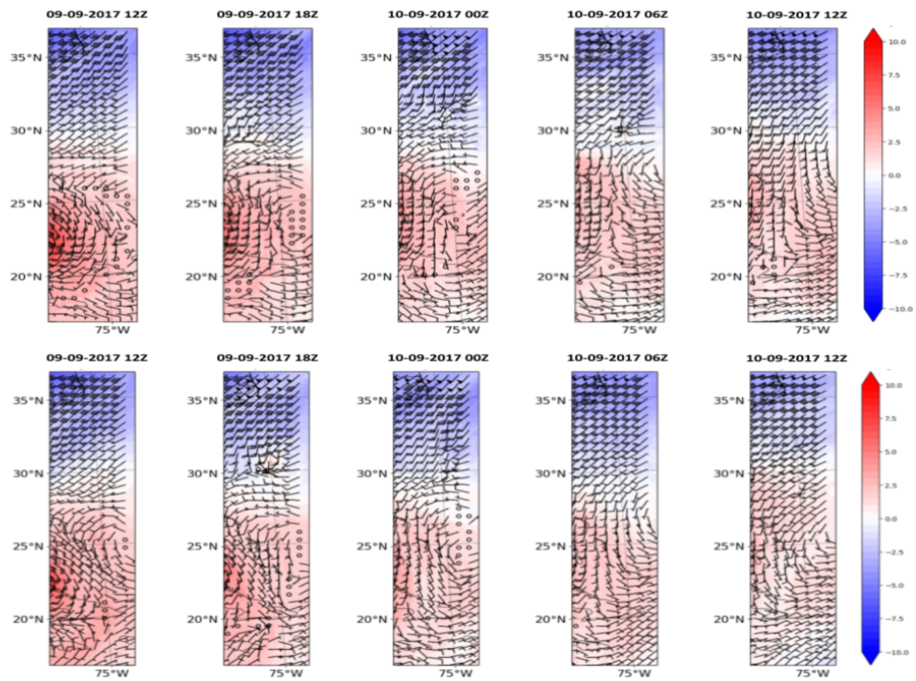

Figure 2.9: The 250-hPa temperature anomaly (K, shaded) and wind barbs (m/s, standard convention) are shown for the 50-hPa model top (top) and the 10-hPa model top (bottom) simulations of Hurricane Irma from 1200 UTC 9 September to 1200 UTC 10 September 2017.

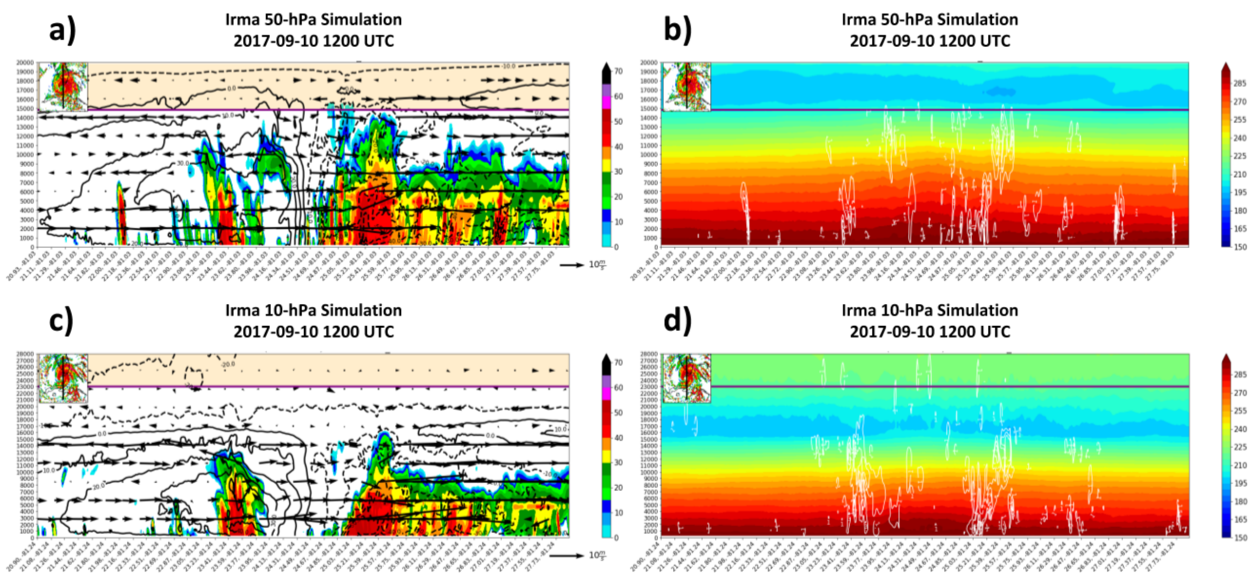

Figure 2.10: North–south cross section of the 50-hPa model top simulation of Hurricane Irma (2017) at 1200 UTC 10 September: a) reflectivity (dBZ, shaded), tangential wind (m/s, contours), radial wind (m/s, quivers), as well as the damping layer (yellow), with the bottom of this layer represented by the purple line, and b) temperature (K, shaded), upward vertical motion (m/s, contours), as well as a purple line representing the bottom of the damping layer. North–south cross section of the 10-hPa model top simulation of Hurricane Irma (2017) at 1200 UTC 10 September, c) same as a) and d) same as b).

3. Tropical cyclone convection

This chapter will discuss the spatial and temporal distribution of non-rotating and rotating convective cells in tropical cyclones Harvey and Irma (2017). The differences in the convective environments will also be investigated. Composite vertical cross sections will be used to identify discernible differences between the non-rotating and rotating cells, and emphasis will be placed on the differences in the environments across the PBL schemes.

The distributions of rotating and non-rotating cells are examined with respect to vertical wind shear and with respect to geographic north. Card (2019) and the storm tracks in Figures 2.3 and 2.5 showed that for hurricanes Harvey and Irma (2017), the storm motion was mostly northerly making the results very comparable to the distributions with respect to geographic north. In Card (2019), the number of identified rotating storms outnumbered the identified non-rotating storms by a factor of two to three in both Harvey and Irma (2017). In Hurricane Harvey, most rotating and non-rotating storms occurred directly downshear, with non-rotating storms generally occurring at more distant radii (Fig. 1.6). Most of the rotating storms in Hurricane Irma occurred directly downshear, while most of the non-rotating storms occurred upshear right in both the NCAR ensemble and in observations (Fig. 1.7).

3.1 Cell identification

To investigate the effects PBL parameterizations have on the distribution of rotating and non-rotating convection, an analysis using techniques similar to Card (2019) and Carroll-Smith et al. (2019) are conducted on the 1-km WRF domain. First, individual convective cells are identified using local maxima in model reflectivity exceeding the 99.9^{th} percentile across all the hours of a simulation. The identified cells are referred to as rotating convective cells if the 0–3-km updraft helicity exceeds the 99.95^{th} percentile, similar to the tropical cyclone tornado surrogates in Carroll-Smith et al. (2019) and Card (2019). The identified cells that had values of 0–3-km updraft helicity less than or equal to zero and that exceeded the 99.9^{th} percentile in updraft velocity, are referred to as non-rotating convective cells. Based on these criteria, the non-rotating convective cells have no updraft helicity but strong updraft velocities, while rotating cells have large updraft helicity. These percentile values for hurricanes Harvey and Irma (2017) can be seen in Tables 3.1 and 3.2, respectively. Identified cells were also restricted from being with 5 km radius of other identified cells to reduce the double counting of individual cells. The 5 km radius is set based on the observations of Eastin and Link (2009) which saw rotating cells in Hurricane Ivan were typically 2.5–3.5 km in radius.

The rotating and non-rotating cell thresholds show the first indication of differences across PBL schemes. The 99.9^{th} percentile in model reflectivity, 99.9^{th} percentile in updraft velocity, and the 99.95^{th} percentile in 0–3-km updraft helicity were all statistically significantly[1] different across the PBL parameterizations. Tables 3.1 and 3.2 also show that the 99.9^{th} percentile in updraft velocity and the 99.95^{th} percentile in 0–3-km updraft helicity was statistically significantly lower in the simulations using the MYNN3 PBL scheme.

Once cell types are identified, how varying the planetary boundary layer scheme changes the spatial distribution of rotating and non-rotating convective cells will be examined with respect to both the cell distance from the coast and the organization around the tropical cyclone.

3.2 Convective cell distribution

3.2.1 Spatial distribution of convection

The location of convection in tropical cyclones can be influenced by two main factors, the location of land that can be described in a geographical-relative sense and vertical wind shear that can be described in a shear-relative sense.

The location of both rotating and non-rotating convective cells summed across all the

[1]Statistical significance is determined via a two sided t-test for the means of two independent samples at the 99% confidence level.

Harvey simulations is shown in Figure 3.1. The distribution with respect to north is shown in Figure 3.1a and the distribution with respect to shear is shown in Figure 3.1b for Hurricane Harvey from 0000 UTC 26 August 2017 to 1200 UTC 27 August 2017. In the simulations of Hurricane Harvey, more non-rotating cells were identified compared to rotating cells, with 4261 and 3319, cells respectively. The simulations of Harvey showed that the number of identified non-rotating cells are about 22% greater than the number of identified rotating cells (Fig. 3.1). In Figure 3.1a, the non-rotating cells are located generally east and southeast of the tropical cyclone center with the rotating cells located generally northeast of the tropical cyclone center.

Figure 3.2 shows the distribution of rotating and non-rotating cells with respect to the geography of the region in the three PBL simulations. Most of the rotating convection is near and over the Texas coast, and penetrates further inland than the non-rotating cells. The non-rotating cells are generally located over the Gulf of Mexico. In Figure 3.1b, both the rotating and non-rotating convective cells occur directly downshear of the tropical cyclone center; however, the rotating cells tend to be located closer the the center compared to the non-rotating cells. An astute eye may notice that the rotating and non-rotating cells tend to be identified along curved arcs around the tropical cyclone center, which can be best summarized as rainbands. The rainbands, rotating, and non-rotating cells can be seen in the reflectivity of the Harvey simulations [`http://www.atmos.albany.edu/student/dcard/files/Animation_Harvey_1km.html`].

Figure 3.3 shows the breakdown of rotating and non-rotating cells for each PBL scheme simulation for Hurricane Harvey. As in Figure 3.1, for all individual PBL schemes tested, the number of identified non-rotating cells outnumber the number of identified rotating cells. The YSU, MYNN3, and ACM2 simulations of Harvey show that the number of identified non-rotating cells is 14%, 36%, and 8% greater than the number of identified rotating cells, respectively (Fig. 3.3). The MYNN3 PBL scheme identified more rotating cells (∼100 more) and many more non-rotating cells compared to the YSU and ACM2 PBL schemes. There are also some differences in the distributions of the rotating and non-rotating cells across the different PBL schemes. With respect to north, the YSU scheme shows the non-rotating cells in the southeast quadrant, more spatially confined than in the other two simulations, with very few non-rotating cells beyond 250 km from the center in this quadrant (Fig. 3.3a). The non-rotating cells are mainly confined to the southeast quadrants in the YSU and ACM2 simulations. The non-rotating cells tend to spread further into the northeast quadrant in the MYNN3 simulation. With respect to shear in Figure 3.3b, most identified rotating convection in each simulation is located in the downshear-left quadrant, while the non-rotating convection is generally identified directly downshear. In the MYNN3 simulation, there tends to be more non-rotating cells identified in the downshear-right quadrant, which is very different from the other two simulations.

Figure 3.4 shows the distributions of distances of the rotating and non-rotating cells from the center of Hurricane Harvey. The mean distances of rotating cells from the center are 234 km, 278 km, and 235 km for the YSU, MYNN3, and ACM2 PBL simulations, respectively. The mean distances of non-rotating cells from the center are 286 km, 378 km, and 316 km for the YSU, MYNN3, and ACM2 PBL schemes, respectively. Across the PBL schemes, rotating cells are statistically significantly[2] closer to the tropical cyclone center than the non-rotating cells ($p < 0.001$). The identified rotating cells from the MYNN3 simulation are statistically significantly further from the center of Hurricane Harvey compared to both the YSU ($p < 0.001$) and ACM2 ($p < 0.001$) simulations. There was no statistical significance between the distances from the center in the YSU and ACM2 simulations ($p < 0.248$). The identified non-rotating cells in the MYNN3 simulation are statistically significantly further from the center of Hurricane Harvey compared to the YSU ($p < 0.001$) and ACM2 ($p < 0.001$) simulations, even though the storm was smaller in the MYNN3 simulation (Fig. 2.7). The non-rotating cells in the YSU are also statistically significantly closer the the tropical cyclone center compared to the ACM2 ($p < 0.001$) simulation.

[2]Statistical significance is determined via a Mann-Whitney rank test at the 99.5% confidence level.

Figure 3.5 shows the locations for both rotating and non-rotating convective cells summed across all of the Irma simulations. Figure 3.5a shows the distribution with respect to north and Figure 3.5b shows the distribution with respect to shear from 1200 UTC 10 September to 0000 UTC 12 September 2017. In the simulations of Hurricane Irma, similar numbers of non-rotating cells are identified compared to rotating cells, with 1272 and 1543 cells, respectively. The simulations of Irma showed that the number of identified non-rotating cells are about 18% less than the number of identified rotating cells (Fig. 3.5). In Figure 3.5a, the non-rotating cells are located generally east of the tropical cyclone center with the rotating cells located generally northeast of the tropical cyclone center.

Figure 3.6 shows the locations of identified rotating and non-rotating convection in the three PBL simulations of Hurricane Irma. Most of the identified cells are off the east coast of Florida; however, the non-rotating cells tend to be located over the ocean more than over land. In Figure 3.5b, similar to Hurricane Harvey, both the rotating and non-rotating cells tend to be located directly downshear of the tropical cyclone center. Some non-rotating cells extend into the upshear-right quadrant of Irma. Again as in Hurricane Harvey, the identified rotating and non-rotating cells tend to be positioned along curved arcs representing that they are part of hurricane rainbands. The rainbands, rotating, and non-rotating cells can be seen in the reflectivity of the Irma simulations [`http://www.atmos.albany.edu/student/dcard/files/Animation_Irma_1km.html`].

Figure 3.7 shows the breakdown of rotating and non-rotating cells for each PBL scheme simulation. The YSU and MYNN3 simulations of Irma show that the number of identified non-rotating cells is 46% and 16% less than the number of identified rotating cells, respectively (Fig. 3.7). The ACM2 simulation of Irma show the number of identified non-rotating cells is 18% greater than the number of identified rotating cells, which is in line with the results from the Harvey simulations (Fig. 3.7). The MYNN3 PBL scheme identified more rotating (∼100–200 more) and non-rotating (∼100–200 more) cells compared to the YSU and ACM2 PBL schemes. The YSU simulation is interesting in that it is the only simulation which identified more rotating cells than non-rotating cells in the Irma simulations. There are also some differences in the distributions of the rotating and non-rotating cells across the different PBL schemes. With respect to north, all simulations show that most non-rotating cells are identified in the northeast quadrant, although the MYNN3 simulation does show some non-rotating cells in the southeast quadrant (Fig. 3.7a). The YSU and MYNN3 simulations show the non-rotating cells are mainly displaced further radially outward from the center compared to the rotating cells (Fig. 3.7a). With respect to shear (Fig. 3.7b), most identified rotating and non-rotating convection in each simulation is located in the downshear quadrants; however, the non-rotating cells tend to be located further radially outward from the tropical cyclone center in the YSU and MYNN3 simulations. In the MYNN3 simulation, there tends to be more non-rotating cells identified in the downshear-right quadrant, which is very different from the other two simulations.

Figure 3.8 shows the distributions of distances of the rotating and non-rotating cells from the center of Hurricane Irma. The mean distances of rotating cells from the center of Irma are 297 km, 284 km, and 284 km for the YSU, MYNN3, and ACM2 PBL schemes, respectively. The mean distances of non-rotating cells from the center of Irma are 365 km, 372 km, and 336 km for the YSU, MYNN3, and ACM2 PBL schemes, respectively. Like in the simulations of Harvey, the rotating cells in the simulations of Irma are statistically significantly closer to the tropical cyclone center than the non-rotating cells ($p < 0.001$) across all PBL schemes. None of the simulations show statistically significantly different distances for the rotating cells across the PBL schemes ($p > 0.005$). The identified non-rotating cells in the ACM2 simulation are statistically significantly closer to the center of Hurricane Irma than both the YSU ($p < 0.001$) and MYNN3 ($p < 0.001$) simulations. There is not a statistically significance difference between the distance of non-rotating cells from the center in the YSU and MYNN3 ($p = 0.005$) simulations.

To summarize, the distribution of identified non-rotating cells in the simulations of both hurricanes Harvey and Irma occur east of the tropical cyclone center and in the downshear, particularly, downshear-right quadrants. Cells identified as rotating are generally located in the northeast quadrant and typically downshear, especially in the downshear-left quadrant. This distribution is largely in agreement with the expected distribution of convection downshear in tropical cyclones experiencing vertical wind shear (Corbosiero and Molinari 2003). The typical locations of rotating convection in the northeast quadrant (with respect to north), seen in Figures 3.1a and 3.5a, concurs with the findings of McCaul (1991), Schultz and Cecil (2009), and Edwards (2012), which examined various periods of tropical cyclone tornado reports and also found a maximum in the northeast quadrant. Card (2019) examined the location of rotating and non-rotating convection in hurricanes Harvey and Irma using the NCAR ensemble (Figs. 1.6 and 1.7), the results of which are very similar to the distributions shown in these simulations (Figs. 3.1 and 3.5). The analyses conducted also show that there are variations in the distributions across the three PBL schemes tested. The MYNN3 PBL scheme identifies more rotating and non-rotating cells than the YSU and ACM2 in both hurricanes Harvey and Irma. The identified rotating cells tend to be statistically significantly closer to the tropical cyclone center compared to the non-rotating cells in both hurricanes Harvey and Irma as well as across all PBL schemes tested. Note that the rotating cells being closer to the center suggests that the non-rotating cells are located at the beginning of the rainbands while rotating cells are located in the more mature part of the rainband (i.e., closer to the terminus), closer to the center of the tropical cyclone.

3.2.2 Temporal distribution of convection

Over the run time of the simulations, the number of rotating and non-rotating convective cells at any given time is expected to vary. The number of rotating and non-rotating cells over time are shown in Figures 3.9 and 3.10 for Harvey and Irma, respectively.

The number of rotating and non-rotating cells in the YSU and ACM2 PBL schemes are similar over most time periods in the simulations of Hurricane Harvey (Fig. 3.9). The MYNN3 simulation shows a slight under prediction of rotating cells in the first 16 h of analysis and a general over prediction of non-rotating cells compared to the YSU and ACM2 simulations in Harvey (Fig. 3.9). The number of identified non-rotating cells tends to follow a diurnal cycle increasing in frequency in the early morning hours (0700 UTC, 2 AM CDT), peaking around 1400 UTC (9 AM CDT), and declining in frequency through a minimum at around 0000 UTC (7 PM CDT) in all simulations, although the magnitudes differ (Fig. 3.9). The frequency of rotating cells tends to vary less over the diurnal cycle compared to the non-rotating cells. In the YSU and ACM2 PBL simulations, the number of rotating cells tends to have a broad peak beginning in the morning (1200 UTC, 7 AM CDT) and ending in the early afternoon (1800 UTC, 1 PM CDT) before hitting a minimum in the evening (2000 UTC, 3 PM CDT); however, the MYNN3 PBL simulation shows a more static number of rotating cells over time (Fig. 3.9).

The number of rotating cells in the simulations of Hurricane Irma is similar across all of the PBL schemes; however, in the second half of the first 24 h of the simulations, analysis period the MYNN3 PBL scheme tends to have more identified rotating cells than the YSU and ACM2 simulations (Fig. 3.10). In Hurricane Irma there tends to be a broad peak in both rotating and non-rotating cells in Figure 3.10 from the afternoon hours local time (2000 UTC, 4 PM EDT) through the early morning hours (0900 UTC, 5 AM EDT).

The peaks in rotating and non-rotating cells are different when comparing the simulations of hurricanes Harvey and Irma, even with respect to local time. The pattern of peaks in the rotating cells from the simulations directly contradicts the results of numerous studies that looked at the diurnal signal in tropical cyclone tornado reports. McCaul (1991) showed that 57% of tropical cyclone tornadoes occur between 1400–2300 UTC (corresponding roughly to 0900–1800 local time in the southeastern U.S.). Schultz and Cecil (2009) concurred, finding a pronounced peak in tropical cyclone tornado reports in the early to mid afternoon, with similar findings in Edwards (2012). The observed tornado reports from Harvey show a peak from 0400–1000 UTC and between 1700–2300 UTC in Irma (Figs. 1.4 and 1.5), which does not align well with the expected distributions for the previously discussed climatological studies (McCaul 1991; Schultz and Cecil 2009; Edwards 2012). The identified rotating cells in the Harvey simulations peak between 0400 and 1200 UTC on 26 August, corresponding to 2300–0700 local time (Fig. 3.9 top), and the increase in frequency of the identified rotating cells in the Irma simulations tended to be broad and occur overnight between 2000–0900 UTC, corresponding to 1600–0500 local time (Fig. 3.10 top).

The peaks in identified rotating convection occur at different times than climatologies of observed tropical cyclone tornado reports (McCaul 1991; Schultz and Cecil 2009; Edwards 2012), but align well with the observed peaks in tornado reports in both Harvey and Irma (Figs. 1.4 and 1.5). The observed peaks in tornado reports aligns well with peaks in the identified rotating cells in the simulations suggesting that the identification techniques for tropical cyclone tornado surrogates are appropriate for the simulations of hurricanes Harvey and Irma, as well as in the simulation of Hurricane Ivan from Carroll-Smith et al. (2019). This could be for two reasons. First, since the past literature relies on observations (McCaul 1991; Schultz and Cecil 2009; Edwards 2012), there may be a bias towards tornado reports during the day, as well as bias in reporting due to evacuations and/or verifying reports in areas of substantial post storm damage (caused by wind, flooding, or storm surge) as noted in Edwards (2012). Lastly, there are generally no reports of tornadoes over the ocean (water spouts), although strongly rotating cells have been identified approaching the coastline in observations and model simulations (Baker et al. 2009; Eastin and Link 2009; Card 2019).

3.3 Convective cells and geography

As discussed in the Introduction, the convective environments can largely differ between the land and ocean. Differences both spatially and temporally in the identified cells in both hurricanes Harvey and Irma suggest that the location of identified rotating and non-rotating convection may be sensitive to the location of the coastline.

The counts of identified rotating cells over land and over ocean in the simulations of Hurricane Harvey are shown in Figure 3.11. The number of rotating cells over land generally outnumbers the number of rotating cells over the ocean; at some times, this difference is a factor of three across the different PBL schemes. There is also much more variability in the number of rotating cells over the land compared to over the ocean. Included in that variability is somewhat of a diurnal cycle in the rotating convection over land with a broad peak in rotating cell identification from 0600 UTC (12 AM CDT) to 1600 UTC (11 AM CDT). This variation does not occur over the ocean, with the number of rotating cells in each simulation being very consistent with time.

The counts of identified non-rotating cells over land and over ocean for Hurricane Harvey are shown in Figure 3.12. Unlike the identified rotating cells, the identified non-rotating cells tend to have diurnal variation over both the land and ocean. The number of non-rotating cells on land is fairly similar across all the PBL schemes. The number of oceanic non-rotating cells, however, outnumbers the land cells by a factor of three to four in the MYNN3 simulation over the first 18 h of the analysis.

The counts of identified rotating cells over land and over ocean in the simulations of Hurricane Irma are shown in Figure 3.13. There are generally more rotating cells identified over the ocean compared to land. The identification of oceanic rotating cells has a broad peak from 2000 UTC (4 PM EDT) through 1200 UTC (8 AM EDT). Between 0200 UTC and 1200 UTC, the number of identified rotating land cells in the MYNN3 simulation of Hurricane Irma is much greater than in the YSU or ACM2 simulations.

The counts of identified non-rotating cells over land and over ocean in the simulations of Hurricane Irma are shown in Figure 3.14. There are very few non-rotating cells over land in the Hurricane Irma simulations and many more over the ocean, not surprising since the land area of the Florida peninsula is small. The oceanic non-rotating cells show somewhat of a diurnal signal with a peak around 0100 UTC (9 PM EDT). Similar to the simulations of Hurricane Harvey, the MYNN3 PBL simulations of Irma also have periods where there are two to three times more oceanic non-rotating cells are identified compared to the YSU and ACM2 PBL schemes.

It is important to note that the analysis of the number of cells on land and over the ocean is highly dependent on the local geography. The track plots (Figs. 3.2 and 3.6) show the extent of land area in both simulation differs drastically. The Harvey simulations have much more land than the Irma simulations. Although the simulations produced similar sized storms with respect to the area of the tropical storm forced winds (Fig. 2.7), the MYNN3 PBL simulations did create a smaller storm in comparison to the YSU and ACM2 simulations in both Harvey and Irma. Figure 3.15 shows the locations of identified rotating and non-rotating cells with respect to the geography of the individual simulations from 0000 UTC 26 August through 1200 UTC 27 August in Hurricane Harvey (Fig. 3.15 top) and 1200 UTC 10 September through 0000 UTC 12 September in Hurricane Irma (Fig. 3.15 bottom). In the simulations of Hurricane Harvey across all three PBL schemes (Fig. 3.15 top), there are more rotating cells over Texas and Louisiana than non-rotating cells (Fig. 3.2). There is a similar trend in the simulations of Hurricane Irma across all three PBL schemes (Fig. 3.15 bottom), where there are more rotating cells over Florida and Georgia compared to non-rotating cells (Fig. 3.6).

Rotating cells tend to be closer to the coast than non-rotating cells. Figures 3.16 and 3.17 show the frequency of the distance of both rotating and non-rotating cells from land for the simulations of Hurricane Harvey and Hurricane Irma, respectively. For the simulations of Hurricane Harvey (Fig. 3.16), the mean distance from land of the rotating cells is 65 km for the YSU simulation, 100 km for the MYNN3 simulation, and 60 km for the ACM2 simulation. The mean distance from land of non-rotating cells is 70 km for the YSU simulation, 130 km for the MYNN3 simulation, and 65 km for the ACM2 simulation. For each of the Harvey simulations, the non-rotating cells were statistically significantly further from land than the rotating cells ($p < 0.001$). Both the rotating and non-rotating cells in the MYNN3 Harvey simulation were statistically significantly further from the coast than both the YSU ($p < 0.001$) and ACM2 ($p < 0.001$) simulations. The rotating cells in the ACM2 Harvey simulation were also statistically significantly further from the coast than the rotating cells in the YSU simulation ($p = 0.003$). There was no statistical significance between the distance from the coast in the non-rotating cells in the YSU and ACM2 simulations ($p = 0.303$).

For the simulations of Hurricane Irma (Fig. 3.17), the mean distance from land of the rotating cells is 105 km for the YSU simulation, 120 km for the MYNN3 simulation, and 90 km for the ACM2 simulation. The mean distance from land of the non-rotating cells is 190 km for the YSU simulation, 205 km for the MYNN3 simulation, and 150 km for the ACM2 simulation. For each of the Irma simulations, the non-rotating cells were statistically significantly further from land than the rotating cells ($p < 0.001$). The rotating cells in the MYNN3 Irma simulation were statistically significantly further from the coast than the YSU simulation ($p < 0.004$); however, distances in the ACM2 simulation are not statistically significantly different from the YSU ($p = 0.066$) and MYNN3 ($p = 0.166$) simulations. With respect to non-rotating cells in the simulations of Hurricane Irma, both the YSU and MYNN3 are statistically significantly further from the coast than the ACM2 simulation ($p < 0.001$); however, there is no statistical significance between the cell distance to the coast of non-rotating cells in the YSU and MYNN3 simulations ($p = 0.061$).

In summary, the simulations of Hurricane Harvey showed that rotating cells were identified with more frequency over and near land compared to over the ocean, while non-rotating cells were identified with greater frequency over the ocean, especially in the MYNN3 PBL simulation (Figs. 3.11 and 3.12). The non-rotating cells in the Hurricane Irma simulations were identified with more frequency over the ocean (Fig. 3.14) much like the non-rotating cells of the Harvey simulations (Fig. 3.12). Contradictory to the identified rotating cells in the Harvey simulations, the simulations of Hurricane Irma showed more identified rotating cells over the ocean compared to the land (Fig. 3.13). This apparent contradiction may be of little importance since the land area is much larger in the Harvey simulations compared to the Irma simulations. For this reason, the distance from the coastline may be a more useful metric to distinguish the locations of identified rotating and non-rotating cells. In fact, the rotating cells in both the simulations of hurricanes Harvey and Irma are identified closer and more frequently over land compared to over the ocean. The identified non-rotating cells occur more frequently over the ocean and at further distance from land. The distribution of the rotating and non-rotating cells with respect to the coast is in large agreement with observations of convective cells in Hurricane Ivan (Baker et al. 2009; Eastin and Link 2009), which showed that non- or weakly-rotating convection typically exists offshore and begins to rotate more vigorously once the cells approach and make landfall. The YSU PBL scheme, in both simulations of hurricanes Harvey and Irma, produced both rotating and non-rotating cells that are statistically significantly closer to the coast compared to the rotating and non-rotating cells in the MYNN3 simulations. Loops of the reflectivity for the Harvey simulations can be found at `http://www.atmos.albany.edu/student/dcard/files/Animation_Harvey_1km.html` and the Irma simulations at `http://www.atmos.albany.edu/student/dcard/files/Animation_Irma_1km.html`.

3.4 Differences in the 0–3-km updraft helicity

The first environmental difference was highlighted in the thresholds used to identify rotating cells in both the simulations of hurricanes Harvey and Irma. The 99.9^{th} percentile in model reflectivity, 99.9^{th} percentile in updraft velocity, and the 99.95^{th} percentile in 0–3-km updraft helicity were all statistically significantly[1] different across the PBL parameterizations. Tables 3.1 and 3.2 also show that the 99.9^{th} percentile in updraft velocity and the 99.95^{th} percentile in 0–3-km updraft helicity was statistically significantly lower in the simulations using the MYNN3 PBL scheme. The winds in the boundary layer are likely to differ between the different PBL schemes tested, as the different schemes handle the mixing of momentum differently that can affect the low-level updraft helicity and updraft velocities, this will be further examined in Chapter 3.

Figures 3.18 and 3.19 show the distributions of the 0–3-km updraft helicity across the simulations of hurricanes Harvey (0000 UTC 26 August – 1200 UTC 27 August) and Irma (1200 UTC 10 September – 0000 UTC 12 September), respectively. In the simulations of

Hurricane Harvey, the values of 0–3-km updraft helicity across the simulations spanned from around -200 m^2/s^2 to 300 m^2/s^2 with many values near zero such that the means of all the simulations are all near zero (Fig. 3.18, left). The distribution differences in Figure 3.18 (right) show the more nuanced differences between the updraft helicity in the PBL schemes. The distribution of 0–3-km updraft helicity in the MYNN3 PBL scheme has a larger peak (i.e., more near zero values) than the distributions in the YSU and ACM2 schemes (Fig. 3.18, right). The YSU and ACM2 PBL simulations produced 0–3-km updraft helicity distributions that are more broad and contain more frequent higher values and less frequent lower values than the MYNN3 simulation; however, the distributions of the YSU and ACM2 PBL schemes did not differ much from one another (Fig. 3.18, right). The distribution of 0–3-km updraft helicity in the MYNN3 PBL scheme simulation is statistically significantly[3] different than the YSU ($p < 0.001$) and ACM2 ($p < 0.001$) PBL simulations. There is no statistical significance between the YSU and ACM2 simulations ($p = 0.842$).

In the simulations of Hurricane Irma, the values of 0–3-km updraft helicity spanned from around -300 m^2/s^2 to more than 500 m^2/s^2 and, as in the Harvey simulations, the means of all the Irma simulations are near zero (Fig. 3.19, left). The differences in the 0–3-km updraft helicity distributions show that again, like the Harvey simulations, the MYNN3 PBL simulation has a larger peak (i.e., more near zero values), and a lower frequency of high values of 0–3-km updraft helicity compared to the YSU or ACM2 simulations (Fig. 3.19, right). Also, as in the Harvey simulations, the differences in the distributions of 0–3-km updraft helicity in the YSU and ACM2 simulations of Irma did not show statistical significance ($p = 0.003$). The MYNN3 PBL simulation was statistically significantly different than the YSU ($p < 0.001$) and ACM2 ($p < 0.001$) PBL simulations.

The 0–3-km updraft helicity is a function of both the 0–3-km helicity and the 0–3-km vertical velocity, such that it is important to determine which of these variables drives

[3]Statistical significance is determined via a two sided t-test of two independent samples at the 99.95% confidence level.

the differences between the PBL schemes seen in the 0–3-km updraft helicity. There is high rotating-cell activity at 0900 UTC 26 August for Hurricane Harvey and 0000 UTC 11 September for Hurricane Irma (Figs. 3.9 and 3.10), so these times will be the focus of the upcoming analysis. Figure 3.20 shows the difference in the 0–3-km helicity in the MYNN3 PBL simulation compared to the YSU and ACM2 simulations at the times of high rotating-cell activity in hurricanes Harvey and Irma. The spatial distribution of 0–3-km helicity in the MYNN3 simulation of Hurricane Harvey shows more 0–3-km helicity close to the center of the storm; however, outside this area, the 0–3-km helicity is generally higher in the YSU and ACM2 simulations, particularly on the eastern side of the storm (Fig. 3.20, left). A very similar spatial distribution of 0–3-km helicity is shown in the simulations of Hurricane Irma. The 0–3-km helicity is higher at smaller radii in the MYNN3 PBL simulation; however, outside this area, the 0–3-km helicity is generally higher in the YSU and ACM2 simulations, again particularly on the eastern side of the storm (Fig. 3.20, right).

Figure 3.21 shows the difference in the 0–3-km vertical velocity in the MYNN3 PBL simulation compared to the YSU and ACM2 simulations at the times of high rotating-cell activity in hurricanes Harvey and Irma. In both hurricanes Harvey and Irma, the spatial distribution of 0–3-km vertical velocity is very fragmented, with differences only showing up on the scale of the individual convective cells (Fig. 3.21). The differences in the 0–3-km updraft helicity across the whole storm are mainly dictated by the 0–3-km helicity as it contributes much more to the variability seen in the differences between the PBL schemes on the synoptic scale. On the convective cell scale, the both the 0–3-km vertical velocity and the 0–3-km helicity can be large making both important in terms of the 0–3-km updraft helicity at the mesoscale.

The cumulative frequency by altitude distributions (CFADs) in Figure 3.22 show the frequency of different values of vertical motion from 0000 UTC 26 August through 1200 UTC 27 August for Harvey and 1200 UTC 10 September through 0000 UTC 12 September for Irma. The CFADs show the majority of vertical motions in all of the simulations are near zero. Didlake and Houze (2009) showed that CFADs of vertical motion in the stratiform area of Hurricane Katrina (2004) had a near vertical line with high frequencies of near zero vertical motion; however, their convective area Katrina CFAD was more broad and lacked high frequencies of near zero vertical velocities in the midlevels. These observations are very similar to the bulk CFAD of vertical motion in Figure 3.22, with the Irma simulations being more akin to the convective area CFADs and the Harvey simulations being more akin to the stratiform CFAD from Didlake and Houze (2009).

Figure 3.23 shows the differences in the CFADs between the MYNN3 and both the YSU and ACM2 simulations. The first noticeable difference is in the amount of near zero vertical velocities through most of the atmosphere. The blue colors represent where the YSU and ACM2 have more frequent values of vertical velocities. In most of the atmosphere, the YSU and ACM2 schemes have more frequent near zero values of vertical velocity compared to the MYNN3 simulation (Fig. 3.23). In the lowest 3 km, however, there is a switch such that the YSU simulations have more frequent stronger vertical velocities (both positive and negative) than the MYNN3 simulation. Figure 3.24 also shows the CFAD differences between the Irma MYNN3 and the YSU and ACM2 simulations. Again, like in Harvey, over most of the atmosphere, the YSU and ACM2 simulations have more frequent values of vertical velocity near zero. In the lowest 4 km, the situation is flipped such that the YSU simulation has more frequent stronger values of vertical velocity (both positive and negative) (Fig. 3.24).

In terms of momentum differences across the PBL schemes, it was shown that in both Harvey and Irma, the MYNN3 simulations generally had less 0–3-km updraft helicity compared to the YSU and ACM2 simulations (Figs. 3.18 and 3.19). In fact, this difference was statistically significant. Most of the difference in the large scale 0–3-km updraft helicity was driven by differences in the 0–3-km helicity in the outer core region, particularly on the eastern half of the storms, and not the 0–3-km vertical velocity. The CFADs of vertical velocity (Fig. 3.22) showed similarities with the observations from Didlake and Houze (2009), however, the Irma simulations showed frequencies most similar to the convective area CFAD and the Harvey simulations were most similar to the stratiform area from Didlake and Houze (2009). The difference CFADs of vertical motion (Figs. 3.23 and 3.24) in both Harvey and Irma show two distinct parts of the atmosphere, best described as a mixing layer, which was generally below 3 km and the free atmosphere, which extends above that. There are more frequent stronger vertical velocities in the YSU simulations compared to the MYNN3 simulations in the mixing layer. In the free atmosphere, both the ACM2 and YSU simulations showed more near zero values of vertical motion compared to the MYNN3 simulation.

3.5 Geographic differences in the 0–3-km vertical wind shear

In the previous section, the effect of geography on the rotating and non-rotating cells was examined. Baker et al. (2009) and Eastin and Link (2009) showed in observations of Hurricane Ivan (2004) that non- or weakly-rotating convection typically exists offshore and begins to rotate more vigorously once the cells approach and make landfall as they encounter higher low-level vertical shear. McCaul and Weisman (1996) showed that large low-level helicity (shear) was very important to the development of rotating cells in tropical cyclones.

Figure 3.25 shows the hodograph and 0–3-km vertical shear across the coastline along a rainband in Hurricane Harvey. The hodographs in all three simulations (upper left) show that the curvature is similar between the ocean and land potions of each cross section. The major difference in the hodographs in the transition from land to ocean is the elongation over land in the lowest levels, which can be attributed to friction slowing the wind (Fig. 3.25). The 0–3-km vertical wind shear from A–B across the coastline for the simulations of Hurricane Harvey at 0800 UTC 26 August is shown in Figure 3.25 (right). In the YSU simulation of Harvey, the 0–3-km vertical wind shear over the ocean ranges from 3–15 m/s with a mean of 8.47 m/s. There is an increase in the 0–3-km vertical wind shear across the coastline. Over land, the YSU simulation of Harvey had a 0–3-km vertical wind shear ranges from 8–26 m/s with a mean of 18.16 m/s. In the MYNN3 simulation of Harvey, the

0–3-km vertical wind shear over the ocean ranges from 4–8 m/s with a mean of 5.92 m/s. Again, as in the YSU simulation, the 0–3-km vertical wind shear in the MYNN3 simulation increases across the coastline and over land. The 0–3-km vertical wind shear over land in the MYNN3 simulation of Harvey ranges from 15–23 m/s with a mean of 18.71 m/s. The ACM2 simulation of Harvey had a 0–3-km vertical wind shear over the ocean that ranges from 3–17 m/s with a mean of 11.16 m/s. Yet again, across the coastline, the 0–3-km vertical wind shear increases. Over the land, the 0–3-km vertical wind shear in the ACM2 simulation ranges from 12–25 m/s with a mean of 19.62 m/s. In all three simulations of Harvey, the 0–3-km vertical wind shear was statistically significantly higher over land compared to over the ocean (p=0.00). In the simulations of Harvey, the MYNN3 simulation has the lowest mean 0–3-km shear over the ocean and the YSU simulation has the lowest mean 0–3-km shear over the land.

Like in the simulations of Harvey, Figure 3.26 shows the hodographs and 0–3-km vertical wind shear across the coastline along a rainband in Hurricane Irma. The hodographs in all three simulations (upper left) shows that again, the curvature is similar with the major difference being in the elongation of the hodograph in the low levels due to friction from the transition from the ocean to the land (Fig. 3.26). The 0–3-km vertical wind shear from A–B across the coastline for the simulations of Hurricane Irma at 2200 UTC 10 September are shown in Figure 3.26 (right). Over the ocean, the YSU simulation of Irma had a 0–3-km vertical wind shear that ranges from 17–38 m/s with a mean of 26.97 m/s. There is a slight increase in the 0–3-km vertical wind shear across the coastline. In the YSU simulation over the land, the simulation of Irma had a 0–3-km vertical wind shear that ranges from 26–48 m/s with a mean of 36.69 m/s. The MYNN3 simulation of Irma had a 0–3-km vertical wind shear over the ocean that ranges from 18–26 m/s with a mean of 21.61 m/s. In the MYNN3 simulation over the land, the 0–3-km vertical wind shear ranges from 22–32 m/s with a mean of 26.81 m/s. The ACM2 simulation of Irma had a 0–3-km vertical wind shear over the ocean that ranges from 10–36 m/s with a mean of 24.74 m/s. There is again, a slight increase in the 0–3-km vertical wind shear across the coastline in the ACM2 simulation. Over the land, the ACM2 simulation of Irma had a 0–3-km vertical wind shear that ranges from 24–46 m/s with a mean of 33.07 m/s. As in Harvey, all three simulations of Irma had a 0–3-km vertical wind shear that was statistically significantly higher over land compared to over the ocean (p=0.00). In the simulations of Irma, the MYNN3 simulation has the lowest mean 0–3-km shear over both the ocean and the land.

3.6 Differences in relative humidity and convective available potential energy (CAPE)

Other than momentum (wind), the PBL schemes can also influence the low-level distribution of moisture and heat. The PBL schemes can lead to differences in the relative humidity and CAPE in the boundary layer across the different simulations, which can affect the convective environment.

Figure 3.27 shows the CFADs of relative humidity for 0000 UTC 26 August through 1200 UTC 27 August for the Harvey simulations and from 1200 UTC 10 September through 0000 UTC 12 September for the Irma simulations. Between 17 and 18 km in height in both Harvey and Irma, there is a large frequency of relative humidity values less than 20% (Fig. 3.27), which is unsurprising considering that generally it would be expected that moisture content becomes lower into the stratosphere. In the lowest 5 km of the simulations is where the largest frequency of high relative humidity occurs (Fig. 3.28); however, there is large variability across the different PBL schemes. In both the YSU and ACM2 simulations of hurricanes Harvey and Irma, there are large frequencies of relative humidity above 95% that extend from 5 to 0.5 km and then tend to linearly decrease towards the surface; the MYNN3 simulations, however, show the largest frequency of relative humidity above 95% extending from 5 to around 0.25 km before decreasing linearly towards the surface (Fig. 3.28). The larger frequencies of high relative humidity below 0.5 km suggests that moisture is generally more abundant close to the surface in the MYNN3 simulations, as the frequency in the linear decrease results in more frequent higher values of relative humidity from 0.5 km to the surface. The YSU simulations show that the linear decrease in relative humidity results in the most frequent values of relative humidity around 75–85% near the surface. In the ACM2 simulations, the linear decrease in relative humidity is more narrow, resulting in more frequent values of relative humidity very close to 80% (Fig. 3.28). The MYNN3 simulations show more frequent values of relative humidity around 80–95% near the surface (Fig. 3.28).

The distribution of CAPE also differs in the vertical across the PBL simulations, which is unsurprising given the differences seen in the relative humidity. Figure 3.29 shows the CFAD for the CAPE from 0000 UTC 26 August through 1200 UTC 27 August in Hurricane Harvey and from 1200 UTC 10 September through 0000 UTC 12 September in Hurricane Irma. In the Harvey simulations (Fig. 3.29, top) all of the PBL schemes exhibit a large frequency of near zero CAPE. The largest frequencies of the highest values of CAPE generally occur below 3 km. The MYNN3 simulation of Harvey shows the most frequent values of high CAPE in the lowest 3 km, around 300 J/kg. The YSU and ACM2 simulations show the maximum CAPE in the lowest 3 km around 250 and 200 J/kg, respectively. The simulations of Irma show again that the most frequent high values of CAPE occur below 3 km (Fig. 3.29, bottom). The YSU and ACM2 simulations of Irma show a maximum in the frequency of high CAPE very close to the surface of 500 and 450 J/kg, respectively. The MYNN3 simulations shows this maximum at approximately 1 km, with a value of 500 J/kg, but it does not extend to the surface as in the other simulations of Irma.

As shown above, the CAPE varies in a bulk sense across the vertical in both the Harvey and Irma simulations. Figure 3.30 shows that the 0–3-km CAPE also varies by the shear quadrant in the simulations of Hurricane Harvey. The downshear quadrants show the highest values of 0–3-km CAPE, especially in the first 18 h of the simulations (Fig. 3.30). In the downshear quadrants, the CAPE also varies across the PBL schemes, with the MYNN3 simulation showing the lowest values 0–3-km CAPE compared to the YSU and

ACM2 simulations (Fig. 3.30). In Figure 3.31, the 0–3-km CAPE also shows variation by shear quadrant with both the downshear and the upshear-right quadrants exhibiting higher 0–3-km CAPE than the upshear-left quadrant in Hurricane Irma. In both the right-of-shear quadrants, the MYNN3 PBL simulation produces less 0–3-km CAPE than the YSU or ACM2 simulations (Fig. 3.31).

The moisture and CAPE environments across the PBL schemes tested showed variations that can certainly affect the convection in tropical cyclones. Moisture within the boundary layer varied by altitude between the simulations, with the MYNN3 simulations showing the most frequent high values of relative humidity in the lowest 1 km. Numerous studies have highlighted that the MYNN3 PBL scheme, and other local PBL schemes, tend to have difficulty generating large eddies (Nakanishi and Niino 2006; Cohen et al. 2015). The differences in moisture content of the boundary layer are likely driven by the inability of local PBL schemes to deeply mix moisture from the PBL into the free atmosphere. The most frequent values of high CAPE occur below 3 km in all of the simulations in both hurricane Harvey and Irma (Fig. 3.29). The simulations that used the MYNN3 PBL scheme tend to have high values of CAPE, although the high values of CAPE lacked depth (Fig. 3.29). The CFADs of CAPE in Hurricane Irma (Fig. 3.29, bottom) show higher frequencies of larger values of CAPE than the simulations of Hurricane Harvey (Fig. 3.29, top). This is directly connected to what was seen in the CFADs of vertical velocity (Fig. 3.22), which showed that the Irma simulations had more frequent larger values of vertical velocity than simulations of Harvey. Larger CAPE is associated with stronger upward and downward vertical velocities. The 0–3-km CAPE was concentrated mainly in the downshear quadrants, but in Hurricane Irma, there was also abundant 0–3-km CAPE in the upshear-right quadrant (Figs. 3.30 and 3.31). The 0–3-km CAPE in the simulations of Harvey and Irma are similar to the distributions of column-deep CAPE in past literature (Molinari and Vollaro 2010; Molinari et al. 2012). In both hurricane simulations, the MYNN3 PBL tended to produce less 0–3-km CAPE in the downshear quadrants compared to the YSU and ACM2 schemes (Figs. 3.30

and 3.31).

3.7 Structure of convection

In the previous section, it was shown that the convective environment, in terms of wind, moisture, and heat, differed across the PBL schemes tested. The CAPE analysis in Figures 3.30 and 3.31 showed that most of the variability in CAPE occurred within the first 24 h of the analysis. To investigate how these differences affect the local convective environments of the identified rotating and non-rotating cells, composites of both land and ocean, rotating and non-rotating cells, were constructed from 0000 UTC 26 August through 0000 UTC 27 August for the Harvey simulations and 1200 UTC 10 September through 1200 UTC 11 September for the Irma simulations. In the previous section, the 0–3-km vertical wind shear was shown to be drastically different between the ocean and land. As such, the composites of both the rotating and non-rotating cells will be separated based on if the cell is over the ocean or over the land to investigate the differences caused by the geographical differences in the cell locations.

3.7.1 Harvey non-rotating composite cells

Figure 3.32 shows the composite of the YSU (n=106, top), MYNN3 (n=177, middle), and ACM2 (n=151, bottom) identified non-rotating land cells. The height radius cross sections show the reflectivity (a) and relative humidity (b) of the cells with the zero radius representing the center of the cell composite with positive radius being radially outward from the center of the tropical cyclone. The model-computed (as described in the Introduction) PBL height (purple line) does not vary across the simulations and is around 500 m in all the land non-rotating cell composites (Fig. 3.32). The reflectivity in the YSU simulation extends from near the surface to above 12 km. The core of the reflectivity (>40 dBZ) is vertically erect. In the YSU non-rotating land cell composite, the height of the maximum vertical motion is 5.5 km, with a small area of 6 m/s. There is also a broad maximum in the tangential wind of 20 m/s on the radially outward side of the composite cell at a height of 2–8 km (Fig. 3.32a, top). The radial wind has an interesting pattern within the YSU simulation, such that the radial wind is maximized above the surface on the radially outward side just below the maximum in vertical motion (Fig. 3.32, top). The relative humidity in the YSU non-rotating land cell composite ranges from about 60–100% in the cross section, with a maximum located at the center of the cell at a height of 4.5 km (Fig. 3.32b, top). In Figure 3.32b (top), the three-dimensional convergence of the YSU simulation is weak ($\sim -0.05 * 10^{-3}$ $1/s$) and is located above the surface on the radially outward side of the composite cell.

The reflectivity in the MYNN3 non-rotating land cells is not as high as the YSU simulation and only extends to 10 km. The core of the reflectivity (>40 dBZ) is vertically erect. Like the YSU composite, the MYNN3 composite has a maximum in vertical motion at 5.5 km with a magnitude of 6 m/s. There is also a spatially small maximum in the tangential wind of 18 m/s on both sides of the composite cell at about 2 km in height (Fig. 3.32a, middle). The radial wind in the non-rotating land composite of the MYNN3 simulation is maximized near the surface and decreases fairly linearly aloft (Fig. 3.32, middle). The relative humidity in the MYNN3 non-rotating land cell composite ranges from about 55–100% in the cross section, with a maximum located at the center of the cell at a height of 4 km (Fig. 3.32b, middle). It is dry in the upper levels (around 11 km) on the radially inward side of the cell, in a similar area to where there is a lack of reflectivity (Fig. 3.32, middle). The three-dimensional convergence of the MYNN3 simulation is weak ($\sim -0.05 * 10^{-3}$ $1/s$), is located above the surface directly under the relative humidity maximum in the composite cell, and encompasses a smaller area compared to the YSU cell composite.

The reflectivity in the ACM2 non-rotating land cells extends from the surface to just above 12 km. The reflectivity core (>40 dBZ) is vertically erect like the the YSU and MYNN3 non-rotating land cell composites (Fig. 3.32a, bottom). The ACM2 composite has a maximum in vertical velocity at 6 km, with a magnitude of 6 m/s, and also has the most broad area of vertical motion of the three composites. As in the other two composites, the

ACM2 simulation has a maximum in the tangential wind of 20 m/s at about 3.5 km from the center of the composite on the radially outward side with height ranging from 5–7.5 km (Fig. 3.32, bottom). The relative humidity in the ACM2 non-rotating land cell composite ranges from about 60–100% in the cross section, with a maximum located at the center of the cell at a height of 5 km (Fig. 3.32b, bottom). The three-dimensional convergence of the ACM2 simulation is weak ($\sim -0.05 * 10^{-3}$ $1/s$) and is located above the surface at the center of the composite cell; however, on the radially outward side the convergence extends to the surface.

Figure 3.33 shows the composite of the YSU (n=189, top), MYNN3 (n=598, middle), and ACM2 (n=194, bottom) identified non-rotating ocean cells. The model-computed PBL height does not vary much across the simulations and is around 500 m in all the oceanic non-rotating cell composites (Fig. 3.33). The reflectivity in the YSU non-rotating ocean cells extends from the surface to just above 12 km on the radially outward side, but has a lack of reflectivity above 10 km on the radially inward side (Fig. 3.33a, top). The core of the reflectivity (>40 dBZ) is vertically erect. Like the YSU non-rotating land cells, the YSU non-rotating ocean cells have a maximum in vertical velocity at 6 km in height, with a magnitude of about 6 m/s, but more broad than the land cell. The radial inflow of the YSU oceanic non-rotating cell composite is much deeper than the land counterpart and there is no tangential wind maximum (Fig. 3.33, top). The relative humidity in the YSU non-rotating ocean cells is much less in the upper levels compared to the YSU land non-rotating cells, and is maximized at the center of the cell composite at a height of 4 km (Fig. 3.33b, top). The three-dimensional convergence of the YSU non-rotating ocean cell composite is weak ($\sim -0.1 * 10^{-3}$ $1/s$), although slightly stronger than the land non-rotating cell composite and located about 1 km above the surface at the center of the composite cell.

The reflectivity in the MYNN3 non-rotating ocean cells extends from the surface to 9 km and is vertically erect, which is very similar to the land composite (Fig. 3.33a, top). The maximum in the vertical velocity is located at 5.5 km, with a magnitude of 6 m/s. Like the

YSU non-rotating ocean cells, the MYNN3 non-rotating ocean cells also have deep radial inflow, which is deeper than the land counterpart and there is no tangential wind maximum (Fig. 3.33 middle). The relative humidity in the MYNN3 non-rotating ocean cell composite is maximized at 4 km. Again, the upper levels are much drier in the oceanic MYNN3 composite for the non-rotating cells compared to the MYNN3 non-rotating land cells (Fig. 3.33b, middle). The three-dimensional convergence is again weak with a magnitude around $-0.1 * 10^{-3}$ $1/s$ and is located about 1 km above the surface at the center of the composite cell (Fig. 3.33b, middle).

The reflectivity of the ACM2 non-rotating ocean cell composite extends from the surface to above 12 km on the radially outward side; however, the reflectivity only extends to around 8 km on the radially inward side of the cell (Fig. 3.33a, bottom). Like the YSU and MYNN3 non-rotating ocean cell composites, the core of the reflectivity (>40 dBZ) is vertically erect in the ACM2 composite. Unlike the other oceanic non-rotating cells, the ACM2 non-rotating ocean cell composite shows a tangential wind maximum of 20 m/s at a height of 5 km and about 4 km from the center of the cell (Fig. 3.33, bottom). The maximum in vertical velocity is again stronger in the ACM2 simulation compared to the other non-rotating ocean cell composites, with a magnitude of 8 m/s, and is located at a height of 6 km. Like the other two oceanic non-rotating cell composites, the radial inflow depth is deeper than the land counterparts by 1–2 km (Fig. 3.33, bottom). The relative humidity in the ACM2 non-rotating ocean cell composite is maximized at 4 km, much like the non-rotating ocean cell composites of the other two PBL schemes. Again, the upper levels, particularly on the radially inward side, are drier than the ACM2 non-rotating land cell composite (Fig. 3.33b, bottom). The three-dimensional convergence is weak ($\sim -0.1 * 10^{-3}$ $1/s$), very much like the other two composites of non-rotating ocean cells, and is maximized about 1 km above the surface at the center of the cell composite (Fig. 3.33b, bottom).

Generally, the non-rotating cell composites in the Harvey simulations show that the reflectivity core (>40 dBZ) tends to be vertically erect with the maximum vertical velocity located between 5.5 and 6 km (Figs. 3.32a and 3.33a). The difference in the radial inflow between PBL schemes over land is that the YSU and ACM2 non-rotating cell composites show the inflow is maximized above the surface where in the MYNN3 composite the radial inflow is located at the surface. Over the ocean, the radial inflow is 1–3 km deeper than in the land composites (Fig. 3.32a). The tangential wind maxima occurred in only the land non-rotating cell composites and the ACM2 ocean cell composite and has a height that ranges between 2–8 km. The tangential wind maxima tends to be located about 2.5–4 km from the cell center on the radially outward side of the composite, ranges in magnitude from 18–20 m/s, and is generally broad in the ACM2 and YSU composites (Fig. 3.32a). The maximum in relative humidity tends to be confined to the center of the composite cells and located directly below the maximum in vertical velocity around 4–5 km (Figs. 3.32b and 3.33b). The three-dimensional convergence in these composite cells is generally weak and located at the center of the composite cells about 1 km above the surface and extending downward on the radially outward side (Figs. 3.32b and 3.33b).

3.7.2 Harvey rotating composite cells

Figure 3.34 shows the composite of the YSU (n=227, top), MYNN3 (n=218, middle), and ACM2 (n=289, bottom) identified rotating land cells. The model-computed PBL height in the YSU and ACM2 rotating land composites are around 1000 m, while the MYNN3 rotating land composite is around 500 m (Fig. 3.34). The reflectivity in the YSU simulation extends from near the surface to about 10.5 km and is tilted with height. In the YSU rotating land cell composite, the height of the maximum vertical motion is 3 km with a magnitude of 4 m/s. This maximum in vertical motion is much lower, closer to the surface, than the non-rotating cell composites (Figs. 3.32a and 3.33a). There is a maximum in the tangential wind of 26 m/s on the radially outward side about 1 km from the composite center at a height of about 2.5 km (Fig. 3.34a, top). The radial wind in the YSU rotating land cell composite shows a more shallow inflow layer compared to the YSU non-rotating land cell composite.

The inflow begins to turn to radial outflow just below the maximum in vertical motion as expected based on numerous composites from Houze (2010), Moon and Nolan (2015b), and Card (2019) (Fig. 3.34, top). The YSU rotating land cell composite shows a maximum in the relative humidity located at the center of the cell at a height of 3 km (Fig. 3.34b, top), much lower than the maximum in moisture seen in the non-rotating cell composites (Figs. 3.32b and 3.33b). The three-dimensional convergence of the YSU simulation is stronger than the non-rotating cell composites around $-0.25 * 10^{-3}$ $1/s$ that extends to the surface on the radially outward side of the composite cell wrapping around the maximum in the tangential wind, with the convergence maximum located directly beneath the center of the composite cell.

The reflectivity in the MYNN3 simulation extends from the surface to about 9.5 km. The MYNN3 rotating land cell composite has a maximum in vertical velocity (4 m/s) at 3 km. There is a noticeable maximum in the tangential winds of 24 m/s on the radially outward side about 1 km from the cell center and at a height of 2 km (Fig. 3.34a, middle). Like in the YSU rotating land cell composite, the vertical motion maximum in the MYNN3 rotating land cell composite is much closer to the surface than the MYNN3 non-rotating cell composite (Figs. 3.32a and 3.33a). The radial wind in the MYNN3 rotating land cell composite is more shallow than the MYNN3 non-rotating land cell composite by approximately 2 km (Fig. 3.34, middle). The MYNN3 rotating land cell composite has a maximum in relative humidity at the center of the composite cell at a height of 2.5 km (Fig. 3.34b, middle). The maximum in the relative humidity is much lower than the height of the maximum relative humidity in the non-rotating cell composites (Figs. 3.32b and 3.33b). The three-dimensional convergence in the MYNN3 rotating land cell composite is weaker than the YSU rotating land cell composite; however, it is still much stronger than the non-rotating cells, around $-0.15 * 10^{-3}$ $1/s$. The convergence also extends to the surface on the radially outward side wrapping around the maximum in the tangential wind speed of the composite cell with the maximum in convergence located directly beneath the center of the composite cell (Fig.

3.34b, middle).

The reflectivity in the ACM2 rotating land cell composite extends from the surface to about 10.5 km. The ACM2 rotating land cell composite has a vertical velocity maximum at 3 km (the strongest of any of the rotating land cell composites at 6 m/s). Again, like the other rotating cell composites, the ACM2 composite maximum in vertical velocity is much closer to the surface than the ACM2 non-rotating cell composite by 3 km (Figs. 3.32a and 3.33a). There is a maximum in the tangential wind from 28–30 m/s located on the radially outward side about 1 km from the composite center at a height of around 2 km (Fig. 3.34a, bottom). The radial wind in the ACM2 rotating land cell composite is more shallow by 3.5 km than the ACM2 non-rotating cell composite (Fig. 3.34, bottom). The maximum in the relative humidity is at the center of the composite cell at a height of 3 km (Fig. 3.34b, bottom). Much like the YSU and MYNN3 rotating land cell composites, the ACM2 composite has a physically lower maximum in relative humidity than ACM2 non-rotating composite cells. In Figure 3.34b (bottom), the three-dimensional convergence in the ACM2 rotating land cell composite is stronger than the non-rotating cells around $-0.25 * 10^{-3}$ $1/s$. The convergence extends to the surface on the radially outward side of the composite cell wrapping around the maximum in the tangential wind. The maximum in convergence is located directly beneath the maximum in vertical motion at the center of the composite cell (Fig. 3.34b, bottom).

Figure 3.35 shows the composite of the YSU (n=118, top), MYNN3 (n=166, middle), and ACM2 (n=89, bottom) identified rotating ocean cells. The model-computed PBL heights in the MYNN3 and ACM2 rotating ocean composites are around 500 m, while the YSU rotating ocean composite is around 250 m (Fig. 3.35). The reflectivity in the YSU rotating ocean cells extends from the surface to just below 12 km on the radially outward side, but there is a lack of reflectivity above 6.5 km on the radially inward side (Fig. 3.35a, top). The reflectivity also appears tilted with height, like the rotating land cell composites. Like the YSU rotating land cells, the YSU rotating ocean cells has a maximum in vertical velocity of 6 m/s at 3 km, which is half the height of the YSU non-rotating ocean cell composite. There is a tangential wind maximum of 24 m/s located on the radially outward side around 1.5 km from the composite cell center at a height of 2.5 km (Fig. 3.35, top). The radial inflow is deeper than the land counterpart by about 2 km (Fig. 3.35, top). The relative humidity in the YSU rotating ocean cells is much less in the upper levels compared to the YSU land rotating cells by about 15%, and is maximized at the center of the cell composite at a height of 3 km (Fig. 3.35b, top). In Figure 3.35b (top), the three-dimensional convergence of the YSU rotating ocean cell composite is weaker than the YSU rotating land cell composite and about $-0.1 * 10^{-3}$ $1/s$. The convergence extends to the surface on the radially outward side of the composite cell, but does not wrap around the maximum in the tangential wind. The convergence maximum is located directly beneath the maximum in vertical velocity at the center of the composite cell.

The reflectivity in the MYNN3 rotating ocean cells extends from the surface to around 8 km on the radially outward side and around 7 km on the radially inward side (Fig. 3.35a, middle). Again, the reflectivity appears tilted with height. The height of the maximum in vertical velocity is at 3.5 km with a magnitude of 6 m/s, which is much shallower than the MYNN3 non-rotating ocean cell composite by about 1.5 km. There is a tangential wind maximum of 16 m/s on the radially outward side about 1 km from the cell composite center at a height of 2 km (Fig. 3.35, middle). The radial inflow of the MYNN3 rotating ocean cell is deeper than the MYNN3 rotating land cell by about 4 km (Fig. 3.35, middle). The MYNN3 rotating ocean cells have less relative humidity in the upper levels compared to the MYNN3 land rotating cells by about 15% maximized at the center of the cell at a height of 2.5 km (Fig. 3.35b, middle). The three-dimensional convergence of the MYNN3 rotating ocean cell composite is around $-0.1 * 10^{-3}$ $1/s$. The convergence is weaker than the rotating land cell composite by $0.05 * 10^{-3}$ $1/s$ and more similar to the MYNN3 non-rotating cell composite that is maximized about 1 km above the surface in the center of the composite cell (Fig. 3.35b, middle).

The reflectivity in the ACM2 rotating ocean cells extends from the surface to 10 km on the radially outward side and around 7 km on the radially inward side (Fig. 3.35a, bottom). Like the other rotating composites, the reflectivity is tilted with height. The ACM2 rotating ocean cell composite has a maximum in vertical velocity at a height of 3 km, and also has the strongest vertical velocity of all of the rotating oceanic cell composites at 8 m/s. Again, the maximum in vertical velocity is much shallower than the ACM2 non-rotating ocean cell composite by 1.5 km (Fig. 3.35a, bottom). There is a tangential wind maximum of 24 m/s on the radially outward side of the composite cell about 1.5 km from the center at a height of 3 km (Fig. 3.35, bottom). Like the other rotating cell composites, the ACM2 has a deeper inflow than the ACM2 rotating land cell by about 2 km (Fig. 3.35, bottom). The ACM2 rotating ocean cell composite also has less relative humidity in the upper levels by around 15% compared to the ACM2 rotating land cell and the relative humidity is maximized at 2 km (Fig. 3.35b, bottom). The three-dimensional convergence is weaker than the rotating land cell composite around $-0.1 * 10^{-3}$ $1/s$ and more similar to the ACM2 non-rotating cell composite where it is maximized about 1 km above the surface in the center of the composite cell and extends down to the surface on the radially outward side (Fig. 3.35b, bottom).

Generally, the rotating cell composites in the Harvey simulations show that the reflectivity tends to be vertically tilted with height (Figs. 3.34a and 3.35a). Also, the depth of the reflectivity in the rotating cell composites is less than the non-rotating cell composites (Figs. 3.32a, 3.33a, 3.34a, and 3.35a). The maximum vertical velocity located between 3 and 3.5 km is about half of that of the non-rotating cell composites (Figs. 3.34a and 3.35a). Both the land and ocean rotating composites have a tangential wind maximum that ranges from 16–30 m/s on the radially outward side of the cell about 1–1.5 km from the composite center (Figs. 3.34 and 3.35). The height of the tangential wind maximum in the rotating cell composites ranges from 2–3 km. The tangential wind maximum in the rotating cell composites tends to be closer to the center of the cell composite by around 1.5–2.5 km and stronger by 2–10 m/s compared to the non-rotating cell composites. The MYNN3 simulation produced the weakest tangential wind maximum when compared to the other PBL schemes for both the land and ocean composites, respectively. The relative humidity tends to be confined to the center of the composite cells and located directly below the maximum in vertical velocity (2–3 km) (Figs. 3.34b and 3.35b). The three-dimensional convergence in these composite cells is strong in the rotating land composite cells ranging from $-0.15 * 10^{-3}$ to $-0.25 * 10^{-3}$ $1/s$ located at the center of the composite cells and extending to the surface (Figs. 3.34b and 3.35b) wrapping around the maximum in the tangential wind.

Not only were there differences between the non-rotating and rotating composite cells but also between the oceanic and land cells. The biggest difference between land and ocean cells was the extent of dry air in the upper levels. The ocean cell composites consistently had more dry air in the upper levels compared to the land cells, with many composites showing some areas of relative humidity less than 50% (Figs. 3.33b and 3.35b). The composites of both rotating and non-rotating cells showed that the radial inflow near the surface was generally deeper in the oceanic cells by a factor of two compared to the land cells (Figs. 3.32, 3.33, 3.34, and 3.35). The PBL heights in the land cell composites showed much more variation than the oceanic cell composites (Figs. 3.32, 3.33, 3.34, and 3.35).

Differences in the non-rotating and rotating cell composites were also seen across the PBL schemes, particularly in reference to the distribution of moisture in the low levels, as well as momentum differences in the low levels driven by differences in the radial inflow and vertical motion. The MYNN3 cell composites show the shortest heights for the vertical extent of the model reflectivity by 1–2 km. The ACM2 scheme consistently showed the largest vertical motions in each composite by 1–2 m/s. The MYNN3 composites showed that the radial inflow was maximized near the surface in the non-rotating cells, while the YSU and ACM2 showed the radial inflow maximized above the surface (Figs. 3.32 and 3.33).

3.7.3 Irma non-rotating composite cells

Figure 3.36 shows the composite of the YSU (n=9, top), MYNN3 (n=12, middle), and ACM2 (n=8, bottom) identified non-rotating land cells. Note that the number of non-rotating land cells in the simulations of Irma are low (Fig. 3.14). The model-computed PBL height in the YSU non-rotating land composite varies between 500 m on the radially inward side of the composite and 1000 m on the radially outward side of the composite, while the MYNN3 non-rotating land composite is around 500 m, and the ACM2 non-rotating land composite is around 1000 m (Fig. 3.36).

The reflectivity in the YSU simulation extends from near the surface to around 10.5 km and the core of the reflectivity (>40 dBZ) is vertically erect with height and expansive. The height of the maximum vertical motion is 5.5 km with a magnitude of 10 m/s. There is a maximum in the tangential wind of 40 m/s on the radially outward side about 5 km from the composite center at a height of 5 km (Fig. 3.36a, top). Like the Harvey YSU non-rotating cell composite, the Irma composite also shows that the radial wind is maximized above the surface (2 km) on the radially outward side just below the maximum in vertical motion (Fig. 3.36, top). The relative humidity in the YSU non-rotating land cell composite ranges from about 60–100% in the cross section, with a maximum in the relative humidity located at the center of the cell at a height of 5 km (Fig. 3.36b, top). The three-dimensional convergence of the YSU simulation is around $-0.25 * 10^{-3}$ $1/s$, with the largest convergence located above the surface on the radially outward side of the composite cell, concurrent with the location of the maximum in vertical motion.

The reflectivity in the MYNN3 non-rotating land cell composite extends to around 10 km in height, but the core of the reflectivity (>40 dBZ) shows some tilting radially outward with height. The MYNN3 composite has a maximum in vertical motion at 4.5 km with a magnitude of 4 m/s. There is a maximum in the tangential wind of 46 m/s on the radially outward side about 3.5 km from the composite center and is around 2 km in height (Fig. 3.36a, middle), which is much lower than the YSU non-rotating cell composite. The radial wind is maximized near the surface, decreases fairly linearly aloft, and is shallower than the YSU non-rotating land composite (Fig. 3.36, middle). The relative humidity in the MYNN3 non-rotating land cell composite ranges from about 55–100% in the cross section, with a maximum in the relative humidity located at the center of the cell at a height of 4.5 km; there is also high relative humidity near the surface (Fig. 3.36b, middle). The three-dimensional convergence of the MYNN3 simulation is $-0.3 * 10^{-3}\ 1/s$ and is located at the surface directly under the strong vertical velocity in the composite cell.

The reflectivity in the ACM2 non-rotating land cells extends from the surface to just below 11 km, very similar to the YSU composite, and the core reflectivty (>40 dBZ) is also upright (Fig. 3.36a, bottom). The ACM2 composite has a maximum in vertical velocity at 5 km, and has a magnitude of 14 m/s. The ACM2 composite shows the strongest and most broad area of vertical motion of the three non-rotating land composites of Hurricane Irma. Like in the YSU non-rotating land cell composite, the ACM2 non-rotating land composite radial wind is maximized above the surface, increases in height (from 1–2.5 km) as it approaches the center of the composite cell, and has a magnitude around 15 m/s (Fig. 3.36, bottom). The ACM2 simulation has a broad maximum in the tangential wind of 38 m/s on the radially outward side around 2.5 km from the composite center at a height ranging from 2–5 km (Fig. 3.36, bottom). The relative humidity in the ACM2 non-rotating land cell composite ranges from about 60–100% in the cross section, with a maximum in the relative humidity located at the center of the cell at a height of 4 km (Fig. 3.36b, bottom). The three-dimensional convergence of the ACM2 simulation is $-0.4 * 10^{-3}\ 1/s$, and extends from the surface to directly under the strong vertical velocity in the composite cell.

Figure 3.37 shows the composite of the YSU (n=100, top), MYNN3 (n=239, middle), and ACM2 (n=169, bottom) identified non-rotating ocean cells. The model-computed PBL height does not vary much across the simulations and is around 500 m in all the oceanic non-rotating cell composites (Fig. 3.37). The reflectivity in the YSU non-rotating ocean cells extends from the surface to just under 12 km on the radially outward side, but has a lack of reflectivity above 10.5 km on the radially inward side (Fig. 3.37a, top). The core of the reflectivity (>40 dBZ) is upright. The YSU non-rotating ocean cell composite has a maximum in vertical velocity at 6.5 km. The radial inflow is much deeper than the land counterpart by about 4 km (Fig. 3.37, top). The YSU non-rotating ocean cell composite has a maximum in the tangential wind of 30 m/s on the radially outward side around 3 km from the composite center at a height of 3 km (Fig. 3.37, top). The relative humidity in the YSU non-rotating ocean cells is less in the upper levels compared to the YSU land non-rotating cells by approximately 10%, and is maximized at the center of the cell composite at a height of 4 km (Fig. 3.37b, top). The relative humidity ranges from around 55% to 100%, with the lowest relative humidity aloft on the radially inward side of the cell composite (Fig. 3.37b, top). The three-dimensional convergence of the YSU non-rotating ocean cell composite is weak, around $-0.1*10^{-3}$ $1/s$, and generally located under the maximum in relative humidity about 1 km above the surface at the center of the composite cell; however, it extends to the surface on the radially outward side.

The reflectivity in the MYNN3 non-rotating ocean cells extends from the surface to around 10 km, which is very similar to the MYNN3 land non-rotating cell composite, and the height of the reflectivity is lower on the radially inward side (Fig. 3.37a, top). The core of the reflectivity (>40 dBZ) is vertically erect in the ocean MYNN3 composite, unlike the land composite. The MYNN3 non-rotating ocean cell composite has a maximum in the tangential wind of 30 m/s on the radially outward side around 4 km from the composite center at a height of 3 km (Fig. 3.37, middle). The maximum in the vertical velocity is located at 5 km and has a magnitude of 6 m/s. Like the YSU non-rotating ocean cells, the MYNN3 non-rotating ocean cells also have a deep radial inflow, which is deeper than the land counterparts by approximately 4.5 km (Fig. 3.37, middle). The relative humidity in the MYNN3 non-rotating ocean cell composite is maximized at 3.5 km. Again, the upper levels are drier in the oceanic MYNN3 composite for the non-rotating cells compared to the MYNN3 non-rotating land cells by 10% (Fig. 3.37b, middle). The relative humidity ranges from about 50% to near 100% (at the center of the composite cell) in the MYNN3 non-rotating ocean cell composite (Fig. 3.37b, middle). The three-dimensional convergence is again weak, around $-0.05 * 10^{-3}$ $1/s$, in the MYNN3 non-rotating ocean cell composite;

in fact, it is weaker than the other non-rotating ocean cell composites by $0.05 * 10^{-3}$ to $0.15 * 10^{-3}$ $1/s$, and extends from the surface to just below the center of the maximum in relative humidity of the composite cell (Fig. 3.37b, middle).

The reflectivity of the ACM2 non-rotating ocean cell composite extends from the surface to above 12 km on the radially outward side; however, the reflectivity only extends to around 10.5 km on the radially inward side of the cell (Fig. 3.37a, bottom), but the reflectivity core (>40 dBZ) is vertically erect. The ACM2 non-rotating ocean cell composite shows a tangential wind maximum of 38 m/s at a height of 3 km on the radially outward side about 4 km from the composite center (Fig. 3.37, bottom). The maximum in vertical velocity is 8 m/s and is located at a height of 5 km. Like the other two oceanic non-rotating cell composites, the radial inflow depth is deeper than the land counterpart by approximately 2 km and looks similar to the ocean non-rotating cell composites of the YSU and MYNN3 simulations (Fig. 3.37, bottom). The relative humidity in the ACM2 non-rotating ocean cell composite is maximized at 4 km. Again, the upper levels, particularly on the radially inward side, are drier than the ACM2 non-rotating land cell composite by about 5% (Fig. 3.37b, bottom). The relative humidity ranges from 55–100% and is maximized at the center of the ACM2 non-rotating ocean cell composite (Fig. 3.37b, bottom). Three-dimensional convergence is around $-0.2 * 10^{-3}$ $1/s$, very much like the other two composites of non-rotating ocean cells, and extends to the surface on the radially outward side of the composite cell to just under the relative humidity maximum (Fig. 3.37b, bottom).

Generally, the non-rotating cell composites in the Irma simulations show that the core of the reflectivity (>40 dBZ) tends to be vertically erect with the maximum vertical velocity located between 4.5 and 6.5 km (Figs. 3.36a and 3.37a). The height of the tangential wind maximum ranges from 2–5 km with magnitudes that vary between 30–46 m/s. The tangential wind maxima are located on the radially outward side of the composites and ranges between 2.5–5 km from the composite center in the non-rotating cells (Figs. 3.36a and 3.37a). The maxima in relative humidity tends to be confined to the center of the composite cells and located directly below the maximum in vertical velocity at a height between 3.5–4.5 km (Figs. 3.36b and 3.37b). The three-dimensional convergence in the ocean composite cells is generally weaker than the land composite cells by about $0.2 * 10^{-3}$ $1/s$, extends from the surface on the radially outward side, and is maximized just below the maximum in vertical velocity (Fig. 3.37b).

3.7.4 Irma rotating composite cells

Figure 3.38 shows the composite of the YSU (n=32, top), MYNN3 (n=84, middle), and ACM2 (n=25, bottom) identified rotating land cells. The model-computed PBL height in the YSU rotating land composite is around 1500 m, while the MYNN3 is around 500 m, and the ACM2 is around 1000 m (Fig. 3.38). The reflectivity in the YSU rotating land cell composite extends from near the surface to about 10.5 km and is vertically tilted with height. In the YSU rotating land cell composite, the height of the maximum vertical velocity is at 2.5 km and has a magnitude of 8 m/s. This maximum in vertical motion is closer to the surface by 3 km compared to the non-rotating land cell composites (Figs. 3.36a and 3.37a). There is a maximum in the tangential wind of 42 m/s on the radially outward side of the cell around 1.5 km from the composite center at a height of about 2 km (Fig. 3.38a, top). The radial wind shows a more shallow inflow layer compared to the YSU non-rotating land cell composite by about 1.5 km. The inflow begins to turn to radial outflow just below the maximum in vertical motion (Fig. 3.38, top). The YSU rotating land cell composite shows a maximum in the relative humidity located at the center of the cell at a height of 4 km; however, this maximum in relative humidity is broad, extending toward the radially inward side of the composite (Fig. 3.38b, top). This height of maximum relative humidity is of similar height to the maximum in moisture seen in the non-rotating cell composites (Figs. 3.36b and 3.37b). In Figure 3.38b (top), the three-dimensional convergence of the YSU simulation is $-0.45 * 10^{-3}$ $1/s$, which is stronger than the any of the non-rotating cell composites, extends to the surface on the radially outward side of the composite cell, and the maximum is located directly beneath the maximum in vertical velocity at the center of the composite cell.

The reflectivity in the MYNN3 simulation extends from the surface to about 10 km and is tilted with height. The MYNN3 rotating land cell composite has a maximum in the vertical velocity at 2.5 km with a magnitude of 6 m/s. Like the YSU rotating land cell composites, the vertical motion maximum in the MYNN3 is closer to the surface by about 1.5 km compared to the MYNN3 non-rotating cell composites (Figs. 3.36a and 3.37a). There is a noticeable maximum in the tangential winds of 48 m/s on the radially outward side of the cell about 2 km from the composite center at a height of 2 km (Fig. 3.38a, middle). The radial wind in the MYNN3 rotating land cell composite has a depth of about 1.5 km, which is very similar to the MYNN3 non-rotating land cell composite (Fig. 3.38, middle). The MYNN3 rotating land cell composite has a maximum in relative humidity at the center of the composite cell at a height of 4 km, which is broad like the YSU rotating land composite and extends to the radially inward side of the cell (Fig. 3.38b, middle). Again, there is a lower height of the maximum relative humidity by about 1 km compared to the non-rotating cell composites (Figs. 3.36b and 3.37b). The three-dimensional convergence in the MYNN3 rotating land cell composite is $-0.45 * 10^{-3}$ $1/s$, which is much stronger than the non-rotating cells. The convergence extends to the surface on the radially outward side of the composite cell with the maximum located directly beneath the maximum in vertical velocity at the center of the composite cell (Fig. 3.38b, middle).

The reflectivity in the ACM2 rotating land cell composite extends from the surface to just under 11 km and is vertically tilted with height. The ACM2 rotating land cell composite has a vertical velocity maximum at 3 km with a magnitude of 10 m/s and is the strongest of any of the rotating land cell composites by 2–4 m/s, although there are fewer cells in the land composites of Hurricane Irma. Again, like the other rotating cell composites, the ACM2 rotating land cell composite maximum in vertical velocity is much closer to the surface then the ACM2 non-rotating cell composite by about 2 km (Figs. 3.36a and 3.37a). There is a maximum in the tangential wind between 42–44 m/s located on the radially outward side of the cell around 2 km from the composite center at a height of 2.5 km (Fig. 3.38a, bottom). The radial wind in the ACM2 rotating land cell composite is more shallow than the ACM2 non-rotating cell composite by about 1.5 km (Fig. 3.38, bottom). The maximum in the relative humidity is at the center of the composite cell at a height of 4.5 km, and it is very broad compared to the other Irma rotating land cell composites. The maximum in relative humidity extends to the surface on the radially inward side of the composite cell (Fig. 3.38b, bottom). In Figure 3.38b (bottom), the three-dimensional convergence in the ACM2 rotating land cell composite is $-0.5*10^{-3}$ $1/s$, which is stronger than the non-rotating cells, but again recall there are fewer cells in the land cell composites of Hurricane Irma. The convergence extends to the surface on the radially outward side of the composite cell with the maximum located directly beneath the maximum in vertical motion at the center of the composite cell (Fig. 3.38b, bottom).

Figure 3.39 shows the composite of the YSU (n=181, top), MYNN3 (n=191, middle), and ACM2 (n=113, bottom) identified rotating ocean cells. The model-computed PBL height does not vary much across the simulations and is around 500 m in all the oceanic rotating cell composites (Fig. 3.39). The reflectivity in the YSU rotating ocean cells extends from the surface to around 10 km on the radially outward side (Fig. 3.39a, top). The reflectivity appears vertically tilted with height. Like the YSU rotating land cells, the YSU rotating ocean cells have a maximum in vertical velocity at 3 km, which is half the height of the YSU non-rotating ocean cell composite and has a magnitude of 8 m/s. There is a tangential wind maximum of 40 m/s located on the radially outward side of the cell about 2 km from the composite center at a height of 2 km (Fig. 3.39 top). The radial inflow of in the YSU oceanic rotating cell is much deeper than its land counterpart by 2 km (Fig. 3.39 top). The relative humidity in the YSU rotating ocean cells is less in the upper levels compared to the YSU land rotating cells and is maximized at the center of the cell composite at a height of 3.5 km (Fig. 3.39b, top). In Figure 3.39b (top), the three-dimensional convergence of the YSU rotating ocean cell composite is $-0.3 * 10^{-3}$ $1/s$, which is weaker than the YSU rotating land cell composite, but does extend to the surface on the radially outward side of the composite cell with the maximum located directly beneath the maximum in vertical velocity at the center of the composite cell.

The reflectivity in the MYNN3 rotating ocean cells extends from the surface to around 9 km and is tilted with height (Fig. 3.39a, middle). The height of the maximum in vertical velocity in the MYNN3 rotating ocean cell composite is at 3 km and has a magnitude of 8 m/s. The height of the maximum in vertical velocity is 2 km shallower than the MYNN3 non-rotating ocean cell composite. There is a tangential wind maximum of 40 m/s on the radially outward side of the cell around 1.5 km from the composite center at a height of 2 km (Fig. 3.39, middle). The radial inflow of the MYNN3 rotating ocean cell is 1.5 km deeper than the MYNN3 rotating land cell (Fig. 3.39, middle). The MYNN3 rotating ocean cells have less relative humidity in the upper levels compared to the MYNN3 land rotating cells that is maximized at the center of the cell at a height of 3 km (Fig. 3.39b, middle). The three-dimensional convergence of the MYNN3 rotating ocean cell composite is $-0.3 * 10^{-3}$ $1/s$, which is weaker than the rotating land cell composite and extends to the surface on the radially outward side of the composite cell with the maximum located directly beneath the maximum in vertical velocity at the center of the composite cell (Fig. 3.39b, middle).

The reflectivity in the ACM2 rotating ocean cells extends from the surface to just under 12 km on the radially outward side and around 10.5 km on the radially inward side (Fig. 3.39a, bottom), and appears tilted with height. The ACM2 rotating ocean cell composite has a maximum in vertical velocity at a height of 3.5 km with a magnitude of 12 m/s, which is the strongest vertical velocity of all of the rotating oceanic cell composites. Again, the maximum in vertical velocity is about 2 km shallower than the ACM2 non-rotating ocean cell composite (Fig. 3.39a, bottom). There is a tangential wind maximum of 44 m/s on the radially outward side of the composite cell about 2 km from the composite center at a height of 2.5 km (Fig. 3.39, bottom). Like the other rotating cell composites, the ACM2 rotating ocean cell has a deeper inflow than the ACM2 rotating land cell by approximately 1 km (Fig. 3.39, bottom). The ACM2 rotating ocean cell composite also has the relative humidity maximized at 3.5 km (Fig. 3.39b, bottom). The three-dimensional convergence of the ACM2 rotating ocean cell composite is $-0.4 * 10^{-3}$ $1/s$, which is slightly weaker than the ACM2 rotating land cell composite, extends down to the surface on the radially outward side, and is maximized just below the maximum in vertical velocity (Fig. 3.39b, bottom).

Generally, the rotating cell composites in the Irma simulations show that the reflectivity tends to be vertically tilted with height (Figs. 3.38a and 3.39a). Our comparisons of the distance of cells from the center showed that the rotating cells tended to be closer to the tropical cyclone center and, therefore, in environments experiencing higher vertical wind shear (Fig. 3.8). Also, the depth of the reflectivity in the rotating cell composites is less than the non-rotating cell composites (Figs. 3.36a, 3.37a, 3.38a, and 3.39a). The maximum vertical velocity is located between 2.5 and 3.5 km, which is about half of that of the non-rotating cell composites (Figs. 3.38a and 3.39a). Both the land and ocean rotating composites have a tangential wind maximum that ranges from 40–48 m/s on the radially outward side of the cell about 1.5–2 km from the composite center (Figs. 3.38 and 3.39). The rotating cell composites have a stronger tangential wind maximum by 2–10 m/s that is closer to the center of the cell composite by about 1–2 km compared to the respective non-rotating cell composites. The tangential wind maximum ranges in height from 2–2.5 km in the rotating cell composites, which like the vertical motion, is also lower than the non-rotating composites by 1–3 km. and The maximum relative humidity tends to be confined to the center of the composite cells and generally located directly below the maximum in vertical velocity (also radially inward in the oceanic rotating cells). The three-dimensional convergence in these composite cells is generally stronger in the rotating land composite cells by $-0.1 * 10^{-3}$ to $-0.2 * 10^{-3}$ $1/s$ compared to the rotating ocean composite cells and located at the center of the composite cells and extends to the surface (Figs. 3.38b and 3.39b).

Not only were there differences between the non-rotating and rotating composite cells, but also between the oceanic and land cells. The biggest difference between land and ocean cells was the extent of dry air in the upper levels. The ocean cell composites consistently had more dry air in the upper levels compared to the land cells, with many composites showing some areas of relative humidity less than 50% (Figs. 3.37b and 3.39b). The composites of both rotating and non-rotating cells showed that the radial inflow near the surface was generally deeper by a factor of two compared to the oceanic cells (Figs. 3.36, 3.37, 3.38, and 3.39). The PBL heights in the oceanic cell composites were all very similar and around 500 m between the different PBL schemes; however, the land cell composites showed PBL heights which varied between 500–1000 m depending on the PBL scheme (Figs. 3.36, 3.37, 3.38, and 3.39). Differences in the non-rotating and rotating cell composites were also seen across the PBL schemes, particularly in reference to the distribution of moisture in the low levels, as well as, momentum differences in the low levels driven by differences in the radial inflow and vertical motion. The MYNN3 cell composites showed the lowest extent of the model reflectivity around 0.5-1.5 km more shallow than the YSU or ACM2 composites in both the rotating and non-rotating cell composites. The ACM2 scheme consistently showed the largest vertical motions by 1–3 m/s in each composite.

3.7.5 CAPE cell composites

As seen previously, the ACM2 simulations of both hurricanes Harvey and Irma produce the most 0–3-km CAPE, particularly downshear (Figs. 3.30 and 3.31). Higher CAPE generally leads to stronger upward vertical motions. Both storms showed that the ACM2 rotating and non-rotating cell composites had stronger upward vertical motion compared to the YSU and MYNN3 composites counterparts (Figs. 3.32, 3.33, 3.34, 3.35, 3.36, 3.37, 3.38, and 3.39).

Figure 3.40 shows the composite CAPE from each grid point treated as a parcel in the non-rotating land cells. In the YSU non-rotating land composites (top), the CAPE has a maximum of around 800 J/kg in Harvey and 1100 J/kg in Irma located below the PBL height (~ 0.5 km in Harvey and ~ 1 km in Irma) on the radially outward side of the cell composite. The CAPE above the PBL is much weaker at approximately 100–250 J/kg, while near the surface the CAPE is about 250 J/kg in the Harvey composite and less than 100 J/kg in the Irma composites. These low values of CAPE extend to around 3.5 km in height in Harvey and 2 km in height in Irma. In the MYNN3 non-rotating land composites (middle), the CAPE in both Harvey and Irma is maximized just below the PBL on either side of the cell's center with a magnitude of around 750 J/kg. Near the center of the cell composite, the CAPE extends above the PBL in the updraft to about 5–6 km in height, but is only 100–150 J/kg in the Harvey composite and between 100–250 J/kg in the Irma composite. The ACM2 non-rotating land composites (bottom) shows that much like the YSU composites, the CAPE has a maximum of 750–1000 J/kg on the radially outward side of the cell composite below the height of the PBL. In the Harvey composite, the CAPE above the PBL is mainly confined to the radially outward side of the cell composite with a magnitude ranging from 100–500 J/kg that decreases in height up to about 3 km. In the Irma composite, the CAPE above the PBL near the center of the cell composite extends upward into the updraft through the entire depth of the cell composite, ranging from 100–250 J/kg.

The non-rotating ocean cell composites of CAPE are shown in Figure 3.41. In the YSU non-rotating ocean cell composite (top), the CAPE is maximized below the PBL on the radially outward side of the composite cells in both Harvey and Irma with magnitudes that exceed 1200 J/kg. At the center of the cell composite, the CAPE extends above the PBL height to 8 km in the Harvey YSU simulations and 4.5 km in the Irma YSU simulation. The CAPE above the PBL at the center of the cell composite is weaker than within the PBL with magnitudes ranging from 100–200 J/kg. At the surface at the center of the composite cells the CAPE is at its minimum in the PBL around 700 J/kg. Both the Harvey and Irma MYNN3 non-rotating cell composites (middle) show similar CAPE of 1200 J/kg and 1000 J/kg, respectively, on both the radially inward and outwards side of the composite cells.

Above the PBL at the center of the cell composite the CAPE is reduced to 100–150 J/kg and extends to about 5 km in the Harvey MYNN3 simulation and to 8 km in the Irma MYNN3 simulation. The CAPE is at a minimum within the PBL at the center of the cell composite with a magnitude around 700 J/kg. The ACM2 non-rotating ocean cell composite (bottom) for both Harvey and Irma shows the largest CAPE of any of the non-rotating cell composites with magnitudes of 1200 J/kg in and around the PBL height on both the radially inward and outward sides of the composite cells. At the center of the ACM2 non-rotating ocean cell composite the CAPE ranges between 100–250 J/kg and extends to a height of around 8–8.5 km in both Harvey and Irma. The minimum CAPE within the PBL at the center of the cell composite has a magnitude of around 800 J/kg.

Figure 3.42 shows the CAPE for the land rotating cell composites. The YSU rotating land cell composite (top) for the Harvey simulation shows the CAPE is maximized on the radially outward side of the cell with a magnitude of around 400 J/kg. Above the PBL at the center of the Harvey cell composite the CAPE extends to about 3.5 km varying from 100–200 J/kg. In the YSU rotating land cell composite for Irma, the CAPE is maximized on the radially inward side of the cell composite with a magnitude around 300 J/kg. The CAPE at the center of the Irma rotating land cell composite extends to approximately 3.5 km but is weaker than the Harvey composite ranging in magnitude from 100–150 J/kg. The CAPE in the MYNN3 rotating land cell composite (middle) for both Harvey and Irma is maximized in the PBL with a magnitude of around 400 J/kg and 250 J/kg, respectively. Like in the other cell composites, the CAPE extends in the vertical at the center of the cell composite to a height of around 3.5 km with a magnitude ranging between 100–200 J/kg in both the Harvey and Irma MYNN3 rotating land cell composites. The ACM2 rotating land cell composites (bottom) show that the CAPE in the PBL is maximized on the radially outward side of the cell with a magnitude of around 600 J/kg in the Harvey composite and around 400 J/kg in the Irma composite. In the Harvey ACM2 rotating land cell composite, the CAPE extends to 4 km in the center of the composite cell ranging in magnitude from

100–250 J/kg. The CAPE at the center of the Irma ACM2 rotating land cell composite extends in the vertical to 4 km ranging between 100–200 J/kg, with additional CAPE of about 100 J/kg aloft at approximately 6.5 km. In all of the rotating land cell composites, the CAPE in the updraft above the PBL is located on the radially inward side of the center of the cell composite.

The rotating ocean cell composites of CAPE are shown in Figure 3.43. In the YSU rotating ocean cell composite (top), the CAPE is maximized below the PBL. In the Harvey composite, CAPE magnitudes exceed 1200 J/kg in the PBL and are deeper on the radially outward side of the composite cells (as the PBL is deeper there by about 300 m). The CAPE decreases with height from about 1100 J/kg just above the PBL at the center of the Harvey cell composite to no CAPE at about 6 km. The Irma composite CAPE is maximized on the radially outward side where the PBL height is also a few 100 m deeper with a magnitude of around 1100 J/kg. At the center of the Irma cell composite the CAPE decreases with height from around 600 J/kg at the top of the PBL to no CAPE at about 4 km. The MYNN3 rotating ocean cell composites (middle) show maxima in CAPE located within the PBL in both Harvey and Irma. The maximum in CAPE in the Harvey rotating cell composite flanks the center, on both the radially inward and outward sides of the composite cell with a magnitude of around 1100–1200 J/kg. At the center of the Harvey cell composite above the PBL, the CAPE is around 600 J/kg and decreases with height through around 5.5 km. In the Irma rotating ocean cell composite, the CAPE is maximized in the PBL with a magnitude ranging between 600–1000 J/kg. The CAPE in the Irma cell composite extends above the PBL to a height of around 4.5 km and ranges in magnitude between 100–600 J/kg. The ACM2 rotating ocean cell composites (bottom) show that the CAPE in the PBL is more than 1200 J/kg. At the center of the Harvey composite cell there is a peak in CAPE that extends above the PBL to around 4.5 km and ranges in magnitude from 100–700 J/kg. In the Irma ACM2 rotating ocean cell composite on the radially outward side within the PBL the magnitude of the CAPE is around 900 J/kg. The CAPE at the center of the Irma ACM2 rotating ocean cell composite extends in the vertical to 6.5 km ranging between 100–600 J/kg. Again, like in the rotating land cell composites, the rotating ocean cell composites also have CAPE above the PBL maximized in the updraft on the radially inward side of the cell composite.

Consistently across the cell composites of both Harvey and Irma, the ACM2 produced the most abundant CAPE, particularly with parcels originating in the boundary layer and extending vertically in the center of the cell composites. In the rotating cell composites, the CAPE above the boundary layer in the updraft is maximized on the radially inward side of the composite cell. The increased CAPE in the ACM2 simulations can be linked back to the stronger vertical motion seen in all the cell composites for the Harvey and Irma non-rotating and rotating cells. In the following chapter, the mechanisms of the ACM2 PBL scheme will be investigated to understand why the ACM2 simulation showed increased CAPE in the cell composites. The maximum of the CAPE was about 20% less in the land non-rotating cell composites compared to the ocean non-rotating cell composites (Figs. 3.40 and 3.41). The maximum of the CAPE was about 130% less in the land rotating cell composites compared to the ocean rotating cell composites (Figs. 3.42 and 3.43).

3.8 Summary and discussion

This chapter has explored the convective cell distributions (both spatially and temporally), and how the locations of the non-rotating and rotating cells vary in relation to geography. Furthermore, this chapter has identified convective environmental differences in momentum, moisture, and CAPE between the different PBL schemes tested. Lastly, comparisons were drawn between the composite vertical structure of non-rotating and rotating convective cells over the ocean and over land.

The spatial distribution of identified non-rotating cells in the simulations of both hurricanes Harvey and Irma occur east of the tropical cyclone center and in the downshear, particularly, downshear-right quadrants. Cells identified as rotating are generally located in the northeast quadrant and typically downshear, especially in the downshear-left quadrant. This distribution of convective cells is largely in agreement with the expected distribution of convection downshear in tropical cyclones experiencing vertical wind shear (Corbosiero and Molinari 2003). The typical locations of rotating convection in the northeast quadrant seen in Figures 3.1a and 3.5a concurs with the findings of McCaul (1991), Schultz and Cecil (2009), and Edwards (2012), who examined tropical cyclone tornado reports and found a maximum in the northeast quadrant. The distribution is also similar to that of the NCAR ensemble model seen in Card (2019).

Card (2019) showed that the total number of rotating cells outnumbered the total number of non-rotating cells by a factor of 2–3 times in the NCAR ensemble. In the simulations of Hurricane Harvey, the number of identified non-rotating cells is about 22% greater than the number of identified rotating cells (Fig. 3.1). In the Irma simulations, the number of identified non-rotating cells is about 18% less than the number of identified rotating cells (Fig. 3.5). Both the simulations showed much less of a differential in the number of identified non-rotating versus rotating cells compared to the NCAR ensemble simulations of Harvey and Irma.

The MYNN3 PBL scheme identifies more rotating and non-rotating cells than the YSU and ACM2 in both hurricanes Harvey and Irma. The identified rotating cells tend to be statistically significantly closer to the tropical cyclone center compared to the non-rotating cells in both hurricanes Harvey and Irma, as well as across all PBL schemes (Figs. 3.4 and 3.8), indicative of the respective locations along the rainbands. In reference to the local geography, the rotating cells in both the simulations of hurricanes Harvey and Irma are identified closer to the coast and more frequently over land compared to over the ocean, and the identified non-rotating cells occur more frequently over the ocean and at further distances from land (Figs. 3.2 and 3.6). The YSU PBL scheme in both simulations of hurricanes Harvey and Irma produced both rotating and non-rotating cells that are statistically significantly closer to the coast compared to the rotating and non-rotating cells in the MYNN3 simulations

(Figs. 3.16 and 3.17). The distance from the coasts of the rotating and non-rotating cells is in large agreement with observations of convective cells in Hurricane Ivan (Baker et al. 2009; Eastin and Link 2009), in which it was shown that non- or weakly-rotating convection typically existed offshore and began to rotate more vigorously once the cells make landfall.

Rotating cells in the simulations of both Harvey and Irma extended further into the downshear-left quadrant than the non-rotating cells that are located right-of-shear (Figs. 3.1 and 3.5). The portion of the rainband cells in the downshear-left quadrant is closer to the center of the tropical cyclone than right-of-shear rainband cells as cyclonic inflow brings these cells closer to the center of the tropical cyclone, as they traverse the rainband. As noted previously, the rotating cells were closer to the center of the tropical cyclone compared to the non-rotating cells (Figs. 3.4 and 3.8). One would expect that the stratiform (mature) part of the tropical cyclone rainband in the downshear-left quadrant would be less supportive of strong low-level updrafts given the low-level sinking motion associated with stratiform precipitation; however, favorable environmental conditions such as high 0–3-km helicity allow for the maintenance of rotating cells in this region.

In a temporal sense, the rotating cells in Hurricane Harvey tend to peak between 0400 and 1200 UTC on 26 August (2300–0700 local time) and the rotating cells in Hurricane Irma tend to peak between 2000–0900 UTC (1600–0500 local time), both occurring in the evening and overnight hours (Figs. 3.9 and 3.10). The broadness of the peak in identified rotating convective cells shows that, in general, both hurricanes were capable of producing tornadoes almost constantly and almost regardless of the time of day. It still remains unclear if certain times of the day are more favored for tropical cyclone tornadoes and if this varies by each individual storm. The number of identified rotating cells over land in Hurricane Harvey shows a peak between 0400 and 1600 UTC (2300–1100 local time) 26 August, similar to the peak in the total identified rotating cells (Fig. 3.11 top). Although the number of identified rotating cells over land in the Hurricane Irma simulations are low, there is an increase in identified rotating land cells between 2100 and 0900 UTC (1700–0500 local time). To compare to the observed tornado reports (Figs. 1.4 and 1.5, right) Harvey showed a peak between 0400–1000 UTC and Irma showed a peak between 1700–2300 UTC, aligning very well with the peak in rotating cell activity in the Harvey simulations, but earlier than the increased activity in the rotating cell activity in the Irma simulations.

In the simulations of hurricanes Harvey and Irma, the peaks in identified rotating convective cells tends to be in the late afternoon and into the early morning hours. This timing is noticeably different from observational studies such as McCaul (1991), which showed that 57% of tropical cyclone tornadoes occur between 1400–2300 UTC (corresponding roughly to 0900–1800 local time in the southeastern U.S.). Schultz and Cecil (2009) concurred with this and found a pronounced peak in tropical cyclone tornado reports in the early- to mid-afternoon, with similar findings in Edwards (2012). Given that the temporal distribution of rotating cells aligns better with the observations of tropical cyclone tornadoes in Harvey and Irma compared to the past literature (McCaul 1991; Schultz and Cecil 2009; Edwards 2012) it is suggested that the variability in tropical cyclone tornadoes is more dependent on individual storms and that storm's environment.

Two factors may complicate this temporal analysis of land rotating cells and the comparison to observed tornado reports. First, the identified rotating cells may not be representative of where tropical cyclone tornado reports may occur in hurricanes Harvey and Irma, although Carroll-Smith et al. (2019) has shown that the use of tropical cyclone tornado surrogates was successful at identifying where observed tornado reports were likely to occur in high-resolution simulations of Hurricane Ivan (2004). Second, there may be biases in the observed tornado reports in tropical cyclones due to the daytime bias in tornado reports, evacuations, and/or the difficulty verifying reports in areas of substantial post-storm damage (caused by wind, flooding, or storm surge).

The convective environments differed between the YSU, MYNN3, and ACM2 PBL schemes, since these schemes work to resolve sub-grid scale mixing of momentum, heat, and moisture in the boundary layer in different ways. In terms of momentum differences across the PBL schemes, it was shown that in both Harvey and Irma, the MYNN3 simulations generally had less 0–3-km updraft helicity compared to the YSU and ACM2 simulations (Fig. 3.18 and 3.19); in fact, these differences were statistically significant. Most of the large-scale difference in the 0–3-km updraft helicity was driven by differences in the 0–3-km helicity and not the 0–3-km vertical velocity; however, on the scale of individual cells, the 0–3-km vertical velocity also plays a comparable contribution to the 0–3-km updraft helicity on the individual cell scale (Figs. 3.20 and 3.21). In all of the PBL schemes in both the simulations of Harvey and Irma, the 0–3-km vertical wind shear over the land was statistically significantly larger than over the ocean (Figs. 3.25 and 3.26). In the Harvey simulations, the 0–3-km vertical wind shear was 76–216% higher over land compared to over the ocean. In the Irma simulations, the 0–3-km vertical wind shear was 24–36% higher over land compared to over the ocean. Baker et al. (2009) showed that 0–1-km vertical wind shear was 37% greater over land compared to over the ocean, which is comparable to the simulations of both Harvey and Irma. The increase in the 0–3-km vertical wind shear coincides with the location of the coastline. The key driving factor that influenced the increase in 0–3-km vertical wind shear from ocean to land is the friction that causes an elongation of the hodograph over the transition from ocean to land (Figs. 3.25 and 3.26).

The vertical velocity CFADs (Fig. 3.22) over the entire storm showed similarities with numerous observational and model studies (Didlake and Houze 2009; Rogers et al. 2007, 2012; DeHart et al. 2014; Zhang et al. 2017). Rogers et al. (2007) compared Doppler-derived vertical velocity to model simulations of hurricanes Bonnie (1998) and Floyd (1999), in both the eyewall region and stratiform region. In the eyewall region, the vertical velocities are centered around zero with frequencies of vertical velocity above 5% from -3 to 3 m/s (Rogers et al. 2007). Zhang et al. (2017) studied model simulations of hurricanes Bill (2009), Earl (2010), Karl (2010), and Irene (2011). The CFADs of vertical motion in the eyewalls of these modeled storms ranged generally between -1–2 m/s, which was very similar to the observations of these storms from Doppler radar (Zhang et al. 2017). The observed CFAD of the convective region of Hurricane Katrina (2005) from Didlake and Houze (2009), aligns well with CFAD in vertical motion for the simulations of Hurricane Irma. The simulations of Hurricane Harvey show a vertical motion CFAD more akin to the stratiform region of Hurricane Katrina (Didlake and Houze 2009). The stratiform region CFAD of vertical velocity is very similar to that of Didlake and Houze (2009), showing vertical motion frequencies above 5% ranging in magnitude from -2 to 2 m/s. DeHart et al. (2014) investigated the vertical velocity in the eyewall from aircraft Doppler-derived vertical velocity between 2003–2010. In the eyewall, the vertical motion is dominated by updrafts such that the CFADs are skewed to positive vertical motion, and show a maximum in frequency between -1 and 2 m/s between 1–6 km (DeHart et al. 2014). In an analysis of the kinematic structure of tropical cyclones using airborne Doppler radar data, Rogers et al. (2012) showed that for the entire radial domain the bulk of the vertical velocities fell between -2 and 2 m/s. The analysis of the vertical velocity CFADs (Fig. 3.22) from the simulations of hurricanes Harvey and Irma showed that the frequencies of vertical velocities above 5% are between -1 and 1 m/s, which are very similar to what has been documented in observed storms (Didlake and Houze 2009; Rogers et al. 2012; DeHart et al. 2014) and modeled storms (Rogers et al. 2007; Zhang et al. 2017).

The differences in the CFADs of vertical velocity in both Harvey and Irma show two distinct parts of the atmosphere, best described as a mixing layer, which was generally below 3 km, and the free atmosphere, which extends above the mixing layer. There are more frequent stronger vertical velocities in the YSU simulations compared to the MYNN3 simulations in the mixing layer. In the free atmosphere, both the ACM2 and YSU simulations showed more near zero values of vertical motion compared to the MYNN3 simulation; however, in the low levels at certain times, the YSU and ACM2 simulations showed stronger upward and downward vertical motions compared to the MYNN3 simulation (Figs. 3.23 and 3.24). The moisture and CAPE environments across the PBL schemes tested showed variations that can certainly affect the convection in tropical cyclones.

Moisture within the boundary layer varied by altitude between the simulations, with the MYNN3 simulations showing the most frequent high values of relative humidity in the lowest 1 km, unlike the YSU and ACM2 simulations (Fig. 3.28). Numerous studies have highlighted that the MYNN3 PBL scheme, and other local PBL schemes, tends to have difficulty generating large eddies and mixing moisture (Nakanishi and Niino 2006; Cohen et al. 2015). As stated previously, the MYNN3 simulations of both Harvey and Irma showed the most identified rotating cells compared to the YSU and ACM2 simulations and the MYNN3 simulation also showed the highest relative humidity in the low levels. This result supports the findings of Curtis (2004), which showed that high relative humidity from the surface to 900 hPa and drier air above 700 hPa is environmentally favorable for tropical cyclone tornado outbreaks.

Differences in CAPE seen in the PBL schemes are directly connected to the moisture as it affects the convective potential. CAPE is very closely tied to the vertical distribution of relative humidity, specifically that lower values of relative humidity in the mid-levels and higher values of relative humidity in the lower-levels promotes a higher CAPE environment. Very moist low levels like seen in the MYNN3 simulations can limit low level CAPE as seen in Figures 3.28 and 3.29 (bottom) for Hurricane Irma. The most frequent values of high CAPE occurred below 3 km in all of the simulations in both hurricane Harvey and Irma (Fig. 3.29). The simulations that used the MYNN3 PBL scheme tend to have high values of CAPE, although the high values of CAPE lacked depth (Fig. 3.29). This result is directly connected to what was seen in the CFADs of vertical velocity (Fig. 3.22), which showed that the Irma simulations had more frequent larger values of vertical velocity than the simulations of Harvey. More CAPE leads to increase convection as well as stronger upward and downward vertical velocities. The 0–3-km CAPE was concentrated mainly in the downshear quadrants similar to the distribution of most unstable CAPE in Molinari and Vollaro (2008), Molinari and Vollaro (2010), and Molinari et al. (2012), but, in the case of the simulations of Hurricane Irma, there was also abundant 0–3-km CAPE in the upshear-right quadrant (Figs. 3.30

and 3.31). In both hurricanes Harvey and Irma, the MYNN3 PBL tended to generate less 0–3-km CAPE compared to the YSU and ACM2 simulations in the downshear-right quadrant (Figs. 3.30 and 3.31). Many studies have highlighted that 0–3-km CAPE as it is associated with more effective interaction between low-level shear and low-level updrafts (McCaul 1991; McCaul and Weisman 1996; Rasmussen 2003). McCaul and Weisman (1996) showed that supercells in land-falling tropical cyclone environments can develop low-level updrafts that achieve the intensities that are equal to or can exceed those observed in Great Plains supercells. Both supercells are forced predominantly by dynamically-induced pressure gradients, which result from the interaction between the updraft and the very strong low-level vertical wind shear; thus, maximizing the CAPE and low-level vertical wind shear is favorable to the development of rotating convection in the tropical cyclone environment.

The geography has an impact on the rotating and non-rotating cells examined. Baker et al. (2009) and Eastin and Link (2009) showed in observations of Hurricane Ivan (2004) that non- or weakly-rotating convection typically exists offshore and begins to rotate more vigorously once the cells approach and make landfall as they encounter higher low-level vertical shear. In all of the PBL schemes, in both the simulations of Harvey and Irma, the 0–3-km vertical wind shear over the land was statistically significantly larger than over the ocean (Figs. 3.25 and 3.26). The increase in the 0–3-km vertical wind shear coincides with the location of the coastline. As mentioned previously, the 0–3-km vertical wind shear plays an important role in the development of rotating convection in tropical cyclones (McCaul and Weisman 1996). The key driving factor that influenced the increase in 0–3-km vertical wind shear from ocean to land is the friction, which causes an elongation of the hodograph over the transition from ocean to land (Figs. 3.25 and 3.26).

The vertical structure of the composite non-rotating and rotating cells identified had many differences between the cell types as well as differences between land and ocean cells, and across the different PBL schemes. The general rotating cell (Figs. 3.34, 3.35, 3.38, and 3.39) has reflectivity that is tilted in the vertical as seen in many observational studies

(Barnes et al. 1983; Hence and Houze 2008; Yu and Tsai 2013; Moon and Nolan 2015a; Tang et al. 2018b). The maximum in vertical velocity in the rotating cells is between 2.5 and 3.5 km. The rotating cell composites have maxima in tangential wind on the radially outward side that is closer to the composite center by about 1–3 km and stronger by about 2– 10 m/s compared to the respective non-rotating cell composites. The three-dimensional convergence is also generally strong and maximized just below the height of maximum vertical velocity, extending to the surface on the radially outward side. In the rotating cells, the maximum in the relative humidity lies directly below the maximum in vertical velocity, typically around 2 to 3.5 km wrapping around the tangential wind maximum.

The rotating cell composites where similar to the rotating cells observed in aircraft observations from Hurricane Ivan presented in Eastin and Link (2009). The observed rotating cells had updrafts which had a depth of around 6–7 km above the boundary layer, which was very similar to the 5–7 km depths in the rotating cell composites. Eastin and Link (2009) also showed that the maximum in the vertical velocity observed in each of the cells ranged between 6–11 m/s and the composite of the rotating ocean cells presented here showed vertical velocity magnitude ranging from 6–12 m/s (Figs. 3.35 and 3.39). The heights of these vertical motion maxima in the observed cells from Eastin and Link (2009), which ranged from 2.5 and 3.5 km, were nearly identical to the maxima in vertical motions in the rotating cell composites which ranged from 2.5 to 3.5 km. Overall, there was a high degree of similarity between the observed rotating cells of Hurricane Ivan from Eastin and Link (2009) and the cell composites for the identified rotating cells in both hurricanes Harvey and Irma. A schematic of the identified rotating cells in tropical cyclones is provided in Figure 3.44 which highlights the important characteristics of the rotating cell composites similar to the observed cells in Hurricane Ivan from Eastin and Link (2009).

The rotating cell schematic is very similar to the schematic of a cross section through the mature cell embedded within a principal rainband presented in Hence and Houze (2008) and Card (2019), as the reflectivity signature tends to tilt radially outward with height (extending to approximately 8 km) and a maximum in the tangential wind appears on the radially outward side about 1–2 km from the composite center and between 2 and 4 km in height. Hence and Houze (2008) and Li and Wang (2012) described the life cycle of convective cells in the rainbands of tropical cyclones. The convective cells tend to form at the start of the rainband and on the radially inward side of the rainband (generally in the upshear-right quadrant). The cells propagate along the rainband and mature as they migrate from the radially inward side of the rainband to the radially outwards side with an updraft increasing in intensity and reflectivity beginning to tilt radially outward with height.

The general non-rotating cell (Figs. 3.32, 3.33, 3.36, and 3.37) has reflectivity that is vertically erect, much like a non-mature principal rainband cell (Hence and Houze 2008; Li and Wang 2012). The non-rotating cells typically have a maximum in vertical velocity between 4.5 and 6.5 km, about double the height of the rotating cell composites. The vertical motion maxima range in intensity from 6–8 m/s. In the non-rotating cells, the maximum in the relative humidity lies directly below the maximum in vertical velocity, typically around 3.5 to 5 km. The non-rotating cell composites typically have weaker maximum in tangential wind on the radially outward side of the composite that are also located further from the composite center. Given that the non-rotating cells are typically located start of the rainband the tangential wind maximum in the composites is similar to the jet seen in the Hence and Houze (2008). The three-dimensional convergence is also generally weak and maximized about 1 km above the surface. In the modeled tropical cyclone in Li and Wang (2012), the cross section of a non-mature principal rainband cell showed a maximum in vertical velocity at around 9 km, with a magnitude around 5 m/s, which is higher in height and similar in magnitude to the non-rotating cell composites. Idealized simulations using the tropical cyclone model version four (TCM4) (Wang 2007) in different vertical wind shear conditions showed that updrafts in the outer rainbands (r>100 km) possessed heights up to 4–6 km, similar in height to updrafts in the non-rotating cell composites and to the updraft observed in other modeling studies (Li and Fang 2018). A schematic of the identified non-rotating cells in tropical cyclones is provided in Figure 3.45, which shows the features highlighted in the non-rotating cell composites similar to what is expected of a non-mature cell embedded within the principal rainband from Hence and Houze (2008) and Li and Wang (2012).

Not only were there differences between the non-rotating and rotating composite cells, but also between the oceanic and land cells. The biggest difference between land and ocean cells was the extent of dry air in the upper levels. The ocean cell composites consistently had more dry air in the upper levels compared to the land cells, with many composites showing some areas of relative humidity less than 50% (Figs. 3.33b, 3.35b, 3.37b and 3.39b). The oceanic principal rainbands from Hurricane Katrina in Hence and Houze (2008) showed that the radially inward side of the rainband tended to be drier and have less reflectivity in the upper levels. Both Yu and Tsai (2013) and Tang et al. (2018b), which examined the principal rainbands of typhoons Longwang (2005) and Hagupit (2008), respectively, noting that the there was dry air aloft on both the radially inward and outward sides of the rainbands much like seen in many other observations of principal rainband convection (Hence and Houze 2008). The environmental vertical wind shear is mainly from the southwest in both simulations of hurricanes Harvey and Irma putting the downshear quadrants over Texas and Florida, respectively. The identified rotating and non-rotating distributions (Figs. 3.1 and 3.5) were typically located in the downshear quadrants, which was expected to be an active area for convection (Corbosiero and Molinari 2003) with general upward vertical motion lofting more moisture higher into the atmosphere.

The composites of both rotating and non-rotating cells showed that the radial inflow near the surface was generally deeper in the oceanic cells. Radial inflow was about twice as deep over the ocean compared to over the land. Giammanco et al. (2013) showed from dropsonde observations of hurricanes from 1997–2005 that over the ocean the inflow depth increased at further radii from the storm center. The land–sea roughness differences have been shown in modeling experiments to increase the radial inflow depth over land compared to the ocean (Wong and Chan 2007), contrary to what is observed in the cell composites in the simulations of hurricanes Harvey and Irma. The PBL heights as computed by the model in the land cell composites showed much more variation than the oceanic cell composites, generally ranging between 0.5 and 1.5 km in depth (Figs. 3.32, 3.33, 3.34, 3.35, 3.36, 3.37, 3.38, and 3.39). The PBL height of the land cell composites in the YSU and ACM2 simulations were higher than the MYNN3 simulation by about 1 km. Due to the increase in surface roughness, the dynamic boundary layer would be expected to increase in depth over land compared to the ocean (Garratt 1990; Tang and Tan 2006; Hirth et al. 2012; Williams 2019; Alford et al. 2020).

The CAPE environments also differed between the land and ocean. The maximum in CAPE in the non-rotating land cell composites was about 20% less than in the non-rotating ocean cell composites (Figs. 3.40 and 3.41). The maximum in CAPE in the rotating land cell composites was about 130% less than in the rotating ocean cell composites (Figs. 3.42 and 3.43). Baker et al. (2009) showed that the 0–3-km CAPE was generally about 35% less over land compared to over the ocean in the observations of Hurricane Ivan. These two results are similar to one another and is important to note since McCaul and Weisman (1996) suggested that both updraft strength and vorticity were enhanced when buoyancy is concentrated in the low levels.

Differences in the non-rotating and rotating cell composites were also seen across the PBL schemes, particularly in reference to the vertical distribution of moisture, as well as momentum differences in the low levels driven by differences in the radial inflow and vertical motion. The MYNN3 cell composites showed the lowest extent of the model reflectivity around 0.5–2 km more shallow than the YSU or ACM2 composites in both the rotating and non-rotating cell composites. The ACM2 composites consistently showed that vertical velocities are 1–3 m/s higher than in the YSU and MYNN3 composites (Figs. 3.32, 3.33, 3.34, 3.35, 3.36, 3.37, 3.38, and 3.39). The ACM2 composites also showed increased CAPE in the boundary layer parcels compared to the YSU and MYNN3 composites (Figs. 3.40, 3.41, 3.42, and 3.43). The CAPE in the rotating cell composites is maximized above the PBL and into the updraft on the radially inward side of the composite center. The aforementioned differences noted across PBL schemes will be examined further in the following chapter to identify mechanisms within the PBL schemes which may play a role in generating these differences.

3.9 Tables and figures

Table 3.1: Percentile threshold values for cell type identification for Hurricane Harvey (2017). The model reflectivity values for the 99.9^{th} percentile, 0–3-km updraft helicity values for the 99.95^{th} percentile, and updraft velocity values for the 99.9^{th} percentile are shown.

WRF Model Runs	**Model Reflectivity (dBz)**	**0–3-km Updraft Helicity (m^2/s^2)**	**Max Updraft Velocity (m/s)**
Harvey (2017):	99.9^{th} percentile	99.95^{th} percentile	99.9^{th} percentile
WDM6-YSU	51.18	33.64	15.33
WDM6-MYNN3	50.61	21.89	11.31
WDM6-ACM2	51.23	33.92	16.42

Table 3.2: Same as Table 3.1, but the percentile threshold values for cell type identification for Hurricane Irma (2017).

WRF Model Runs	Model Reflectivity (dBz)	0–3-km Updraft Helicity (m^2/s^2)	Max Updraft Velocity (m/s)
Irma (2017):	99.9th percentile	99.95th percentile	99.9th percentile
WDM6-YSU	52.34	98.45	20.16
WDM6-MYNN3	51.91	65.43	13.98
WDM6-ACM2	52.59	113.50	18.31

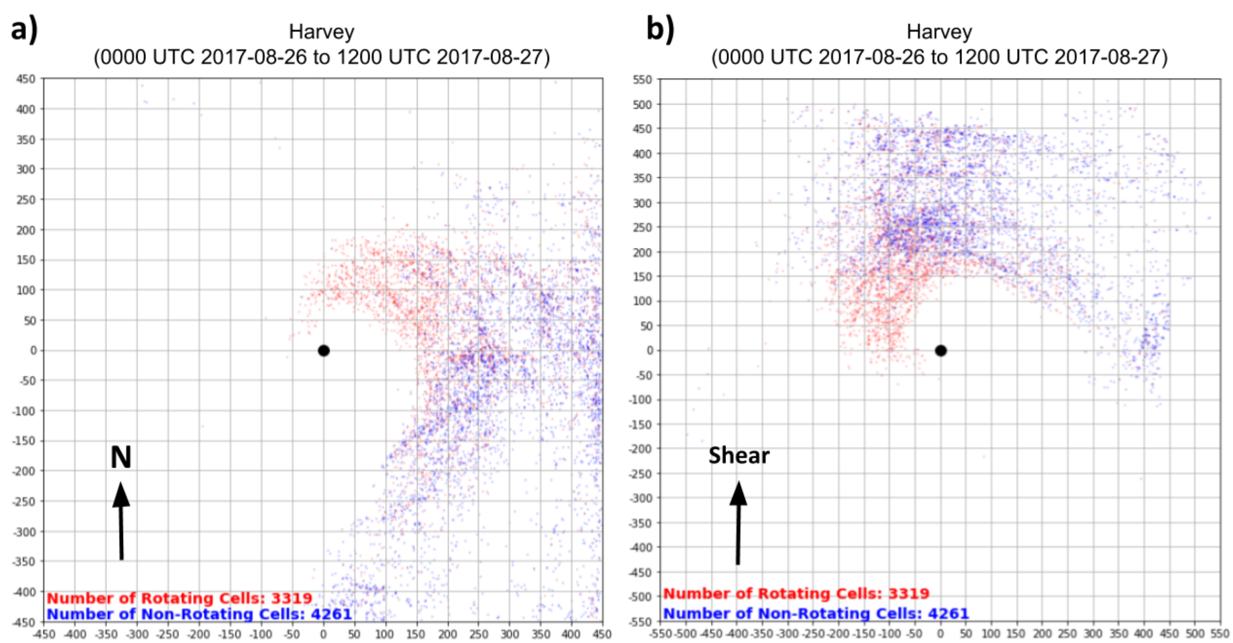

Figure 3.1: Distribution of rotating (red) and non-rotating (blue) cells in simulations of tropical cyclone Harvey (2017) from 0000 UTC 26 August through 1200 UTC 27 August a) with respect to geographic north and b) with respect to shear.

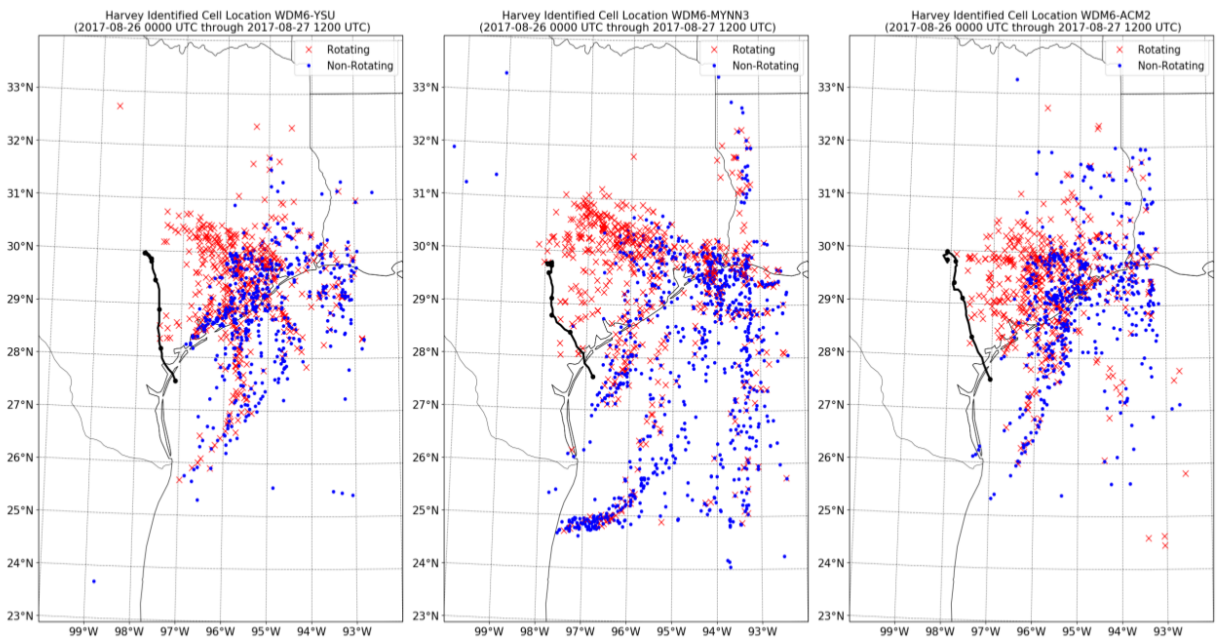

Figure 3.2: Distribution of the rotating (red x), non-rotating (blue dot) cells, and the storm tracks (black solid) in simulations of Harvey (2017) from 0000 UTC 26 August through 1200 UTC 27 August.

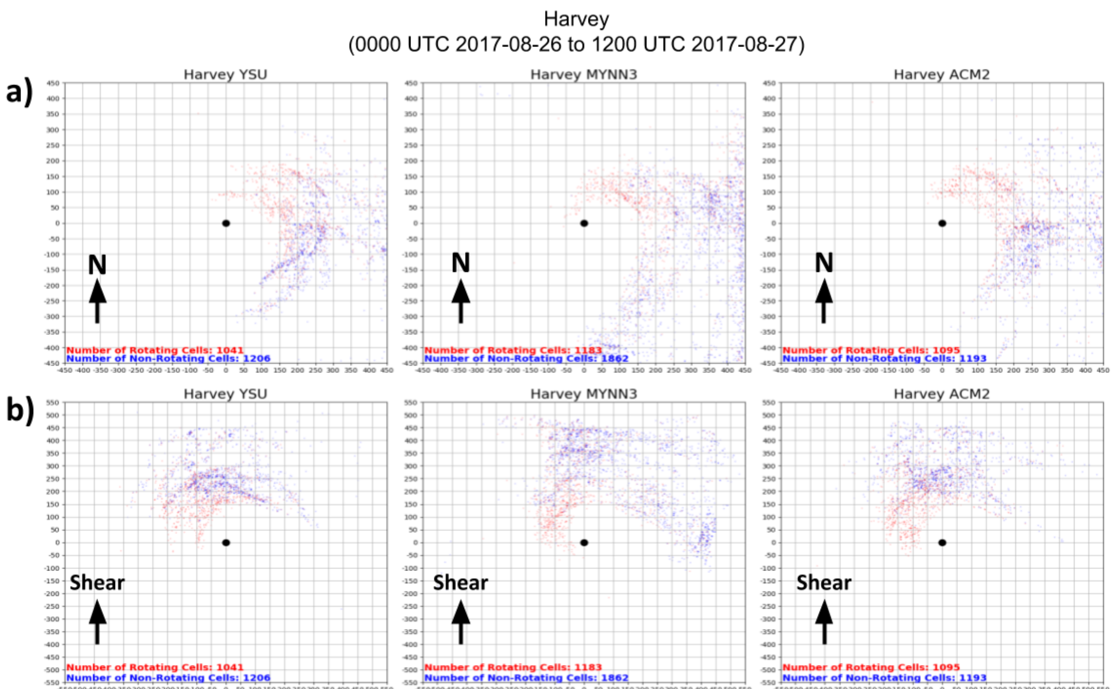

Figure 3.3: Distribution of rotating (red) and non-rotating (blue) cells in simulations of Harvey (2017) from 0000 UTC 26 August through 1200 UTC 27 August a) with respect to geographic north and b) with respect to shear for each PBL scheme.

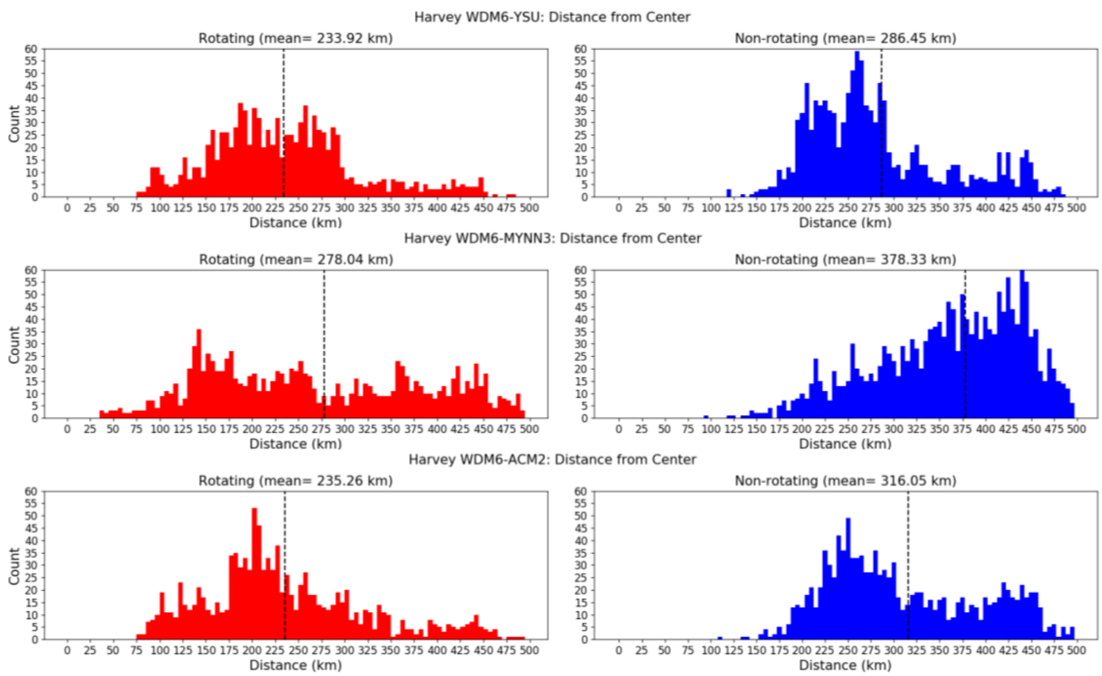

Figure 3.4: Distribution of the distance of rotating (red) and non-rotating (blue) cells from the center of the tropical cyclone and the mean distance (dashed) in simulations of Harvey (2017) from 0000 UTC 26 August through 1200 UTC 27 August.

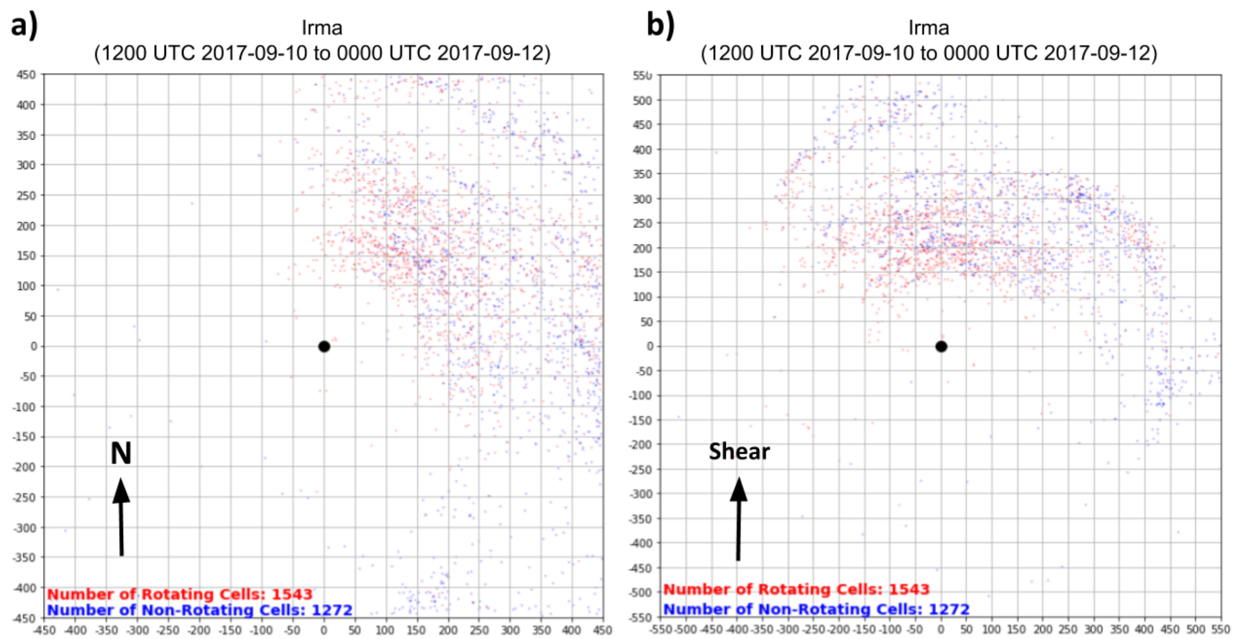

Figure 3.5: Distribution of rotating (red) and non-rotating (blue) cells in simulations of tropical cyclone Irma (2017) from 1200 UTC 10 September through 0000 UTC 12 September a) with respect to geographic north and b) with respect to shear.

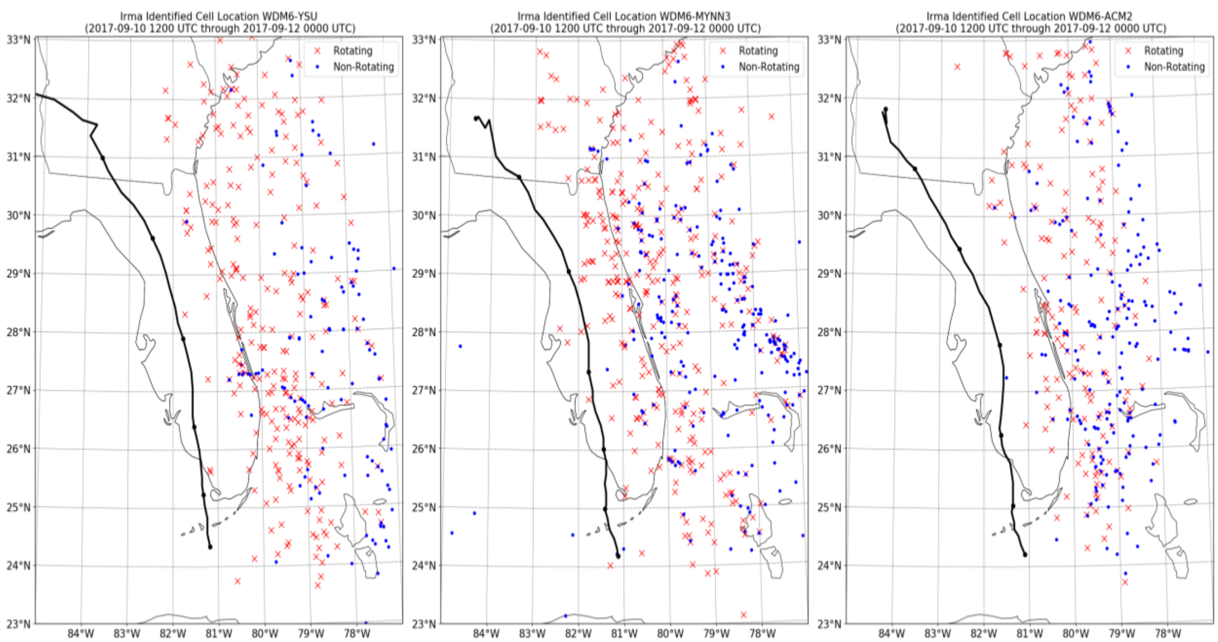

Figure 3.6: Distribution of the rotating (red x), non-rotating (blue dot) cells, and the storm tracks (black solid) in simulations of Irma (2017) from 1200 UTC 10 September through 0000 UTC 12 September.

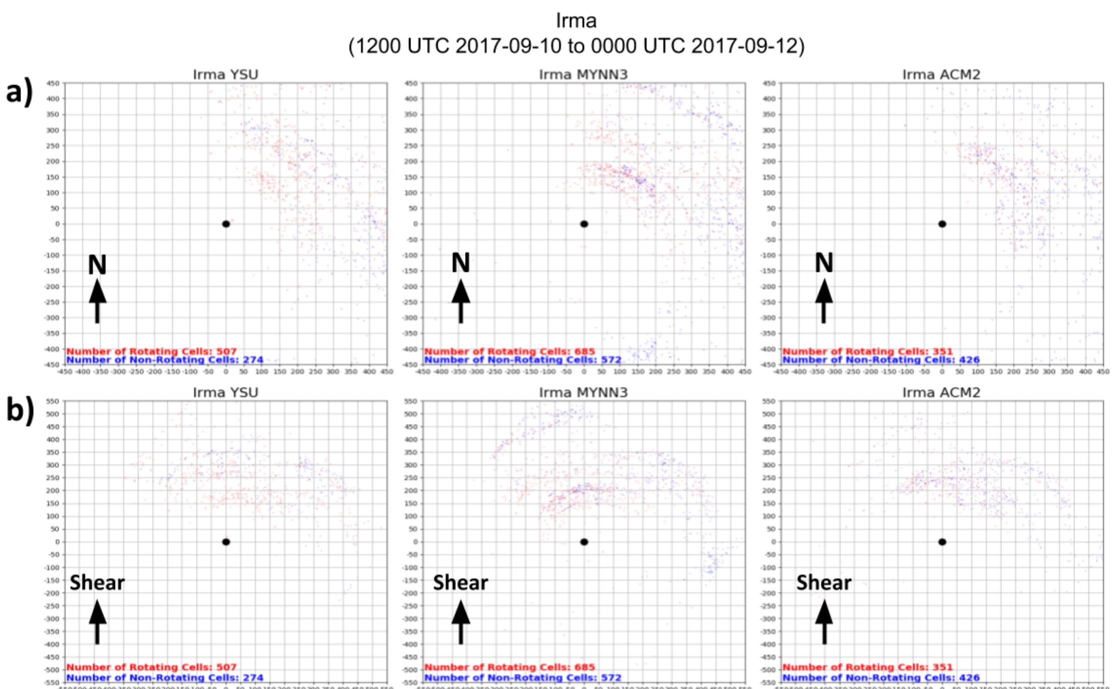

Figure 3.7: Distribution of rotating (red) and non-rotating (blue) cells in simulations of Irma (2017) from 1200 UTC 10 September through 0000 UTC 12 September a) with respect to geographic north and b) with respect to shear for each PBL scheme.

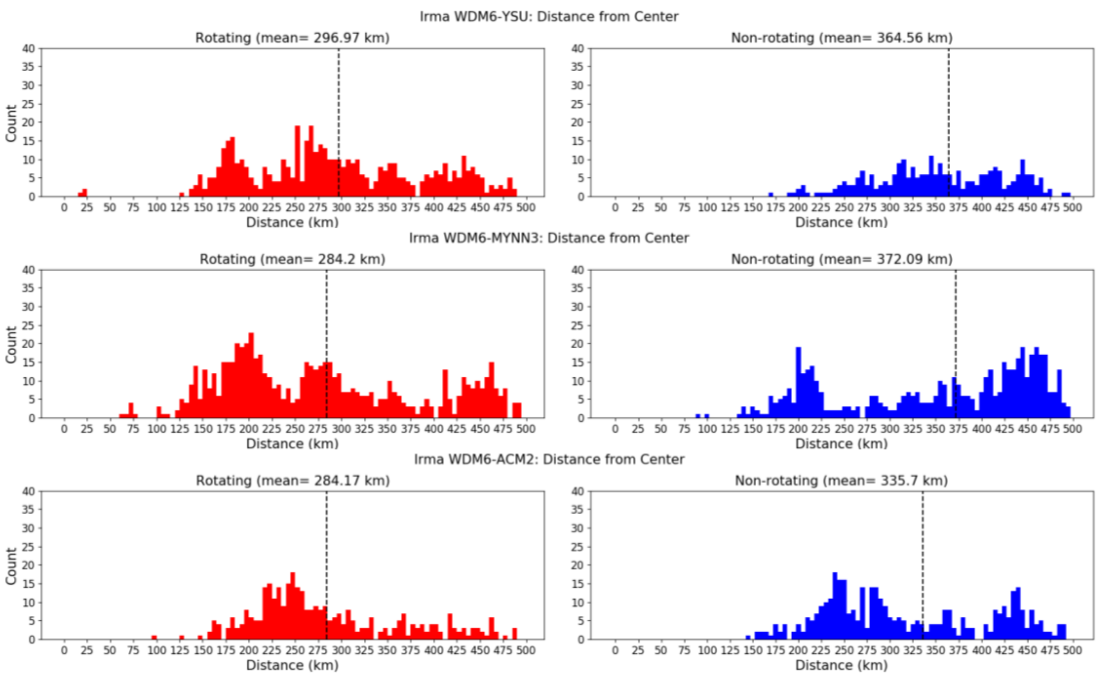

Figure 3.8: Distribution of the distance of rotating (red) and non-rotating (blue) cells from the center of the tropical cyclone and the mean distance (dashed) in simulations of Irma (2017) from 1200 UTC 10 September through 0000 UTC 12 September.

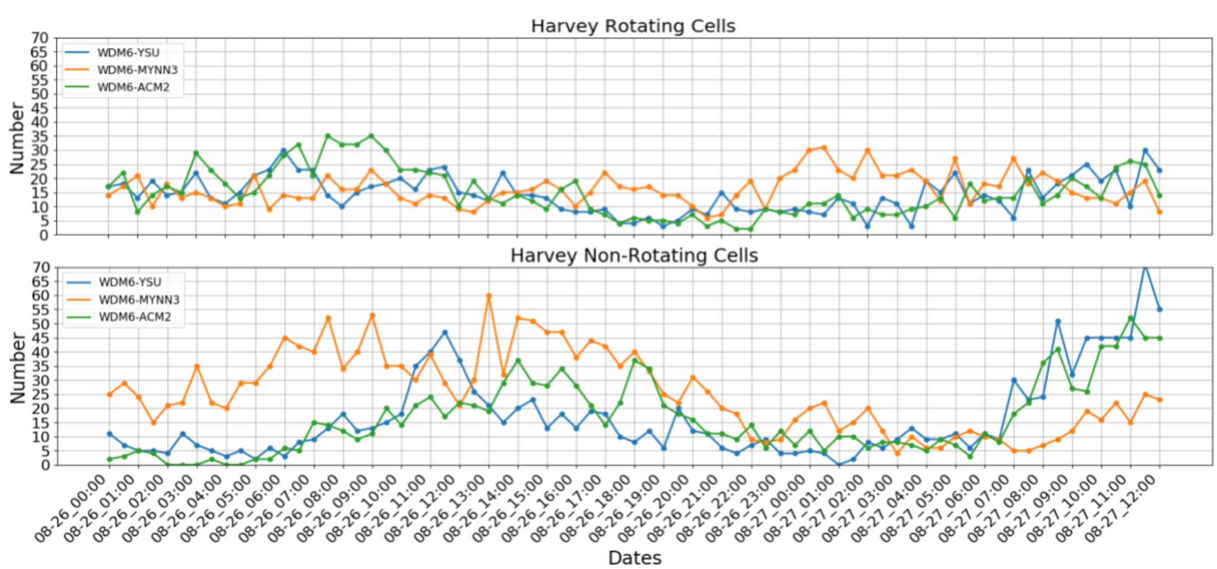

Figure 3.9: Number of rotating (top) and non-rotating (bottom) cells in simulations of Harvey (2017) from 0000 UTC 26 August through 1200 UTC 27 August.

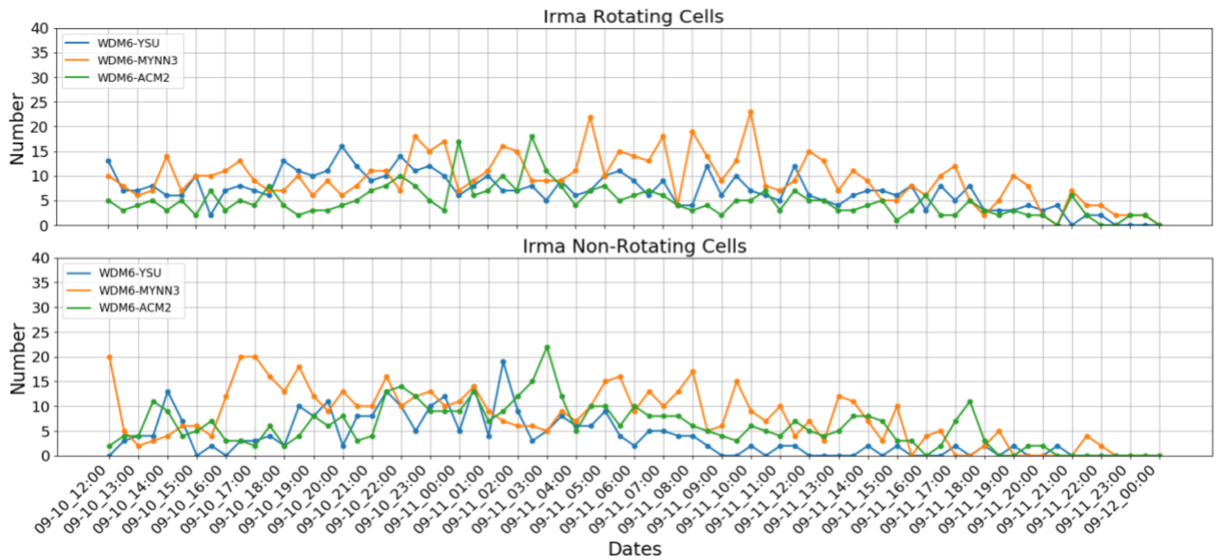

Figure 3.10: Number of rotating (top) and non-rotating (bottom) cells in simulations of Irma (2017) from 1200 UTC 10 September through 0000 UTC 12 September.

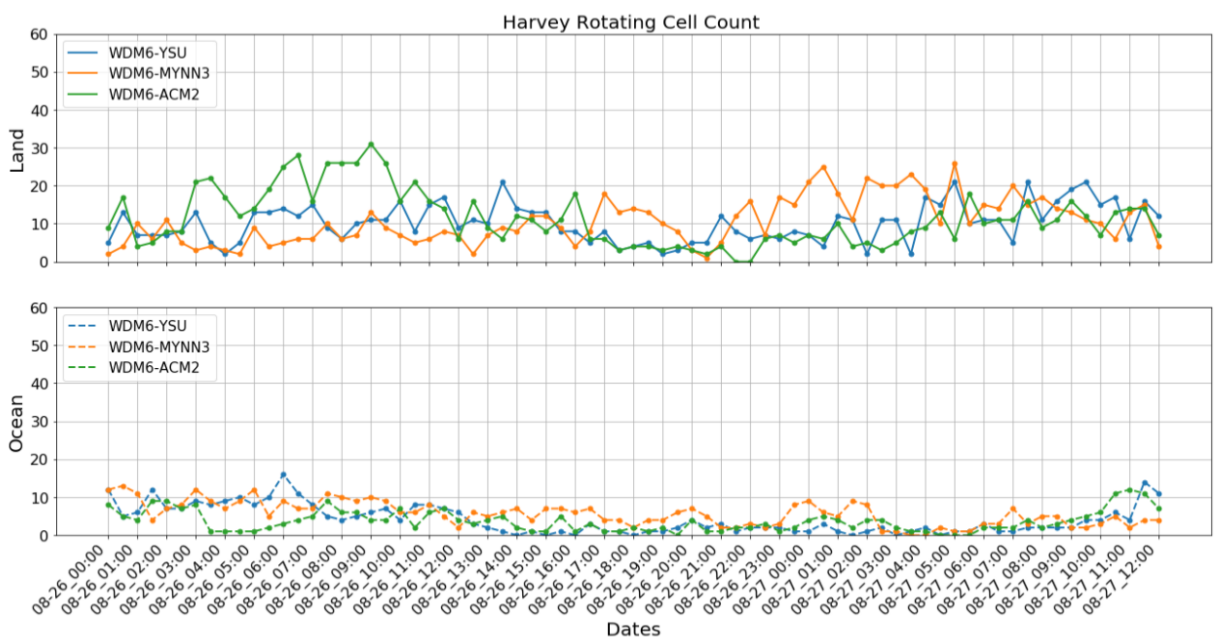

Figure 3.11: Number of rotating cells over land (top) and over ocean (bottom) in simulations of Harvey (2017) from 0000 UTC 26 August through 1200 UTC 27 August.

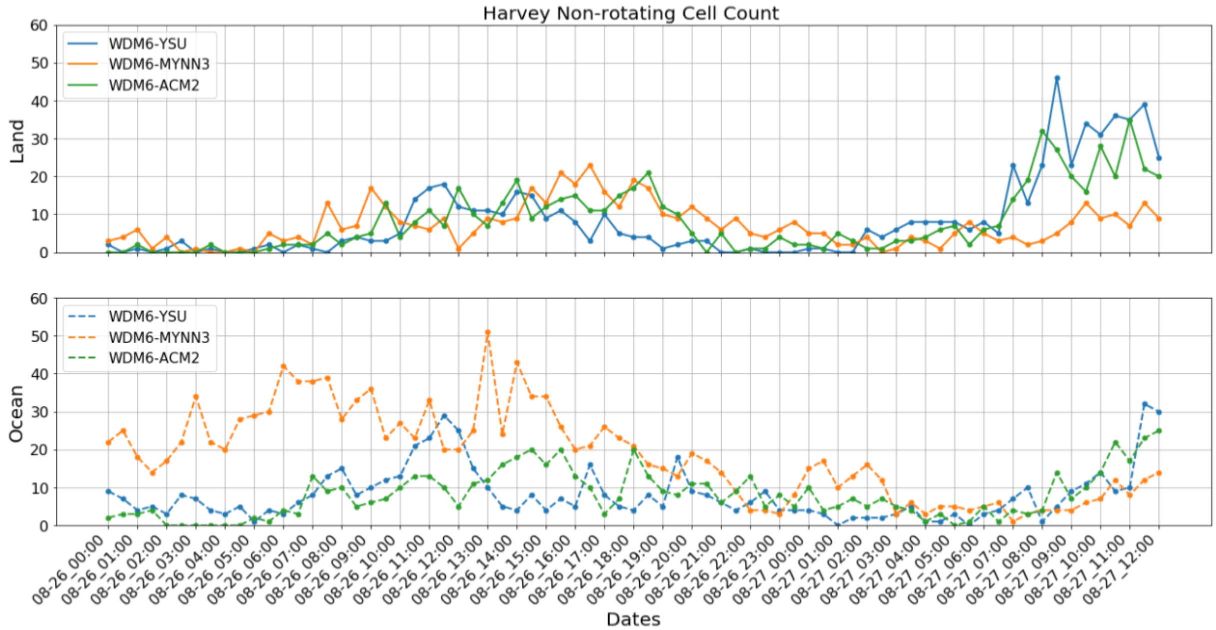

Figure 3.12: Number of non-rotating cells over land (top) and over ocean (bottom) in simulations of Harvey (2017) from 0000 UTC 26 August through 1200 UTC 27 August.

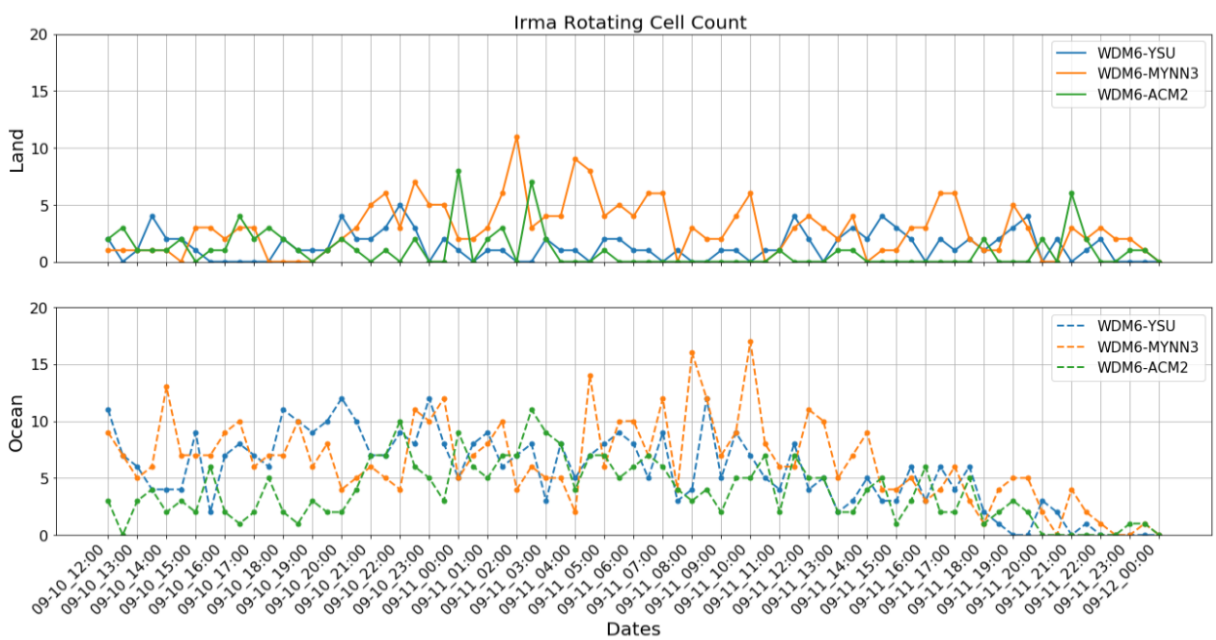

Figure 3.13: Number of rotating cells over land (top) and over ocean (bottom) in simulations of Irma (2017) from 1200 UTC 10 September through 0000 UTC 12 September.

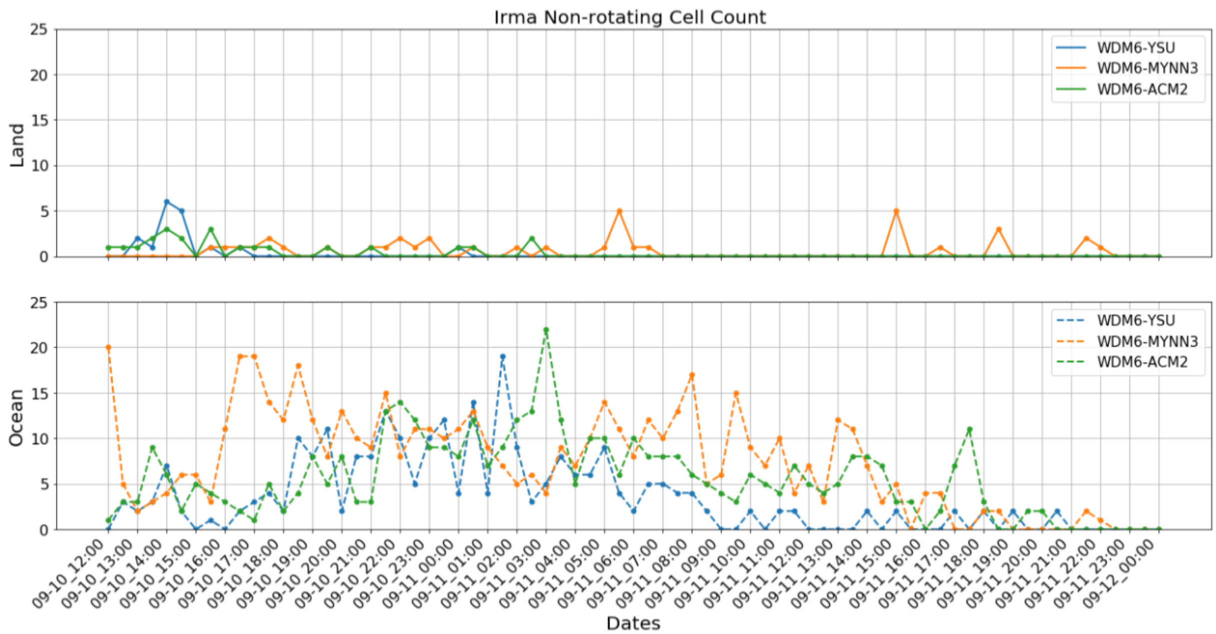

Figure 3.14: Number of non-rotating cells over land (top) and over ocean (bottom) in simulations of Irma (2017) from 1200 UTC 10 September through 0000 UTC 12 September.

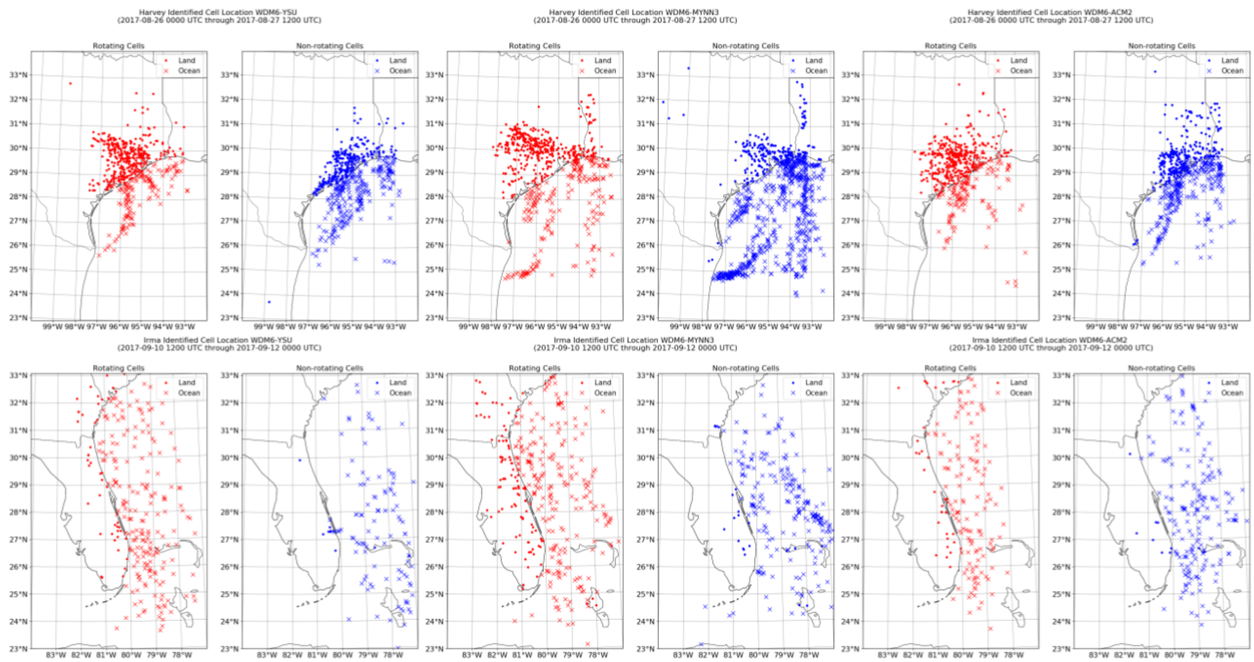

Figure 3.15: Distribution of the rotating (red) and non-rotating (blue) cells that are on land (dot) or over ocean (x) in simulations of Harvey (2017) from 0000 UTC 26 August through 0000 UTC 27 August (top) and Irma (2017) from 1200 UTC 10 September through 1200 UTC 11 September (bottom).

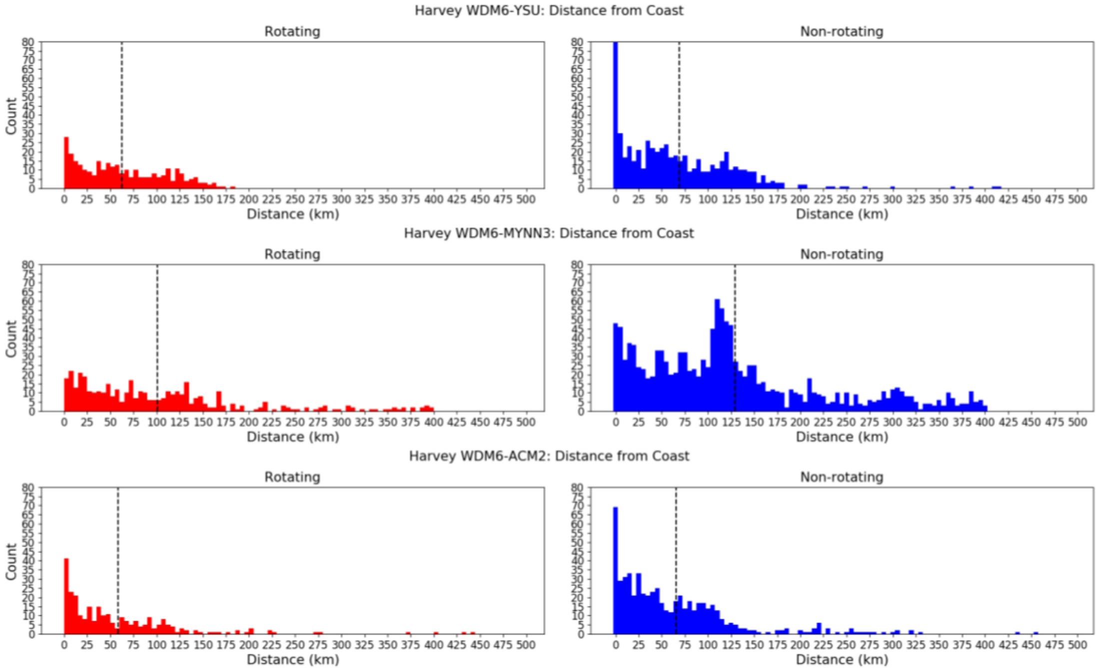

Figure 3.16: Distribution of the distance of rotating (red) and non-rotating (blue) cells from the coast and the mean distance (dashed) in simulations of Harvey (2017) from 0000 UTC 26 August through 0000 UTC 27 August.

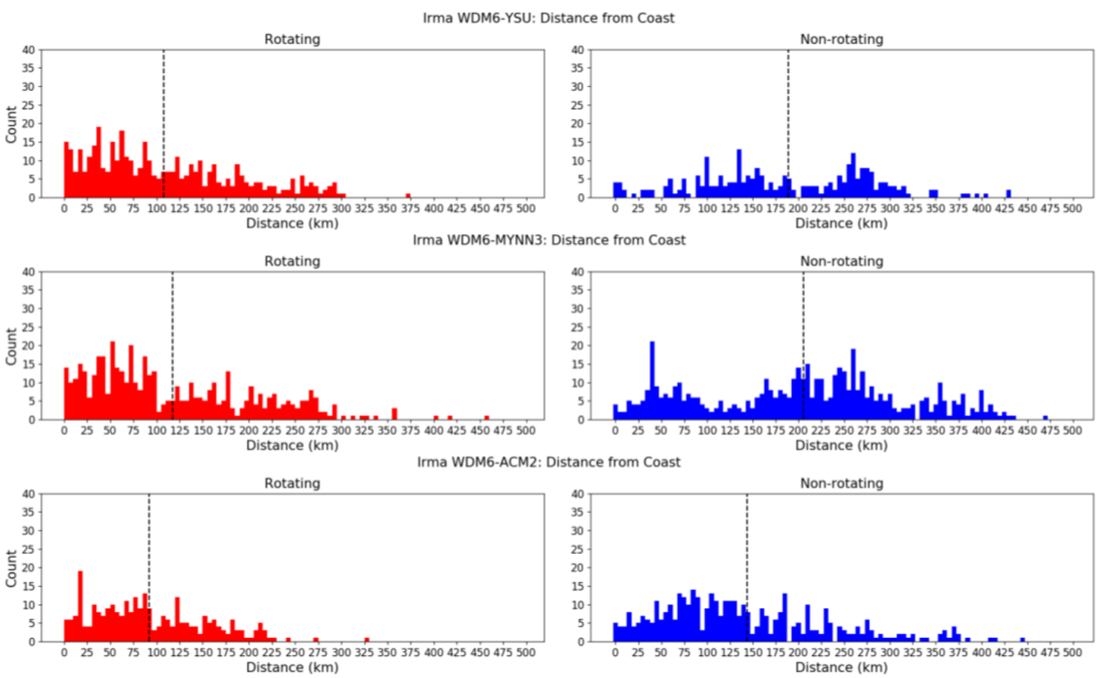

Figure 3.17: Distribution of the distance of rotating (red) and non-rotating (blue) cells from the coast and the mean distance (dashed) in simulations of Irma (2017) from 1200 UTC 10 September through 1200 UTC 11 September.

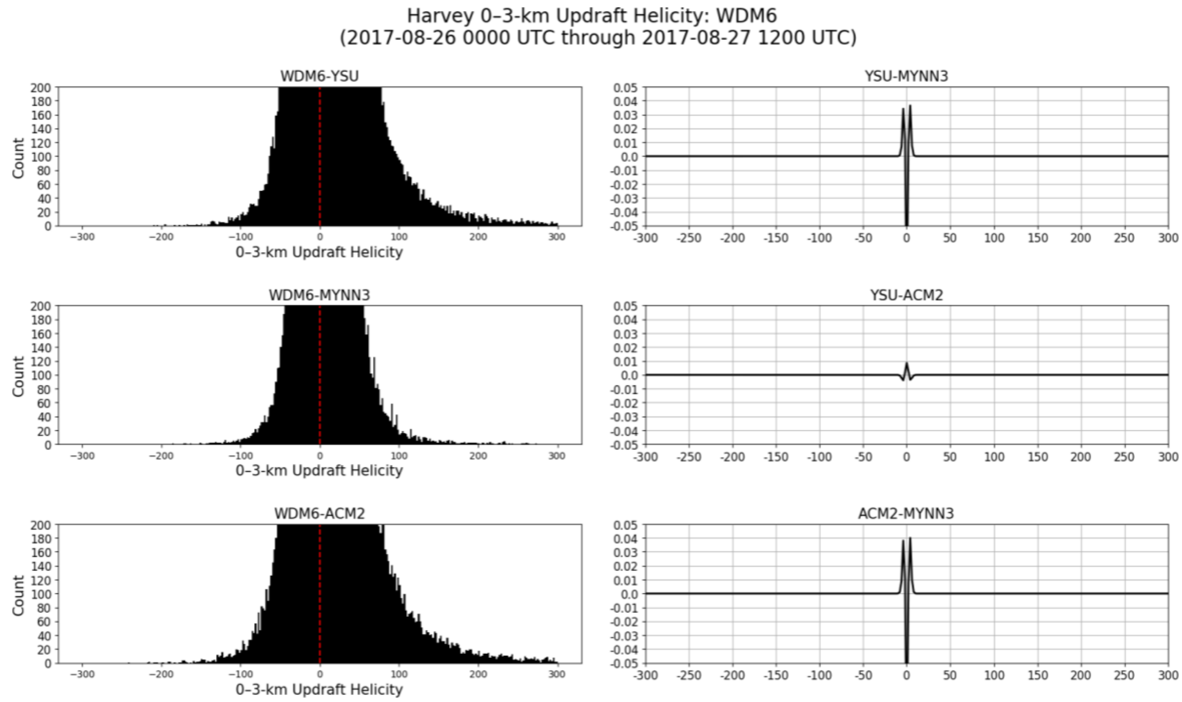

Figure 3.18: Frequency distribution of the 0–3-km updraft helicity and distribution mean (m^2/s^2, dashed red), as well as the differences in the distributions across the PBL schemes from 0000 UTC 26 August through 1200 UTC 27 August for the simulations of Harvey.

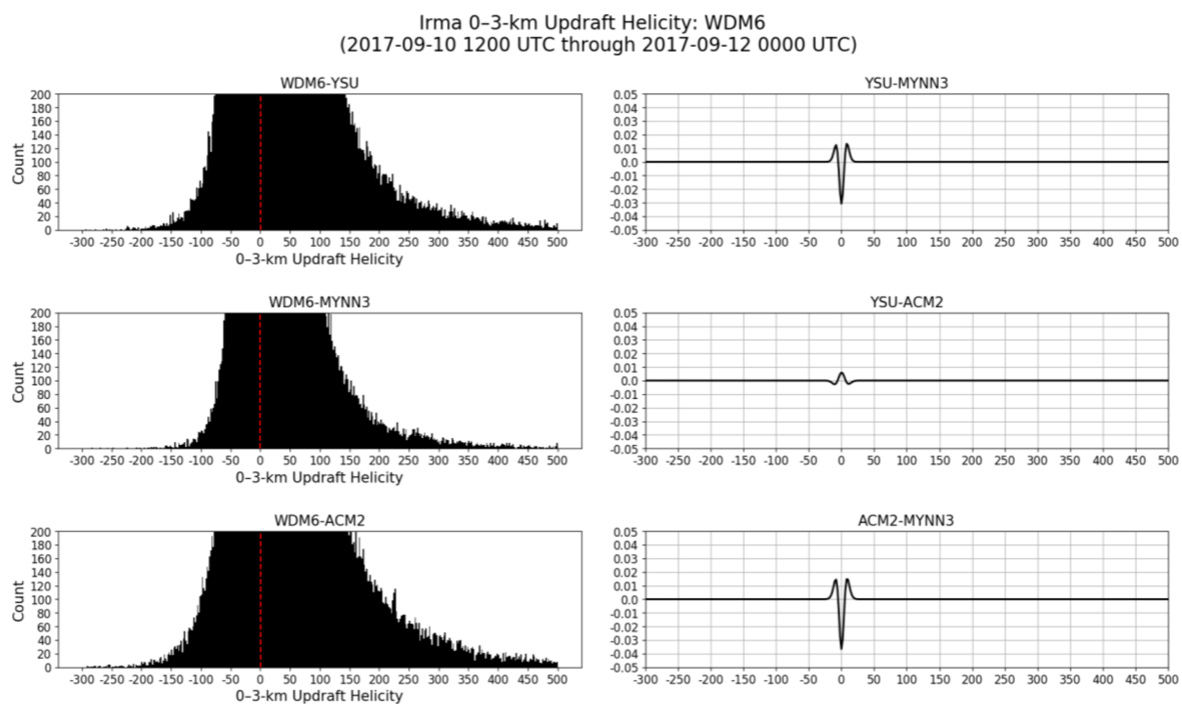

Figure 3.19: Same as Figure 3.18, but for Irma from 1200 UTC 10 September through 0000 UTC 12 September.

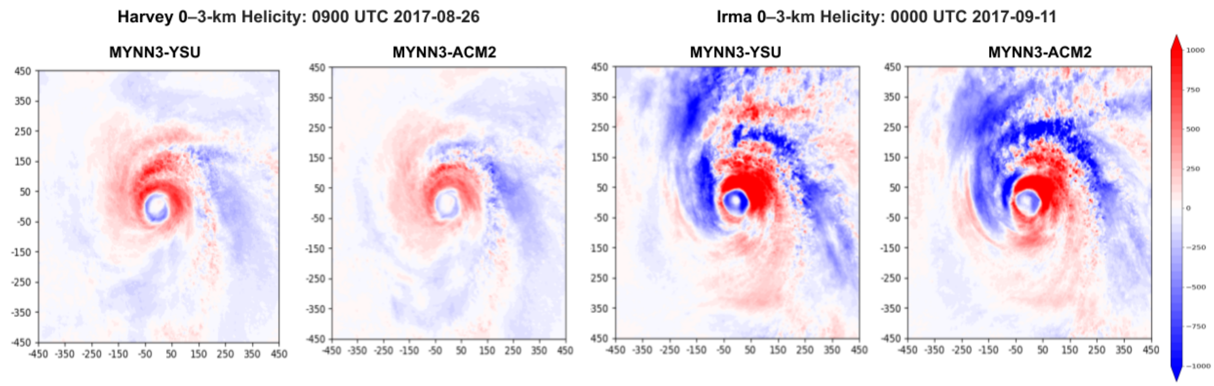

Figure 3.20: Difference in the 0–3-km helicity (m^2/s^2 between the YSU, MYNN3, and ACM2 PBL schemes at 0900 UTC 26 August (Harvey) and 0000 UTC 11 September (Irma).

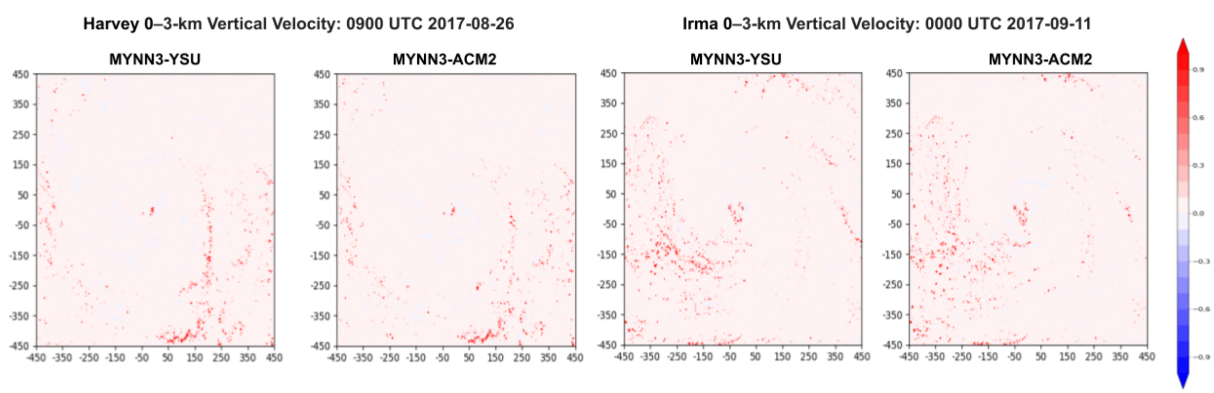

Figure 3.21: Difference in the 0–3-km vertical velocity (m/s) between the YSU, MYNN3, and ACM2 PBL schemes at 0900 UTC 26 August (Harvey) and 0000 UTC 11 September (Irma).

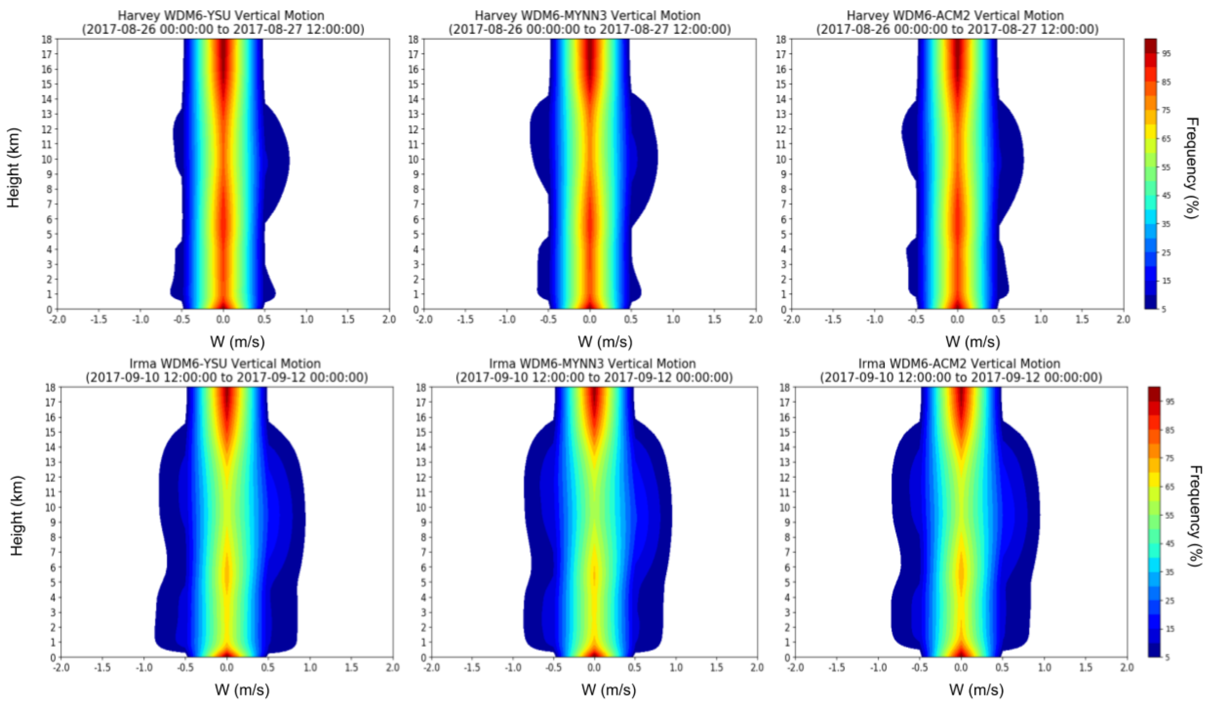

Figure 3.22: Cumulative frequency by altitude diagrams (CFADs) for vertical velocity (m/s) from 0000 UTC 26 August through 1200 UTC 27 August for Harvey (top) and 1200 UTC 10 September through 0000 UTC 12 September for Irma (bottom).

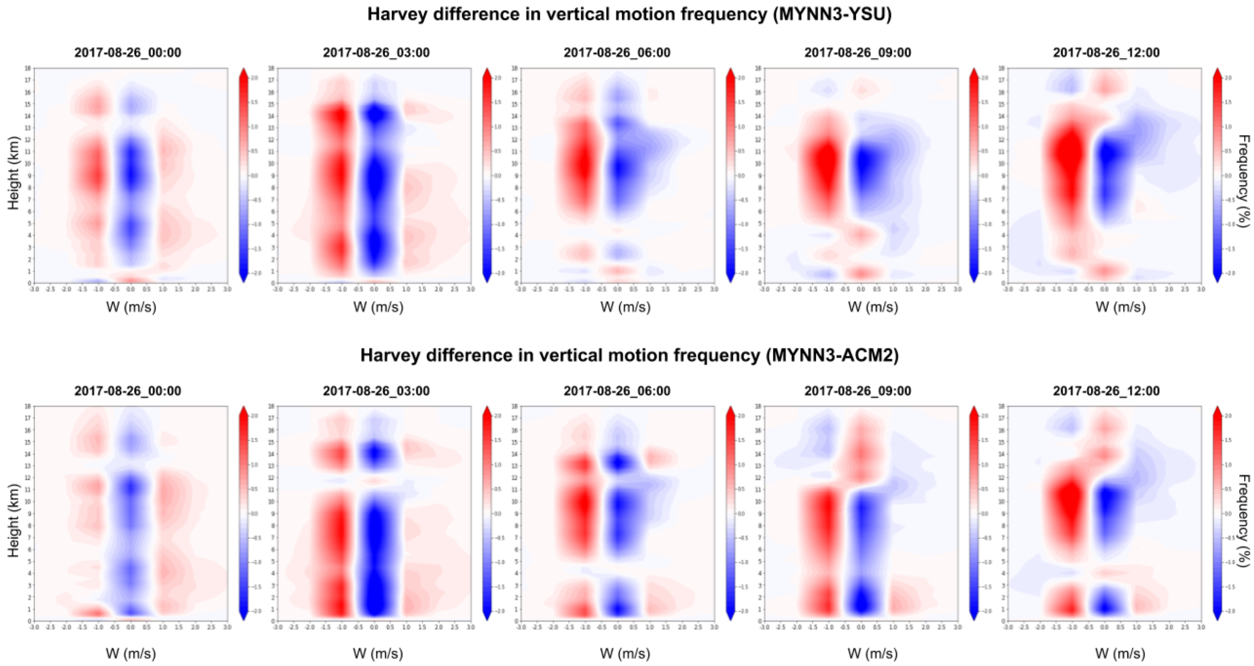

Figure 3.23: Differences between the MYNN3 simulation and the YSU (top), and ACM2 (bottom), simulations CFADs for vertical velocity in Harvey from 0000 UTC–1200 UTC 26 August.

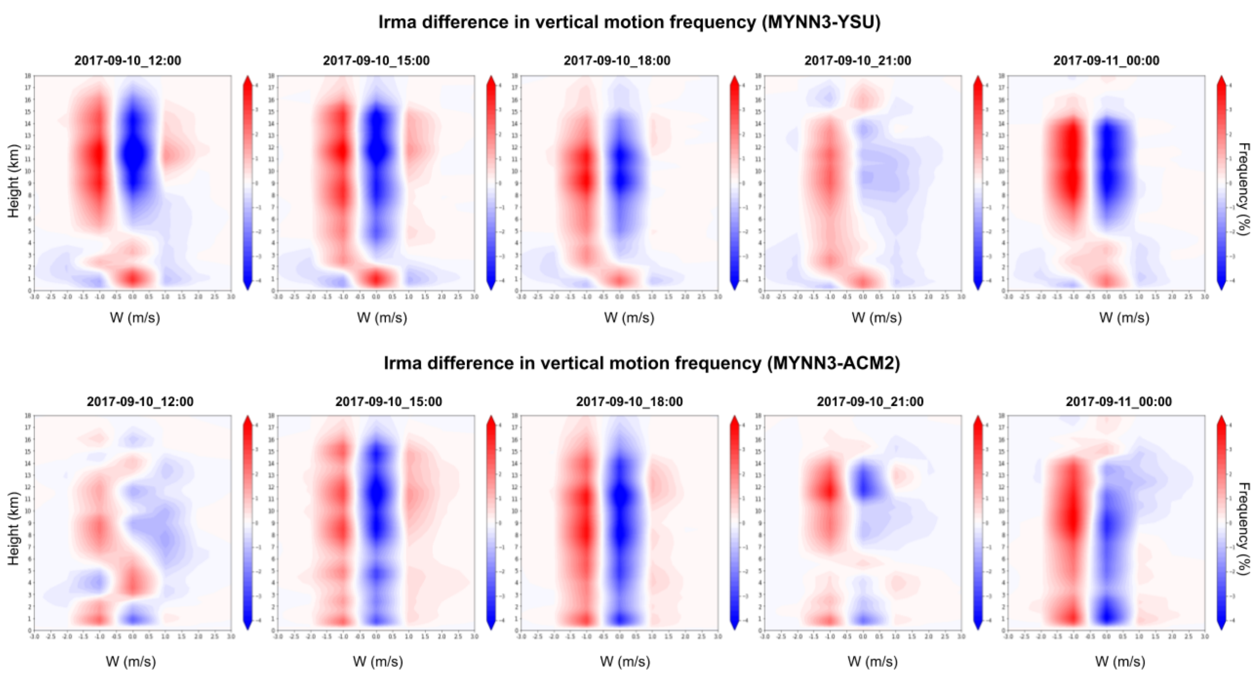

Figure 3.24: Same as Figure 3.23, but for Irma from 1200 UTC 10 September through 0000 UTC 11 September.

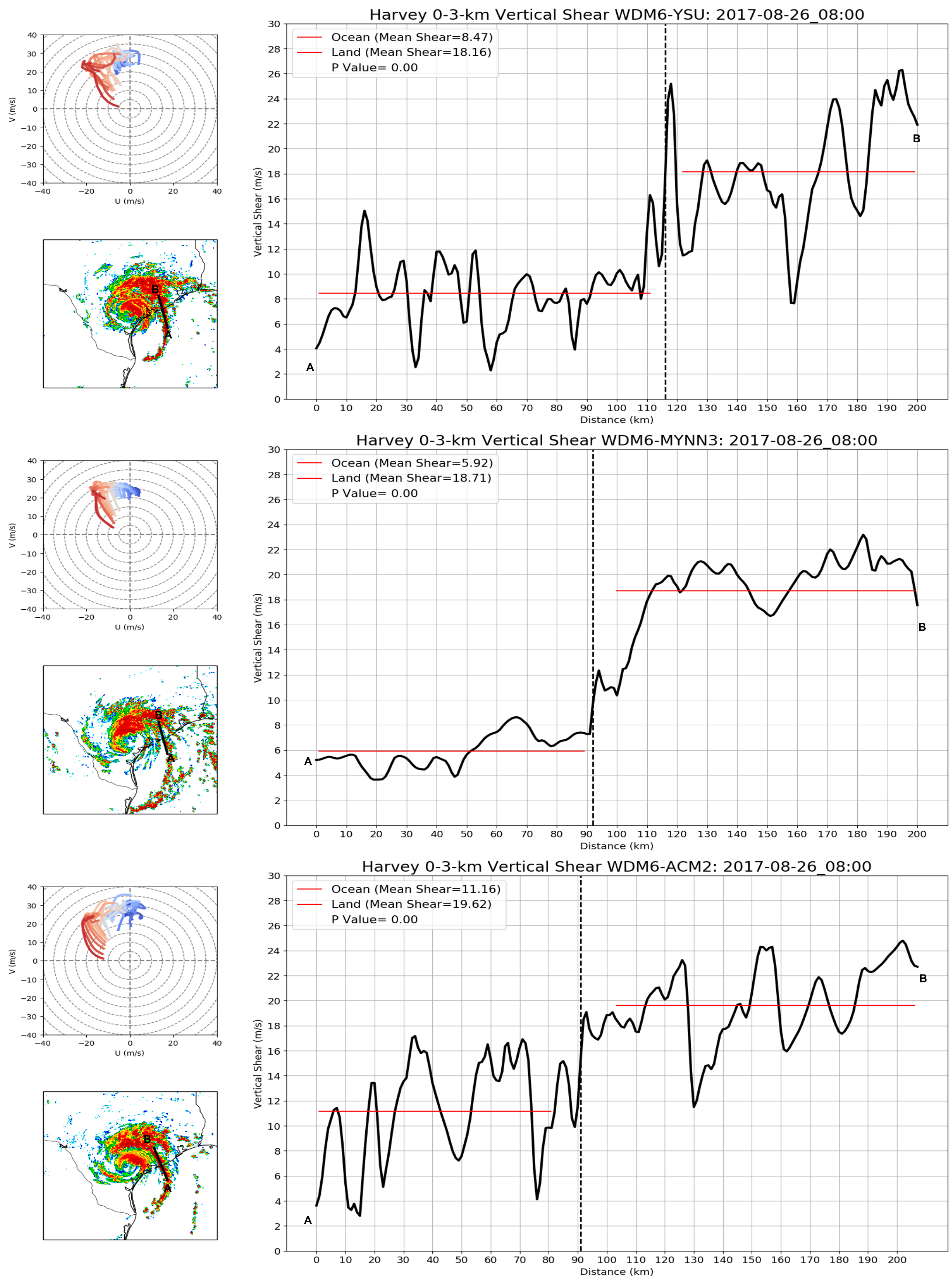

Figure 3.25: The 0–3-km hodographs (shaded cool to warm colors representing the cross section from A–B) and reflectivty (dBz, shaded) with the cross section (A–B). The line plot shows the 0–3-km vertical shear (m/s, solid black), land–ocean interface (dashed, black), and the mean ocean and land 0–3-km vertical shear (m/s, solid red) across the cross section from A–B for the YSU, MYNN3, and ACM2 Harvey simulations (top to bottom) at 0800 UTC 26 August.

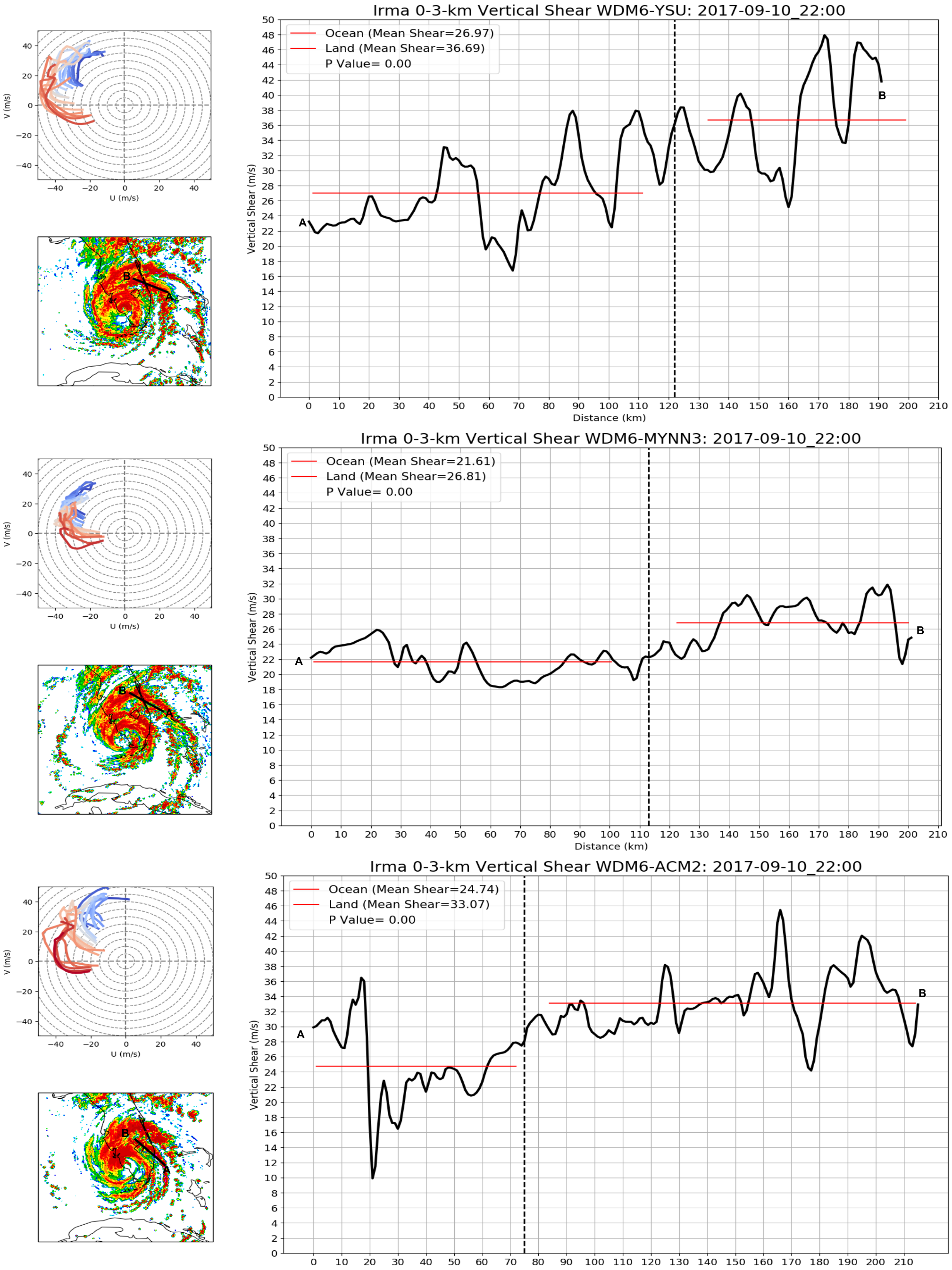

Figure 3.26: The 0–3-km hodographs (shaded cool to warm colors representing the cross section from A–B) and reflectivty (dBz, shaded) with the cross section (A–B). The line plot shows the 0–3-km vertical shear (m/s, solid black), land–ocean interface (dashed, black), and the mean ocean and land 0–3-km vertical shear (m/s, solid red) across the cross section from A–B for the YSU, MYNN3, and ACM2 Irma simulations (top to bottom) at 2200 UTC 10 September.

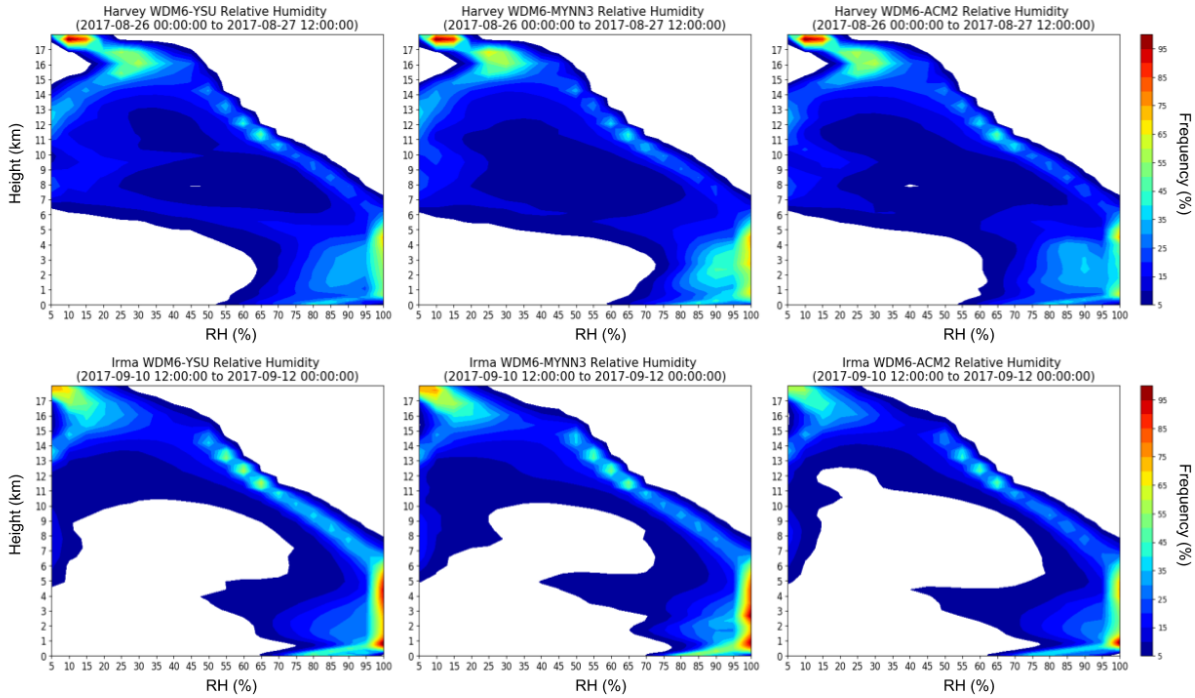

Figure 3.27: CFADs for relative humidity (%) from 0000 UTC 26 August through 1200 UTC 27 August for Harvey (top) and 1200 UTC 10 September through 0000 UTC 12 September for Irma (bottom).

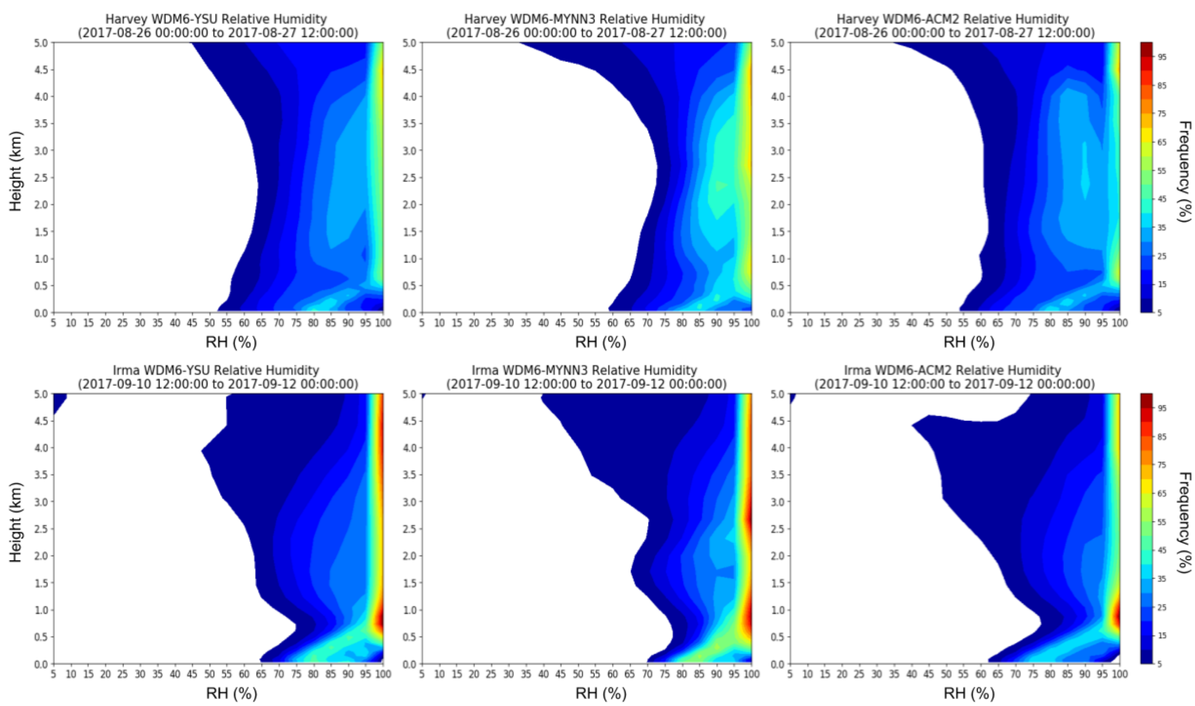

Figure 3.28: Same as Figure 3.27, but from 0–5 km in height.

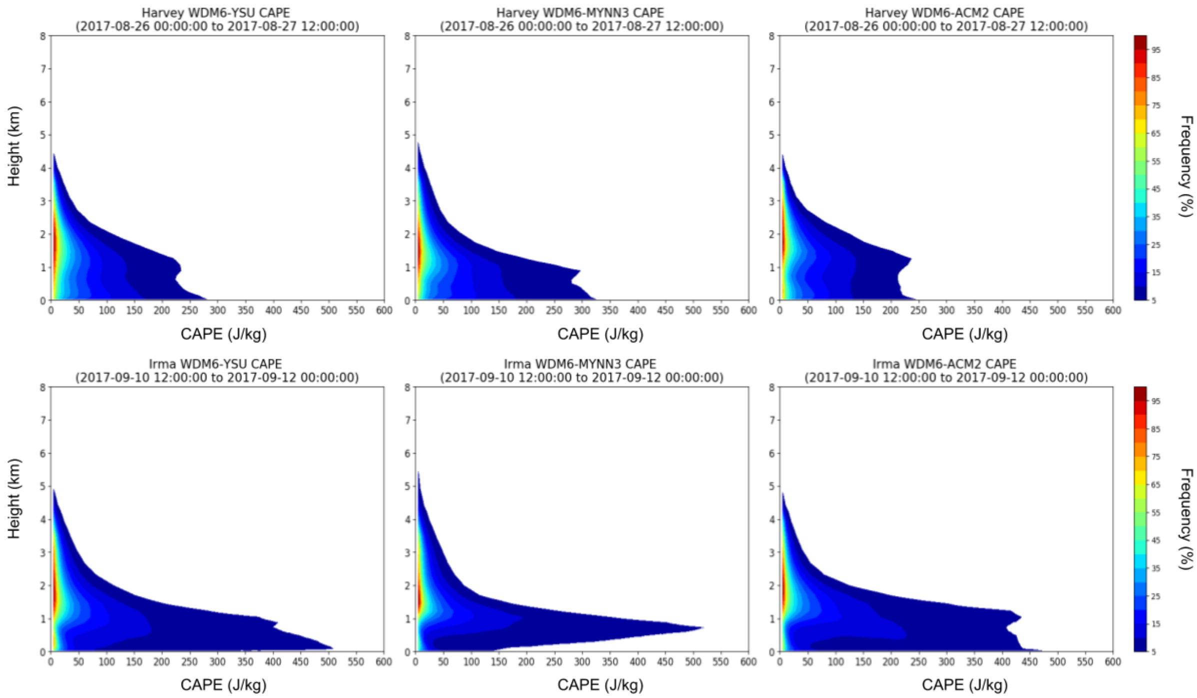

Figure 3.29: CFADs for convective available potential energy (CAPE, J/kg) from 0000 UTC 26 August through 1200 UTC 27 August for Harvey (top) and 1200 UTC 10 September through 0000 UTC 12 September for Irma (bottom).

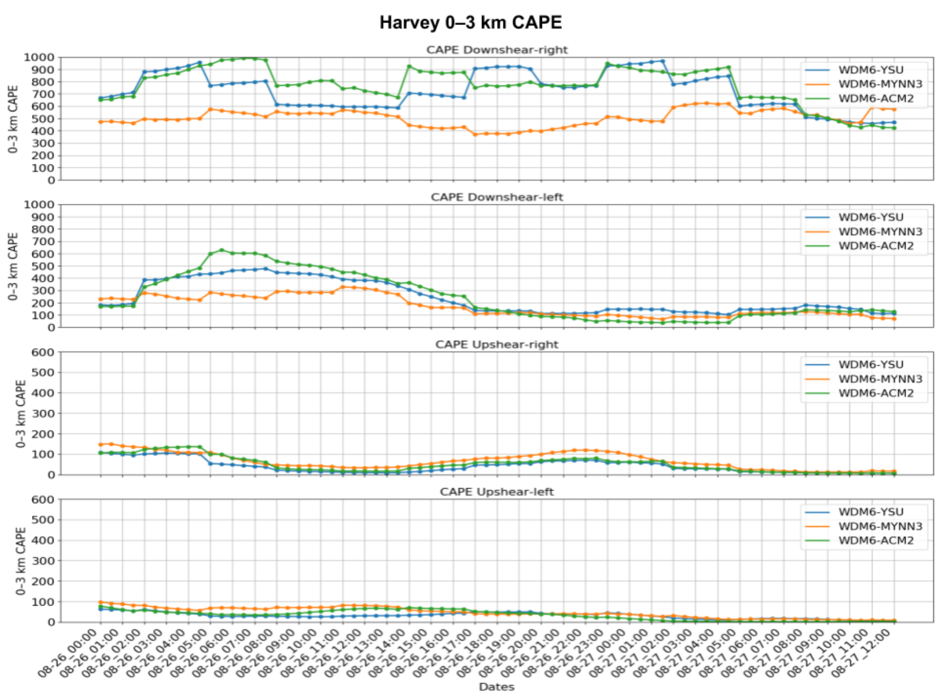

Figure 3.30: Distributions of CAPE by shear quadrant from 0000 UTC 26 August through 1200 UTC 27 August for Harvey.

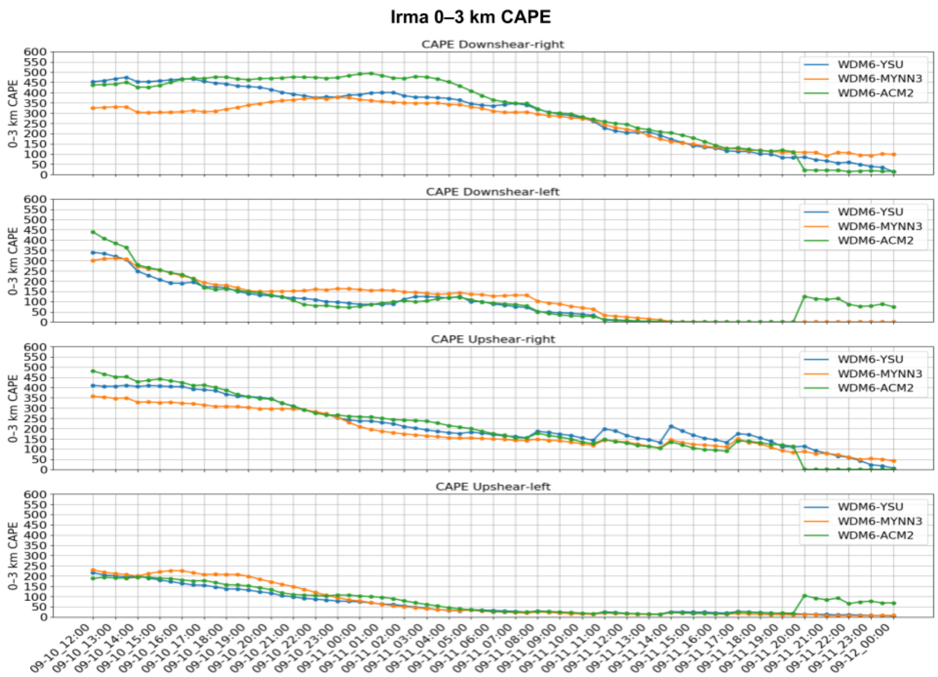

Figure 3.31: Distributions of CAPE by shear quadrant from 1200 UTC 10 September through 0000 UTC 12 September for Irma.

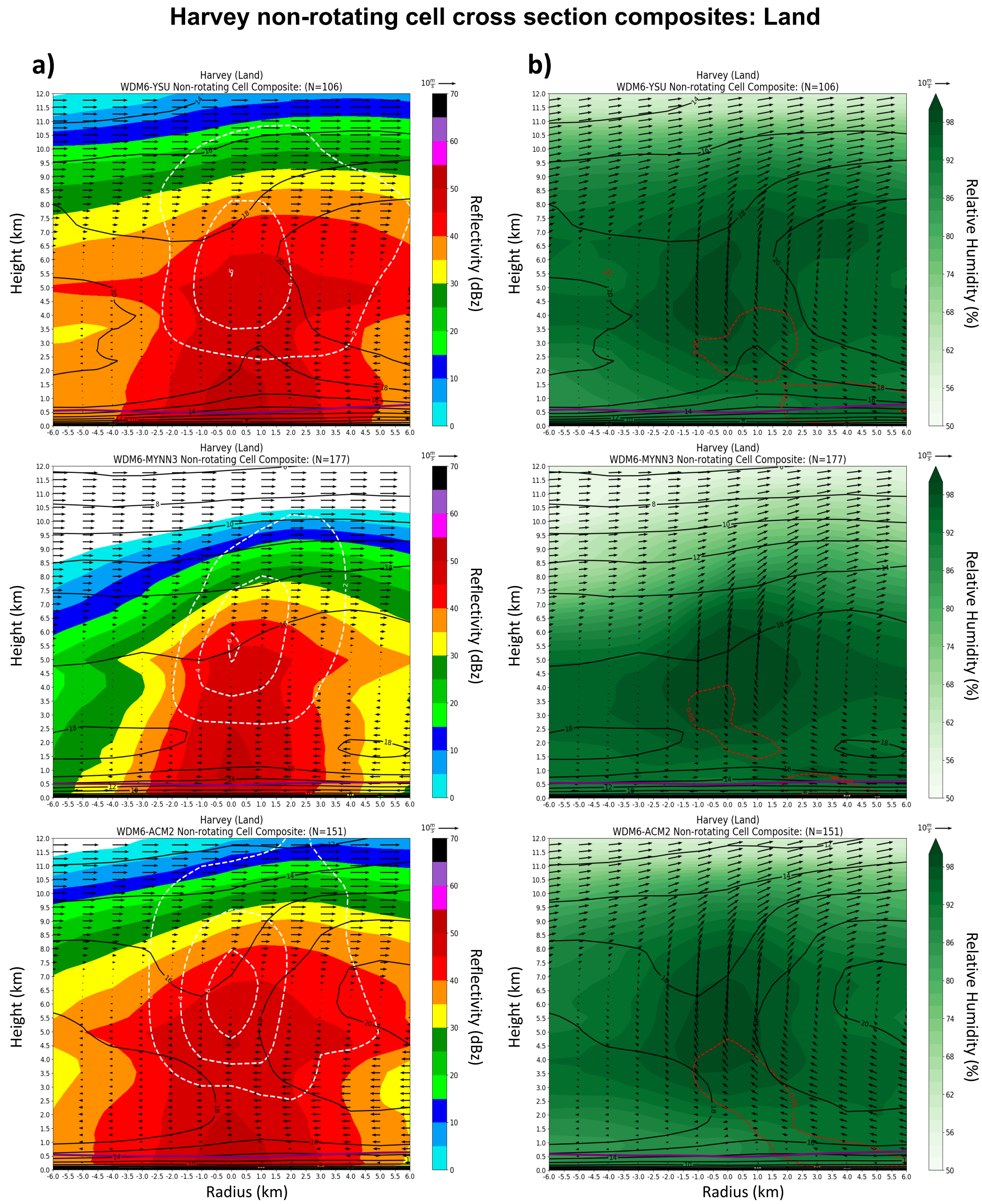

Figure 3.32: Cross-section composites of non-rotating land cells in Harvey for the YSU, MYNN3, and ACM2 simulations (top to bottom) from 0000 UTC 26 through 0000 UTC 27 August. Column a: reflectivity (dBZ, shaded), vertical motion (m/s, dashed white), tangential wind (m/s, solid black), and radial wind (quiver). Column b: relative humidity (%, shaded), 3D convergence (10^{-3} $1/s$, dashed red), tangential wind (m/s, solid black), and radial and vertical wind (quiver). The model-calculated PBL height is also shown (km, solid purple).

Harvey non-rotating cell cross section composites: Ocean

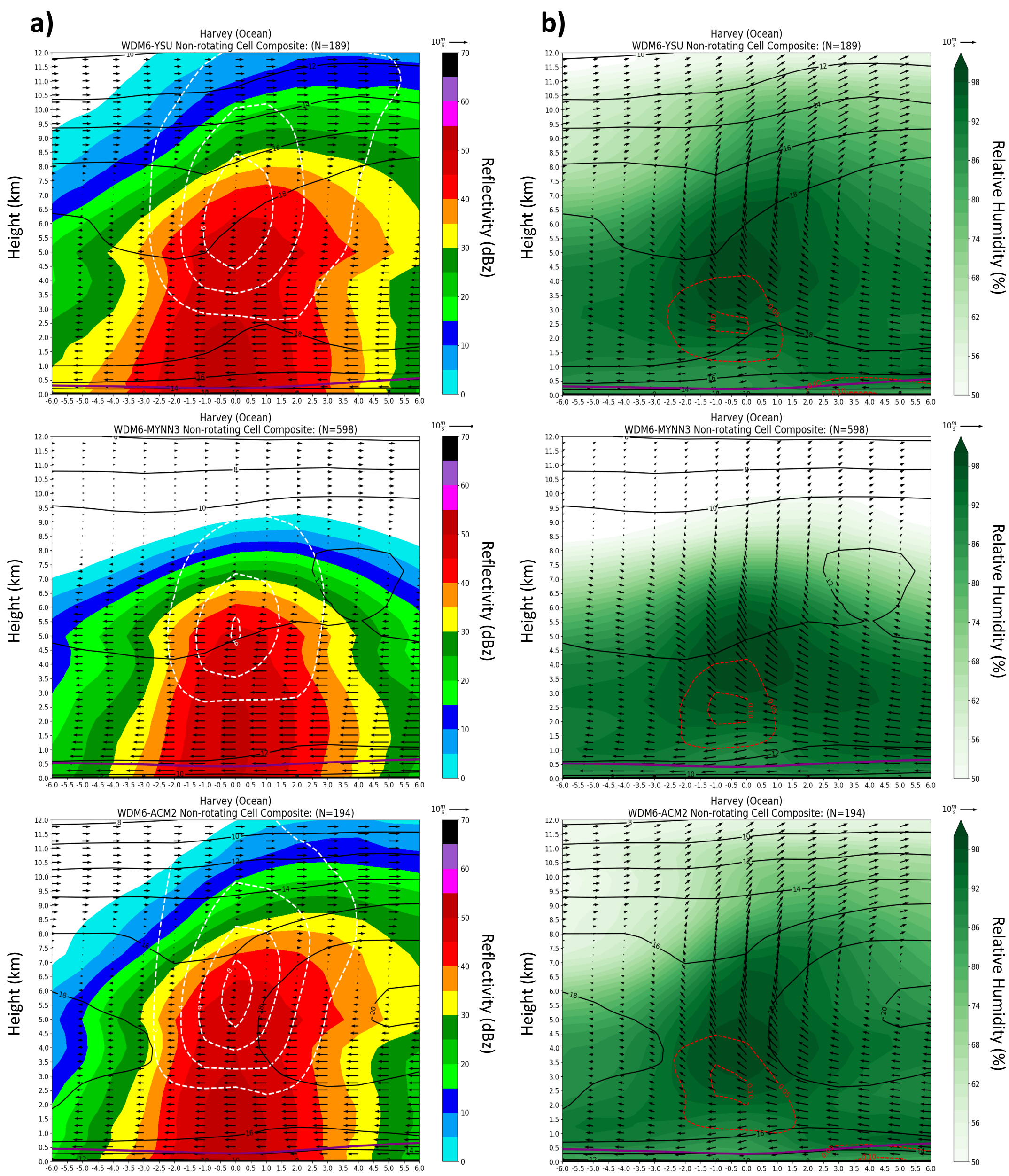

Figure 3.33: Same as Figure 3.32, but for identified non-rotating ocean cells.

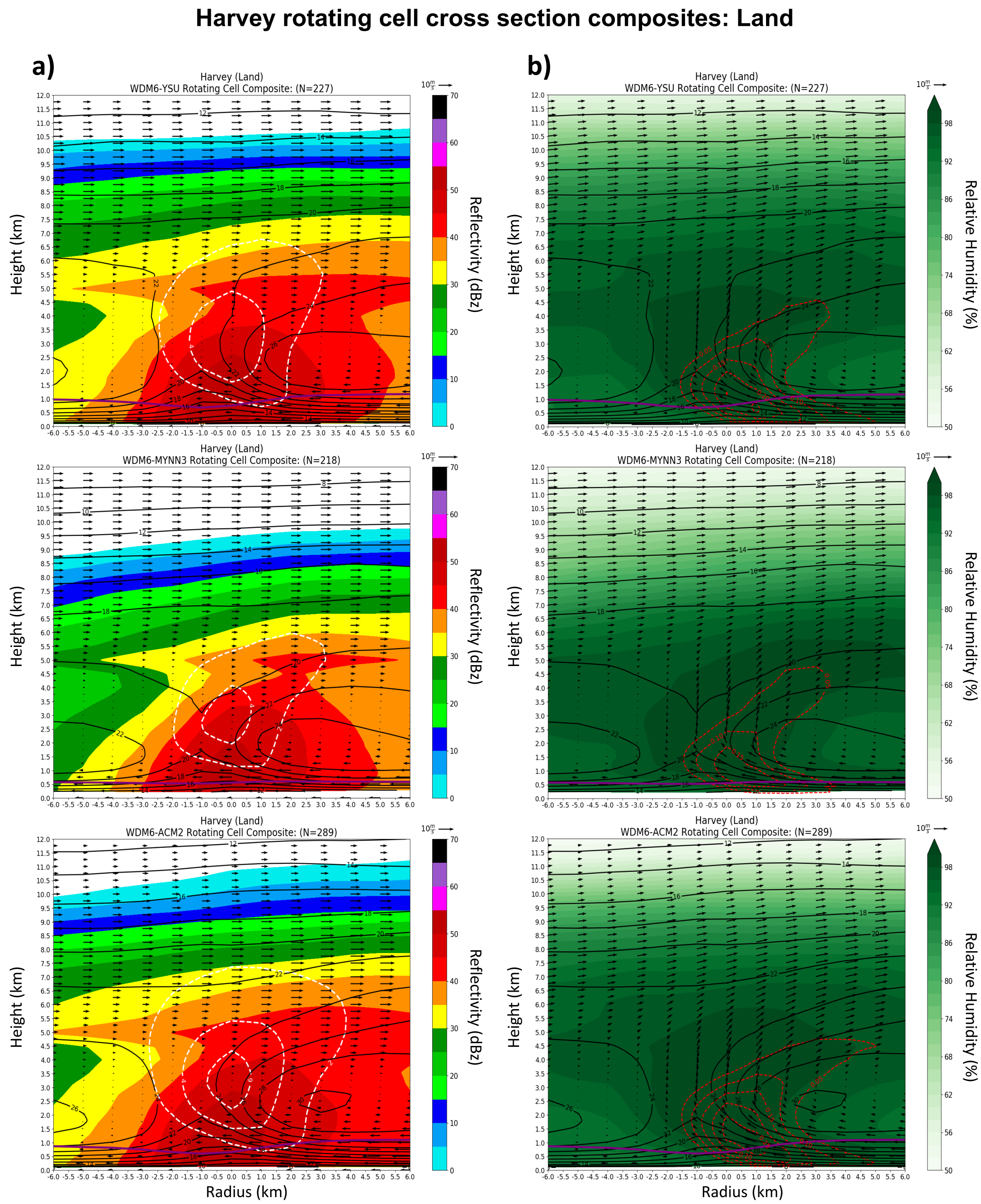

Figure 3.34: Same as Figure 3.32, but for identified rotating land cells.

Harvey rotating cell cross section composites: Ocean

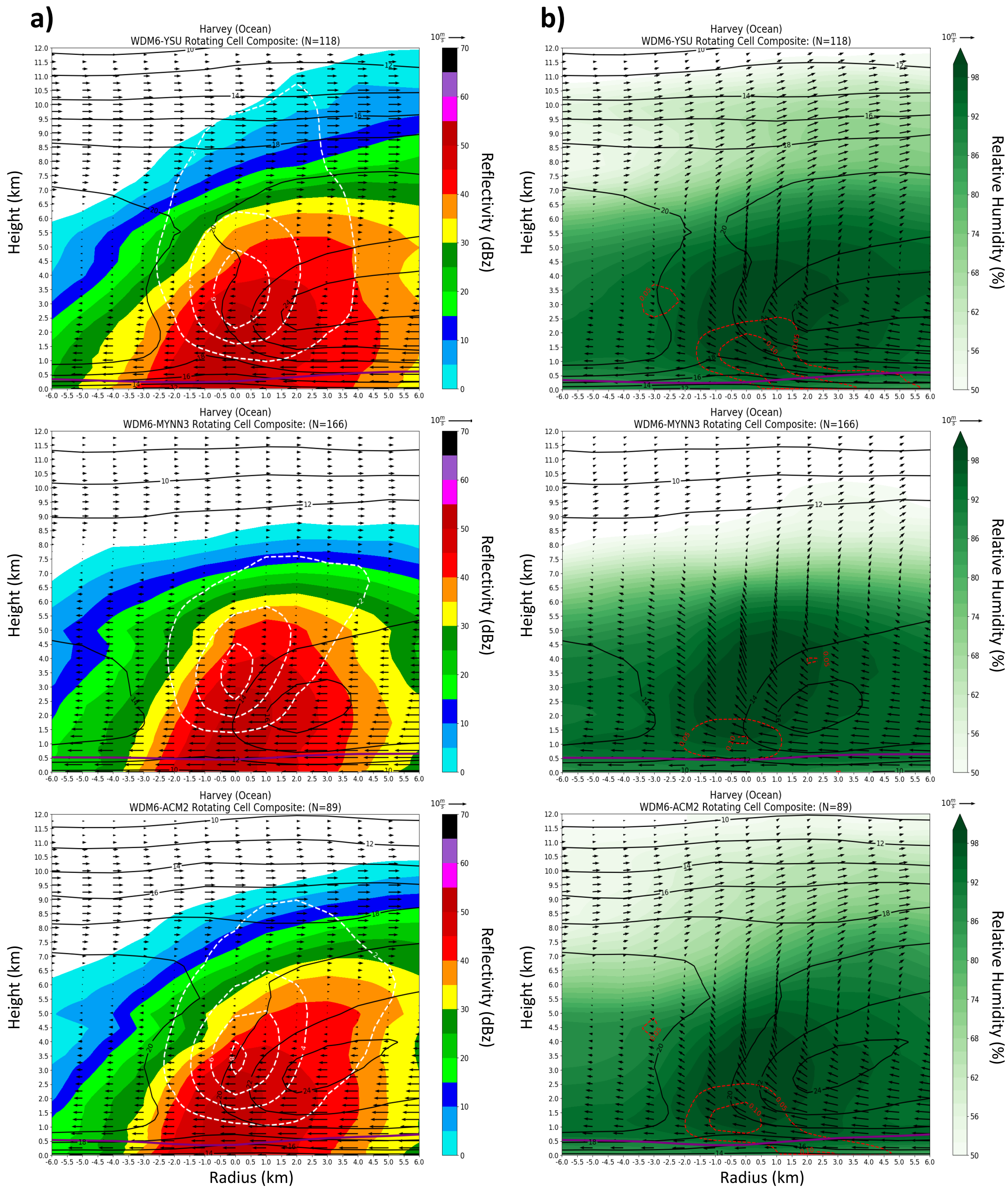

Figure 3.35: Same as Figure 3.32, but for identified rotating ocean cells.

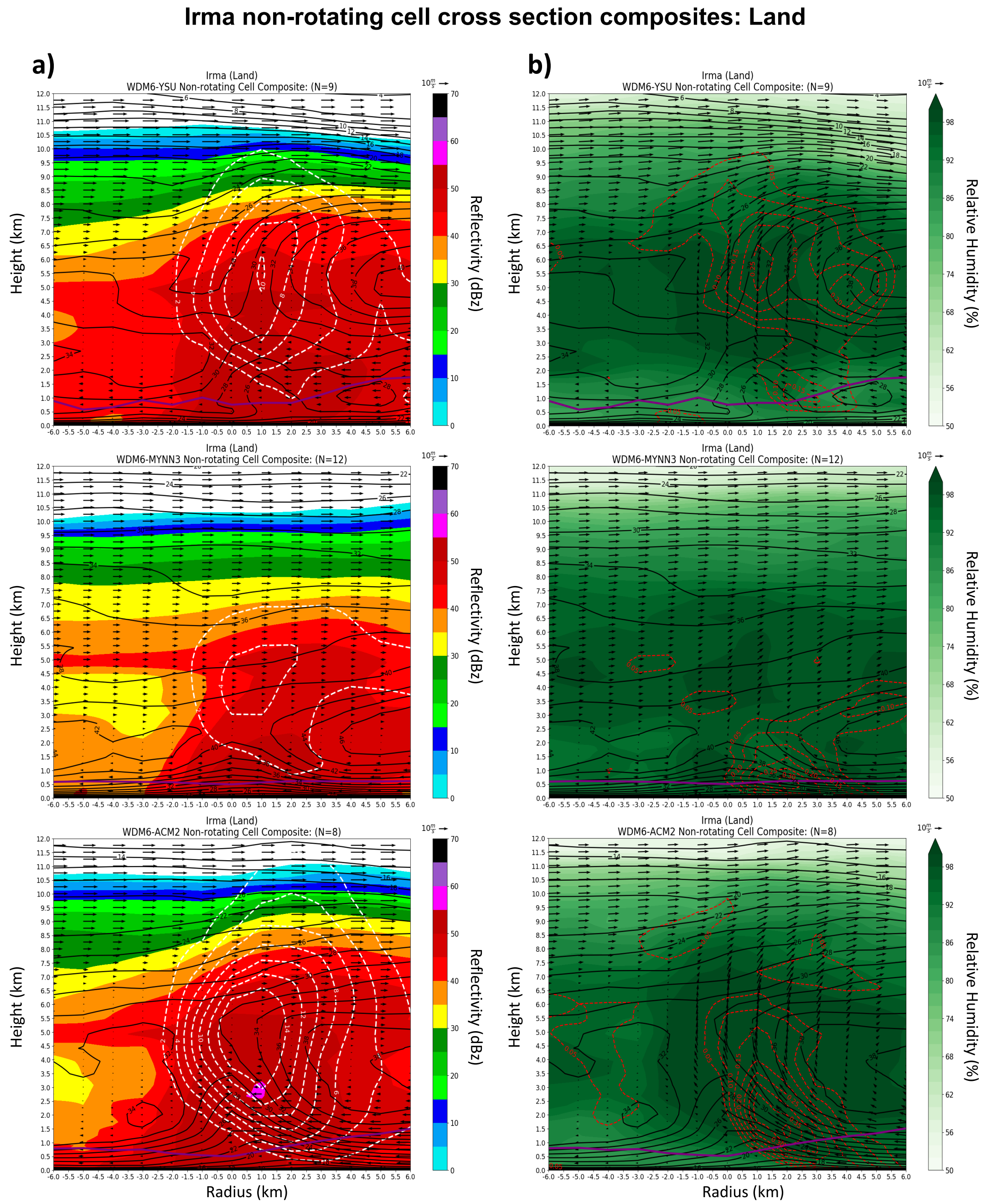

Figure 3.36: Cross-section composites of non-rotating land cells in Irma for the YSU, MYNN3, and ACM2 simulations (top to bottom) from 1200 UTC 10 through 1200 UTC 11 September. Column a: reflectivity (dBZ, shaded), vertical motion (m/s, dashed white), tangential wind (m/s, solid black), and radial wind (quiver). Column b: relative humidity (%, shaded), 3D convergence (10^{-3} $1/s$, dashed red), tangential wind (m/s, solid black), and radial and vertical wind (quiver). The model-calculated PBL height is also shown (km, solid purple).

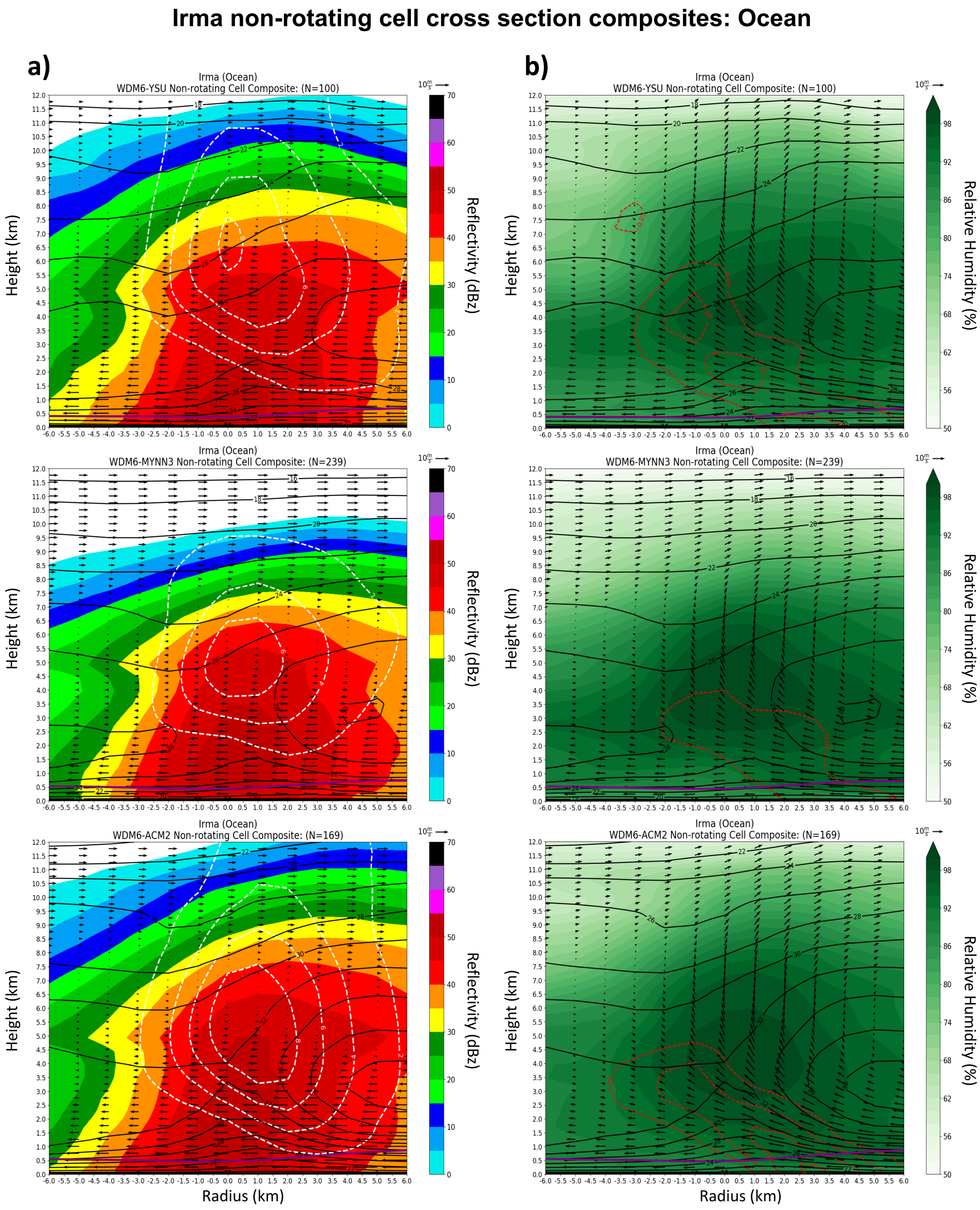

Figure 3.37: Same as Figure 3.36, but for identified non-rotating ocean cells.

Irma rotating cell cross section composites: Land

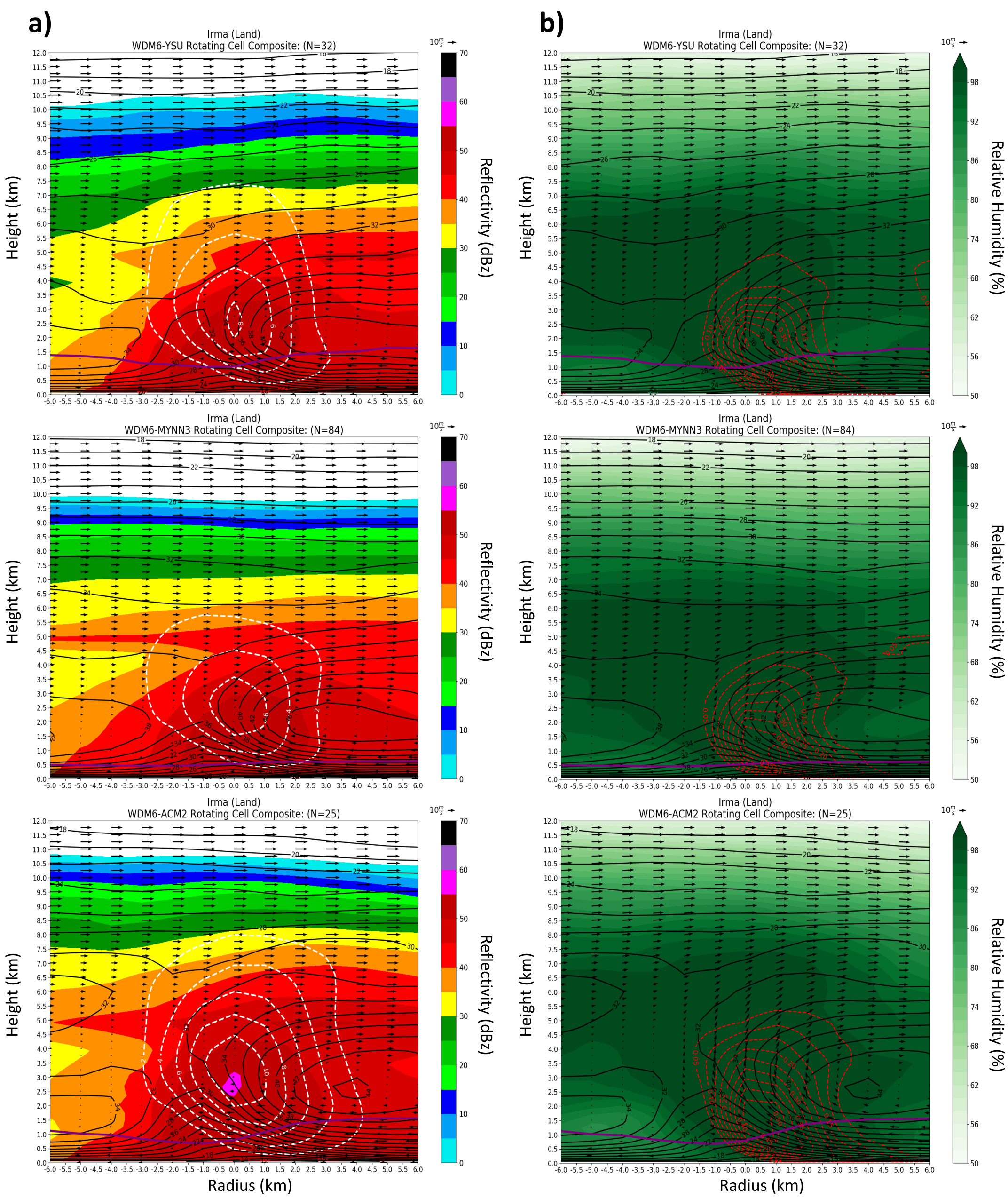

Figure 3.38: Same as Figure 3.36, but for identified rotating land cells.

Irma rotating cell cross section composites: Ocean

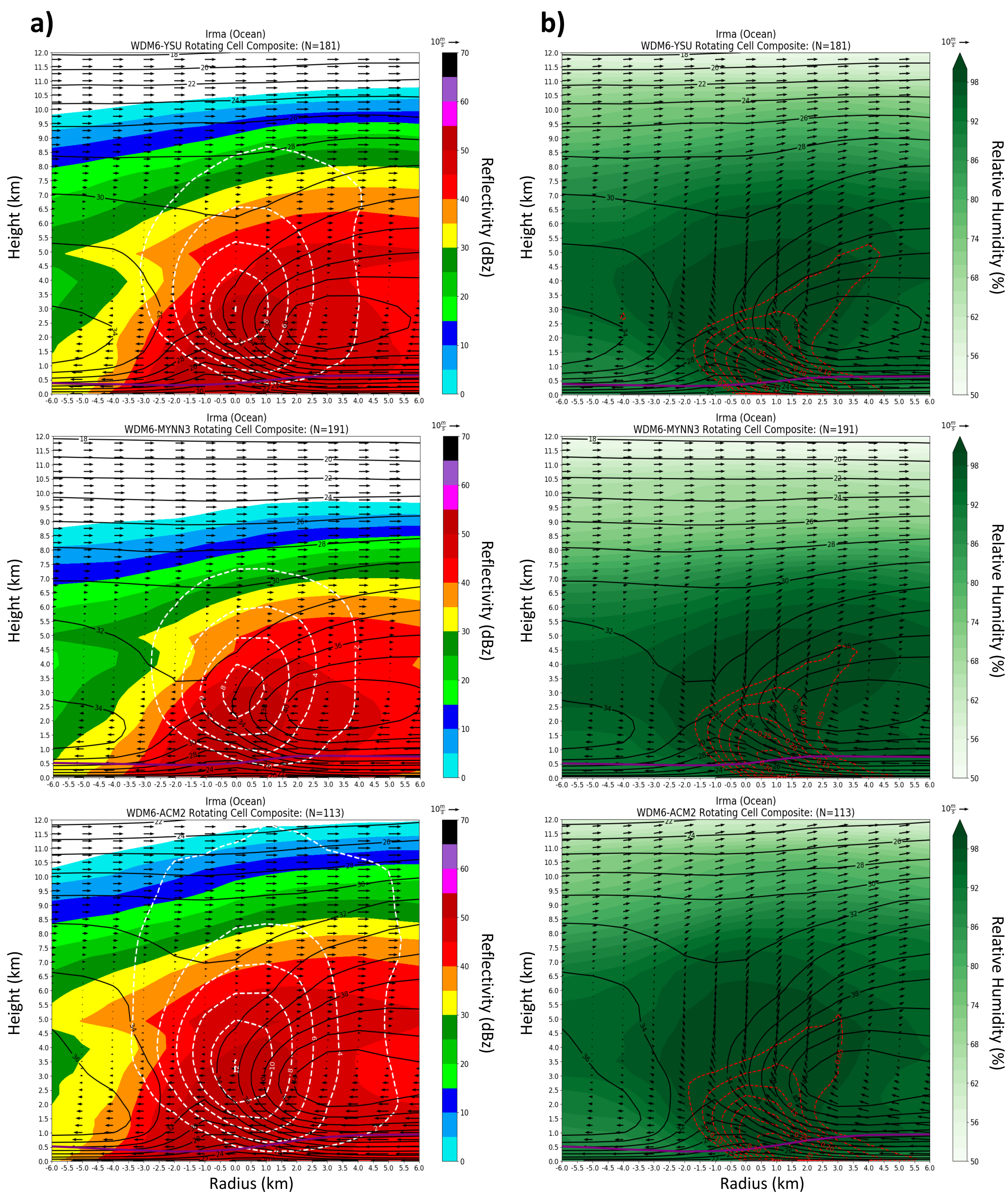

Figure 3.39: Same as Figure 3.36, but for identified rotating ocean cells.

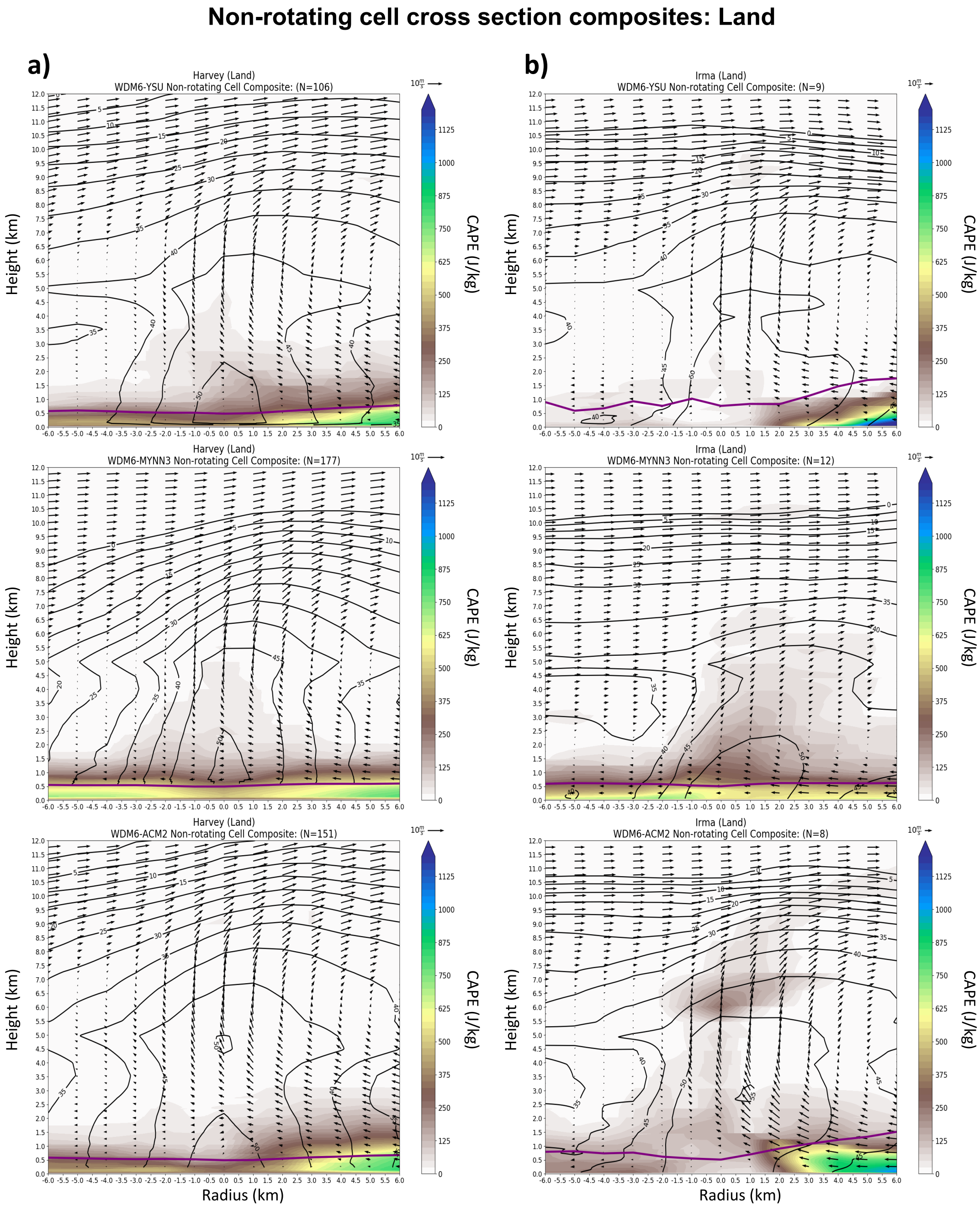

Figure 3.40: Cross-section composites of non-rotating land cells in Harvey (a) and Irma (b) for the YSU, MYNN3, and ACM2 simulations (top to bottom) for the times in Figures 3.32 and 3.36. CAPE for parcels at every grid point in the cross-section (J/kg, shaded), model reflectivity (dBZ, solid black), and radial and vertical wind (quiver). The model-calculated PBL height is also shown (km, solid purple).

Non-rotating cell cross section composites: Ocean

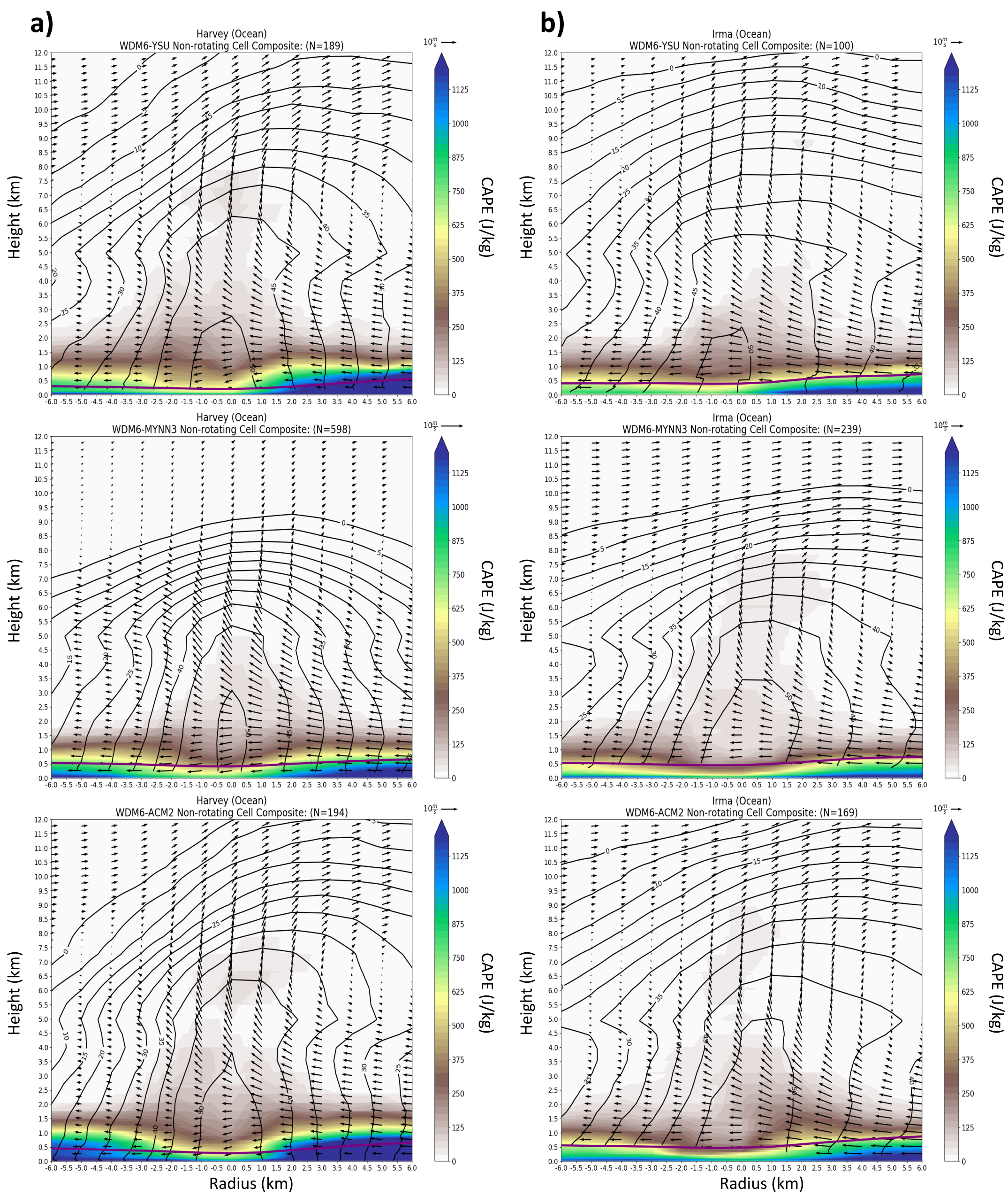

Figure 3.41: Same as Figure 3.40, but for identified non-rotating ocean cells.

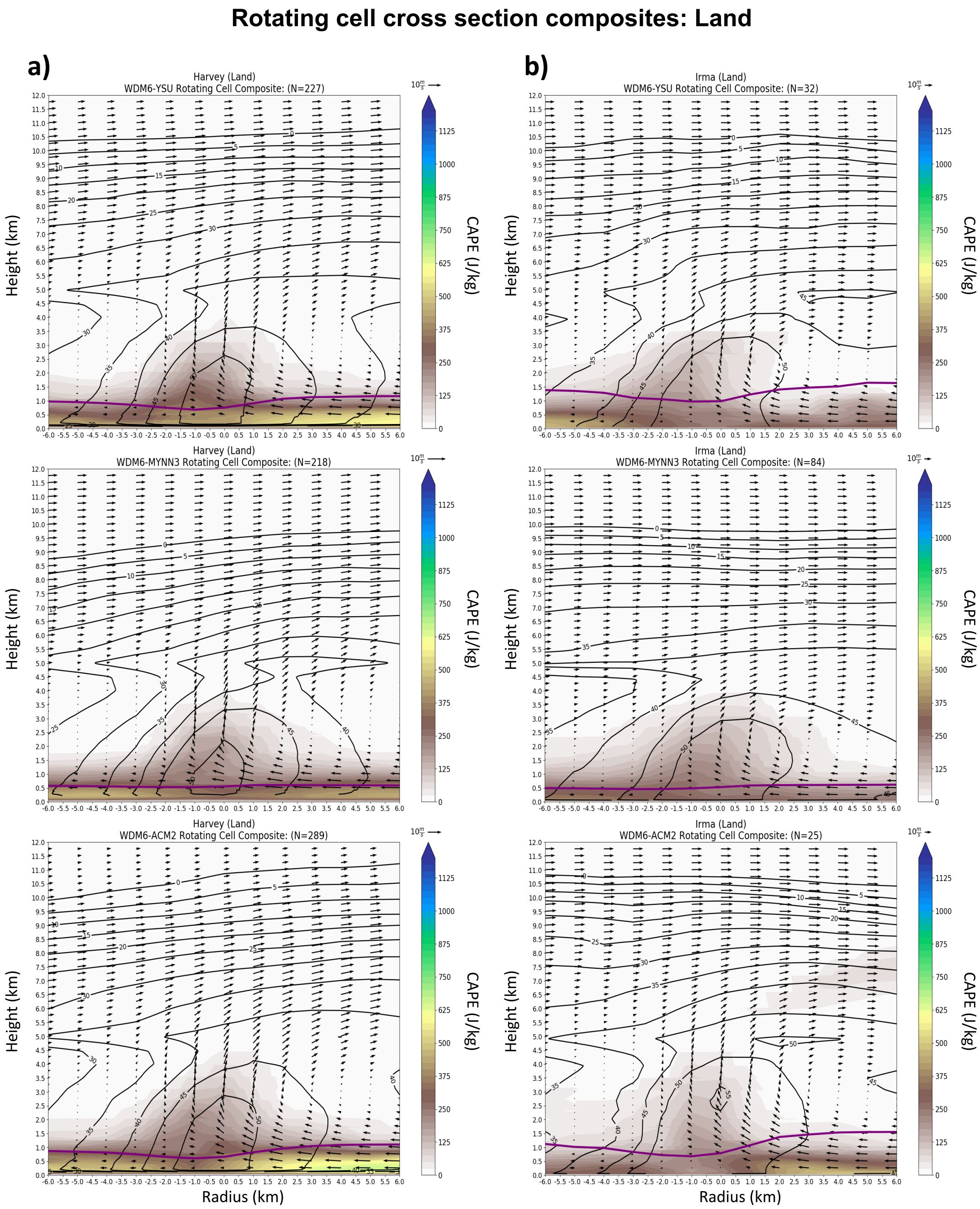

Figure 3.42: Same as Figure 3.40, but for identified rotating land cells.

Rotating cell cross section composites: Ocean

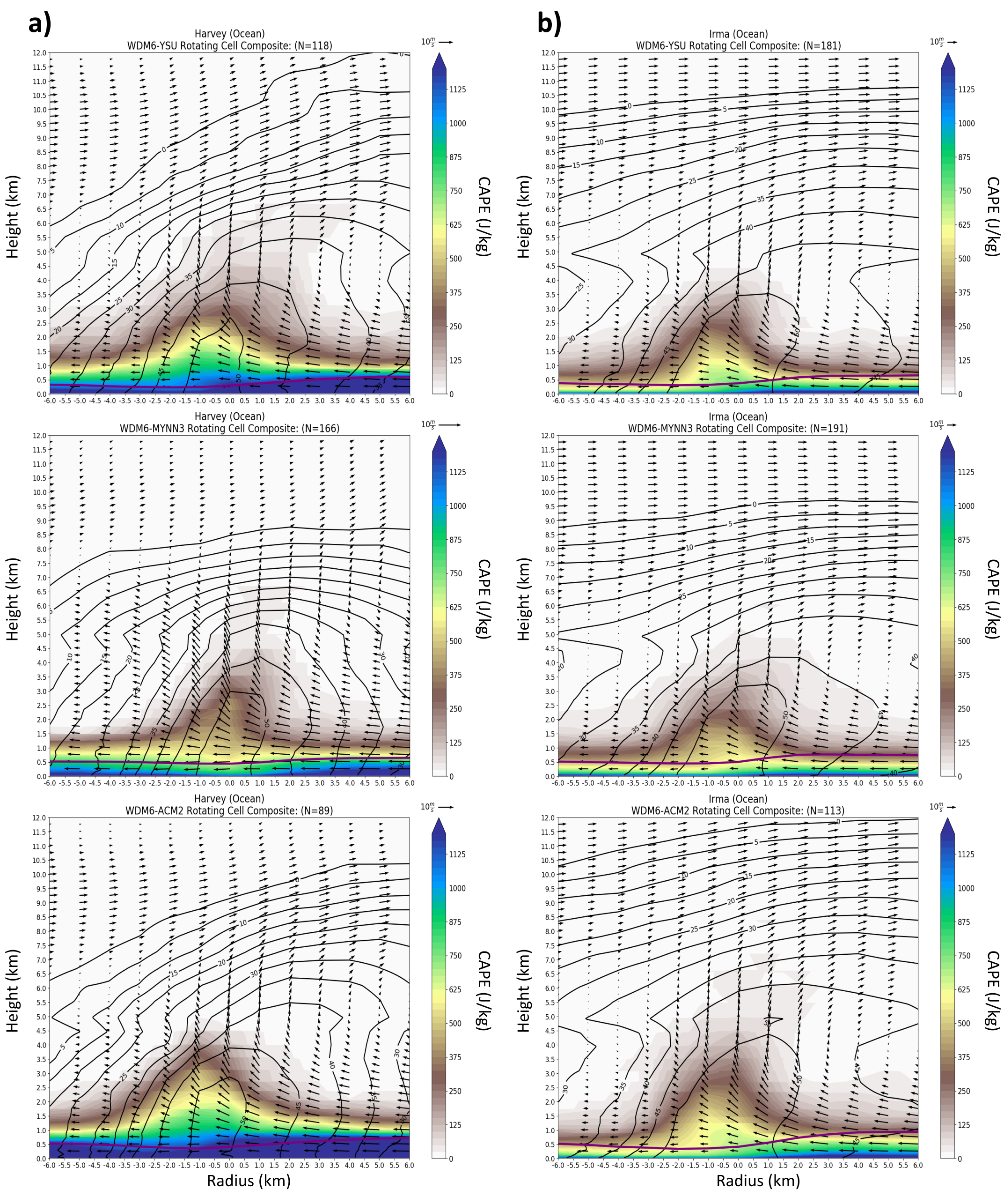

Figure 3.43: Same as Figure 3.40, but for identified rotating ocean cells.

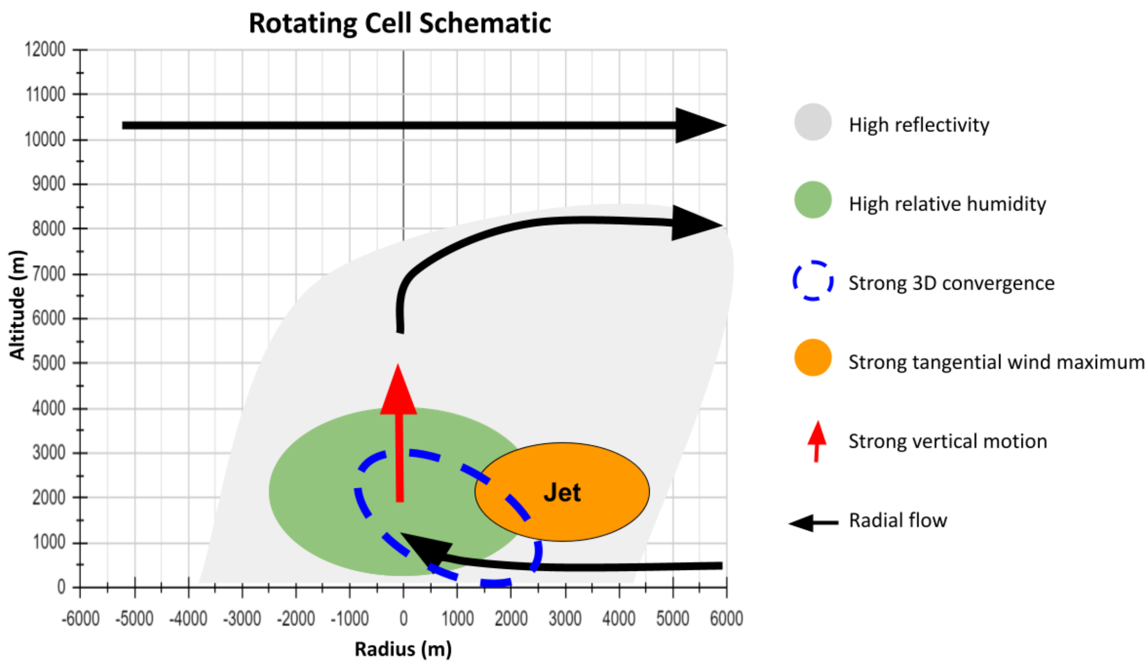

Figure 3.44: Schematic showing the important features from the rotating cell composites.

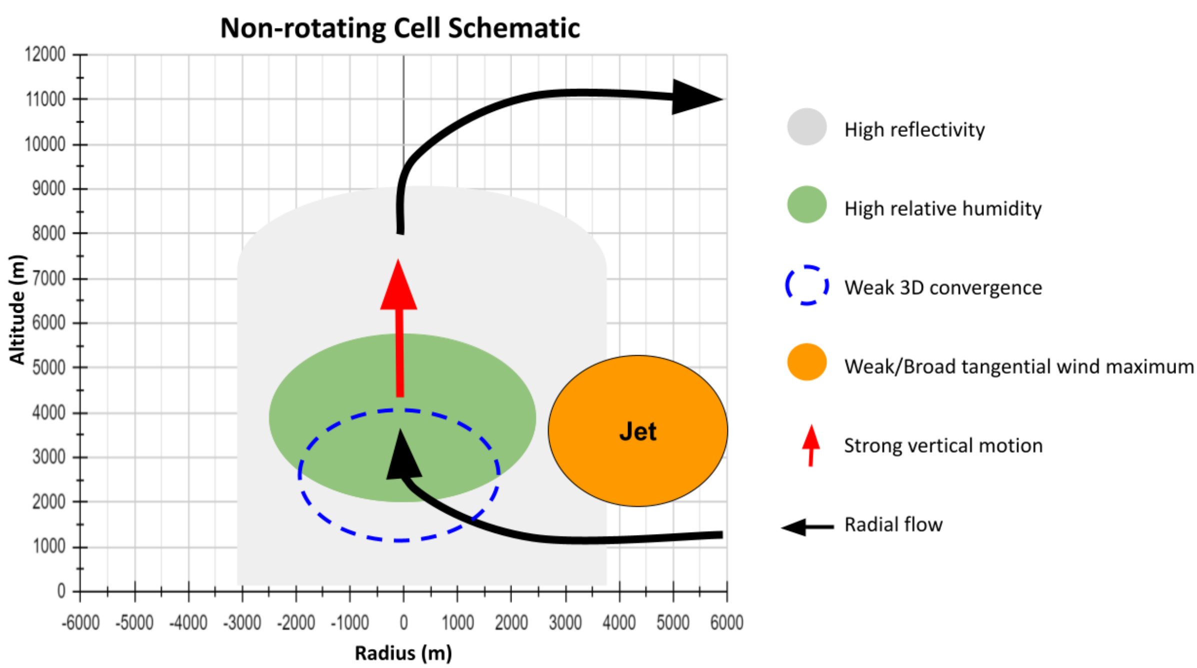

Figure 3.45: Schematic showing the important features from the non-rotating cell composites.

4. Sensitivities of planetary boundary layer (PBL) schemes in tropical cyclones

In the previous chapter, it was seen that the PBL schemes affected some of the bulk convective environmental variables, such as low-level relative humidity, CAPE, as well as the low-level wind. On the scale of individual cells, both non-rotating and rotating cell composites showed differences in the magnitude of the vertical motion, as well as differences in the vertical extent of relative humidity and radial inflow. The land cell composites also showed larger variation in the model-computed PBL height than the oceanic cells. This chapter will investigate the PBL parameterization mechanisms which affect the differences highlighted in the previous chapter such as: Why does the PBL height differ between land and ocean identified cells? Why did the MYNN3 simulations produce less 0–3-km vertical wind shear compared to the YSU and ACM2 simulations (Figs. 3.25 and 3.26)? Why is the relative humidity concentrated in the low levels in the MYNN3 simulations (Fig. 3.28)? Why do the ACM2 cell composites produce more low-level CAPE compared to the other PBL schemes?

4.1 Depth of the boundary layer

As discussed in the Introduction, the YSU, MYNN3, and ACM2 PBL schemes calculate the model planetary boundary layer height (PBLH) differently. The depth of the PBL is very important in numerical weather models as it defines the layer over which turbulent eddies are parameterized. In the YSU and ACM2 PBL schemes, the PBLH is used in many calculations within the PBL schemes, while in the MYNN3, the PBLH is not. As discussed in the Introduction, the PBL parameterization is used in numerical model simulations across the entire mixed layer and into parts of the surface layer and free atmosphere (Fig. 1.8). The PBLH in the cross sections of the rotating and non-rotating cells in the previous chapter showed differences in the depths of the PBL in the cells over land and over the ocean. As with the cell composites, the focus will be from 0000 UTC 26 August–0000 UTC 27 August for the Harvey simulations and 1200 UTC 10 September–1200 UTC 11 September for the

Irma simulations. Over these time periods, the CAPE environments differed and there was also differences in the number of identified land and ocean non-rotating and rotating cells (Figs. 3.11, 3.12, 3.13, and 3.14).

As discussed in the Introduction, the YSU, MYNN3, and ACM2 PBL schemes all calculate the PBLH differently. The MYNN3 scheme is a local scheme and uses a critical value of turbulent kinetic energy (TKE) to determine the PBLH that is not used in calculations within the PBL scheme. In the case of the MYNN3 parameterization in WRF version 4.1, a critical TKE value of $1.0 * 10^{-6} \frac{m^2}{s^2}$ is used. Both the YSU and ACM2 are non-local and use the critical Richardson number (CRN) to determine the PBLH, which is treated as a prognostic variable for other calculations within the PBL scheme. The YSU PBL scheme uses a CRN of zero for unstable boundary layers, 0.25 for stable land boundary layers, and the CRN is a function of wind speed for stable ocean boundary layers. The ACM2 PBL scheme uses a CRN of 0.25 for both unstable and stable boundary layers both over the land and over the ocean; however, the degree of local or non-local mixing is determined by the stability.

Interesting differences appear in the PBLHs of the YSU and ACM2 (Figs. 4.1 and 4.3) simulations compared to the MYNN3 (Fig. 4.2) simulations in both hurricanes Harvey (top) and Irma (bottom). The YSU simulations in both hurricanes Harvey and Irma show that the PBLHs over land is generally higher than over the ocean by about 600 m, specifically in the region of tropical cyclone precipitation [`http://www.atmos.albany.edu/student/dcard/files/Animation_Harvey_1km.html` and `http://www.atmos.albany.edu/student/dcard/files/Animation_Irma_1km.html`]. The MYNN3 and ACM2 simulations, on the other hand, show fairly similar PBLH over the land and ocean, although the ACM2 PBLH is generally deeper than the MYNN3 PBLH by about 700 m.

Figures 4.4 and 4.5 show the average PBLH over land (top) and over ocean (bottom) at each time in the simulations of hurricanes Harvey and Irma, respectively. In the simulations of Hurricane Harvey, the YSU and ACM2 schemes between 0000 UTC and 1500 UTC 26

August show fairly similar PBLHs from 1000–1300 m; however, the MYNN3 scheme shows a much lower PBLHs over this time period ranging from around 700–800 m (Fig. 4.4, top). On land after 1500 UTC 26 August, the PBLHs in all the simulations of Hurricane Harvey converge to near 1000 m. Over the ocean, the PBLH shows basically the opposite trend to the land PBLH, such that between 0000 UTC and 1500 UTC 26 August the PBLHs were very similar amongst all of the simulations around 800 m in height. Over the ocean after 1500 UTC 26 August, the PBLHs are more variable ranging from 600–1000 m in depth, with the YSU simulation showing the lowest PBLH during this time (Fig. 4.4, bottom).

In the simulations of Hurricane Irma, like the simulations of Harvey, the PBLHs over land in the YSU and ACM2 schemes between 1200 UTC 10 September and 1200 UTC 11 September are fairly similar, ranging from about 1200–1700 m; however, over this same period, the MYNN3 scheme shows a much lower PBLH around 600–800 m (Fig. 4.5, top). Between 1200 and 1900 UTC 10 September, the PBLHs in the simulations converge slightly to about 100–200 m. Over the ocean between 1200 UTC 10 September and 1200 UTC 11 September, the MYNN3 and YSU schemes both show very similar PBLHs around 700 m, while the ACM2 scheme has a PBLH around 900 m (Fig. 4.5, bottom). The PBLHs in the YSU and ACM2 PBL schemes of both tropical cyclones are lower over the ocean compared to the same PBL scheme over land by 100–900 m (Figs. 4.4 and 4.5). In both hurricanes Harvey and Irma, the separation between the land PBLHs across the PBL schemes was maximized during the overnight to early morning hours, which corresponds to the time in which the land PBL is typically decaying (Liu and Liang 2010). This decay also occurs in a similar time period to when the maximum in the frequency of identified land rotating cells occurred (Figs. 3.11, 3.13, 4.4, and 4.5).

Many studies have investigated the impact of changing the CRN in KPP PBL schemes (Hong and Pan 1996; Cohen et al. 2017; Bu et al. 2017). In general, KPP PBL depths vary linearly with the CRN, such that a larger CRN results in a higher PBLH and increases vertical mixing (Kepert 2012). In the unstable boundary layer, the YSU scheme uses a CRN of zero. The YSU scheme uses a stable boundary layer revision for KPP schemes when the virtual surface potential temperature is less that the virtual potential temperature of the first model level (Hong 2010), which indicates a stable environment with negative surface fluxes. For stable boundary layers, the YSU scheme has a CRN greater than zero, such that over the ocean the CRN is based on the wind as seen in the equations in Hong (2010), while over land the CRN is set to 0.25. Thus, for the stable boundary layer over land, both the YSU and ACM2 schemes use the same CRN. For the unstable boundary layer, the YSU uses a fixed value for the CRN of zero and the ACM2 scheme uses a fixed value for the CRN of 0.25.

To investigate the differences in the PBLHs seen between the land and ocean in Figures 4.4 and 4.5, it is important to know which CRN is used to calculate the model PBLH, particularly in the YSU scheme. Figures 4.6, 4.7, and 4.8 show the differences in virtual potential temperature between the surface and the first model level in both hurricanes Harvey (top) and Irma (bottom) to give an indication of where the stable boundary layer revision may be used in the YSU simulation. The cool colors show were the surface virtual potential temperature is colder than the first model level, which is indicative of where there are negative surface fluxes (i.e., the model is stable). Over the ocean, the surface virtual potential temperature is always warmer than the first model level in all the simulations. The YSU, MYNN3, and ACM2 simulations in both storms show that over land, the surface virtual potential temperature is less than the first model level virtual potential temperature (Figs. 4.6, 4.7, and 4.8), particularly in areas of tropical cyclone precipitation [http://www.atmos.albany.edu/student/dcard/files/Animation_Harvey_1km.html and http://www.atmos.albany.edu/student/dcard/files/Animation_Irma_1km.html]. Locations under the tropical cyclones' precipitation, even during the daytime hours, show that the stable boundary layer conditions are met for the YSU scheme. The locations over land where the PBLH is much higher in the YSU and ACM2 simulations compared to the MYNN3 simulation are areas where the YSU and ACM2 schemes both use a CRN of 0.25 (Figs. 4.1, 4.2, and 4.3). Over the ocean, the surface virtual potential temperature is warmer than the first model level virtual potential temperature (Figs. 4.6, 4.7, and 4.8) resulting in a CRN of zero for the YSU scheme and 0.25 for the ACM2 scheme. In the ACM2 scheme, the CRN over the ocean is equal to the CRN over land, which explains why the PBLH is fairly similar over both the ocean and land in the ACM2 simulations (Figs. 4.3, 4.4, and 4.5).

The differences seen between the model-computed PBL depths and stability over land compared to over ocean motivates looking at vertical cross sections across the coastline. Figure 4.11 shows model reflectivity and cross section radial wind for Harvey at 0000 UTC 26 August. The cross sections show that over land the inflow depth is deeper in the YSU and ACM2 simulations by about 200–400 m compared to the MYNN3 simulations. Both the YSU and ACM2 simulations show PBL heights that are decoupled from this inflow height, unlike the MYNN3 simulations. The YSU and ACM2 simulations also show a large discontinuity in the PBL height right near the coastline. In the YSU PBL scheme, where the PBL scheme transitions from the land to ocean, the CRN changes as described in the previous chapter and the PBL height responds to this change in CRN at the coastline by abruptly dropping from 1800 m in depth to around 300 m. A similar discontinuity is found in the ACM2 simulation where, although the CRN does not change, the stability changes from the land to the ocean, resulting in a drop in the PBL height from around 1600 m to 500 m. Similarly in the simulations of Irma in Figure 4.12 at 1500 UTC 10 September, the YSU and ACM2 simulations show that the PBL heights are decoupled from the inflow heights, unlike the MYNN3 simulation. Again, there is a large discontinuity in the PBL heights near the coastlines in the YSU and ACM2 simulations. Like in the Harvey YSU simulation, the CRN changes from the land to ocean, such that the PBL height responds to this change through and abrupt drop in the PBL height near the coastline from about 1700 m to 500 m. The ACM2 simulation of Irma also shows a drop in the PBL height near the coast as a result of the changing stability resulting in a drop from about 1600 m to 600 m.

In contrast to the coastline, over land at 1000 UTC 26 August, PBL heights in all of the Harvey simulations remain constant and descend slowly towards the center of the tropical cyclone (Fig. 4.13). Over land, the depth of the radial inflow is also very similar to the model-computed (described above) PBL height in all three PBL schemes. In the YSU simulation, the PBL height and inflow depth are both around 1100 m at further than 30 km from the center. The MYNN3 simulation shows a PBL height and inflow depth around 600–800 m. Again beyond 30 km from the center, the ACM2 simulation has a PBL height and inflow depth around 950 m. The times and model cross sections of Harvey will be compared in the next chapter to cross sections from the mobile Doppler radar positioned to capture the landfall of Hurricane Harvey.

Defining the depth of the boundary layer in tropical cyclones is not straight forward. Zhang et al. (2011c) showed from dropsonde observations that different definitions of PBLH can result in substantially different results. Zhang et al. (2011c) investigated various methods of defining the PBLH from 2231 dropsondes from select hurricanes between 1997 and 2005. The PBLH was defined by the height of the maximum wind speed, mixed layer depth, inflow height, and based on a CRN with respect to the radius of maximum wind (RMW) at 2 km (Zhang et al. 2011c). The composite observations from Zhang et al. (2011c) were from dropsonde observations over the ocean, while our simulations also included land vertical profiles. As mentioned previously, the YSU and ACM2 schemes use a CRN in the calculation of the model PBLH. For this analysis, the temporally- and azimuthally-averaged fields will be taken for hurricanes Harvey and Irma from 0000 UTC 26–1200 UTC 27 August and 1200 UTC 10–0000 UTC 12 September, respectively.

Before diving into the different methods of calculating the depth of the PBL, it is important to note that the analysis will use multiples of the RMW allowing for a more fair comparison of the azimuthally-averaged fields within the tropical cyclone. There are large differences in the RMW (at 2 km) between the Harvey and Irma simulations. As shown in the titles of Figures 4.9 and 4.10, the RMW in the Irma simulations is about twice as large as the RMW in the Harvey simulations. When comparing the storms in terms of multiples of the RMW, it is important to acknowledge that these distances can be very different in terms of physical distance. For example, the MYNN3 simulation of Harvey has a RMW of 62 km, while the MYNN3 simulation of Irma has a RMW of 80 km, such that three times the RMW in the Harvey simulation would be 186 km, while in the Irma simulation it would be 240 km. As seen in the relfectivity, [`http://www.atmos.albany.edu/student/dcard/files/Animation_Irma_1km.html`] the Irma simulations had a large eye compared to the simulations of Harvey leading to these differences in the RMW.

First, the PBLH represented by the height of the maximum wind speed is examined. The azimuthally- and temporally-averaged total wind, and the corresponding height of the maximum wind speed is shown in Figures 4.9a and 4.10a, for Harvey and Irma, respectively. For the simulations of Hurricane Harvey, the height of the maximum wind speed in the YSU scheme ranges from about 700–1600 m between the RMW and five times the RMW. The maximum wind height in the MYNN3 simulation of Harvey ranges from about 600–1000 m between the RMW and five times the RMW. For the ACM2 Harvey simulations, the height of the maximum wind ranges from about 500–800 m. For the simulations of Hurricane Irma, the height of the maximum wind speed in the YSU scheme ranges from about 600–1100 m between the RMW and two times the RMW, before plateauing and finally decreasing in height between three and five times the RMW. In the MYNN3 simulation of Hurricane Irma, the height of the maximum wind speed increases from about 500 m at the RMW to about 1200 m at five times the RMW. The ACM2 maximum wind height for Hurricane Irma ranges from 700–1400 m between the RMW and three times the RMW, before decreasing to around 700 m at five times the RMW. It is important to note that, as seen in Figures 4.9a and 4.10a, the winds decrease more rapidly as a function of the RMW in the Irma simulations compared to the Harvey simulations, which changes drastically what is going on outside the RMW.

Second, we consider the mixed layer depth definition of the PBLH as identified by the base of the inversion layer as defined in Zhang et al. (2011c). In Zhang et al. (2011c), the top of the mixed layer is defined as where the virtual potential temperature increases by 0.5 K from the mean virtual potential temperature in the lowest 150 m (Anthes and Chang 1978). A composite analysis of the azimuthally- and temporally-averaged virtual potential temperature difference from the mean virtual potential temperature in the lowest 150 m, and the corresponding height of where the virtual potential temperature difference is 0.5 K is provided in Figures 4.9b and 4.10b, for Harvey and Irma, respectively. In the YSU simulation of Hurricane Harvey, the mixed layer depth is about 700 m at the RMW and decreases to the surface near five times the RMW. In the MYNN3 Harvey simulation, the mixed layer depth is about 500 m at the RMW and decreases to around 100 m at five times the RMW. The ACM2 Harvey simulation shows that the mixed layer is around 500 m at the RMW and increases to about 600 m at five times the RMW. In the simulations of Hurricane Irma, it is interesting that the measure for mixed layer depth does not begin at the center of the storm like in the simulations of Harvey. In Irma, the mixed layer depth does not begin at the center of the storm because the virtual potential temperature is high in the eye, such that it is always warmer than 0.5 K plus the mean virtual potential temperature in the lowest 150 m (which is the defined mixed layer depth). In the YSU simulation of Irma, the mixing depth begins registering just radially inside the RMW, increasing rapidly and plateauing at about 700 m. The MYNN3 simulation of Irma shows that the mixed layer depth begins to register at about 1.5 times the RMW and increases to about 600 m before plateauing. In the ACM2 simulation of Irma, the mixed layer depth begins to register at the RMW and increases to about 700 m before plateauing.

Third, we consider the PBLH calculated from the height of the inflow, defined in Zhang et al. (2011c) as the height where the radial velocity is 10% of the maximum inflow. Figures 4.9c and 4.10c show the azimuthally- and temporally-averaged radial wind and the corresponding height of the radial velocity that is 10% of the maximum inflow. The YSU simulation of Hurricane Harvey has a inflow height of about 700 m at the RMW that increases to around 1000 m at five times the RMW. In the MYNN3 Harvey simulation, the inflow height is near 600 m at the RMW and increases to about 900 m at five times the RMW. The ACM2 Harvey simulation shows an inflow depth of around 400 m at the RMW that increases to about 900 m at five times the RMW. In the YSU simulation of Hurricane Irma, the inflow depth is about is about 1000 m at the RMW and increases rapidly to beyond 3000 m at around two times the RMW. In the MYNN3 Irma simulation, the inflow depth is about 700 m at the RMW and again increases to beyond 3000 m by three times the RMW. The ACM2 Irma simulation is similar in that the inflow depth is about 800 m at the RMW and then increases to beyond 3000 m by three times the RMW. The large differences seen in the inflow depth between the simulations of Harvey and Irma can be attributed to the RMW. The RMW in the Harvey MYNN3 simulation is around 62 km, while in Irma it is around 80 km, such that three times the RMW in Harvey equates to around 186 km, while in Irma it is 240 km.

Comparison of the results of the Harvey simulation to the results of Zhang et al. (2011c) (Fig. 4.9, bottom) show that the MYNN3 and ACM2 simulations preformed best across the three metrics for the boundary layer height. The MYNN3 simulation showed the most comparable PBLH with respect to the total wind (Fig. 4.9a), increasing from around 500 m at the RMW to around 1000 m at five times the RMW, very similar to Zhang et al. (2011c) that shows the total wind PBLH increases from 500 to around 1200 m from the RMW to five times the RMW (Fig. 4.9a). All the simulations showed a decrease in the mixed layer depth beyond three to four times the RMW, which was not present in the observations from Zhang et al. (2011c). Again, the MYNN3 simulation preformed best compared to the observations for the mixed layer depth increasing from around 200 m at the center to about 500 m at the RMW, before plateauing through three times the RMW. The MYNN3 simulation of Harvey did well with the mixed layer depth from the center to about three times the RMW, which is similar to the observations of Zhang et al. (2011c) that showed the mixed layer depth slowly increased from about 200 m at the composite center to about 400 m at five times the RMW (Fig. 4.9b). The MYNN3 simulation of Harvey did well with the mixed layer depth from the center to about three times the RMW. In terms of the radial inflow depth, the simulations were all typically more shallow than the observations from Zhang et al. (2011c). The ACM2 simulation showed the deepest inflow layer depth and, therefore, performed best compared to the results of Zhang et al. (2011c).

The MYNN3 and ACM2 simulations also preformed well in capturing the results of Zhang et al. (2011c) in the Irma simulations in terms of the total winds and mixed layer depth representations of the boundary layer height. The MYNN3 simulation showed the best results for the total wind measure of the PBLH which increased from around 600 m at the RMW to about 1200 m just before five times the RMW, which is very similar to the composite results of Zhang et al. (2011c) that showed the total wind PBLH increases from 500 to around 1200 m from the RMW to five times the RMW (Fig. 4.10a). The ACM2 simulation provided the most similar measure of the mixed layer depth, although, as discussed previously, the measure of the mixed layer depth was undefined until about the RMW, after which the ACM2 simulation mixed layer depth quickly increases to about 600 m and plateaus, which is similar to the mixed layer depth results from Zhang et al. (2011c) that plateaued at about 300–400 m in depth. None of the simulations of Irma did particularly well representing the boundary layer depth from the inflow depth method from Zhang et al. (2011c), specifically from two to three times the RMW where it was typically much deeper (Fig. 4.10c) than observations from Zhang et al. (2011c).

4.2 Eddy diffusivity

Eddy diffusivity is a measure of the turbulent vertical mixing in the PBL. The eddy diffusivity for momentum is the primary driver of vertical mixing in numerical weather simulations. The eddy diffusivity for scalars is related to the eddy diffusivity of momentum through the Prandtl number (Hong and Pan 1996) and, as such, is positively correlated with the eddy diffusivity for momentum (Vaughan and Fovell 2020). To investigate the amount of vertical mixing in the PBL in the simulations of hurricanes Harvey and Irma, the eddy diffusivity for scalars is used. Eddy diffusivity serves as a proxy to describe the magnitude of the vertical mixing. Recall, from the Introduction, that in the YSU scheme the stable boundary layer revision from Hong (2010) alters the parabolic profile of the eddy diffusivity coefficients with height from the original formulation of Hong and Lim (2006) in those areas where the surface virtual potential temperature is less than the first model level virtual potential temperature (Fig. 4.6). For the ACM2 PBL scheme, above the PBL the eddy diffusivity is based on local wind shear and stability, while within the boundary layer the eddy diffusivity is defined similarly to the YSU scheme (Hong et al. 2006; Pleim 2007a) as a parabolic profile of the eddy diffusivity coefficients with height.

Figure 4.14 shows the relationship between the azimuthally-averaged eddy diffusivity and 500 m wind speed from the RMW (stars) radially outward in the simulations of Hurricane Harvey (top) between 0000 UTC 26 August to 0000 UTC 27 August and Hurricane Irma (bottom) between 1200 UTC 10 September to 1200 UTC 11 September. Similar to the results of Gopalakrishnan et al. (2013) and Zhang et al. (2011b), the eddy diffusivity shows that there is more vertical mixing at faster 500 m wind speeds. In both the Harvey and Irma YSU simulations, the mixing is much stronger compared to the observations from Zhang et al. (2011b) at outer radii (squares) with weak 500 m wind speeds (Fig. 4.14), while the MYNN3 and ACM2 schemes show comparable mixing to the observations. Near the RMW (stars) in both hurricanes Harvey and Irma, the MYNN3 and YSU simulations tend to have vertical mixing similar to observations, but the ACM2 scheme, particularly in the Harvey simulations, shows too much vertical mixing is occurring compared to observations (Fig. 4.14, top). The MYNN3 vertical mixing tends to be smaller than the YSU and ACM2 schemes at faster 500 m wind speeds and at radii closer to the RMW. Both the YSU and MYNN3 simulations in show a linear trend between the eddy diffusivity and 500 m wind speed, whereas the ACM2 scheme shows a steeper, more exponential trend (Fig. 4.14).

As mentioned previously, for non-local, KPP, PBL schemes, large CRNs lead to deeper PBLHs and more eddy diffusivity. The YSU and ACM2 schemes tended to have higher

PBLHs over land compared to ocean because the CRN of both over land is 0.25 (Figs. 4.1 and 4.3). Figure 4.15a shows the mean vertical eddy diffusivity in the simulations of Hurricane Harvey over land and over ocean. The YSU land eddy diffusivity peaks around 600 m (50 m^2/s) and drops off to near zero around 2000 m. The YSU ocean eddy diffusivity is more shallow than over land and peaks around 200 m (43 m^2/s) before dropping off to near zero around 1000 m. The MYNN3 land and ocean eddy diffusivities are fairly similar in that they both peak around 200 m above the surface (38 m^2/s and 55 m^2/s, respectively) and drop off to around zero near 1400 m. The ACM2 scheme produces a very different vertical profile of eddy diffusivity compared to the YSU and MYNN3 simulations. In the low levels, the eddy diffusivity peaks near 400 m (30 m^2/s); however, the values of eddy diffusivity do not drop off to zero like the other two schemes. There is a second peak in the ACM2 land eddy diffusivity around 3800 m (70 m^2/s). The ACM2 ocean eddy diffusivity peaks around 200 m (30 m^2/s) and is less than the land eddy diffusivity in the midlevels.

Figure 4.15b shows the mean vertical eddy diffusivity in the simulations of Hurricane Irma over land and over ocean. The YSU land eddy diffusivity peaks around 400 m (60 m^2/s) and drops off to near zero around 1600 m. The YSU ocean eddy diffusivity is shallower than the land and peaks around 200 m (70 m^2/s) before dropping off to near zero around 1000 m. The MYNN3 land and ocean eddy diffusivities are fairly similar in that they both peak around 200 m (40 m^2/s and 75 m^2/s, respectively) and drop off to around zero near 1600 m, similar to the Harvey MYNN3 simulation. The ACM2 scheme, again, produces a very different vertical profile of eddy diffusivity compared to the YSU and MYNN3 simulations, just as in the simulations of Hurricane Harvey. In the low levels, the eddy diffusivity peaks near 400 m (70 m^2/s); however, the values of eddy diffusivity do not drop off to zero like the other two schemes. There is a broad second peak in the ACM2 land eddy diffusivity around 3400 m (50 m^2/s). The ACM2 ocean eddy diffusivity peaks around 400 m (70 m^2/s) and is less than the land eddy diffusivity in the midlevels. The vertical profiles of eddy diffusivity show that the ocean mixing tends to be concentrated closer to the surface than over land in all the simulations, regardless of the PBL scheme. The vertical mixing in both the YSU and MYNN3 simulations tends to drop off to near zero above 1200–1600 m (Fig. 4.15). Over the ocean and land the ACM2 simulations show a much deeper extent to the vertical mixing since the eddy diffusivity does not drop off to near zero like the other two PBL schemes (Fig. 4.15).

Another way to investigate the structure of the eddy diffusivity is by showing the temporally- and azimuthally-averaged eddy diffusivity and radial winds scaled by the maximum inflow as shown in Figure 4.16 for Hurricane Harvey from 0000 UTC 26 August to 0000 UTC 27 August (left) and Hurricane Irma from 1200 UTC 10 September to 1200 UTC 11 September (right). All of the simulations show the eddy vertical mixing is maximized at the RMW; however, the magnitude of the vertical mixing is drastically different between the PBL schemes. In Harvey (Fig. 4.16, left), the mixing maximum is about 45 m^2/s in the YSU and MYNN3 simulations, while the ACM2 has a maximum of 90 m^2/s. In Irma (Fig. 4.16, right), the mixing maxima in the YSU and MYNN3 simulations are around 75 m^2/s, while it is around 90 m^2/s in the ACM2 simulation. Near the RMW the eddy mixing extends to beyond 2 km in height in the ACM2 simulations of both Harvey and Irma. In the YSU simulations, the eddy diffusivity only extends to around 1 km and 1.3 km, respectively. The MYNN3 simulations tend to have a peak in eddy diffusivity near the RWM extending beyond 2 km vertically in the Irma simulation and to 1.4 km in the Harvey simulation. Eddy diffusivity decreases from the maximum value near the RMW to about 1.5–2 times the RMW, after which the eddy diffusivity tends to not change in depth with increasing radius. The eddy mixing in the MYNN3 simulations is about 900 m in depth in Harvey and 1300 m in depth in Irma beyond two times the RMW. The ACM2 has widespread eddy mixing especially within three times the RMW where it extends beyond 2 km in depth. The scaled radial inflow shows that in the Irma simulations beyond two times the RMW the depth of the strong inflow increases as seen in Figure 4.10, which did not compare well with the results of Zhang et al. (2011c), since the winds decreased rapidly as a function of RMW.

Figure 4.17 shows the difference in eddy diffusivity between the rotating and non-rotating identified cells for the different PBL schemes. In the simulations of Hurricane Harvey (Fig. 4.17a), the eddy diffusivity of the YSU scheme is higher from the surface to 5000 m in the rotating identified cells by about 4 m^2/s. In the MYNN3 simulation, the eddy diffusivity between the identified rotating and non-rotating cells is very similar above 1800 m; however, from the surface to about 600 m, the eddy diffusivity is higher in the non-rotating cells by 10 m^2/s. From 600–1800 m, the eddy diffusivity in the rotating cells is higher than in the non-rotating MYNN3 cells by only 2 m^2/s. The ACM2 simulation shows that, overall, there is much more eddy diffusivity in the identified rotating cells below 4600 m compared to the other two PBL schemes. From 400–4800 m in the ACM2 simulation, the rotating cells have 14 m^2/s more eddy diffusivity than the non-rotating cells. Rotating cells generally have larger eddy diffusivity from 600–4000 m compared to non-rotating cells in Harvey. None of the differences between the eddy diffusivity in the rotating and non-rotating cells are statistically significantly different.

In the simulations of Hurricane Irma (Fig. 4.17b), the YSU simulation shows that eddy diffusivity is higher by about 7 m^2/s in the identified rotating cells compared to the non-rotating cells. The MYNN3 simulation shows that identified rotating and non-rotating cells have similar eddy diffusivity above 2800 m. Between 400 and 1600 m, the YSU and MYNN3 differences in eddy diffusivity are very similar. Below 400 m, the MYNN3 simulation shows a decrease in the difference between identified rotating and non-rotating cells, which turns slightly negative below 200 m, showing that the identified non-rotating cells have more eddy diffusivity near the surface by about 2 m^2/s. In the ACM2 simulation, the identified rotating cell eddy diffusivity is much higher than that of the identified non-rotating cells from 400–4800 m by more than 20 m^2/s. In fact in the ACM2 simulation, the rotating cells have statistically significantly (p=0.02) higher eddy diffusivity compared to the non-rotating cells. Rotating cells generally have larger eddy diffusivity from 600–4000 m compared to non-rotating cells in Irma. Like in the Harvey simulations, the differences between the eddy diffusivity in the rotating and non-rotating cells of the YSU and MYNN3 simulations are not statistically significantly different.

The analysis in this section has shown large differences in the vertical and radial distribution of eddy diffusivity between the different PBL schemes tested. With respect to the 500 m wind speed, the YSU simulations of both Harvey and Irma showed more mixing compared to observations at low wind speeds, while the ACM2 simulations both showed more mixing compared to observations at high wind speeds (Fig. 4.14). Overall, the MYNN3 simulation produced mixing in large agreement with the observations of Zhang et al. (2011b). Over the ocean and land in the simulations of Harvey and Irma, the ACM2 simulation produced more eddy mixing than the YSU and MYNN3 simulations (Fig. 4.15) above about 1000 m. Near the surface, the eddy mixing was largest over the ocean, compared to over land in all the PBL schemes. The temporally- and azimuthally-averaged eddy diffusivity and radial winds scaled by the maximum inflow (Fig. 4.16) showed that the eddy diffusivity is generally concentrated at the eyewall (RMW). In the YUS and MYNN3 simulations, the eddy diffusivity at larger multiples of the RMW was trapped below about 900 m in Harvey and 1000 m in Irma (Fig. 4.16). As seen in the overall eddy diffusivity (Fig. 4.15), the ACM2 simulations showed much more mixing in the identified rotating cells compared to the non-rotating cells in both the simulations of Harvey and Irma. Further discussion in the last section of this chapter will link the results here to the differences identified in the previous chapter.

4.3 Moisture, heat, and wind tendencies in the boundary layer

The eddy diffusivity describes the magnitude of the vertical mixing present in the model. The PBL tendencies in the moisture, heat, and wind show if the vertical mixing of the PBL scheme causes an increase or decrease in the variable over time. In the previous section, it was seen that there were differences in the eddy diffusivity over ocean and over land, as well as in the rotating and non-rotating identified cells. The tendencies of the water vapor mixing ratio (moisture), temperature, and wind for the YSU, MYNN3, and ACM2 simulations of Hurricane Harvey are shown in Figures 4.18, 4.19, and 4.20, respectively. In all the simulations, the PBLH is lower in the ocean cells compared to the land cells, as seen previously. The number of cells which make up the tendency composites are the same as in the cell composites from the previous chapter.

Figure 4.18a shows tendencies are generally weak above the boundary layer in the Harvey YSU non-rotating cell composites. The moisture tendency in the land non-rotating cell composite shows a generally weak increase in moisture in the boundary layer around $0.5 * 10^{-5}$ $kg/kg/h$; however, directly above the surface the moisture tendency is negative. The temperature tendency of the land non-rotating cell composite shows a decrease in temperature in the boundary layer around $-0.5 * 10^{-2}$ K/h; however, directly above the surface there is a positive temperature tendency. At around 5 km in height, there is a secondary maximum (minimum) in the moisture (temperature) tendencies, indicating a phase change of the water vapor, consistent with the typical height of the melting levels in tropical cyclones (Houze 2010). The moisture tendency in the ocean non-rotating cell composite is very high in the boundary layer near $2 * 10^{-5}$ $kg/kg/h$. There are also large temperature tendencies near the surface in the boundary layer around $2 * 10^{-2}$ K/h. Again, around 5 km in height, there is a secondary maximum (minimum) in the moisture (temperature) tendency, driven by melting or freezing. In both the land and ocean non-rotating cell composites (Fig. 4.18a), the wind tendencies are generally negative and confined to below the PBLH. The wind tendencies are largest in the boundary layer of the land cells, around -0.06 $m/s/h$, extending from the surface to about 500 m in height. In the ocean cells, the wind tendency tends to be more shallow, around 250 m in height, is around -0.07 $m/s/h$, and is stronger than over land.

Figure 4.18b shows tendencies are generally weak above the boundary layer in the rotating cell composites of the YSU Harvey simulation. The moisture tendency in the land rotating cell composite shows a weak increase in moisture near the PBLH around $0.5 * 10^{-5}$ $kg/kg/h$; however, directly above the surface, the moisture tendency is negative. The temperature tendency of the land rotating cell composite shows a decrease in temperature in the boundary layer around $-0.7 * 10^{-2}$ K/h; however, directly above the surface there is a positive temperature tendency. Like in the non-rotating cell composites at around 5 km in height, there is a secondary maximum (minimum) in the moisture (temperature) tendency in the rotating cell composites, again indicating the melting level (Houze 2010). The moisture tendency in the ocean rotating cell composite is very high in the boundary layer near $2*10^{-5}$ $kg/kg/h$. There is also large temperature tendencies near the surface in the boundary layer around $2 * 10^{-2}$ K/h in the ocean rotating cell composite. In both the land and ocean rotating cell composites (Fig. 4.18b), the wind tendencies are generally positive and located within the boundary layer. The wind tendencies are large and negative in the lower portion of the boundary layer in the land cells, around -0.07 $m/s/h$. The wind tendency turns slightly positive around 0.02 $m/s/h$ near the top of the PBL (500 m). In the ocean rotating cells the wind tendency is around -0.03 $m/s/h$. The rotating ocean cell wind tendency is more shallow than the land cells by about 250 m, because the PBLH is more shallow in the YSU simulations compared to land.

Figure 4.19a shows tendencies are generally weak above the boundary layer in the non-rotating cell composites of the Harvey MYNN3 simulation. The moisture tendency in the land non-rotating cell composite shows a generally weak decrease in moisture in the boundary layer around $-0.2*10^{-5}$ $kg/kg/h$; however, directly above the PBLH the moisture tendency is positive. The temperature tendency of the land non-rotating cell composite shows a weak increase in temperature in the boundary layer around $0.2 * 10^{-2}$ K/h; however, directly above the PBLH there is a negative temperature tendency. The moisture tendency in the ocean non-rotating cell composite is very high near the surface around $2 * 10^{-5}$ $kg/kg/h$. Directly surrounding the PBLH, the moisture tendency is negative. There is also a positive temperature tendency in the boundary layer around $1 * 10^{-2}$ K/h. In the land non-rotating cell composite (Fig. 4.19a), the wind tendencies are negative right near the surface around -0.02 $m/s/h$, extending to about 1000 m, which is just above the PBL top. The ocean non-rotating cells had very weak, and generally negative wind tendencies around -0.01 $m/s/h$ within the PBL.

Figure 4.19b shows tendencies are generally weak above the boundary layer in the rotating cell composites of the Harvey MYNN3 simulation. The moisture tendency in the land rotating cell composite shows a generally weak decrease in moisture in the boundary layer around $-0.1 * 10^{-5}$ $kg/kg/h$; however, directly above the PBLH, the moisture tendency is positive around $0.7 * 10^{-5}$ $kg/kg/h$. The temperature tendency of the land rotating cell composite shows a weak increase in temperature in the boundary layer around $0.2 * 10^{-2}$ K/h; however, directly above the PBLH there is a negative temperature tendency. The moisture tendency in the ocean rotating cell composite is very high near the surface around $2 * 10^{-5}$ $kg/kg/h$. Directly surrounding the PBLH, the moisture tendency is negative. There are also positive temperature tendencies within the boundary layer around $0.7 * 10^{-2}$ K/h. The moisture and temperature tendencies in the MYNN3 rotating land cells tend to be confined to below 3 km. In the land rotating cell composite (Fig. 4.19b), the wind tendencies are negative, and are largest in the boundary layer, exceeding -0.09 $m/s/h$. Directly above the the boundary layer the wind tendency is slightly positive at around 0.01 $m/s/h$. In the ocean cells the wind tendency is very weak around -0.01 $m/s/h$, very similar to the non-rotating ocean cell composite.

Figure 4.20a shows tendencies are generally stronger above the boundary layer in the non-rotating cell composites of the Harvey ACM2 simulation and larger compared to the YSU and MYNN3 simulations. The moisture tendency in the land non-rotating cell composites show that they are weakest in the boundary layer; however, directly above the PBLH, the moisture tendency is negative around $-1.4 * 10^{-5}$ $kg/kg/h$. Above 2.5 km, the moisture tendency becomes positive again. The opposite is seen in the temperature tendency where it is weakly negative in the boundary layer and becomes strongly positive directly above the boundary layer reaching $1 * 10^{-2}$ K/h. Above 2.5 km, the temperature tendency becomes negative again. The moisture tendency in the ocean non-rotating cell composite is very high near the surface around $2 * 10^{-5}$ $kg/kg/h$. Directly above the top of the boundary layer, the moisture tendency is negative around $-1.6 * 10^{-5}$ $kg/kg/h$. In the ocean non-rotating composite, there are positive temperature tendencies at the surface of about $2 * 10^{-2}$ K/h; however, the rest of the shallow boundary layer shows negative temperature tendencies of around $-0.7 * 10^{-2}$ K/h, with strongly positive tendencies just above the boundary layer at around $1.4 * 10^{-2}$ K/h. In the land non-rotating cell composite (Fig. 4.20a), the wind tendencies are weakly negative near the surface at around -0.02 $m/s/h$ and extend to about 250 m above the ground. Directly surrounding the PBL top (about 500 m) the wind tendency is weakly positive at around 0.02 $m/s/h$. In the ocean non-rotating cell composite the wind tendency is negative in the boundary layer from the surface to 500 m at around -0.03 $m/s/h$, with areas of weakly positive wind tendencies at the top of the PBL.

Figure 4.20b shows tendencies are again generally larger in the rotating cell composites of the Harvey ACM2 simulation and larger compared to the YSU and MYNN3 simulations. The moisture tendency in the land rotating cell composites is negative in the boundary layer around $-1.4*10^{-5}$ $kg/kg/h$, however, around 2 km, the moisture tendency is positive and is about $1*10^{-5}$ $kg/kg/h$. The opposite is seen in the temperature tendency where it is positive in the boundary layer around $1*10^{-2}$ K/h and becomes negative around 2 km to $-0.7*10^{-2}$ K/h. The moisture tendency in the ocean rotating cell composites is largest near the surface around $1*10^{-5}$ $kg/kg/h$. Directly above the top of the boundary layer, the moisture tendency is strongly negative around $-2.1 * 10^{-5}$ $kg/kg/h$. In the ocean rotating composite, there are positive temperature tendencies at the surface of $1.4 * 10^{-2}$ K/h; however, the rest of the shallow boundary layer shows negative temperature tendencies around $-0.3 * 10^{-2}$ K/h. The temperature tendency is strongly positive just above the boundary layer, very similar to the non-rotating ocean cells with a magnitude of $2.1 * 10^{-2}$ K/h. In the land rotating cell composite (Fig. 4.20b), the wind tendencies are large and negative, and are maximized in the boundary layer exceeding -0.09 $m/s/h$, extending from the surface to around 1000 m. In the ocean cell composite, the wind tendency is around -0.02 $m/s/h$ within the boundary layer from the surface to around 500 m. From 500–1000 m, just above the PBL, the wind tendency is weakly positive at around 0.03 $m/s/h$, with another layer of negative wind tendency from 1000–2000 m at around -0.02 $m/s/h$. Unlike the YSU and MYNN3 ocean composites, the large wind tendencies in the ACM2 simulation extend beyond the top of the PBL to between 2–3 km above the surface.

The tendencies of moisture, temperature, and wind for the YSU, MYNN3, and ACM2 simulations of Hurricane Irma are shown in Figures 4.21, 4.22, and 4.23 respectively. In all the simulations, the PBLH is lower in the ocean cells compared to the land cells, as was discussed in a previous section. The number of cells which make up the tendency composites are the same as in the cell composites from the previous chapter. Recall in the simulations of Irma that there were very few land rotating and non-rotating cells (Fig. 1.7).

Figure 4.21a shows tendencies of the Irma YSU simulations. The strongest tendencies tend to occur within and directly adjacent to the boundary layer in the non-rotating cells. The moisture tendency in the land non-rotating cell composite shows an increase in moisture in the boundary layer around $1 * 10^{-5}$ $kg/kg/h$; however, directly above the surface, the moisture tendency is negative around $-1 * 10^{-5}$ $kg/kg/h$. The temperature tendency of the land non-rotating cell composite shows a decrease in temperature adjacent to the boundary layer around $-1.5 * 10^{-2}$ K/h; however, directly above the surface, there is a positive temperature tendency of about $1.5 * 10^{-2}$ K/h. The moisture tendency in the ocean non-rotating cell composite is positive through the boundary layer with a maximum around $0.7 * 10^{-5}$ $kg/kg/h$ adjacent to the boundary layer. The temperature tendencies in the boundary layer are also positive around $1 * 10^{-2}$ K/h, but are generally weakly negative above the boundary layer around $-0.4 * 10^{-2}$ K/h. In the land non-rotating cell composite (Fig. 4.21a), the wind tendencies are generally negative around -0.15 $m/s/h$ within the boundary layer (around 1000 m), and do not extend above it. In the ocean non-rotating cell composite, the wind tendencies are much weaker than the land composite and negative at around -0.03 $m/s/h$ within the boundary layer, extending to around 500 m. The wind tendencies are weakly negative just above the boundary layer at around $-0.02\ m/s/h$ through about 1000 m.

Figure 4.21b shows tendencies are generally strongest near and below the PBLH in the rotating cell composites of the YSU simulation. The moisture tendency in the land rotating cell composite shows a generally decrease in moisture near the surface around $-2 * 10^{-5}$ $kg/kg/h$; however, around the PBLH, the moisture tendency is positive with a magnitude of $1.8 * 10^{-5}\ kg/kg/h$. The temperature tendency of the land rotating cell composite shows a decrease in temperature near the PBLH around $-2 * 10^{-2}\ K/h$; however, directly above the surface, there is a large positive temperature tendency around $2 * 10^{-2}\ K/h$. The moisture tendency in the ocean rotating cell composite is positive in the boundary layer around $1.2 * 10^{-5}\ kg/kg/h$. In the ocean rotating cell composite, the strongest temperature tendencies are located near the surface around $1 * 10^{-2}\ K/h$. In the land rotating cell composite (Fig. 4.21b), the wind tendencies are strongly negative in the boundary layer exceeding $-0.20\ m/s/h$, from the surface to around 750 m. Around and just above the boundary layer (between 1000 and 2000 m), the wind tendency is positive around 0.10 $m/s/h$. In the ocean cell composite, the wind tendency is negative in the boundary layer around $-0.10\ m/s/h$ from the surface to around 500 m.

Figure 4.22a shows tendencies are generally weak above the boundary layer in the non-rotating cell composites of the Irma MYNN3 simulation, with most of the tendencies below 3 km. The moisture tendency in the land non-rotating cell composite shows a generally decrease in moisture in the boundary layer around $-1 * 10^{-5}\ kg/kg/h$; however, directly above the PBLH, the moisture tendency is positive around $1 * 10^{-5}\ kg/kg/h$. The temperature tendency of the land non-rotating cell composite shows an increase in temperature in the boundary layer around $1.4 * 10^{-2}\ K/h$. Directly above the top of the PBL, there is a negative temperature tendency around $-1 * 10^{-2}\ K/h$, which is the opposite sign of the moisture tendency. The moisture tendency in the ocean non-rotating cell composite is positive near the surface and above the PBLH around $0.7 * 10^{-5}\ kg/kg/h$. Directly surrounding the PBLH, the moisture tendency is negative around $-0.4 * 10^{-5}\ kg/kg/h$. There are positive temperature tendencies within the boundary layer around $1 * 10^{-2}$ K/h, with negative temperature tendencies above the boundary layer of $-0.3 * 10^{-2}$ K/h. In both the land and ocean non-rotating cell composites (Fig. 4.22a), the wind tendencies are negative, and are largest within the boundary layer extending to about 750 m, around -0.15 $m/s/h$. Above the boundary layer, the wind tendencies are weakly positive around 0.03 $m/s/h$ from 750–2000 m. In the ocean cell composite, the negative wind tendencies are weaker than the land and around -0.05 $m/s/h$ extending from the surface to 500 m.

Figure 4.22b shows tendencies are generally weak above 3 km in the rotating cell composites of the MYNN3 simulation. The moisture tendency in the land rotating cell composite shows a decrease in moisture in the boundary layer around $-1 * 10^{-5}$ $kg/kg/h$; however, directly above the PBLH, the moisture tendency is positive around $0.7 * 10^{-5}$ $kg/kg/h$. The temperature tendency of the land rotating cell composite shows an increase in temperature in the boundary layer around $1 * 10^{-2}$ K/h, but directly above the PBLH there is a negative temperature tendency of around $-0.7 * 10^{-2}$ K/h. The moisture and temperature tendencies appear inverse in spatial structure. The moisture tendency in the ocean rotating cell composite is large near the surface and above the PBLH around $0.7 * 10^{-5}$ $kg/kg/h$. Directly surrounding the PBLH, the moisture tendency is weakly negative at about $-0.1 * 10^{-5}$ $kg/kg/h$. There is a positive temperature tendency in the boundary layer around $2 * 10^{-2}$ K/h, with negative temperature tendencies above the boundary layer around $-0.7 * 10^{-2}$ K/h. In the land rotating cell composite (Fig. 4.22b), the wind tendencies are negative, confined mostly to the boundary layer (below 500 m), and exceed -0.2 $m/s/h$, but are slightly positive above the PBL. In the ocean rotating cell composite, the wind tendency is weaker than the land composite around -0.1 $m/s/h$ in the boundary layer (below 500 m), and slightly positive above the PBL.

Figure 4.23a shows tendencies are generally stronger above the boundary layer in the non-rotating cell composites of the Irma ACM2 simulation and, again, larger compared to the YSU and MYNN3 simulations. The moisture tendency in the land non-rotating cell composite shows a very messy picture of areas of large negative (exceeding $-2*10^{-5}$ $kg/kg/h$) and positive (exceeding $2*10^{-5}$ $kg/kg/h$) tendencies. The areas of positive moisture tendency tend to be located above the PBLH, while the negative tendencies are mainly below the PBLH. The temperature tendency is also very messy and appears to be inverse to the moisture tendency with large negative (exceeding $-2*10^{-2}$ K/h) and positive (exceeding $2*10^{-2}$ K/h) tendencies in the temperature. The moisture tendency in the ocean non-rotating cell composite is positive near the surface and above the boundary layer, and is about $0.7*10^{-5}$ $kg/kg/h$. Directly surrounding the PBLH, the moisture tendency is negative around $-1*10^{-5}$ $kg/kg/h$. In the ocean non-rotating composite there are positive temperature tendencies below 2.5 km at approximately $1*10^{-2}$ K/h to $2*10^{-2}$ K/h. Above 2.5 km, the temperature tendency is mainly negative at about $-0.7*10^{-2}$ K/h. Around 5 km in height, there is a strip of positive (negative) moisture (temperature) tendency, indicative of the tropical cyclone melting level. In the land non-rotating cell composite (Fig. 4.23a), the wind tendencies are negative, and are largest in the boundary layer (below 1000 m), around -0.15 $m/s/h$. Above the PBL the composite shows both positive and negative areas of wind tendencies ranging from -0.10 to 0.10 $m/s/h$. In the ocean non-rotating cell composite, the wind tendency is about -0.05 $m/s/h$ within the boundary layer (below 1000 m). Around 1000 m in height, the ocean composite shows weak negative wind tendencies around -0.01 $m/s/h$.

Figure 4.23b shows tendencies are again generally larger in the rotating cell composites of the Irma ACM2 simulation and larger compared to the YSU and MYNN3 simulations. The moisture tendency in the land rotating cell composite is negative in the boundary layer around $-2.2*10^{-5}$ $kg/kg/h$; however, around the PBLH, the moisture tendency is positive around $2*10^{-5}$ $kg/kg/h$. The opposite is generally seen in the temperature tendency. There are many areas of large positive (around $2*10^{-2}$ K/h) and negative (around $-2*10^{-2}$ K/h) temperature tendencies. The moisture tendency in the ocean rotating cell composite is negative near the surface about $-0.7*10^{-5}$ $kg/kg/h$. Directly above the top of the boundary layer, the moisture tendency is generally positive around $0.7*10^{-5}$ $kg/kg/h$. At around 5 km in height, there is a strip of positive (negative) moisture (temperature) tendency, indicative of the tropical cyclone melting level. In the ocean rotating cell composite, there are positive temperature tendencies within the boundary layer about $2*10^{-2}$ K/h. At around 5 km in height, there is a secondary maximum (minimum) in the moisture (temperature) tendency in both the land and oceanic rotating cell composites, indicative again of the melting layer. In the land rotating cell composite (Fig. 4.23b), the wind tendencies are negative and are largest in the boundary layer (below 1000 m), exceeding -0.20 $m/s/h$. Like in the non-rotating cell ACM2 land composite, above the PBL the rotating cell ACM2 land composite shows both positive and negative areas of wind tendencies ranging from -0.10 to 0.10 $m/s/h$. In the ocean rotating cell composite, the wind tendency is negative within the boundary layer (below 500 m) around -0.10 $m/s/h$. Above the boundary layer, the wind mixing is negative from 500 to about 2500 m around -0.05 $m/s/h$. Unlike the YSU and MYNN3 cell composites, the wind tendency is positive and extends above the top of the boundary layer in the ACM2 simulation.

The largest differences in the tendencies of moisture, heat, and wind appeared between the land and ocean cell composites. This result is expected since over the ocean surface friction is weaker than over land and, thus, tends to slow the winds less. The locations of the maxima in the positive and negative tendencies are closely tied to the height of the boundary layer across all of the composites, as well as the areas of the phase change in water vapor (melting level). Unsurprisingly, the moisture tendency in the ocean composites near the surface is higher than that over land by about $0.7*10^{-5}$ $kg/kg/h$. The ACM2 simulations produce the largest areal extent of large tendencies in moisture, heat, and wind, compared to the YSU and MYNN3 simulations. This stronger and deeper vertical mixing in the ACM2 simulation was noted in Figure 4.15, as well as the strong vertical mixing in the low levels of the MYNN3 simulation. Stronger and deeper vertical mixing results in weaker low-level vertical wind shear, as it acts to homogenize the low-level winds. The simulations of Harvey and Irma all show that the wind tendencies in the boundary layer are lower in value and more shallow over the ocean compared to over the land across all the simulations. In all the simulations, the 0–3-km vertical wind shear is larger over the land compared to over the ocean as identified in the elongation of the hodograph in Figures 3.25 and 3.26, due to surface friction.

The YSU simulations of both hurricanes Harvey and Irma (Figs. 4.18 and 4.21) show that the land composites have the strongest moisture tendency directly surrounding the PBLH, with negative moisture tendencies near the surface, while the ocean composite has the largest moisture tendency below the PBLH. In the YSU simulations, the temperature tendency shows the opposite sign to the moisture tendency, signifying that in areas of increasing moisture there is a decrease in temperature, and vice versa. At around 5 km in both simulations there is a negative temperature tendency and positive moisture tendency indicative of the cooling resulting at the melting layer. The YSU land cells show a similar pattern of negative temperature tendencies and positive moisture tendencies around the height of the PBL, indicative of evaporation, which also cools the atmosphere and to a greater extent than melting.

The MYNN3 simulations of both hurricanes Harvey and Irma (Figs. 4.19 and 4.22) show that the moisture tendency in the ocean composites is negative directly surrounding the PBLH, and positive at the surface and above the PBLH. The land composites in the MYNN3 simulations show negative moisture tendencies in the boundary layer and positive moisture tendencies above the PBLH. The temperature tendency is strongly positive in the boundary layer in all the MYNN3 simulations, with negative temperature tendencies above the PBLH. The MYNN3 simulations did not show the pattern in moisture and temperature at 5 km indicative of the melting level as in the YSU simulations. The wind tendencies in the land cell composites are typically larger than the ocean cell composites in both the Harvey and Irma simulations. In the MYNN3 simulations, the wind tendencies are negative within the boundary layer, do not extend beyond the top of the PBL, and tend to be weaker in the ocean cell composites compared to the YSU or ACM2 simulations. Negative wind tendencies in the low levels act to reduce the low-level vertical wind shear by slowing the radial inflow (Figs. 4.19 and 4.22). The large negative wind tendencies in the boundary layer are caused by the strong vertical mixing seen in the eddy diffusivity (Fig. 4.15). The strong low-level mixing and resulting large negative wind tendencies act to decrease the 0–3-km vertical wind shear by mixing the slowing effect of surface friction in the PBL. The MYNN3 simulations in Harvey and Irma showed the smallest 0–3-km vertical wind shear (Figs. 3.25 and 3.26). The smaller 0–3-km vertical shear results in smaller 0–3-km updraft helicity which impacts the identification of rotating cells since it also decreases the threshold required to exceed the 99.95^{th} percentile; thus, more rotating cells would be expected to be identified. Figures 3.3 and 3.7 showed that the MYNN3 simulations identified more rotating cells compared to the YSU and ACM2 PBL schemes.

The ACM2 simulations of both hurricanes Harvey and Irma (Figs. 4.20 and 4.23) show that above 2 km the moisture tendency is positive and the temperature tendency is negative. There are some differences between the two storms with the tendencies near and in the boundary layer. In the Harvey ACM2 simulation, the moisture tendency is positive below the PBLH and negative above the PBLH to about 2 km. Also in Harvey, the temperature tendency in the ACM2 simulation is strongly positive between the top of the boundary layer and 2 km, and weakly negative in the boundary layer; however, the surface shows positive temperature tendencies. In the Irma ACM2 simulation, the ocean composites show a negative moisture tendency below the PBLH and a positive moisture tendency above the PBLH. The temperature tendency in the ACM2 simulation of Irma is generally positive in the boundary layer. The mixing is much stronger in the ACM2 simulations (Fig. 4.15), leading to more moisture being mixed out of the boundary layer. Again, at around 5 km in both ACM2 simulations, there is a negative temperature tendency and positive moisture tendency indicative of the cooling resulting at the melting layer, as in the YSU simulations. These patterns in water vapor and temperature tendencies in the ACM2 cell composites are indicative of the increase in the low-level gradients of virtual temperature that increase CAPE described in Zhang et al. (2017).

The water vapor tendency over the lowest 500 m shows that over water there is increasing water vapor in all of the simulations, while over land there is decreasing water vapor (Figs. 4.24 and 4.25). In the simulations of Hurricane Harvey, the MYNN3 has the highest total water vapor tendency, with the ACM2 having generally lower water vapor tendency (Fig. 4.24). Similarly, in the simulations of Hurricane Irma, the total water vapor tendency in the YSU and MYNN3 schemes are very similar and positive over almost all times, while the ACM2 scheme shows negative total water vapor tendency over most of the times (Fig. 4.25). This difference is reflective of the distribution of RH seen in the CFAD in Figure 3.28 below 500 m. Strong and shallow mixing over the ocean near the surface in the MYNN3 simulations of both hurricanes Harvey and Irma (Fig. 4.15) drives positive tendencies in water vapor in the lowest 500 m, leading to higher values of RH in the low levels.

4.4 Summary and discussion

In PBL schemes that utilize a KPP approach, such as the YSU and ACM2, the CRN controls many aspects parameterized in the PBL, including but not limited to the depth of the PBL, as well as the magnitude and depth of the eddy mixing vertical profile (Bu et al. 2017). Kepert (2012) showed that all other factors being equal, smaller CRN lowers the PBLH and reduces the eddy diffusivity (vertical mixing) throughout the PBL. Gopalakrishnan et al. (2013) showed that eddy mixing strongly impacts the depth of tropical cyclone inflow levels, intensity, and structure. Excessively deep vertical mixing has also been shown to dry the lower PBL and reduce hurricane intensity (Braun and Tao 2000). Overall, previous studies have found that the vertical mixing is significant for hurricane structure and evolution (Braun and Tao 2000; Gopalakrishnan et al. 2013; Zhang et al. 2015, 2017; Gopalakrishnan et al. 2021), as it can affect the tropical cyclone environment. Gopalakrishnan et al. (2021) showed that in the next-generation, FV3-based, Hurricane Analysis and Forecast System (HAFS) the uncertainty in variables used to define the eddy diffusivity leads to diverse model solutions in model forecasts and that two diverse PBL schemes can create converging forecast results when eddy diffusivity or mixing length when adjusted based on observations. The findings of Gopalakrishnan et al. (2021) highlight the importance of the eddy diffusivity in PBL schemes in hurricane forecasts even in next-generation model frameworks.

In this chapter, the striking differences in model PBLHs (Figs. 4.4 and 4.5) between the KPP PBL schemes (YSU and ACM2) and the TKE scheme (MYNN3) seen over land in both the simulations of hurricanes Harvey and Irma were investigated. It was found that the key mechanism which resulted in the large difference seen between the schemes over land and over the ocean was tied to the use of a CRN to calculate the PBLH. The stable boundary layer revision (Hong 2010) is applied to the YSU scheme when the model surface virtual potential temperature is cooler than the first model level virtual potential temperature, which was the case in the simulations of hurricanes Harvey and Irma (Figs. 4.6, 4.7, and 4.8). In the unstable boundary layer, the CRN is set to a fixed value of zero in the YSU scheme and 0.25 in the ACM2 scheme, whereas in the stable boundary layer, the CRN in the YSU scheme over land is set to 0.25 (Hong 2010). Since the CRN for the stable boundary layer over land is the same in both the YSU and ACM2 schemes, it is not surprising that the PBLHs are very similar (Figs. 4.4 and 4.5). The differences seen in the PBLHs over land between the YSU and ACM2 schemes can be attributed to the entrainment term in the YSU PBL scheme, which acts to modify the PBLH over time, that is not present in the ACM2 PBL scheme. Over the ocean, the ACM2 scheme had the deepest PBLH due to the CRN being 0.25, compared to the CRN of zero for the YSU scheme. The ACM2 PBL scheme alters the mixing from pure local mixing for stable conditions to pure non-local mixing for unstable conditions. The differences in the CRN between the land and ocean in the YSU simulations drives a discontinuity in the PBL height seen in the coastal cross sections (Figs. 4.11 and 4.12). The ACM2 simulation also showed a similar discontinuity in the PBL height at the coastline. The discontinuity is driven by stability differences between the land and ocean that cause changes to the CRN in the YSU scheme and changes to the degree of local versus non-local mixing in the ACM2 scheme. Similar discontinuities are not seen over homogeneous surfaces (i.e., purely land or ocean surfaces) or in the MYNN3 simulations. The discontinuities are only present across the coastline.

Kepert (2012) noted that although non-local, KPP closure, PBL schemes can perform satisfactorily in some situations (Nolan et al. 2009a,b), KPP schemes should be used with caution. The results of the simulations of hurricanes Harvey and Irma would suggest much of the same issuance of caution. The non-local PBL schemes which utilize KPP closure have diagnosed PBLHs that are very different over land compared to PBL schemes that use other methods, mainly because of the use of a CRN (stability) to determine the PBL depth. The PBL height is used as a prognostic variable within KPP schemes such that misrepresentations of the depth of the PBL can affect other mechanisms within the boundary layer, such as the vertical mixing, which then directly affects the environment. In TKE PBL schemes, the PBLH is a calculated variable that is not used for other aspects of the PBL scheme.

Zhang et al. (2011c) showed from dropsonde observations that different definitions of PBLH can result in substantially different results. The measure of the mixing depth is the most shallow PBLH presented in Zhang et al. (2011c), ranging from 200–400 m, increasing from the center to five times the RMW (Figs. 4.9b and 4.10b, bottom). In the simulations of hurricanes Harvey and Irma, the mixed layer depth (Figs. 4.9b and 4.10b) varied between 200–600 m and is also the most shallow measure of the PBLH. In Harvey, the mixed layer depth begins at around 200 m at the center of the storm and increases to around 600 m by the RMW, much like Zhang et al. (2011c); however, after three times the RMW, the mixed layer depth starts to decrease in height. In Irma, the mixed layer depth is not detected until between 1–1.5 times the RMW, since it is very warm in the eye, and it quickly increases to around 700 m before plateauing. As noted earlier, this result may be because the RMW is about twice as large in the Irma simulations compared to the Harvey simulations.

The deepest measure of the PBLH presented in Zhang et al. (2011c) is the inflow height, which ranges from 600–1200 m from the RMW to three times the RMW before decreasing slightly to around 1000 m at five times the RMW (Figs. 4.9c and 4.10c, bottom). The simulations of Hurricane Harvey showed that inflow depth (Fig. 4.9c) ranged from about 600–1000 m between the RMW and five times the RMW, which, like the mixed layer depth, is very similar to the observations of Zhang et al. (2011c). In the simulations of Hurricane Irma, the inflow depth (Fig. 4.10c) ranges from about 800 m at the RMW to over 2000 m at 2.5 times the RMW. Since the RMW in the Irma simulations is twice the RMW in Harvey, the inflow depth seen at large multiples of the RMW in the Irma simulations is most likely more indicative of environmental, and not tropical cyclone winds, since these azimuthal averages are beyond 300 km from the center at four times the RMW.

The height of the maximum wind is the second deepest measure of the PBLH from Zhang et al. (2011c), which ranges from 400–1400 m and increases from the composite center to five times the RMW (Figs. 4.9a and 4.10a, bottom). In simulations of Hurricane Harvey, the height of the maximum wind (Fig. 4.9a) increases from around 200 m at the center of the storm to around 1400 m at five times the RMW, which is again very similar to the observations from Zhang et al. (2011c). The simulations of Hurricane Irma show that the height of the maximum wind (Fig. 4.10a) ranges from 400–1400 m from the center to three times the RMW, which is a very similar range to Zhang et al. (2011c); however, beyond three times the RMW, the height of the maximum wind speed begins to decrease in height.

The CRN is not only responsible for the PBLH in KPP schemes, but is also responsible for the magnitude and depth of the eddy mixing (Bu et al. 2017). The ACM2 has the highest CRN over land and over the ocean in both simulations. Figure 4.14 showed that at 500 m in the ACM2 simulations there is more mixing at higher wind speeds (radii closer to the RMW), compared to observations (Zhang et al. 2011b; Tang et al. 2018a). At weaker wind speeds (farther radii from the RMW), the YSU scheme tended to have more mixing compared to observations (Zhang et al. 2011b; Tang et al. 2018a), and the other two PBL schemes. Overall, the MYNN3 simulations of both hurricanes Harvey and Irma showed the most analogous eddy diffusivity and 500 m wind speed relationship compared to observations (Fig. 4.14). The vertical profiles of eddy diffusivity (vertical mixing intensity) showed that the mixing over the ocean tends to be concentrated closer to the surface than over the land in all the simulations. The mixing in both the YSU and MYNN3 simulations tend to drop off to near zero above 1200–1600 m (Fig. 4.15). Over the ocean and land, the ACM2 simulations show a much deeper extent to the mixing since the eddy diffusivity does not drop off to near zero like the other two PBL schemes (Fig. 4.15). As mentioned in the Introduction, the ACM2 PBL scheme requires eddy diffusivity for all stability conditions within and above the PBL, and above the PBL the mixing is dependent on the wind shear (Pleim 2007b). In general, the ACM2 simulations produced the most eddy diffusivity of the three PBL schemes tested, showing that there is generally more mixing in the ACM2 (Fig. 4.15). The identified rotating cells in the ACM2 simulations had far more eddy diffusivity than the YSU or MYNN3 simulations (Fig. 4.17). Recall from the previous chapter that the ACM2 cell composites showed the strongest updrafts and the most CAPE (Figs. 3.40, 3.41, 3.42, and 3.43). Zhang et al. (2017) showed in simulations of Dennis, Katrina, and Rita (2005) that during landfall, strong vertical mixing resulted in increased simulated CAPE. The results of Zhang et al. (2017) are supported by the increased mixing and the tendencies seen in the ACM2 simulations (Figs. 4.15, 4.20, and 4.23) and the increased CAPE in the boundary layer seen in the identified rotating and non-rotating cell composites (Figs. 3.40, 3.41, 3.42, and 3.43).

The eddy diffusivity shows the magnitude of the vertical mixing, while the individual tendencies show if the vertical mixing results in more or less moisture, heat, or momentum. As seen in the eddy diffusivity of the identified rotating cells (Fig. 4.17), the ACM2 simulations showed more vertical mixing from the PBL top to 6 km than the YSU or MYNN3 simulations. Figures 4.20 and 4.23 showed that this increase in vertical mixing leads to larger magnitudes in the tendencies of moisture, temperature, and wind at higher heights. The MYNN3 simulations showed that the tendencies of moisture, temperature, and wind

(Figs. 4.19 and 4.22) were all confined to below 2–3 km, which coincides well to just above the height at which the eddy diffusivity (vertical mixing) goes to zero in Figure 4.15. In Hill and Lackmann (2009), an idealized tropical cyclone simulation showed that the MYNN3 simulation water vapor mixing ratio tendency tended to be confided to the low levels typically below 2 km. The YSU simulation of Hill and Lackmann (2009) showed a much larger extent of the water vapor mixing ratio tendency extending from 1 km above the surface to 6 km in height, which has a maximum about 1–1.5 km above the ground and a secondary maximum around 4–5 km outside of 50 km from the center. The tendencies in water vapor in the YSU and MYNN3 schemes seen here is largely in agreement with the results seen in Hill and Lackmann (2009) (Figs. 4.18, 4.19 4.21, and 4.22). The ACM2 simulations showed much more variability in the tendencies than the YSU and MYNN3 simulations. Both the YSU simulations and the land MYNN3 simulations show that the moisture and temperature tendencies are inverse in the boundary layer, such that the areas that are getting more moist are also getting cooler, which would be indicative of evaporative cooling. At around 5 km in the YSU and ACM2 simulations, the melting level (Houze 2010) can clearly be seen as an increase in moisture and a decrease in temperature (Figs. 4.18, 4.20, 4.21, and 4.23).

This chapter has shown that the use of a CRN in the KPP schemes and the effects on eddy diffusivity (vertical mixing) are the main drivers of the differences seen between the PBL schemes seen in the previous chapters. The PBL heights differ over the land and ocean in the YSU scheme because a different CRN is used over the land (0.25), which meets the requirements for the stable boundary layer from Hong (2010) to calculate the PBL height. Over the ocean, the YSU scheme used a CRN of zero to calculate the PBL height. In the ACM2 scheme, a CRN of 0.25 is used over both land and ocean, which is why the PBL height is similar over both the land and ocean in the simulations using this PBL scheme and also explains why over land the YSU and ACM2 have similar PBLH (Figs. 4.4 and 4.5).

As mentioned in the previous chapter, the MYNN3 simulations produced less 0–3-km shear than the other PBL simulations (Figs. 3.25 and 3.26). Linked to this lower

0–3-km shear, the 0–3-km updraft helicity, which is used as a threshold for rotating cells (Tables 3.1 and 3.2) was lowest in the MYNN3 simulations of both Harvey and Irma. The MYNN3 simulations showed the shallowest and strongest vertical eddy mixing over the ocean (Fig. 4.15), confined just below the PBLH. This strong mixing leads to large negative wind tendencies in the boundary layer (Figs. 4.19 and 4.22). As noted previously, the strong low-level mixing and resulting large negative wind tendencies acts to decrease the 0–3-km vertical wind shear.

The previous chapter also showed that the ACM2 cell composites showed stronger vertical motions and more CAPE in the low-levels compared to the other PBL schemes. The increased CAPE in the PBL is the result of the increased vertical mixing seen in the ACM2 simulations (Fig. 4.15), which has been noted by Zhang et al. (2017) to increase CAPE in the boundary layer in simulations of land falling tropical cyclones.

The next chapter will focus on the verification of the YSU, MYNN3, and ACM2 simulations using both radiosonde and dropsonde observation in hurricanes Harvey and Irma. The goal will be to determine, despite the differences highlighted in the last two chapters, which PBL scheme produces the most realistic environment. The next chapter will also use a mobile Doppler radar positioned during the landfall of Hurricane Harvey. The goal will be to investigate the inflow depth of a landfalling tropical cyclone and determine what differences are generated by different PBL schemes, as we saw in this chapter that across the coastline the YSU and ACM2 simulations had discontinuities in the PBL height. The mobile Doppler radar will also be used to observe vertical cross sections of reflectivity of rotating and non-rotating cells in Harvey and compare those to the rotating and non-rotating cell composites from the previous chapter.

4.5 Figures

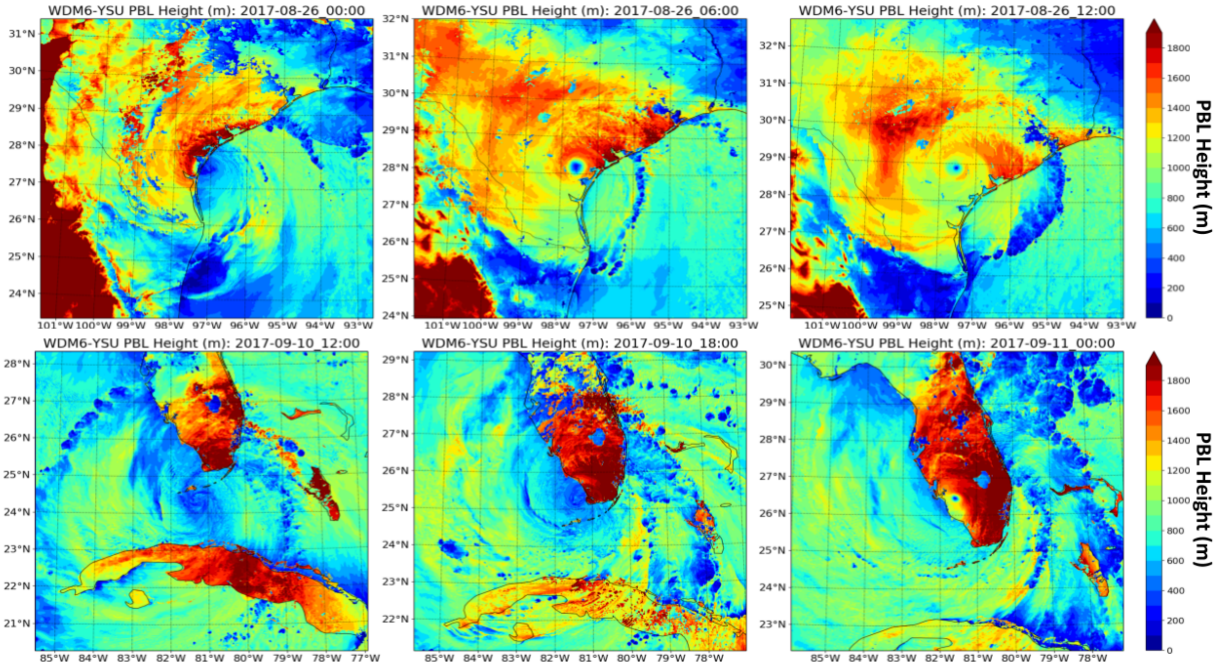

Figure 4.1: Planetary boundary layer (PBL) height (m, shaded) for the YSU simulations of Hurricane Harvey (top) and Hurricane Irma (bottom) every 6 h over the first 12 h of the simulation.

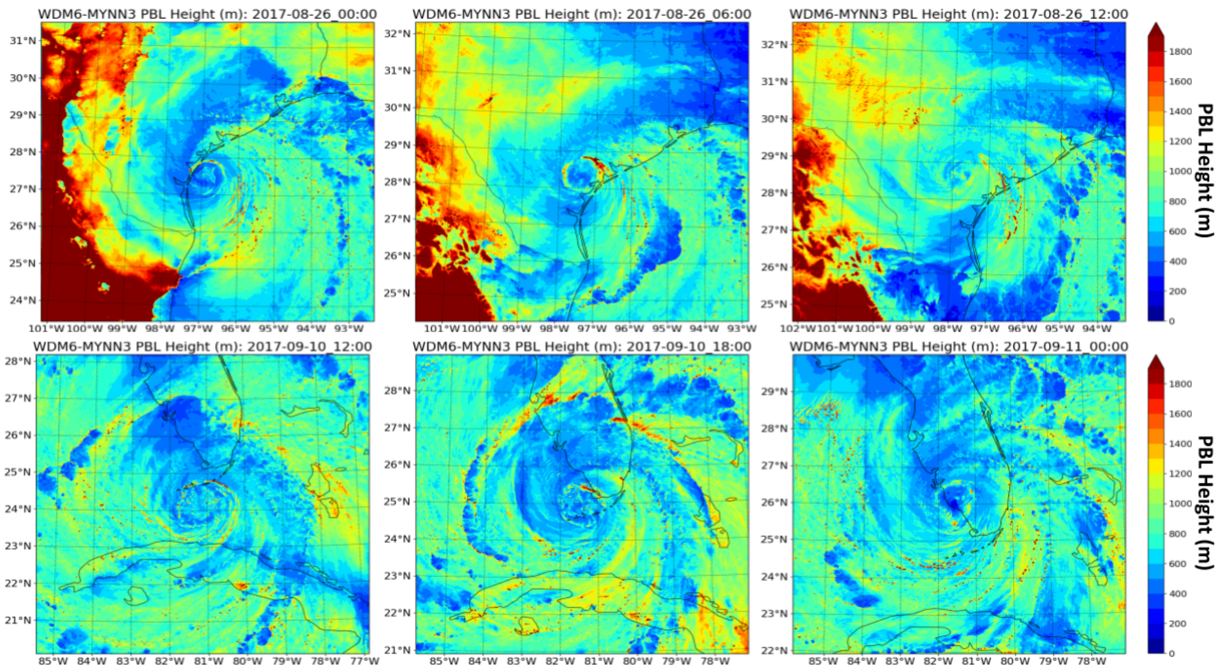

Figure 4.2: Same as Figure 4.1, but for the MYNN3 simulations.

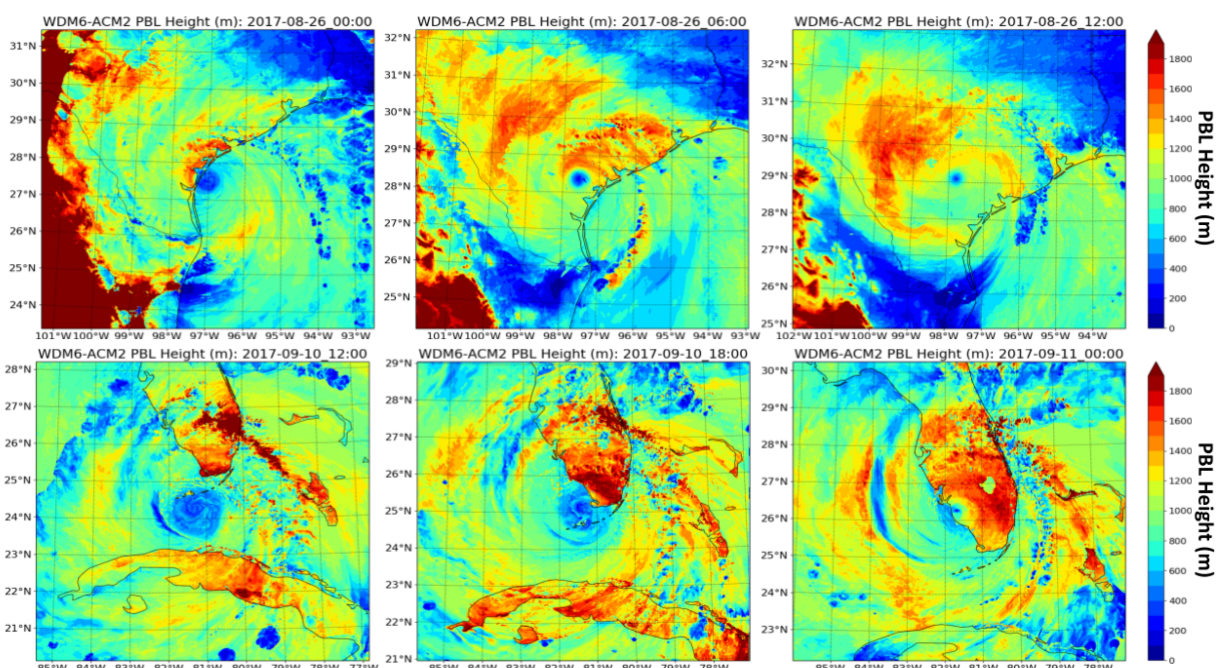

Figure 4.3: Same as Figure 4.1, but for the ACM2 simulations.

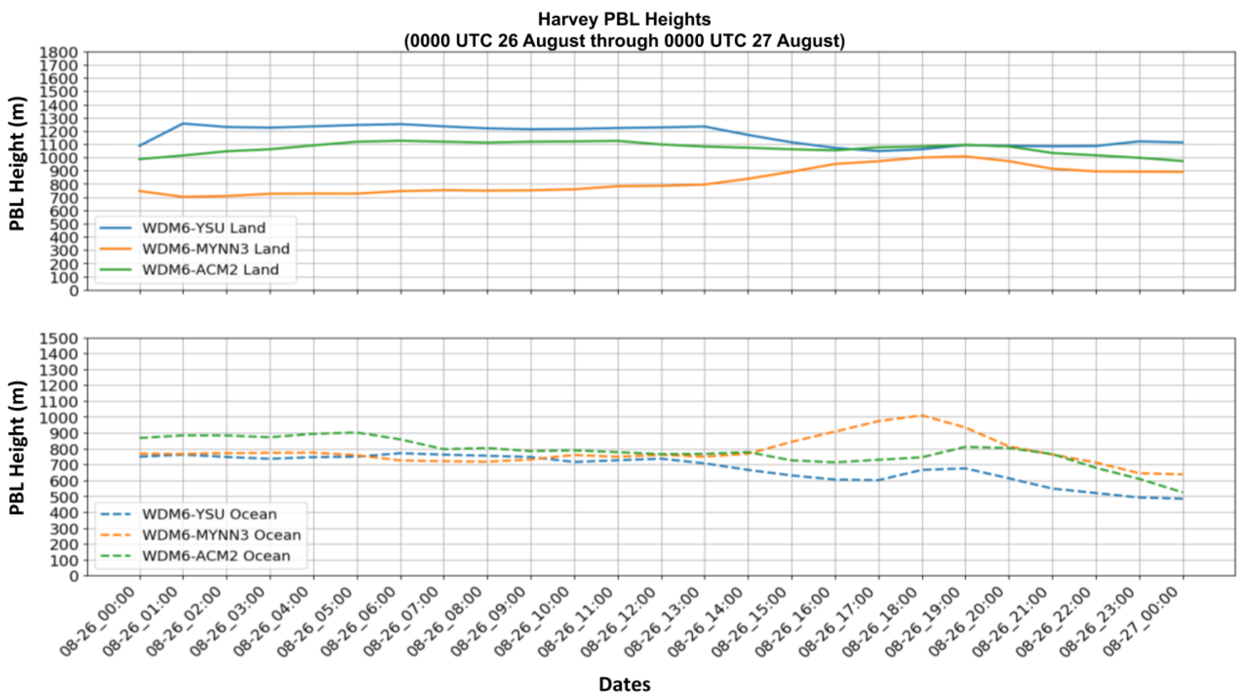

Figure 4.4: PBL height (m, lines) for the simulations of Hurricane Harvey from 0000 UTC 26 August through 0000 UTC 27 August over land (top, solid) and over the ocean (bottom, dashed).

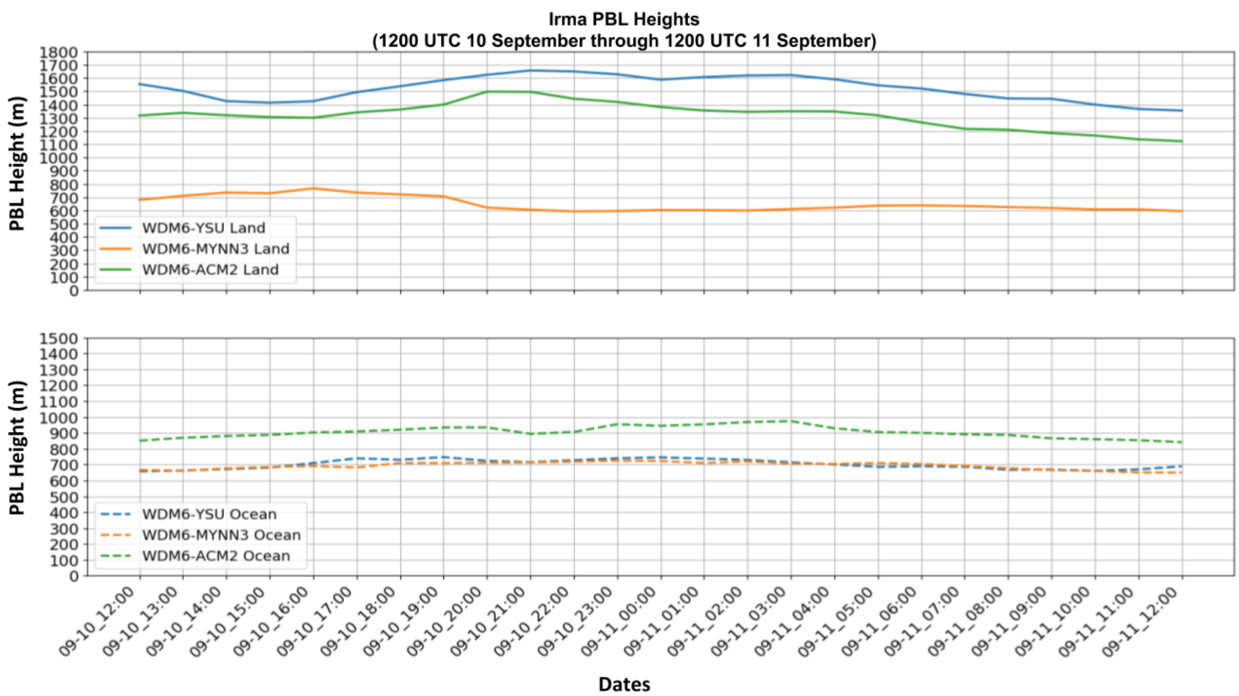

Figure 4.5: PBL height (m, lines) for the simulations of Hurricane Irma from 1200 UTC 10 September through 1200 UTC 11 September over land (top, solid) and over the ocean (bottom, dashed).

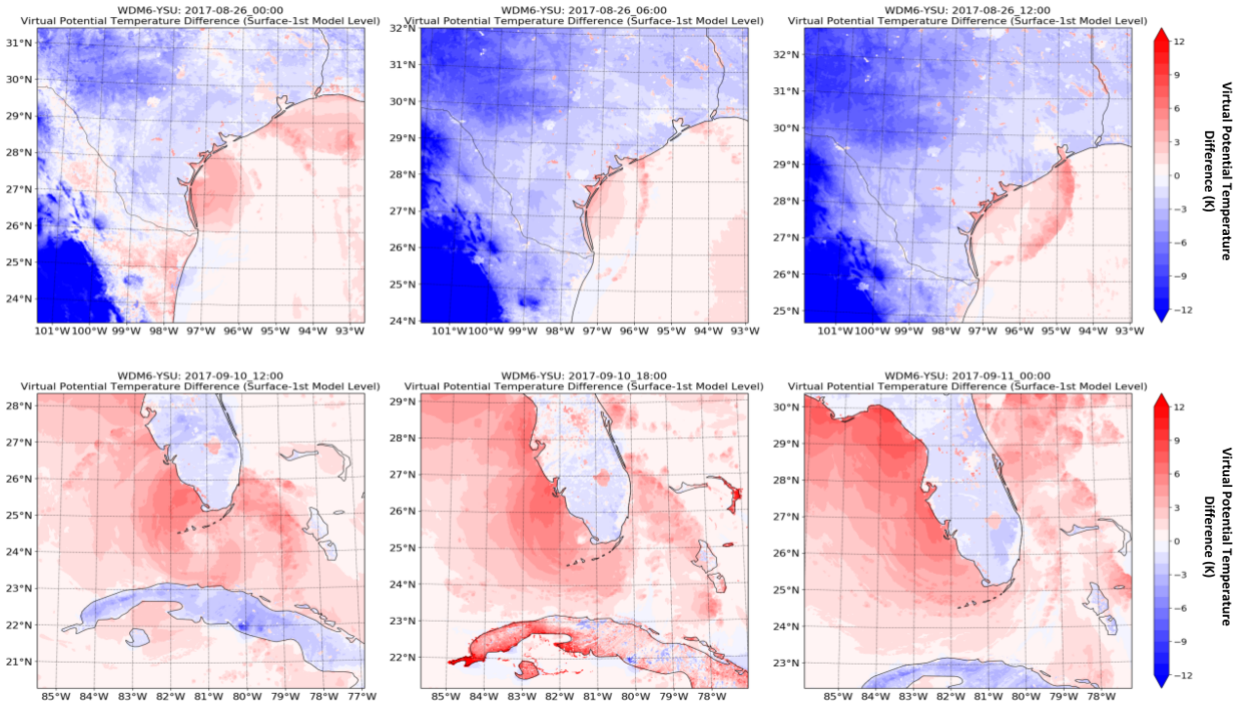

Figure 4.6: Difference between the virtual potential temperatures of the surface and the first model level (K, shaded) for the YSU simulations of Hurricane Harvey (top) and Hurricane Irma (bottom) every 6 h over the first 12 h of the simulation.

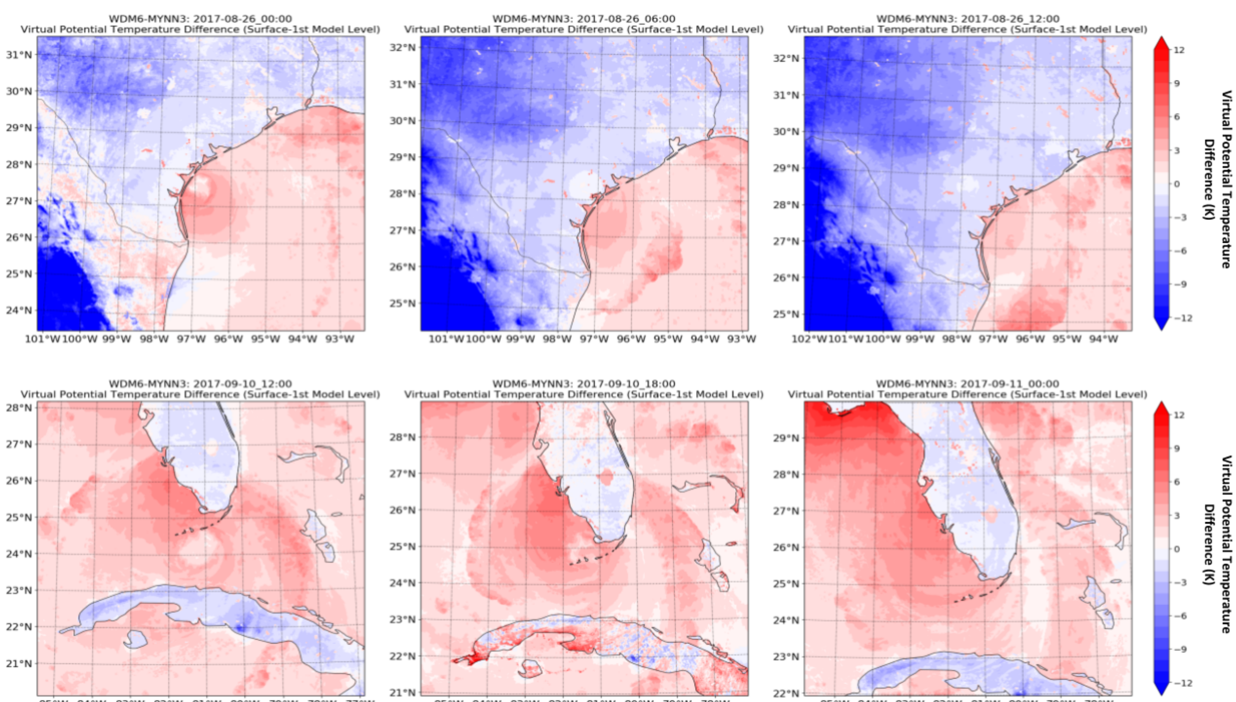

Figure 4.7: Same as Figure 4.6, but for the MYNN3 simulations.

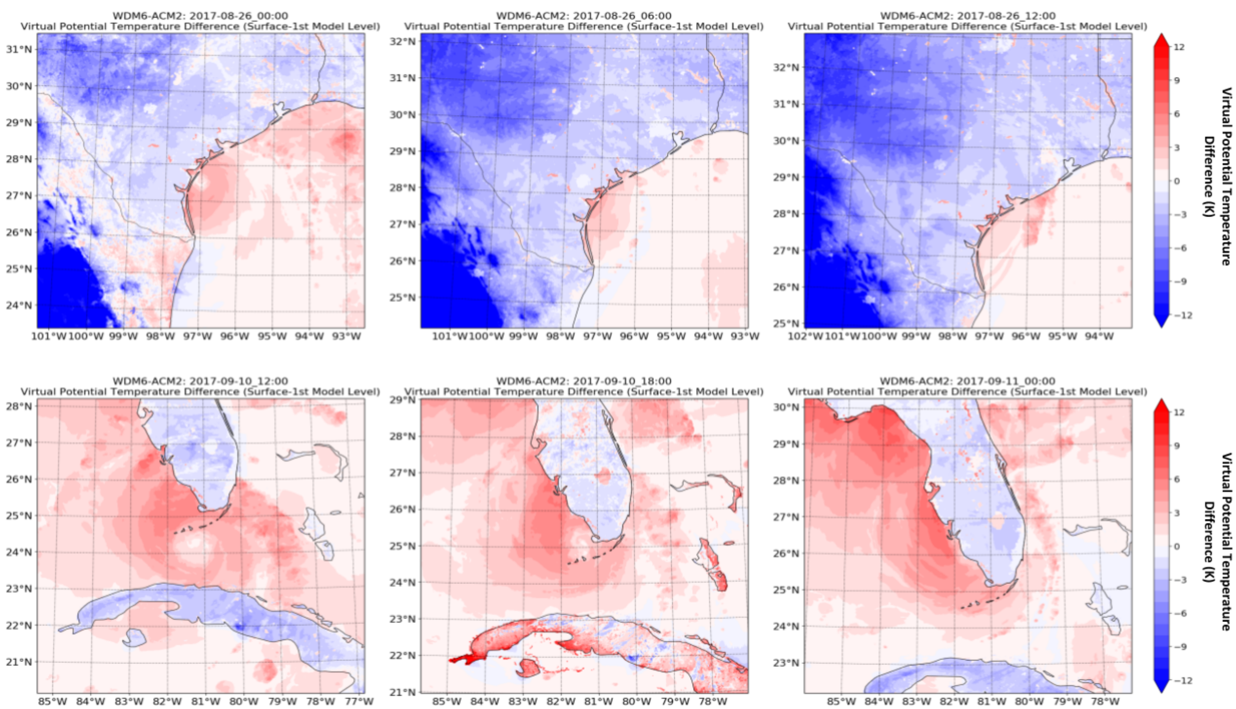

Figure 4.8: Same as Figure 4.6, but for the ACM2 simulations.

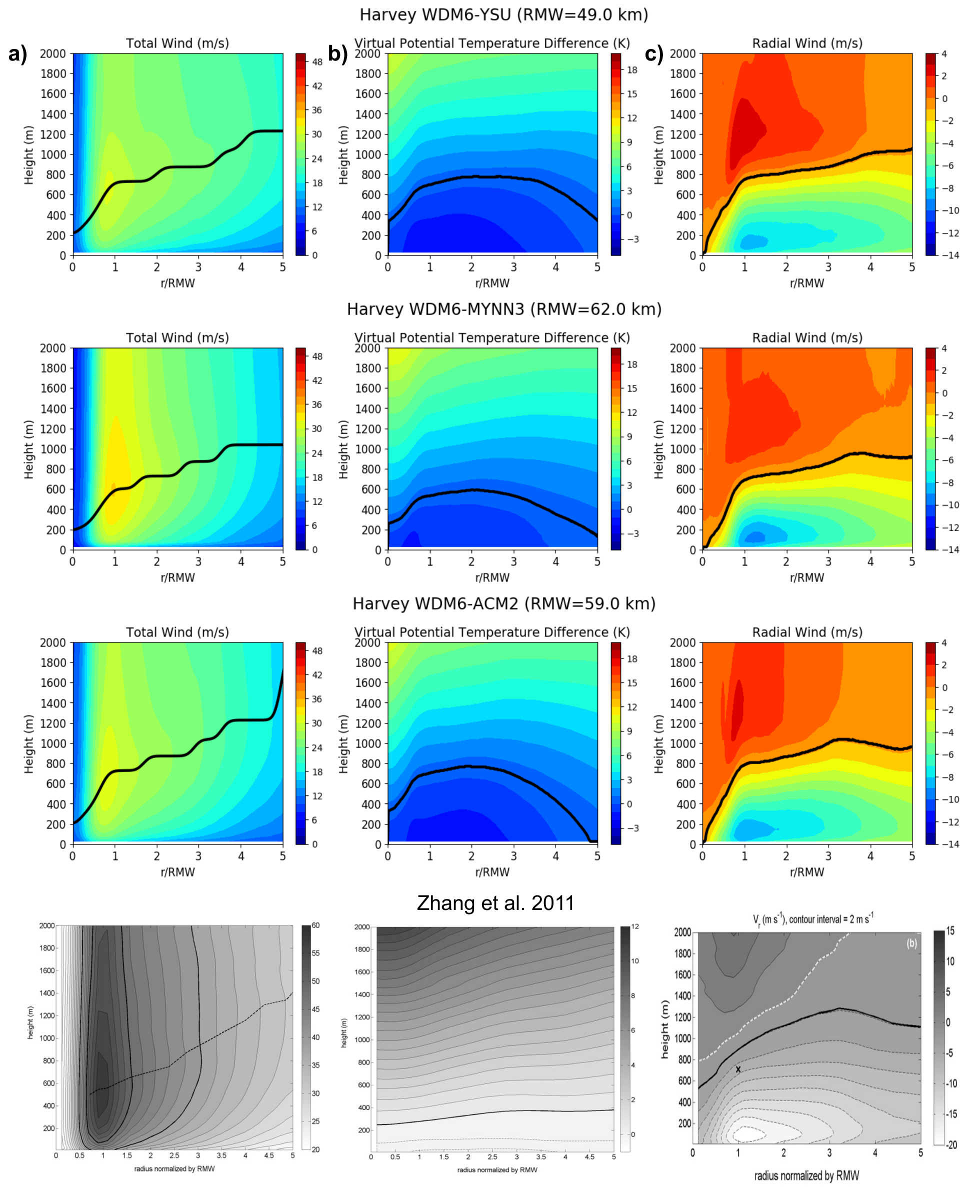

Figure 4.9: Composite analysis of a) total wind speed (m/s, shaded) showing the height of the maximum wind (line), b) virtual potential temperature difference between the virtual potential temperature and the mean virtual potential temperature in the lowest 150 m (K, shaded) with the height of the mixing level as defined by 0.5 K of this difference (line), and c) radial wind (m/s, shaded) and the height that is 10% of the radial inflow maximum (line) for the YSU (top), MYNN3 (middle), and ACM2 (bottom) simulations of Hurricane Harvey from 0000 UTC 26 August to 0000 UTC 27 August 2017. The bottom row shows composites of the dropsonde observations from Figures 4, 5, and 7 of Zhang et al. (2011c) ©2011 American Meteorological Society).

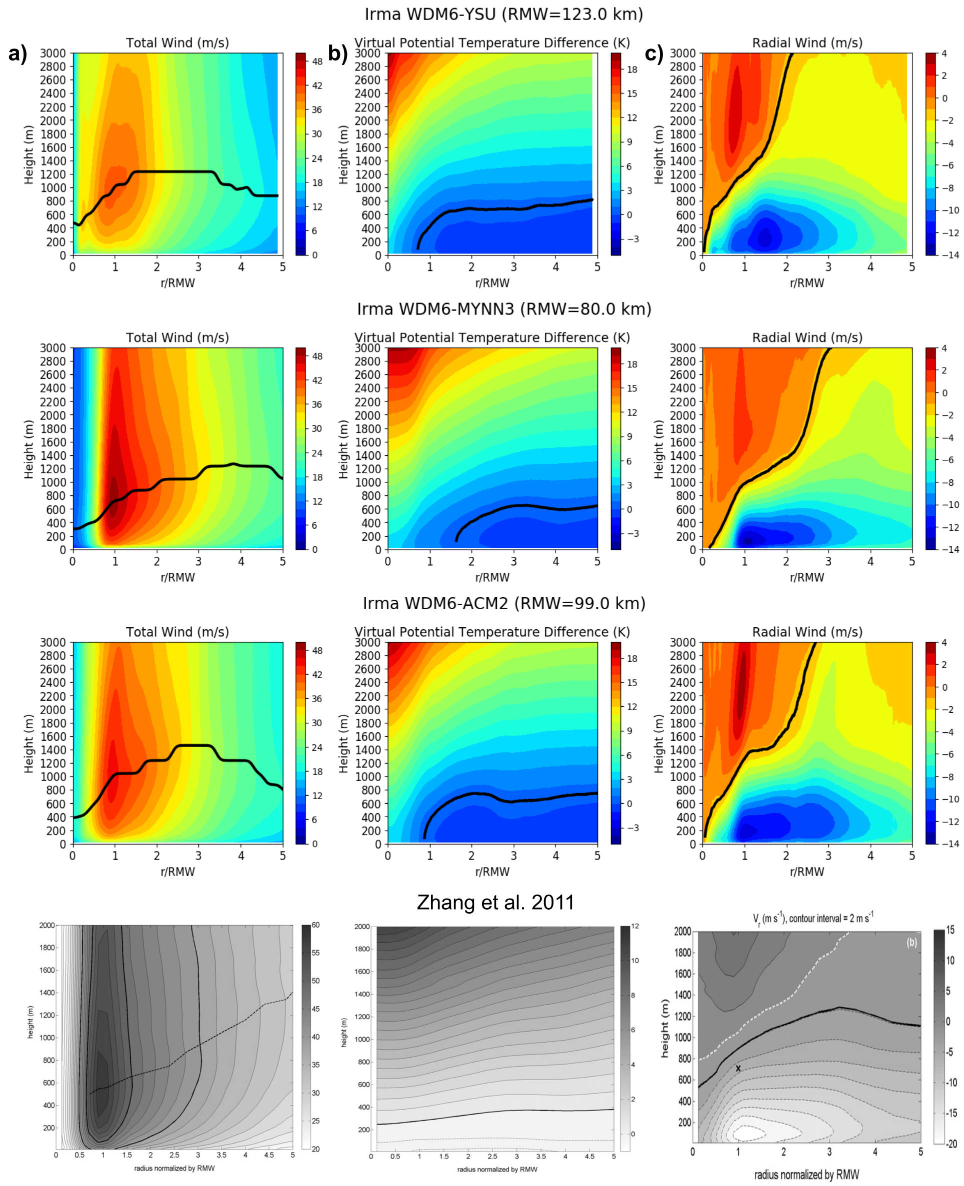

Figure 4.10: Same as Figure 4.9, but for the simulations of Hurricane Irma from 1200 UTC 10 September to 1200 UTC 11 September 2017.

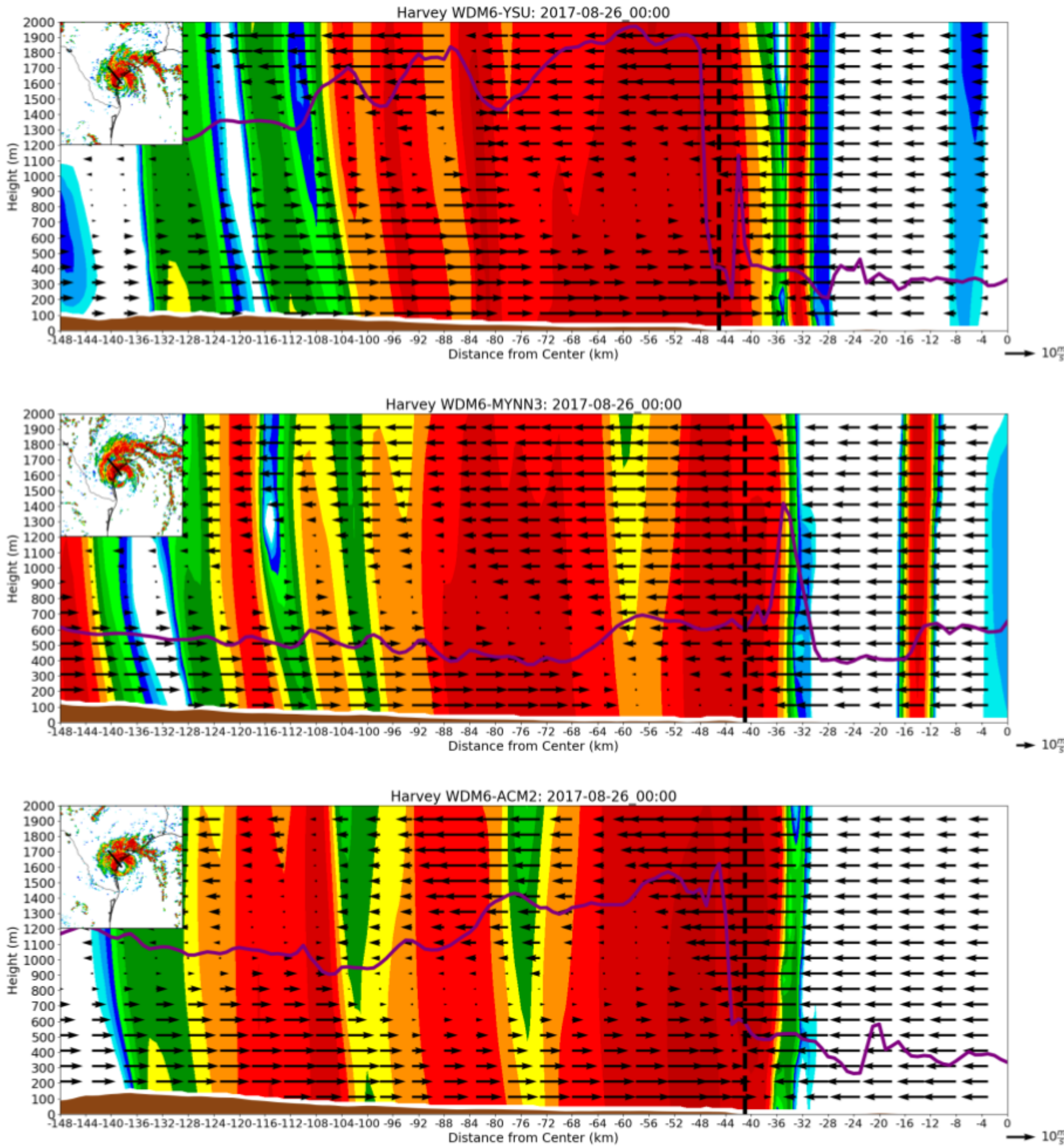

Figure 4.11: Model cross section of reflectivity (dBZ,shaded), radial wind (m/s, quiver), and model computed PBL height (m, purple line) across the coastline (denoted as the vertical dashed line) at 0000 UTC 26 August for Hurricane Harvey.

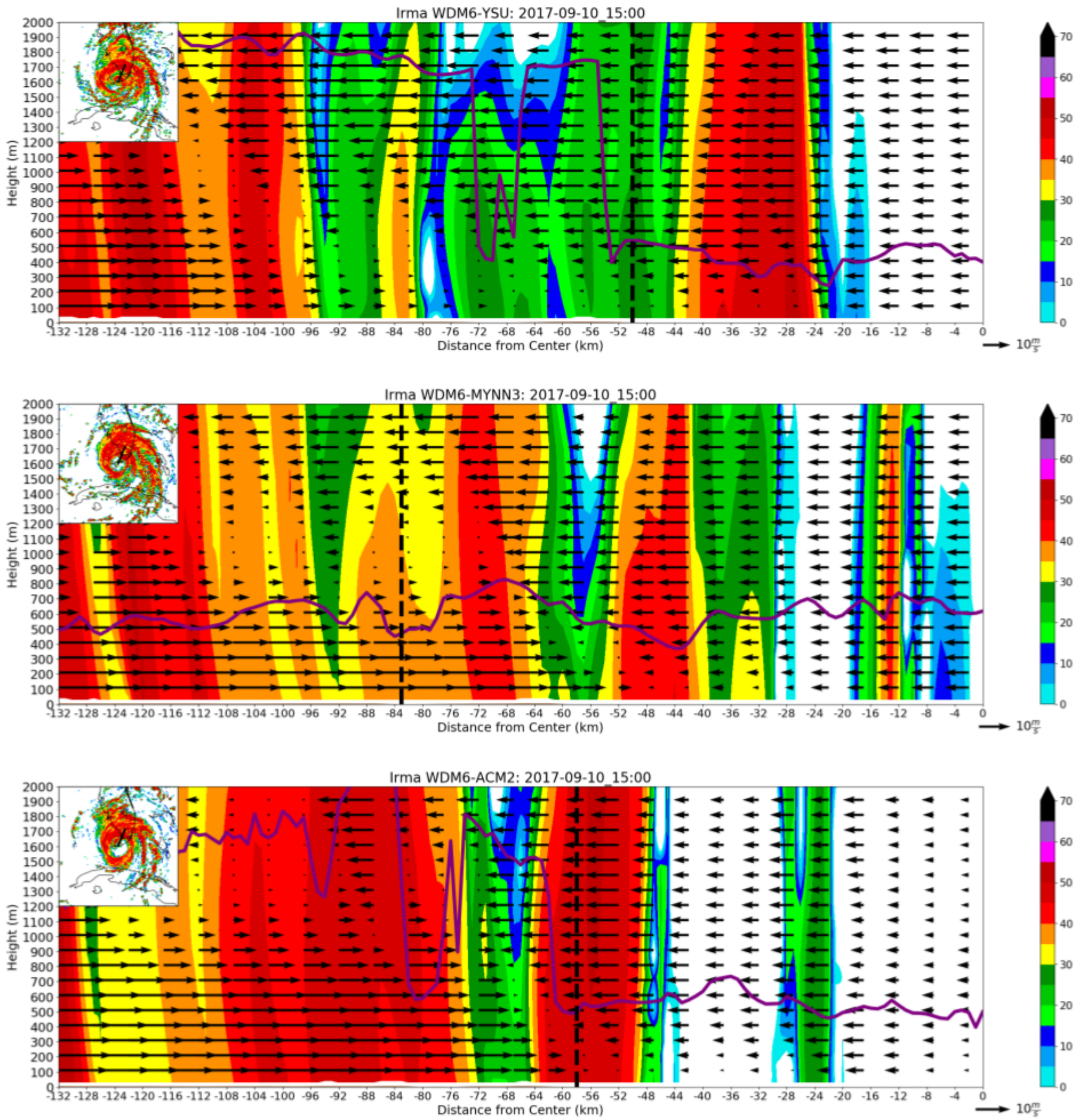

Figure 4.12: Same as Figure 4.11, but for the model simulations of Irma at 1500 UTC 10 September.

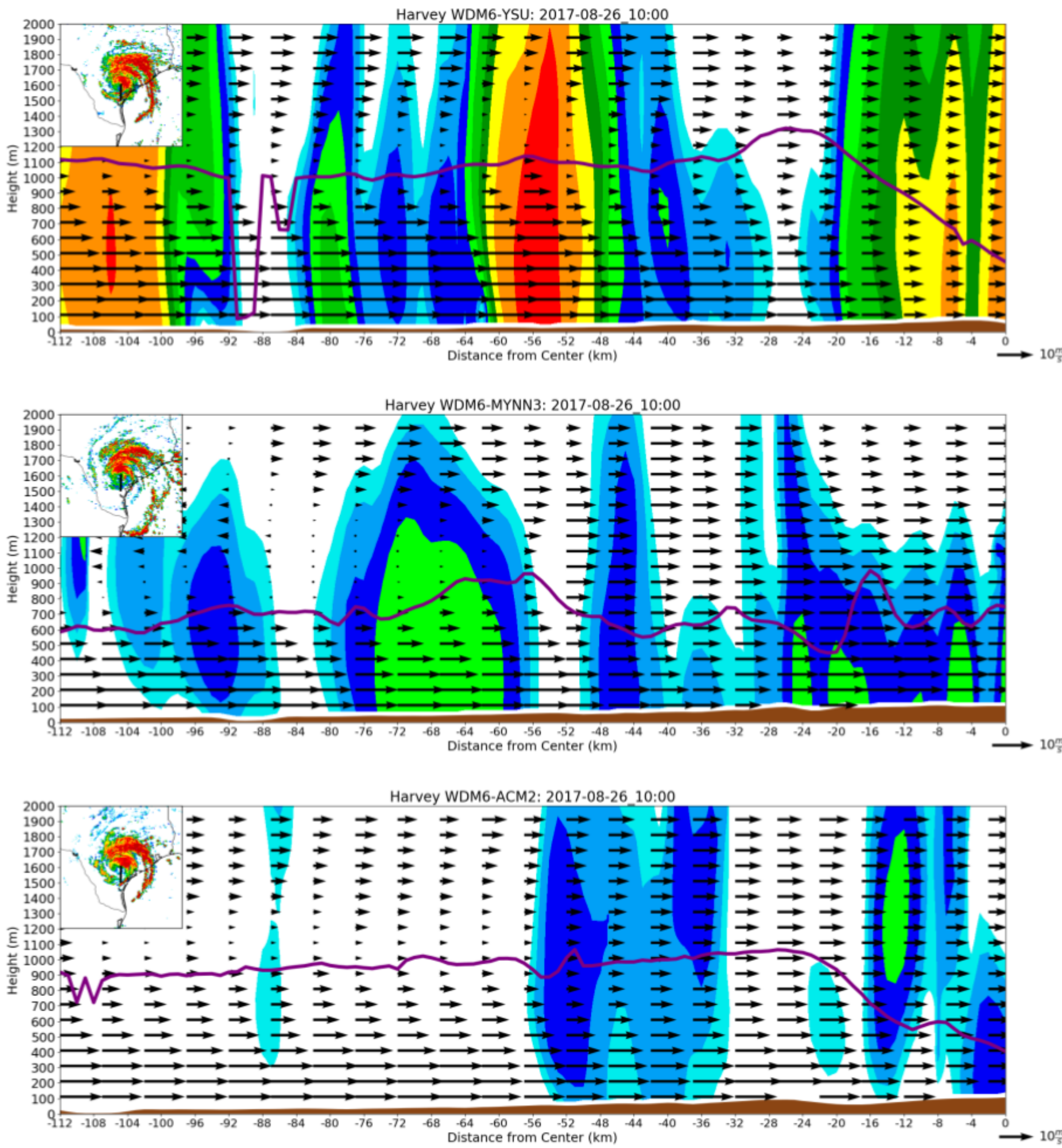

Figure 4.13: Model cross section of reflectivity (dBZ, shaded), radial wind (m/s, quiver), and model computed PBL height (m, purple line) over land at 1000 UTC 26 August for Hurricane Harvey.

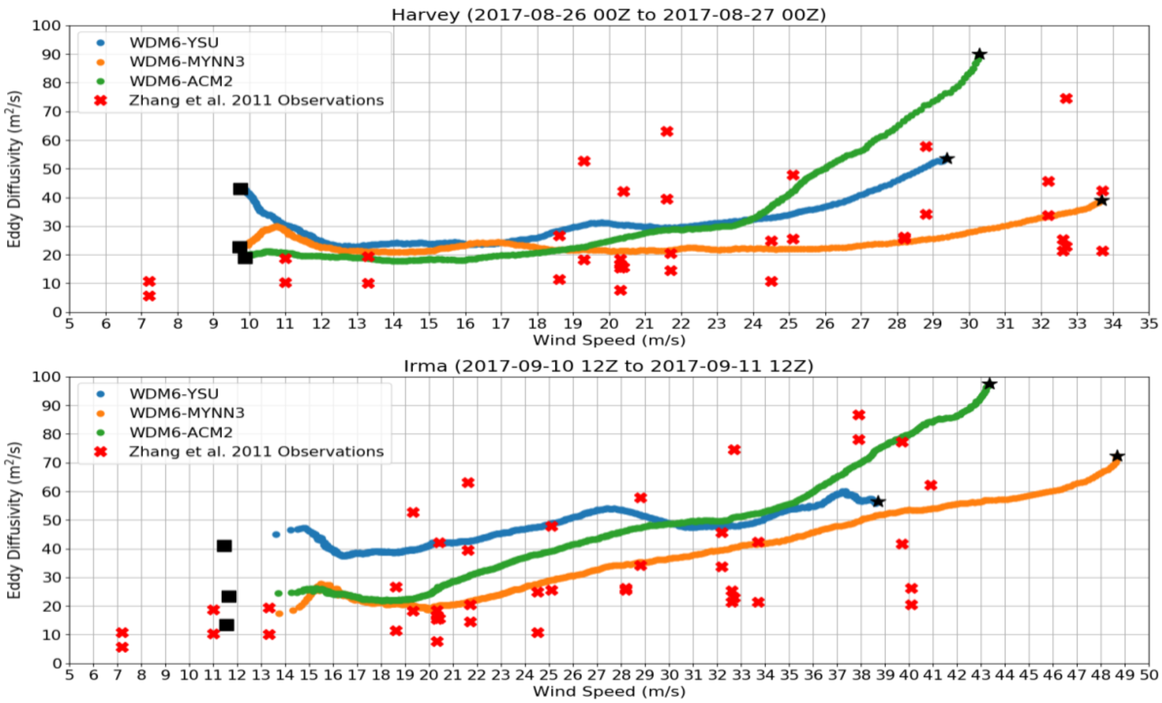

Figure 4.14: Temporally-averaged symmetric eddy diffusivity compared to the mean 500 m wind speed from the radius of maximum wind (stars) to the outermost radius (squares) for Hurricane Harvey from 0000 UTC 26 August to 0000 UTC 27 August (top) and Hurricane Irma from 1200 UTC 10 September to 1200 UTC 11 September (bottom). The observations (red x) from hurricanes Allen (1980), Hugo (1989), and Frances (2004) presented in Zhang et al. (2011b).

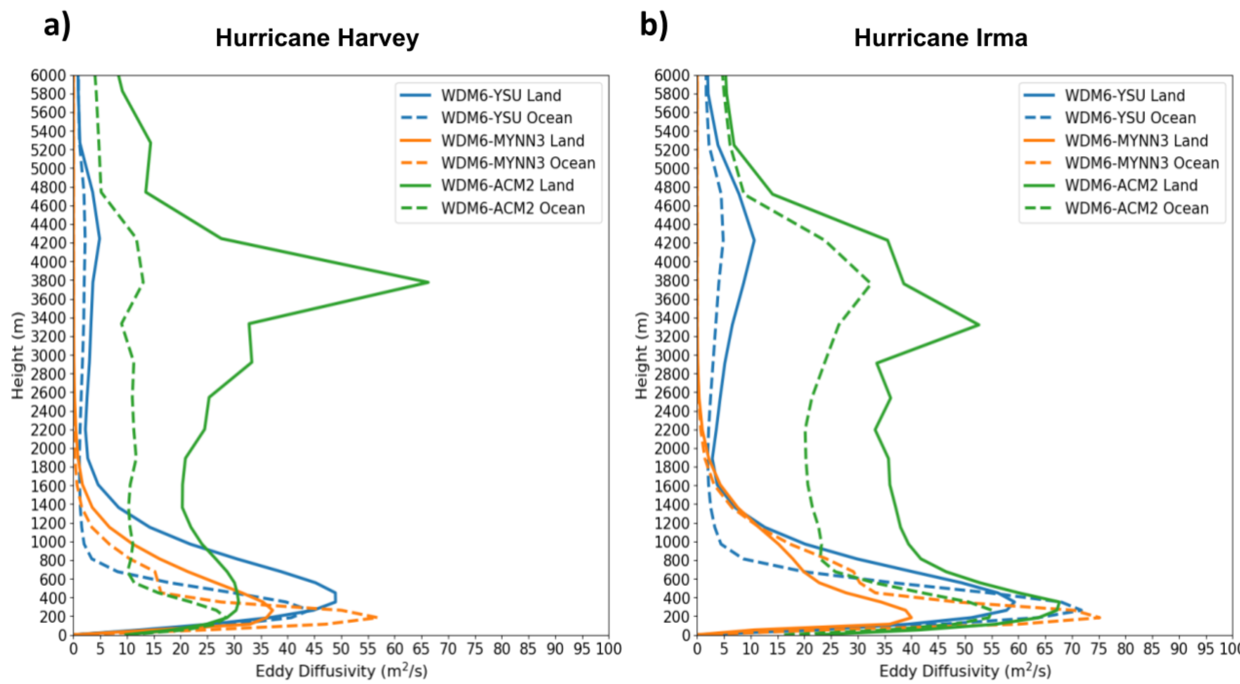

Figure 4.15: Temporally-averaged Eddy diffusivity by height comparing the land and ocean areas of Hurricane Harvey from 0000 UTC 26 August to 0000 UTC 27 August (a) and Hurricane Irma from 1200 UTC 10 September to 1200 UTC 11 September (b).

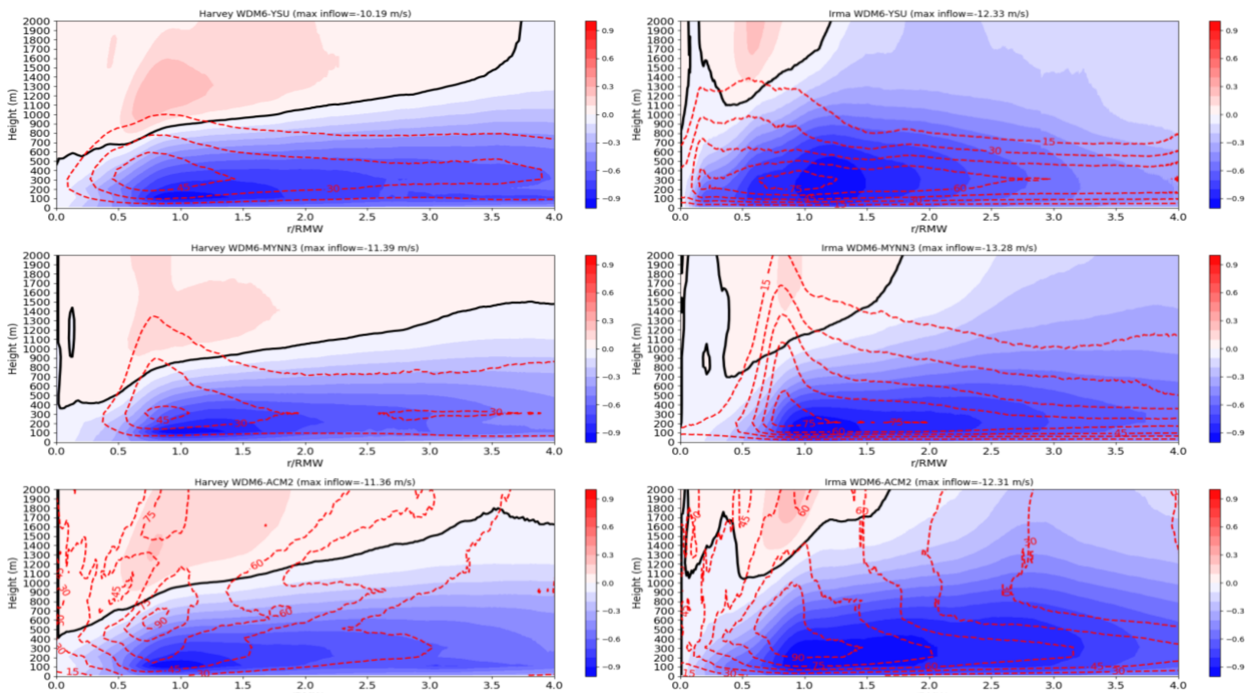

Figure 4.16: Azimuthally- and temporally-averaged radial inflow scaled by the maximum inflow (m/s, shaded) and eddy mixing (m^2/s, contoured) for Hurricane Harvey from 0000 UTC 26 August to 0000 UTC 27 August (left) and Hurricane Irma from 1200 UTC 10 September to 1200 UTC 11 September (right).

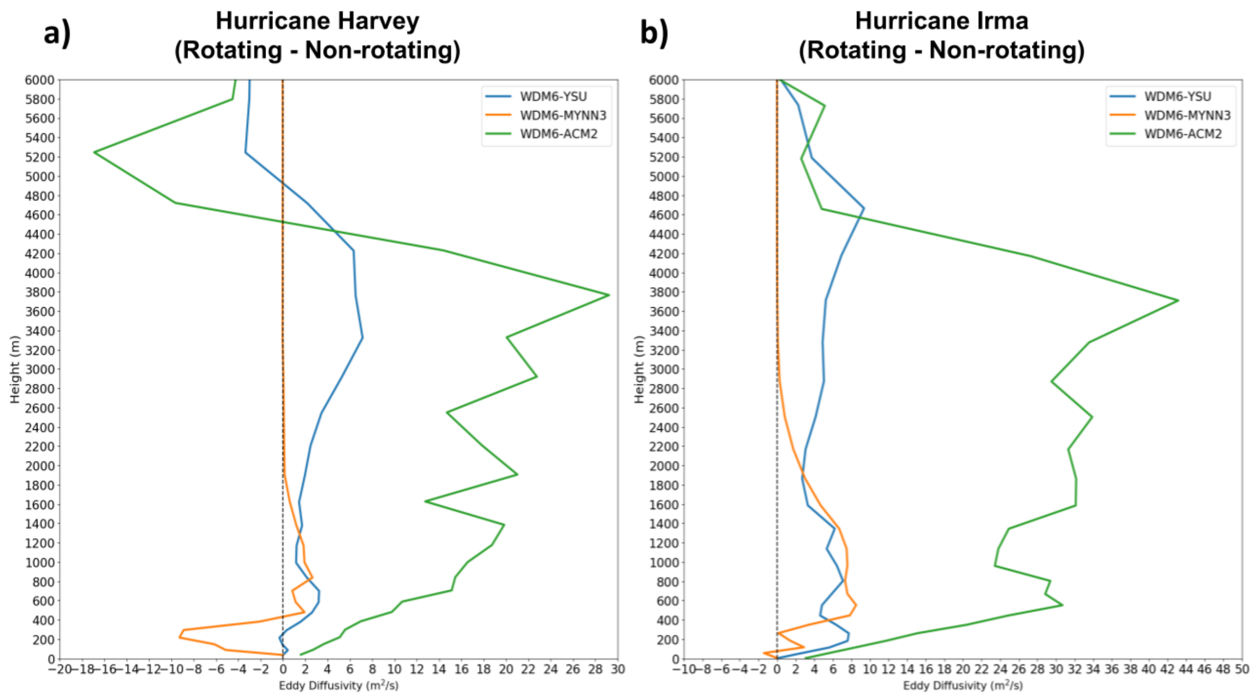

Figure 4.17: Difference in eddy diffusivity by height comparing the rotating and non-rotating cells of hurricanes Harvey (a) and Irma (b).

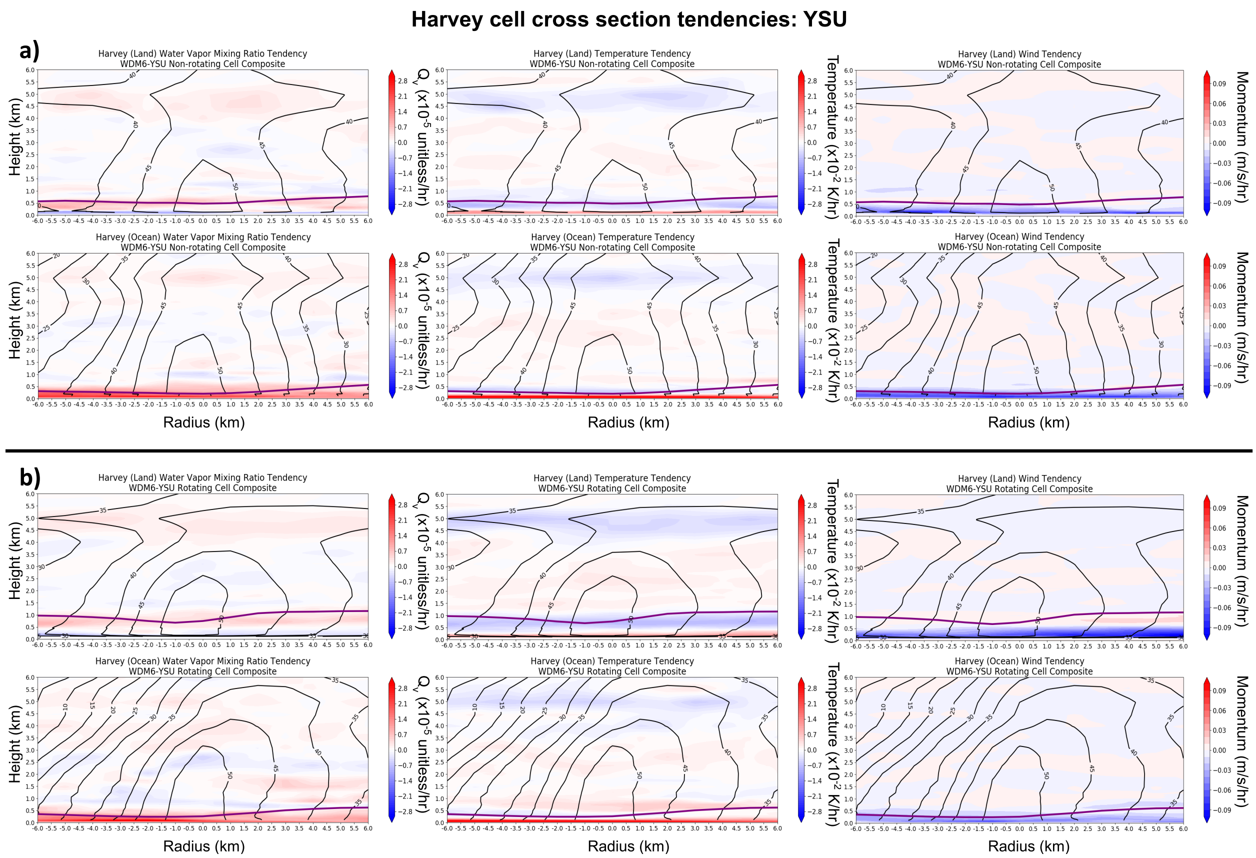

Figure 4.18: Composites of a) land non-rotating (top) and ocean non-rotating (bottom), and b) land rotating (top) and ocean rotating (bottom) identified cell water vapor mixing ratio (X$10^{-5} 1/h$), temperature(X$10^{-2} K/h$), and wind ($m/s/h$) tendencies (shaded), left to right, and composite model reflectivity from 0000 UTC 26 August to 0000 UTC 27 August in the Harvey YSU simulation with the PBLH (purple, line).

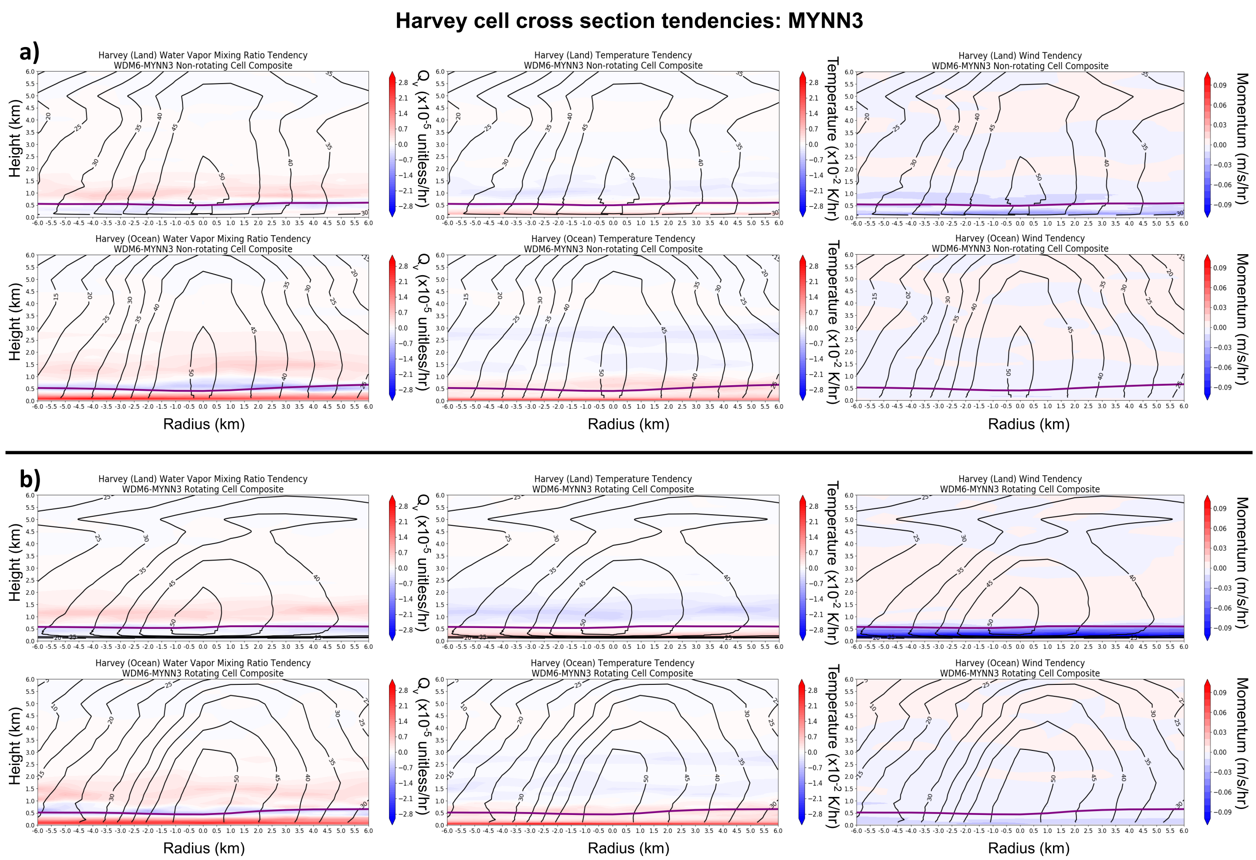

Figure 4.19: Same as Figure 4.18, but for the MYNN3 simulations.

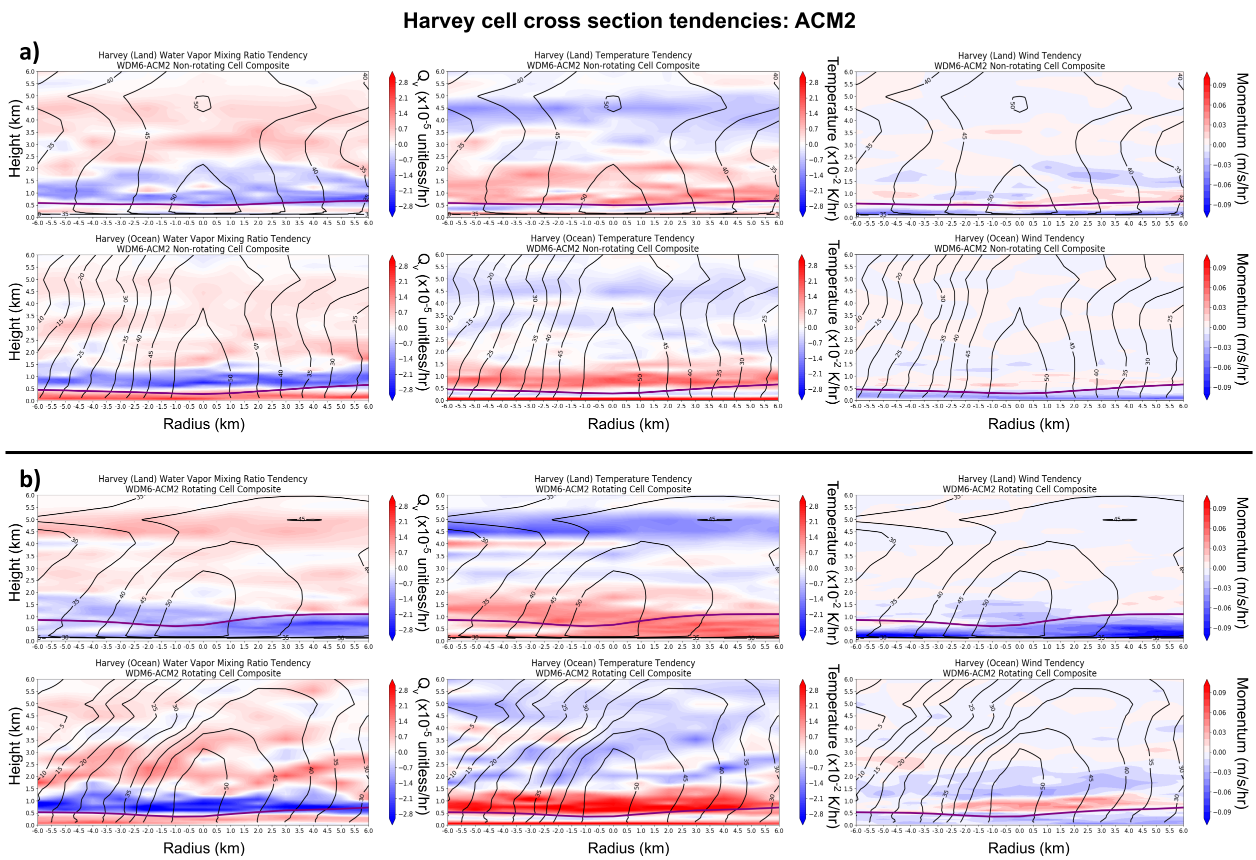

Figure 4.20: Same as Figure 4.18, but for the ACM2 simulations.

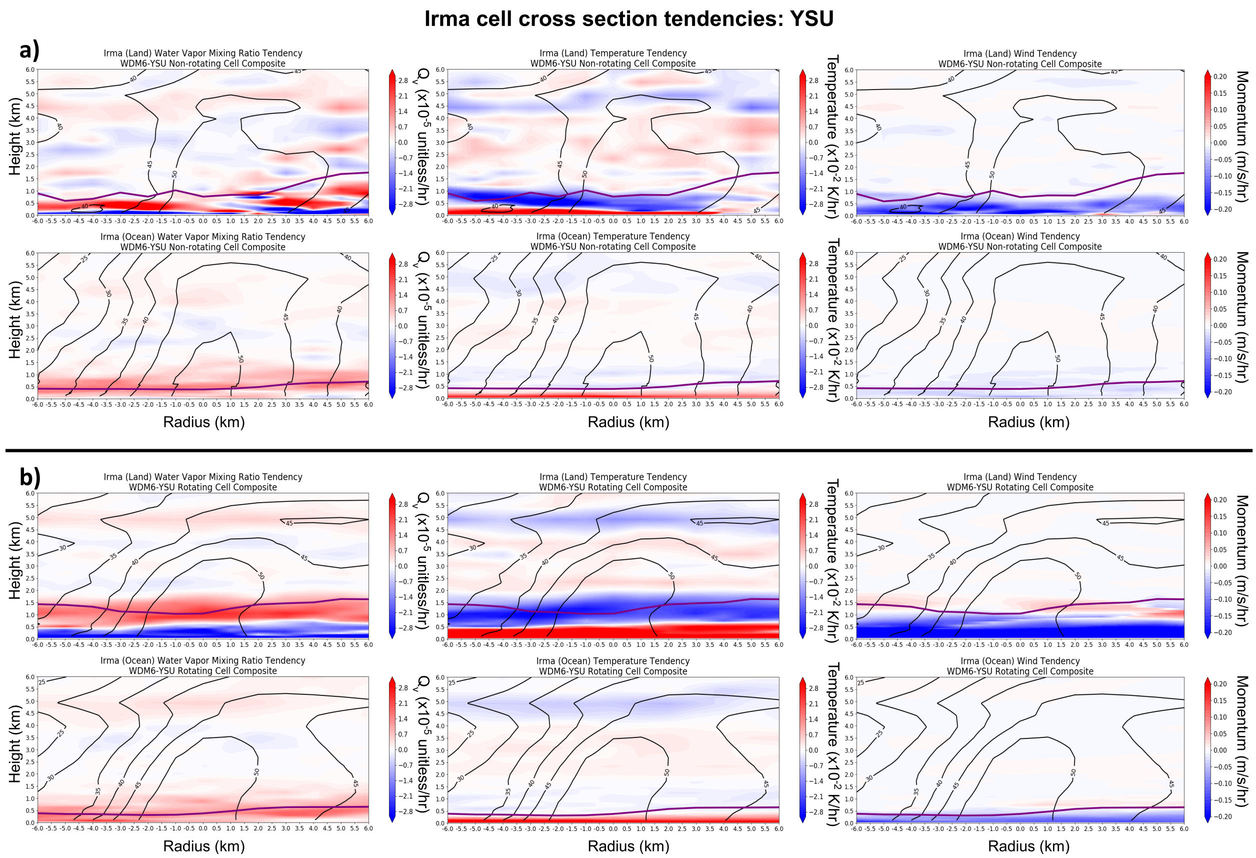

Figure 4.21: Same as Figure 4.18, except for Hurricane Irma.

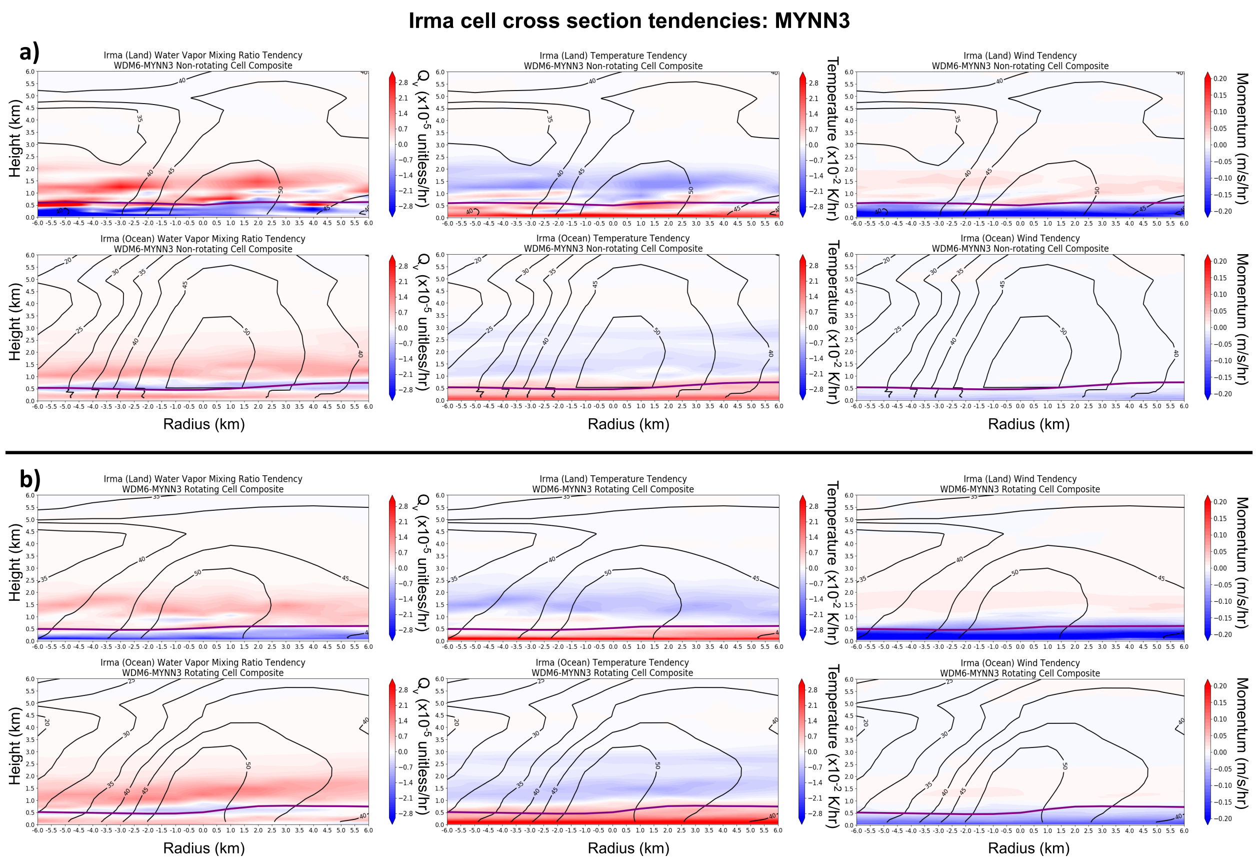

Figure 4.22: Same as Figure 4.21, but for the MYNN3 simulations.

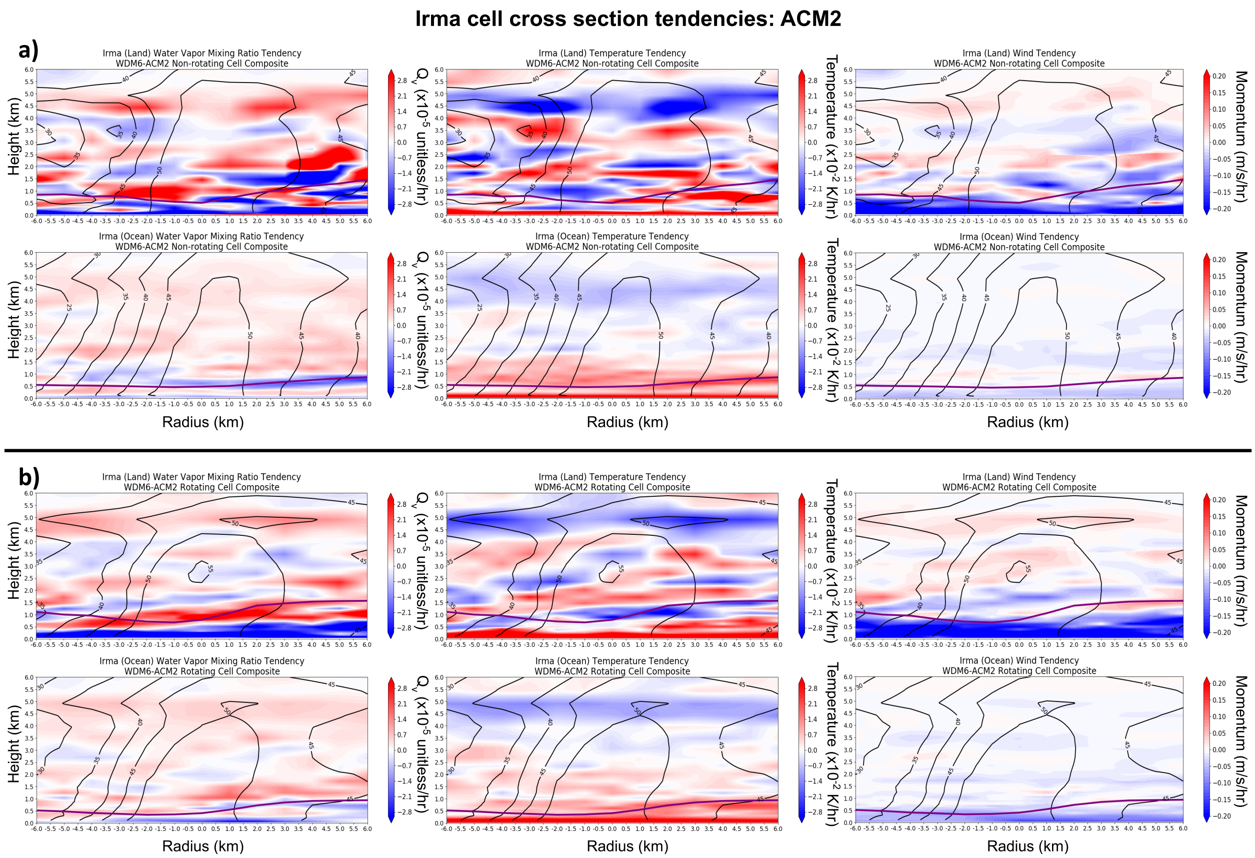

Figure 4.23: Same as Figure 4.21, but for the ACM2 simulations.

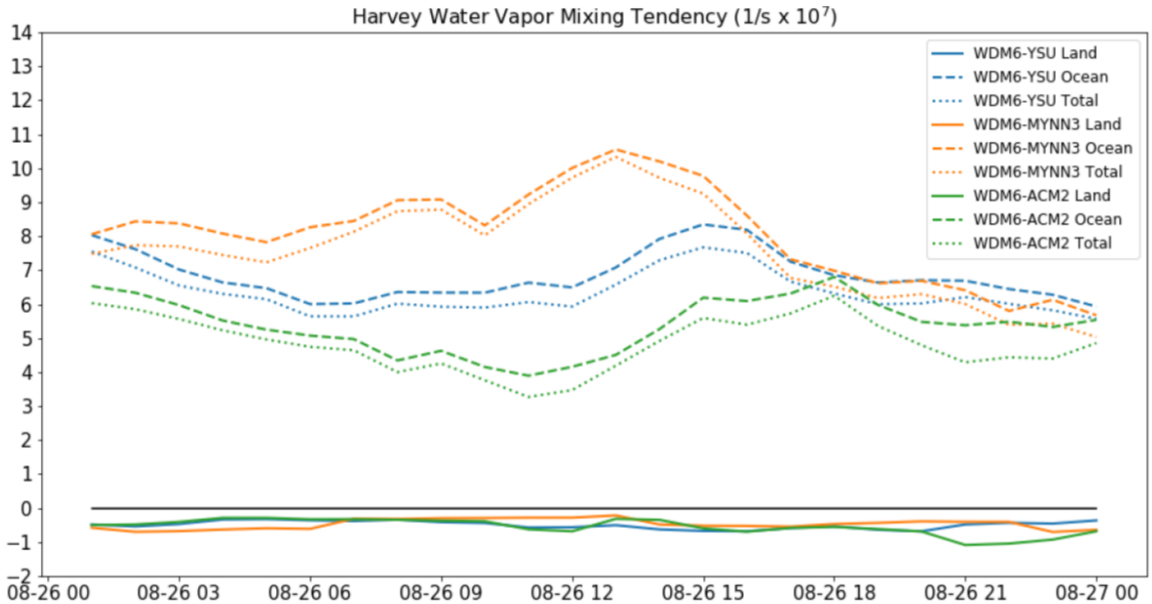

Figure 4.24: Mean water vapor mixing tendency ($X10^{-5} 1/h$) in the lowest 500 m over land and over the ocean in the simulations for Hurricane Harvey from 0000 UTC 26 to 0000 UTC 27 August.

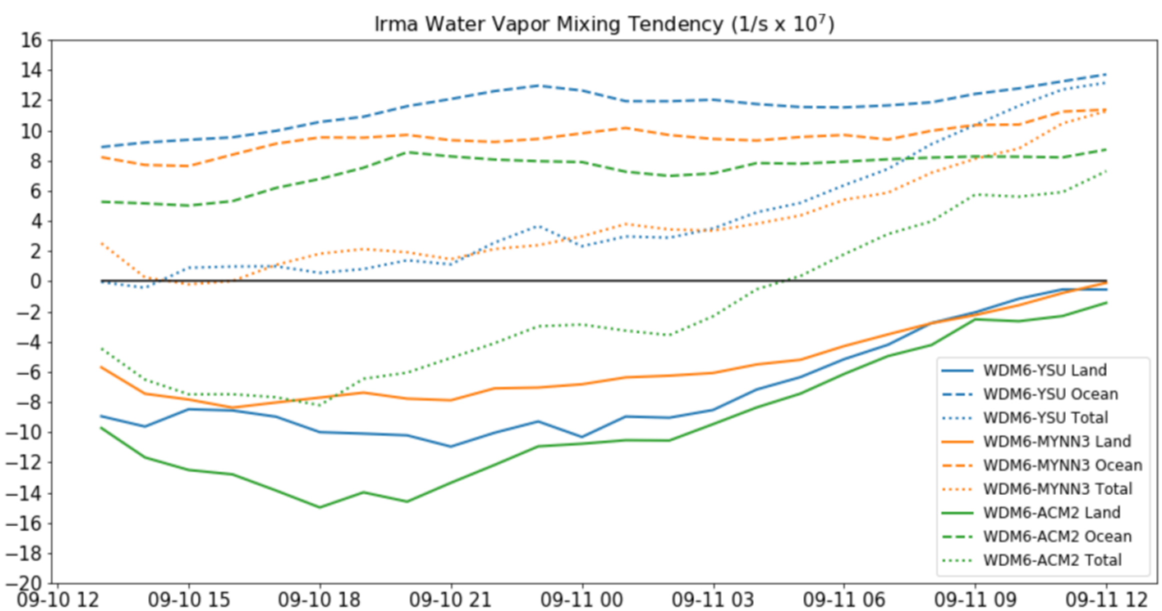

Figure 4.25: Mean water vapor mixing tendency ($X10^{-5} 1/h$) in the lowest 500 m over land and over the ocean in the simulations for Hurricane Irma from 1200 UTC 10 to 1200 UTC 11 September.

5. Planetary boundary layer (PBL) observations and verification

Observations of the atmosphere use a verity of different tools to collect information on the temperature, moisture content, and winds, amongst other variables. One such tool is the radiosondes launched from numerous National Weather Service (NWS) offices twice a day to collect vertical profiles of the atmosphere. Radiosondes are launched via balloons and collect measurements of pressure, height (above ground), temperature, relative humidity (RH), and horizontal wind speed. The NWS uses two types of radiosondes, the first manufactured by Vaisala (RS92-NGP) and the second manufactured by Lockheed Martin (LMS-6). Both types of radiosondes have similar measurement uncertainty with accuracy around 1 hPa, 0.5 $^{\circ}C$, 5%, and 0.15 m/s for the pressure, temperature, RH, and wind speed, respectively (Ingleby 2017). Simulation comparisons to the radiosonde data will include error bars to account for the measurement uncertainties in the temperatures and dew point temperatures.

In tropical cyclones, another such tool that provides vertical profiles of the atmosphere are dropsondes released from research aircraft over the ocean. During decent by parachute, dropsondes measure pressure, height (above ground), temperature, RH, and horizontal wind speed and direction. NCAR's Airborne Vertical Atmospheric Profiling System (AVAPS) is one such dropsonde system, which was used in Hurricane Harvey (2017). During Harvey, the Vaisala RD94 dropsonde was used (Hock and Franklin 1999; Vaisala 2014). Based on information provided by Vaisala (2014), the accuracy of the pressure measurements is 0.4 hPa, the accuracy of the temperature sensor is 0.2 $^{\circ}C$, the accuracy of the RH sensor is 3%, and the horizontal wind sensor has an accuracy of 0.5 m/s. All comparisons to the observed dropsondes, again, will have error bars to represent this uncertainty in the temperature and dew point temperature measurements.

To produce model vertical profiles of temperature and dew point temperature, to compare to observations some corrections must be applied in order to ensure that the model vertical profile is representative of the environment at the sounding or dropsonde observation location. The first correction applied to the model vertical profiles is to correct for differences in the modeled tropical cyclone position compared to observations. To apply this correction, the difference between the best track location and the model center is calculated, and the location of the vertical profile in the model is shifted accordingly. A secondary correction is only applied if the first correction does not place a vertical profile in a location with similar convective features to the observed sounding site using observed and model reflectivity to ensure the vertical profiles are in similar locations in a Eulerian sense. The goal with these corrections is to match model and observed convective areas to ensure vertical profiles are in similar locations in a Eulerian, and not in a Lagrangian, sense.

In the following sections, the observations are compared to the results of the model simulations presented in the previous chapters investigating which PBL scheme produced the most realistic boundary layer in terms of temperature, dew point, and wind in the lowest 3 km. The inflow depth (as defined in Zhang et al. 2011c) will also be examined for select soundings, dropsondes, and vertical profiles in the model simulations later in this chapter. In addition to the vertical profiles, mobile Doppler radar will provide a unique view into the radial inflow and the vertical reflectivity in convective cells from a C-band, dual-polarimetric, Shared Mobile Atmospheric Research and Teaching (SMART) radar (Alford et al. 2019) deployed to capture the landfall of Hurricane Harvey. The SMART radar was located near Rockport, Texas which is approximately 48 km inland of the Gulf of Mexico. During landfall, the SMART radar captured 18 h of dual-Doppler data beginning at approximately 2050 UTC 25 August and concluding at 1435 UTC 26 August; however, from 2310–2349 UTC 25 August and 0140–0310 UTC 26 August the SMART radar was inoperable. The SMART radar had a recorded resolution of 1°. Both the 150°and 360°volume scans were used in the analysis as both operated at the same elevation angles ranging from 0.8–29°. All 18 h of SMART radar data was quality controlled and the Doppler velocity data was dealiased utilizing an automated dealiasing algorithm by Alford et al. (2019).

The goals of these comparisons will be to determine in which capacities different PBL schemes perform better. The vertical profiles will help determine model biases in temperature and dew point temperature. The analysis of the inflow depth of different observation methods will be compared to the model inflow depths and, in the discussion section, compared to the results of Zhang et al. (2011c). Additionally, parallels will be drawn to how differences between the model and observations may have been contributed to by the PBL mechanism differences highlighted in the previous chapter. Finally, mobile Doppler radar cross sections through convective cells will be compared to the composite cross sections from Chapter 3.

5.1 Vertical profiles and verification

5.1.1 Harvey NWS sounding site observations

The NWS sounding sites compared for Hurricane Harvey include Brownsville, Texas (BRO), Corpus Christi, Texas (CRP), and Lake Charles, Louisiana (LCH) from 0000 UTC 26, 1200 UTC 26, and 0000 UTC 27 August. Figures 5.1–5.6 show the vertical profiles from these sounding sites when observations are available. Panel (a) in these figures shows the vertical profiles of temperature and dew point temperature from the observed sounding and the models in the lowest 3000 m at the points shown in the reflectivity images on the right (recall a correction is adopted to account for differences in the tropical cyclone center locations). The insets in (a) show the hodographs of the winds in the lowest 3000 m and the RMSE for the temperature, dew point temperature, wind speed, and wind direction over the entire 3000 m profile. Panel (b) shows the temperature and dew point temperature errors at each observation level as a difference between the model and observation, such that a negative error represents where the model has a lower value than observations and a positive error represents where the model has a greater value than observations.

The vertical profiles of temperature and dew point temperature at Brownsville, TX (BRO) for 0000 UTC 26 August are shown in Figure 5.1a, which, at this time, is south of the tropical cyclone center. The vertical temperature profile shows that in the lowest 1100 m the YSU, MYNN3, and ACM2 simulations are cooler than observations, with the YSU and MYNN3 being the coolest and nearly identical below 600 m. At around 1100 m, the YSU and ACM2 schemes show very similar temperatures to the observations. All three schemes are again cooler than the observations between 1100 and 2000 m. Above 2000 m, the YSU and ACM2 PBL schemes are warmer than observations; however, the MYNN3 simulation is very close to the temperature observations, but slightly cooler above 2600 m. The vertical dew point temperature profiles show that from near the surface to 1500 m, the YSU and MYNN3 schemes are very close to the observations and within the uncertainty of the dew point temperature observations. The ACM2 scheme dew point temperature is higher than observations below 400 m and becomes very similar to the YSU and MYNN3 schemes from 400–1500 m. Between 1600 and 2100 m, the MYNN3 dew point temperatures are larger than the observations, but above 2100 m the MYNN3 simulation is similar to observations through 3000 m. Above 2000 m, the YSU and ACM2 schemes are cooler than observations. The RMSE over the lowest 3000 m in the temperature is 2.05 $°C$, 2.31 $°C$, and 1.09 $°C$ for the YSU, MYNN3, and ACM2 simulations, respectively. The dew point temperature RMSE is 0.55 $°C$, 0.68 $°C$, and 0.94 $°C$ for the YSU, MYNN3, and ACM2 simulations, respectively. The vertical profiles of temperature and dew point temperature were not statistically significantly different from observations in the YSU (p=0.42 and p=0.81), MYNN3 (p=0.27 and p=0.94), and ACM2 (p=0.36 and p=0.85) simulations.

The hodograph inset in Figure 5.1a shows that the curvature in the winds appears very similar in the observations and in the simulations. The wind speed had a RMSE of 1.04 m/s in the YSU simulation, 3.52 m/s in the MYNN3 simulation, and 2.08 m/s in the ACM2 simulation. The MYNN3 simulation wind magnitude was statically significantly (p=0.03) different from the observations, while the YSU and ACM2 simulations showed no statistical significance. The RMSE in the wind direction is 7.02°, 4.60°, and 13.55°, for the YSU, MYNN3, and ACM2 simulations, respectively. The ACM2 simulation wind direction was statically significantly (p=0.01) different from the observations, while the YSU and MYNN3 simulations showed no statistical significance.

The error in Figure 5.1b shows the differences between the model and observations seen in the vertical profiles of temperature and dew point temperature for the BRO sounding for 0000 UTC 26 August. Over the lowest 600 m, the YSU and MYNN3 simulations have very similar temperature errors of around -3.25 $°C$ near the surface; however, the errors in the temperature reduce to around -2.5 $°C$ at 600 m. The ACM2 scheme temperature error is around -1.75 $°C$ near the surface and decreases aloft getting to within the margin of measurement uncertainty around 600 m. Above 600 m, the YSU and MYNN3 temperature errors diverge, with the YSU scheme error continuing to decrease through 1000 m, while the MYNN3 scheme error remains between -3 and -2 $°C$ through about 1700 m. From 1000–2100 m, the YSU and ACM2 simulations, temperature errors are around -1 $°C$ and above 2100 m the error is around 1.5 $°C$. Above 2000 m, the MYNN3 simulation has very low temperature error between -0.5 and 0.5 $°C$. The MYNN3 and ACM2 simulations showed statistically significant temperature differences (p=0.00) from one another. The dew point temperature error is largest near the surface in the ACM3 simulation, as seen in Figure 5.1a, with an error of around 1.25 $°C$. The dew point temperature error in the YSU simulation is very low near the surface and ranges between -0.5 and 0.5 $°C$ through 2000 m. The MYNN3 simulation also has very low dew point temperature error near the surface to 1500 m ranging -0.5–0.5 $°C$. From 2000–3000 m, both the YSU and ACM2 simulations have negative dew point temperature errors around -1 $°C$ and -1.5 $°C$ respectively. The dew point temperatures were statistically significantly (p=0.02) different between the YSU and ACM2 simulations.

The vertical profiles of temperature and dew point temperature at Corpus Christi, TX (CRP) for 0000 UTC 26 August are shown in Figure 5.2a, which is on the western fringe of the tropical cyclone eyewall. The vertical profile shows the temperature and dew point temperature are very close to one another over the lowest 3000 m, indicating a very moist profile, as expected. The temperatures in the YSU and ACM2 schemes in the lowest 900 m are slightly cooler than the observed temperatures and very similar to one another. The

MYNN3 temperature is cooler than observations over the lowest 1000 m. Above 900 m, the YSU and MYNN3 temperatures are nearly identical with both simulations warmer than observations from around 1500–2200 m. The ACM2 temperature remains cooler than the observations above 900 m, where it diverges from the YSU scheme. The vertical dew point temperature profiles show that from near the surface to 900 m, the YSU, MYNN3, and ACM2 schemes are nearly identical to each other and lower than the observations. Above 900 m, the simulated dew point temperatures diverge. Through most of the lowest 3000 m, the YSU dew point temperature is lower than observations. Both the MYNN3 and ACM2 simulation dew point temperatures follow closely with the temperature profiles, which is unsurprising given the high moisture. Like the MYNN3 temperature, the dew point temperature is larger than the observations from 1500–2200 m. In the ACM2 scheme, the temperature is cooler than the observed temperature from 900–2300 m and the dew point temperature is also lower than the observations. The RMSE over the lowest 3000 m in the temperature is 0.70 $°C$, 1.43 $°C$, and 1.04 $°C$ for the YSU, MYNN3, and ACM2 simulations, respectively. The dew point temperature RMSE is 1.48 $°C$, 1.23 $°C$, and 1.08 $°C$ for the YSU, MYNN3, and ACM2 simulations, respectively. The temperatures and dew point temperatures from all three simulations are not statistically significantly different from the observed sounding.

The hodograph inset in Figure 5.2a shows that the winds in the model tend to have a more westerly component near the surface compared to the observations. The MYNN3 scheme shows stronger winds over all heights compared to the other simulations and the observations by 2–5 m/s. The curvature in the winds appears very similar in the observations and in the YSU and ACM2 simulations; however, the curvature of the wind in the MYNN3 scheme is weaker than the observations and other model simulations. The wind speed had a RMSE of 2.99 m/s in the YSU simulation, 7.15 m/s in the MYNN3 simulation, and 3.13 m/s in the ACM2 simulation. The RMSE in the wind direction is 7.73°, 12.04°, and 6.71°, for the YSU, MYNN3, and ACM2 simulations, respectively. Like the at BRO, the MYNN3 simulation 0–3-km wind speed is statistically significantly (p=0.00) faster than the observed

0–3-km wind speed.

Figure 5.2b shows the differences between the model and observations seen in the vertical profiles of temperature and dew point temperature for the CRP sounding for 0000 UTC 26 August. Over the lowest 800 m, the YSU and ACM2 temperature errors are very similar to one another around -1.5 to -0.5 $°C$. The MYNN3 simulation has the largest temperature error of about -2 $°C$ near the surface to -1 $°C$ at around 800 m. Above 800 m, the temperature errors in the YSU and MYNN3 simulations are nearly identical and show that there is a warm temperature error in these two simulations from 1500–2200 m of about 1 $°C$. The ACM2 simulation temperature error diverges from the YSU scheme above 800 m and remains negative, ranging from -1.5 to -0.5 $°C$ through 3000 m. The temperature of the YSu simulation is statistically significantly (p=0.00) higher than the ACM2 simulation. The dew point temperature error is large near the surface in all three PBL schemes, as seen in Figure 5.1a, with an error of around -2 $°C$. Above about 800 m, the dew point temperature errors of all the simulations diverge. The dew point temperature error in the YSU simulation ranges between -1 and -2.5 $°C$ through 3000 m. The MYNN3 simulation also has very low dew point temperature error from 800–1400 m ranging -0.5–0.5 $°C$. Above 1400 m, the MYNN3 simulation has a dew point temperature error around 1–2 $°C$ through 3000 m. The ACM2 has a dew point temperature error that ranges between -1 and -0.5 $°C$ through 3000 m. The YSU simulation dew point temperatures are statistically significantly lower than the MYNN3 (p=0.00) and the ACM2 (p=0.01) simulations.

The vertical profiles of temperature and dew point temperature at Brownsville, TX (BRO) for 1200 UTC 26 August are shown in Figure 5.3a, which is located south of the tropical cyclone. The vertical temperature profiles show an inversion in the low levels in both the observations and the model. The temperature inversion in the model is about 100 m deep, while in the observations it is about 200 m deep. The YSU temperature is higher near the surface than the observations, while the MYNN3 and ACM2 simulations are very close to the observed temperature. Above the surface, all three PBL schemes are colder than observations, especially the MYNN3 and ACM2 simulations through about 1000 m. Above 1000 m, the YSU, MYNN3, and ACM2 simulations are very similar and cooler than the observations through 3000 m. The vertical dew point temperature profiles show that near the surface the model values are lower than observations. Above 100 m, the YSU and ACM2 simulations show very similar dew point temperatures lower than the observations through about 900 m. The MYNN3 simulation also has lower dew point temperatures than the observations near the surface and is within the margin of uncertainty in the dew point temperature measurements from 200–600 m. The MYNN3 has larger dew point temperatures from 600–900 m and then becomes very close to the observed dew point temperature through 3000 m. Above 900 m, the YSU and ACM2 simulations become closer to the observations of the dew point temperature. Above 1300 m, the dew point temperature diverges between the YSU and ACM2 simulations, but both schemes are slightly warmer than the observed dew point temperature. The RMSE over the lowest 3000 m in the temperature is 1.40 $°C$, 2.21 $°C$, and 2.10 $°C$ for the YSU, MYNN3, and ACM2 simulations, respectively. The dew point temperature RMSE is 1.07 $°C$, 0.78 $°C$, and 1.13 $°C$ for the YSU, MYNN3, and ACM2 simulations, respectively. None of the simulations produced temperatures or dew point temperatures that are statistically significantly different from the observed sounding.

The hodograph inset in Figure 5.3a shows that the curvature in the winds appears similar between the observations and in the simulations. The wind speed had a RMSE of 1.94 m/s in the YSU simulation, 1.45 m/s in the MYNN3 simulation, and 1.53 m/s in the ACM2 simulation. The RMSE in the wind direction is 18.37°, 23.46°, and 13.78°, for the YSU, MYNN3, and ACM2 simulations, respectively. As with the temperature and dew point temperature, none of the simulations showed statistically significant differences in the wind speed or direction compared to the observed sounding.

Figure 5.3b shows the differences between the model and observations that are seen in the vertical profiles of temperature and dew point temperature for the BRO sounding for 1200 UTC 26 August. Near the surface, the YSU temperature error is 2 $°C$; however, the error quickly becomes colder than observations above 200 m. The YSU simulation has errors generally around -1.5 $^{\circ}C$ from 300–3000 m, with a peak in the error of -3 $^{\circ}C$ at 1500 m. The MYNN3 simulation has very low temperature error near the surface (around -0.5 $^{\circ}C$). The temperature error in the MYNN3 simulation from 300–2000 m is around -3 $^{\circ}C$, with a reduction in error to around -1 $^{\circ}C$ at around 1200 m. Above 2000 m in the MYNN3 simulation, the temperature error is reduced towards zero. The ACM2 simulation is slightly warmer than observations near the surface around 0.5 $^{\circ}C$ that again quickly becomes negative above the inversion. From 300–600 m, the ACM2 temperature error is around -3 $^{\circ}C$, which decreases toward zero through 3000 m. The YSU simulation temperature is statistically significantly higher (p=0.02) than the MYNN3 simulation. The dew point temperature error is large in both the MYNN3 and ACM2 simulations near the surface, with temperature errors of around -2.25 $^{\circ}C$ and -2.5 $^{\circ}C$, respectively. The YSU has a dew point temperature error of around -1.5 $^{\circ}C$ near the surface. Above 100 m, the YSU and ACM2 simulations have very similar dew point temperature errors which decrease from -1.5 $^{\circ}C$ to near zero error from 100–1400 m. Above 1300 m, the YSU and ACM2 simulations dew point temperature errors diverge, with the YSU scheme peaking at 1.5 $^{\circ}C$ before dropping towards zero error. The ACM2 dew point temperature error goes to zero between 2000 and 3000 m. The dew point temperature error in the MYNN3 simulation between 100–900 m ranges between -1 and 1 $^{\circ}C$. Above 900 m, the MYNN3 dew point temperature error ranges between -0.5 $^{\circ}C$ and 0.5 $^{\circ}C$ which through 3000 m. There are no statistical significant differences in the dew point temperatures of the three simulations.

The vertical profiles of temperature and dew point temperature at Lake Charles, LA (LCH) for 1200 UTC 26 August are shown in Figure 5.4a, which is located near convection in an outer rainband east of the storm center. The observations, MYNN3, and ACM2 simulations all have convection near the vertical profile that is missing from the YSU simulation. The vertical profile shows the temperature and dew point temperature are very close to one another over the lowest 2200 m, showing a very moist profile. The temperatures in the YSU and ACM2 simulations in the lowest 500 m are warmer than the observed temperatures with the YSU simulation being the warmest. The MYNN3 temperature is slightly cooler than observations over the lowest 1100 m. Above 500 m, the YSU simulation temperature is warmer than observations, while the ACM2 simulation is very similar to observations. Like the ACM2 simulation, above 1100 m the MYNN3 simulation is very close to the observed temperatures. The vertical dew point temperature profiles show that from near the surface to 300 m the YSU and ACM2 simulations are very similar to the observed dew point temperatures. From 300–3000 m, the YSU simulation dew point temperature is lower than the observations. The ACM2 simulation remains closer to observations of the dew point temperature, although the ACM2 simulation is lower from 300–600 m and above that level from 900–3000 m. The MYNN3 simulation dew point temperatures are lower than observations from near the surface to around 2100 m, after which the the dew point temperatures in the MYNN3 simulation become slightly greater than the observations. The RMSE over the lowest 3000 m in the temperature is 1.03 $°C$, 0.74 $°C$, and 0.55 $°C$ for the YSU, MYNN3, and ACM2 simulations, respectively. The dew point temperature RMSE is 1.63 $°C$, 2.56 $°C$, and 1.10 $°C$ for the YSU, MYNN3, and ACM2 simulations, respectively. Neither the temperatures or dew point temperatures of the three simulations are statistically significantly different from the observed sounding.

The hodograph inset in Figure 5.4a shows that the winds in the model tend to be a bit weaker than the observed winds. The model winds also have more curvature in the hodograph compared to the observations. The wind speed had a RMSE of 2.51 m/s in the YSU simulation, 2.16 m/s in the MYNN3 simulation, and 1.89 m/s in the ACM2 simulation. The RMSE in the wind direction is 137.25°, 147.76°, and 160.86°, for the YSU, MYNN3, and ACM2 simulations, respectively. The wind direction RMSE is larger than the other three soundings previously discussed due to the location near an isolated convective cell, which makes the wind profile very sensitive to differences between the model and observed vertical profile locations in comparison to the convective cell. Both the MYNN3 and ACM2 simulations show statistically significant wind direction differences compared to the observed wind direction, while the wind speeds showed no statistically significant differences between the model and observations.

Figure 5.4b shows the differences between the model and observations that are seen in the vertical profiles of temperature and dew point temperature for the LCH sounding for 1200 UTC 26 August. The temperature errors from the YSU simulation range between 1–1.5 $^{\circ}C$ in the lowest 300 m, above which the error is reduced to around 0.5 $^{\circ}C$ through 1100 m. Above 1100 m, the temperature error in the YSU simulation ranges between 0.5 and 1 $^{\circ}C$ through 2600 m. The MYNN3 temperature error is around -0.5 $^{\circ}C$ within the lowest 300 m. There is a peak in temperature error of -1.25 $^{\circ}C$ in the MYNN3 simulation at 600 m, which is reduced towards zero error around 1400 m. From 1600–2200 m, the MYNN3 temperature error ranges from 0.5 to 1 $^{\circ}C$, before returning to near zero error above 2200 m. The ACM2 temperature error ranges between 0.5 and 1 $^{\circ}C$ from near the surface to around 500 m. From 500–3000 m, the ACM2 temperature error is less than 0.5 $^{\circ}C$, which represents error remaining within the uncertainty of the observed temperature measurements. The temperatures of all of the simulations are statistically significantly (p=0.00) different from one another. The dew point temperature error is largest in the MYNN3 simulation with an error of -1 $^{\circ}C$ near the surface increasing to between -2.5 and -3.5 $^{\circ}C$ from 200–1700 m, with the error going to zero above 1700 m. There is a peak in the MYNN3 dew point temperature error around 1 $^{\circ}C$ from 2300–2700 m. In the lowest 200 m, the YSU simulation has low dew point temperature error between 0.5 and -0.5 $^{\circ}C$. Above 200 m, the dew point temperature error in the YSU simulation increases from -0.5 to -3 $^{\circ}C$ through 2700 m. Near the surface, the ACM2 simulation has close to zero error in the dew point temperature that increases to -1.5 $^{\circ}C$ at 500 m. The ACM2 dew point temperature error reduces back towards zero between 600 and 700 m before the error increases again. Above 900 m, the dew point temperature error in the ACM2 simulation increases from -0.5 to -3 $^{\circ}C$ at 2700 m. The MYNN3 simulation dew point temperatures are statistically significantly (p=0.00) lower than the ACM2 simulation.

The vertical profiles of temperature and dew point temperature at Brownsville, TX (BRO) for 0000 UTC 27 August are shown in Figure 5.5a, which is well south of the tropical cyclone. The vertical temperature profile shows that in the lowest 900 m the YSU, MYNN3, and ACM2 simulations are cooler than observations, with the YSU and MYNN3 being nearly identical below 500 m and the ACM2 simulation being the coldest. Above 700 m, the temperatures of the YSU and ACM2 simulations are very similar and close to observations though 3000 m. The MYNN3 simulation is colder than observations at all levels through 3000 m. The vertical dew point temperature profiles show that near the surface the YSU and ACM2 simulations' temperatures are only slightly larger than the observations. In the YSU simulation, the dew point temperatures become colder than the observations from around 400–1700 m; above 1700 m, the dew point temperatures are very similar to the observations. The ACM2 simulation dew point temperature is warmer than observations through 600 m. From 600–1500 m, the ACM2 simulation dew point temperatures are lower than observations and from 1700–3000 m they are higher than observations. From near the surface to around 1500 m, the MYNN3 dew point temperature is lower than observations. Above 1500 m, the MYNN3 simulation dew point temperature is higher than observations. The RMSE over the lowest 3000 m in the temperature is 1.28 $°C$, 1.94 $°C$, and 2.19 $°C$ for the YSU, MYNN3, and ACM2 simulations, respectively. The dew point temperature RMSE is 1.27 $°C$, 2.03 $°C$, and 1.02 $°C$ for the YSU, MYNN3, and ACM2 simulations, respectively. The temperatures and dew point temperatures of the simulations are not statistically significantly different from the observations.

The hodograph inset in Figure 5.5a shows that the winds in the model tend to be weaker than the observed winds. The curvature in the winds appears very similar in the in the observations and simulations, although the model tends to have a shorter hodograph than the observations. The wind speed had a RMSE of 4.86 m/s in the YSU simulation, 3.89 m/s in the MYNN3 simulation, and 4.75 m/s in the ACM2 simulation. The RMSE in the wind direction is 28.03°, 20.16°, and 18.09°, for the YSU, MYNN3, and ACM2 simulations, respectively. The wind speeds from all the simulations are statistically significantly ($p=0.00$) lower than the observations.

Figure 5.5b shows the differences between the model and observations that are seen in the vertical profiles of temperature and dew point temperature for the BRO sounding for 0000 UTC 27 August. The temperature errors in all three simulations are negative from near the surface to 600 m with errors of -2 $°C$, -2.25 $°C$, and -3 $°C$ in the YSU, MYNN3, and ACM2 simulations, respectively. The YSU and ACM2 temperature errors drop to near zero at around 800 m and both oscillate between -1 and 0.5 $°C$ error. The MYNN3 has negative temperature errors through the entire lowest 3000 m ranging from -2.5 to -1 $°C$. The YSU temperature is statistically significantly ($p=0.00$) different from the MYNN3 simulation. The dew point temperature errors in the YSU simulation are around 0.75 $°C$ at the surface. The dew point temperature errors turn negative around 300 m, increasing to -3 $°C$ at around 1300 m before returning to near zero error above 1700 m. From near the surface to 500 m, the MYNN3 simulation has dew point temperature errors of around -2 $°C$. Above 500 m, the MYNN3 simulation dew point temperature error peaks at -3.5 $°C$ at around 800 m. At around 1500 m, the MYNN3 dew point temperature errors become positive and increase to 1.5 $°C$ from 1700–2800 m. The dew point temperature errors in the ACM2 simulation are around 1.5 $°C$ near the surface, decreasing to zero error around 700 m. From 700–1400 m, the ACM2 simulation has dew point temperature errors around -1 $°C$, which cross the zero error again at 1600 m and increase to 1.5 $°C$ at 2700 m. The ACM2 dew point temperatures are statistically significantly different from both the YSU ($p=0.01$) and the MYNN3 ($p=0.00$) simulations.

The vertical profiles of temperature and dew point temperature at Corpus Christi, TX (CRP) for 0000 UTC 27 August are shown in Figure 5.6a, which is to the south of the tropical cyclone center. Low values of reflectivity are seen at the sounding site in the observations, but none of the model simulations show reflectivity on the south side of the storm. The temperature profiles of the YSU and ACM2 simulations are lower than the observations through the lowest 3000 m, while the MYNN3 simulation is cooler through about 1200 m before becoming slightly warmer than observations. The dew point temperatures in the models are all very similar to each other, with all three models being cooler than the observations below 500 m. The MYNN3 simulation tends to be very similar to the observations above 500 m. The RMSE over the lowest 3000 m in the temperature is 1.49 $°C$, 1.32 $°C$, and 1.27 $°C$ for the YSU, MYNN3, and ACM2 simulations, respectively. The dew point temperature RMSE is 1.02 $°C$, 0.76 $°C$, and 1.29 $°C$ for the YSU, MYNN3, and ACM2 simulations, respectively. None of the simulations had statistically significantly different temperatures or dew point temperatures compared to the observed sounding.

The hodograph inset in Figure 5.6a shows that the winds in the model tend to be similar to the observations, particularly the MYNN3 simulation. The wind speeds in the YSU and ACM2 simulations are weaker near the surface compared to the observations. The curvature in the model wind profiles is more than that in the observations. The wind speed had a RMSE of 6.91 m/s in the YSU simulation, 2.81 m/s in the MYNN3 simulation, and 6.04 m/s in the ACM2 simulation. Both the YSU and ACM2 simulations' wind speeds are statistically significantly (p=0.00) stronger than the observed wind speed. The RMSE in the wind direction is 10.09°, 8.85°, and 15.53°, for the YSU, MYNN3, and ACM2 simulations, respectively. All three simulations show statistically significantly (p=0.00, p=0.05, p=0.00) different wind directions compared to observations.

Figure 5.6b shows the differences between the model and observations that are seen in the vertical profiles of temperature and dew point temperature for the CRP sounding for 0000 UTC 27 August. The temperature errors in the YSU and ACM2 simulations are similar to one another through the entire 3000 m of the profile. Near the surface, the YSU and ACM2 simulations have a temperature error of -0.5 $°C$. From 100–1200 m, the there is about a 0.5 $°C$ difference in the errors between the YSU and ACM2 simulations, with temperature errors peaking at -2.5 and -2 $°C$, respectively, at around 700 m. Above 1200 m, the YSU and ACM2 temperature errors decrease towards zero through the remaining 2800 m. The MYNN3 simulation temperature error is cooler than the other simulations near the surface with an error of around 1.25 $°C$. The temperature error in the MYNN3 simulation peaks at -2.25 $°C$ at 500 m. Above 500 m, the temperature error goes close to zero in the MYNN3 simulation between 1300–1800 m, before showing a small positive temperature error around 0.75 $°C$ from 1900–2400 m. There is no statistical significant differences between the temperatures of the three simulations. The dew point temperature errors in the three simulations have nearly identically shaped profiles, just shifted in error. The YSU dew point temperature error near the surface is about -2.25 $°C$ and decreases toward zero at around 500 m. The errors in the dew point temperature of the YSU simulation then increase to between -0.5 to -1 $°C$ from 900–2600 m, above which the error is near zero. The MYNN3 simulation has dew point temperature errors that are slightly warmer than the YSU errors. The MYNN3 dew point temperature error is around -1.75 $°C$ and decreases toward zero at around 400 m before rising just above 0.5 $°C$. From 900–1700 m, the MYNN3 simulation has near zero error in the dew point temperature. Above 1900 m, the MYNN3 simulation oscillates between -0.75 and 0.5 $°C$ through 3000 m. The ACM2 simulation has dew point temperature errors slightly lower than the YSU and MYNN3 simulations. Near the surface, the dew point temperature error in the ACM2 simulation is around -2.75 $°C$ and decreases to -0.5 $°C$ from 500–800 m. Above 1000 m, the ACM2 and YSU simulations' dew point temperature errors are nearly identical ranging between -0.5 and -1 $°C$ to 2600 m and going to near zero error above that. The MYNN3 simulation dew point temperatures are statistically significantly different from the YSU (p=0.05) and the ACM2 (p=0.00) simulations.

The RMSEs for temperature and dew point temperature are summarized in Table 5.1. Across the sounding locations, the average RMSEs for temperature are 1.36 $°C$, 1.66 $°C$ and 1.37 $°C$ and the average RMSEs for dew point temperature are 1.17 $°C$, 1.34 $°C$ and 1.09 $°C$ for the YSU, MYNN3, and ACM2 simulations, respectively. Overall, the simulations produced 0–3-km temperature and dew point temperature profiles that were not statistically significantly different from the observed soundings regardless of time or location. As shown in the soundings, most of the PBL schemes were too cold in the lowest 200 m, but these differences were not statistically significant from the observations. Hariprasad et al. (2014) has shown for the tropical coast of India that all PBL schemes tested, including YSU, MYNN, and ACM2, showed systematic cold biases with RMSE around 1 $°C$. In a field campaign over Greece, Banks et al. (2016) found that during Etesians and Saharna flows the WRF simulations exhibited a cold and moist bias, while the local schemes (MYJ and MYNN2) showed the best vertical profiles of temperature and moisture. During continental flow in Greece, Banks et al. (2016) showed a slightly warm and dry bias with the ACM2 simulation showing the best results compared to observations. Generally, the temperature and dew point temperature RMSEs were low among all of the simulations compared to the observed soundings. Across the sounding locations in Hurricane Harvey, the PBL simulations also showed statistically significant differences from one another, most notably during the tropical cyclone landfall at CRP (Fig. 5.2): the YSU simulation showed statistically significantly larger temperatures than the ACM2 simulation (specifically above 1000 m) and statistically significantly smaller dew point temperatures in both the MYNN3 and ACM2 simulations (specifically above 1000 m). Differences across the PBL simulations are expected as each handles vertical mixing differently.

Summarized in Table 5.1 are the RMSEs for the wind speed and direction for the Harvey simulations compared to the observed soundings. The average wind speed RMSEs are 3.38 m/s, 3.50 m/s, and 3.24 m/s, and the average wind direction RMSEs are 34.75°, 36.15°, and 38.07° for the YSU, MYNN3 and ACM2 simulations, respectively. The wind speed and direction in the lowest 3 km did show statistically significant differences between some of the simulations and the observations. The MYNN3 simulation produced statistically significantly faster wind speeds most frequently across the simulations compared to observations. Past literature suggests that the MYNN3 tends to more accurately predict wind speeds in a variety of situations and locations compared to many non-local PBL schemes (Misaki et al.

2019; Dzebre and Adaramola 2020), contradictory to what is observed in the simulations of Hurricane Harvey. Furthermore, past literature has shown that during daytime along the Texas coast, the YSU and ACM2 PBL schemes tend to produce less bias in wind speed profiles in the PBL compared to local PBL schemes for slower wind speeds (Hu et al. 2010). Surussavadee (2017) evaluated the 65- and 90-m wind speeds and directions in Thailand averaged over the months of May, August, and November of 2012. The YSU, MYNN3, and ACM2 schemes were amongst the nine different PBL schemes evaluated. The YSU scheme showed a wind speed RMSEs of 2.36 and 2.51 m/s and wind direction RMSEs of 56.25 and 55.48°, for the 65- and 90-m winds respectively. The MYNN3 scheme showed a wind speed RMSEs of 2.38 and 2.28 m/s and wind direction RMSEs of 56.37 and 55.38°, respectively. The ACM2 scheme showed a wind speed RMSEs of 2.11 and 2.01 m/s and wind direction RMSEs of 55.43 and 55.01°, respectively. It is also important to note that the RMSE in the wind speed increases with increasing wind speed and the wind direction RMSE decreases with increasing wind speed (Surussavadee 2017). Although the ACM2 simulation showed the lowest RMSE in Surussavadee (2017), in the simulations of Hurricane Harvey the ACM2 simulation produced wind directions that were statistically significantly different most frequently across the observed soundings. The wind speeds showed larger RMSEs in the simulations of Hurricane Harvey and the average, wind direction RMSEs for the simulations were less than the what has been seen in past literature (Surussavadee 2017; Misaki et al. 2019; Dzebre and Adaramola 2020). This result is of course, with the caveat that none of these studies looked at tropical cyclone environments.

5.1.2 Irma NWS sounding site observations

The NWS sounding sites for Hurricane Irma include Miami (MFL), Tampa (TBW), and Jacksonville (JAX) Florida from 1200 UTC 10, 0000 UTC 11, and 1200 UTC 11 September. Figures 5.7–5.11 show the vertical profiles from these sounding sites when observations are available.

The vertical profiles of temperature and dew point temperature for Tampa (TBW) at 1200 UTC 10 September are shown in Figure 5.7a, which is on the northwest edge of the tropical cyclone precipitation. Inspection of the vertical temperature profile shows that in the lowest 300 m, the MYNN3 simulation is cooler than observations, while the YSU and ACM2 simulations show very little deviation from the observed temperature over the same layer. From 500–1800 m, the YSU scheme is cooler than observations. The ACM2 and MYNN3 are very similar to observations between 300–1000 m; however, between 1000–2100 m, both schemes are colder than observations. Above 2100 m, all three PBL schemes produced temperatures similar to the observations through 3000 m. The vertical dew point temperature profiles show that from near the surface to 800 m, the MYNN3 and ACM2 schemes are colder than observations, while the YSU scheme is within the range of uncertainty. From 800–1300 m, all three PBL scheme show similar dew point temperatures to observations. The YSU and MYNN3 simulations have slightly higher dew point temperatures than observations from 1300–3000 m. From 1300–2000 m, the ACM2 scheme has a lower dew point temperature than observations, before becoming higher than the observations above 2000 m, like the YSU and MYNN3 schemes. The RMSE over the lowest 3000 m in the temperature is 0.91 $°C$, 1.15 $°C$, and 0.94 $°C$ for the YSU, MYNN3, and ACM2 simulations, respectively. The dew point temperature RMSE is 1.26 $°C$, 2.09 $°C$, and 2.01 $°C$ for the YSU, MYNN3, and ACM2 simulations, respectively. None of the temperatures or dew point temperatures in the PBL simulations are statistically significantly different from the observations.

The hodograph inset in Figure 5.7a shows that the winds in the model tend to be more southerly and the curvature is less than seen in the observation. The wind speed had a RMSE of 7.51 m/s in the YSU simulation, 6.87 m/s in the MYNN3 simulation, and 8.44 m/s in the ACM2 simulation. The wind speed in the YSU (p=0.01) and ACM2 (0.00) simulation are statistically significantly larger than observations. The RMSE in the wind direction is 65.46°, 65.44°, and 65.75°, for the YSU, MYNN3, and ACM2 simulations, respectively. The RMSE in the wind direction is large due to the smaller curvature in the hodograph mentioned above.

Figure 5.7b shows the differences between the model and observations that are seen in the vertical profiles of temperature and dew point temperature for the TBW sounding for 1200 UTC 10 September. Over the lowest 300 m, the YSU and ACM2 simulations show only very slight temperature error generally between -0.5 and 0.5 $°C$, which is within the uncertainty of the temperature observations. The MYNN3 simulation showed a large cool temperature error in the lowest 300 m, which is around -2.25 $°C$ at the surface and improves to near zero error from 300–700 m. From 700–1400 m, the YSU, MYNN3, and ACM2 simulations have very similar temperature errors that increase from about 600 m, reaching a maximum error of -1.75 $°C$, -2 $°C$, and -2.5 $°C$, respectively around 1400 m in height. Beyond 1400 m, all three PBL schemes exhibit a reduction in temperature error to between -0.5 and 0.5 $°C$ above 2300 m. The 1400 m height corresponds to the height of the observed inflow depth in the vertical profile at TBW. The dew point temperature error is largest near the surface in the three PBL schemes, as seen in Figure 5.7a, with errors of -2.25 $°C$, -2.75 $°C$, and -3.5 $°C$ in the YSU, MYNN3, and ACM2 simulations, respectively. Non-local schemes (YSU and ACM2) are known to have stronger warming and drying at low levels within the PBL compared to local schemes (Bright and Mullen 2002; Kain et al. 2005; Hill and Lackmann 2009; Hu et al. 2010). Above 400 m, the YSU and MYNN3 simulations have very similar error in the dew point temperature. From 800–1300 m, the dew point temperature error is near zero in all three simulations. From 1300–2000 m, the ACM2 scheme was cooler than observations, which is seen in the dew point temperature error peaking around -2.5 $°C$ at 1700 m. Above 1000 m, the YSU and MYNN3 simulations show generally higher dew point temperatures than the observations by about 0.5–2.5 $°C$. Around 2500 m, the dew point temperature error in the model simulations converge and are about 2 $°C$ warmer than observations.

The vertical profiles of temperature and dew point temperature at Tampa (TBW) for 0000 UTC 11 September are shown in Figure 5.8a, which is northwest of the center of circulation just outside the eyewall. The vertical profiles show the temperature and dew point temperature are very close to one another over the lowest 3000 m, showing a very moist profile. The temperature profiles in the YSU and ACM2 simulations are very similar to each other and slightly cooler than the observed temperature from 300–800 m. From 1100–2300 m, the YSU and ACM2 temperatures are warmer than observations. The temperatures in the MYNN3 simulation are very close to observations near the surface through about 400 m. From 400–2600 m, the MYNN3 temperature profile is warmer than the observations, especially between 400 and 1400 m. Near the surface, the YSU and ACM2 simulations have lower dew point temperatures than the observations through about 500 m. The MYNN3 simulation dew point temperatures are also lower than the observations near the surface, but become warmer than the observations between 300 and 2600 m. The RMSE over the lowest 3000 m in the temperature is 0.40 $°C$, 0.66 $°C$, and 0.51 $°C$ for the YSU, MYNN3, and ACM2 simulations, respectively. The dew point temperature RMSE is 0.79 $°C$, 0.88 $°C$, and 1.01 $°C$ for the YSU, MYNN3, and ACM2 simulations, respectively. None of the PBL simulations are statistically significantly different from the observations.

The hodograph inset in Figure 5.8a shows that the model simulations have higher wind speeds than the observed wind and also a slightly more northerly wind direction. The curvature in the hodograph is similar in the observations and models even though the hodographs are shifted in wind speed. The wind speed had a RMSE of 8.64 m/s in the YSU simulation, 11.99 m/s in the MYNN3 simulation, and 11.09 m/s in the ACM2 simulation. The wind speeds of both the MYNN3 (p=0.00) and ACM2 (p=0.01) simulations are statistically significantly larger than the observations. The RMSE in the wind direction is 12.83°, 4.59°, and 10.50°, for the YSU, MYNN3, and ACM2 simulations, respectively.

Figure 5.8b shows the differences between the model and observations that are seen in the vertical profiles of temperature and dew point temperature for the TBW sounding for 0000 UTC 11 September. As seen in the vertical temperature profile (Fig. 5.8a), the YSU and ACM2 simulations have very similar temperatures and, thus, have very similar temperature error profiles. The temperature errors near the surface in the YSU and ACM2 simulations are around -1 $°C$ and decrease to near zero error at about 100 m before showing an increase in error again to a peak at around 600 m of about -0.75 $°C$. At 1200 m, the YSU and ACM2 simulations' temperature error profiles diverge to around 0.25 and 0.5 $°C$, respectively. The divergence at 1200 m is just below the PBL height (around 1400 m) in the YSU and ACM2 simulations. The temperature error profiles then converge again above 2000 m, showing a temperature error of around -0.5 $°C$. The MYNN3 simulation temperature error is very low near the surface to about 400 m ranging around -0.25 $°C$ to 0.25 $°C$. Above 400 m, the MYNN3 temperature error grows to around 1 $°C$ between 900 and 1500 m before decreasing back toward zero through 3000 m. The dew point temperature errors in the YSU and ACM2 simulations are higher near the surface around -2.5 and -3 $°C$, respectively, and drop off to near zero error from 700–1000 m. The dew point temperature errors, like the temperature errors, in the YSU and ACM2 simulations diverge around 1200 m, with the error around 0.25 and 0.5 $°C$, respectively, through 2000 m. Above 2000 m, the YSU and ACM2 simulations converge and show dew point temperature errors around -0.5 $°C$. The dew point temperature errors in the MYNN3 simulation are also negative near the surface around -1.25 $°C$ and increase to positive error above 100 m. The dew point temperature errors in the MYNN3 simulation increase to around 0.75 $°C$ at 500 m extending up to about 1100 m. Above 1100 m, the MYNN3 dew point temperature errors, like the temperature errors, decrease through 3000 m.

The vertical profiles of temperature and dew point temperature at Tampa (TBW) for 1200 UTC 11 September are shown in Figure 5.9a, which is on the southern side of the tropical cyclone circulation, in precipitating areas. Above the surface, the temperature profiles of all the simulations are warmer than the observations; however, the profiles tend to get closer to the observations closer to 3000 m. The MYNN3 simulation clearly has the warmest temperatures compared to observations, especially from 500–1700 m. The dew point temperatures are also higher than observations in all the simulations, with the most variation between the simulations from near the surface to around 400 m. The RMSE over the lowest 3000 m in the temperature is 0.55 $°C$, 2.14 $°C$, and 0.98 $°C$ for the YSU, MYNN3, and ACM2 simulations, respectively. The dew point temperature RMSE is 1.04 $°C$, 1.77 $°C$, and 1.37 $°C$ for the YSU, MYNN3, and ACM2 simulations, respectively. Like the previous TBW soundings, none of the PBL simulations show statistical significant differences in temperatures or dew point temperatures compared to the observations.

The hodograph inset in Figure 5.9a shows that the model simulations have similar wind speeds to the observed wind with only slightly stronger winds in the MYNN3 simulation as seen by the extended hodograph. The curvature in the hodograph is similar in the observations and models. The wind speed had a RMSE of 2.03 m/s in the YSU simulation, 7.85 m/s in the MYNN3 simulation, and 2.12 m/s in the ACM2 simulation. The MYNN3 simulation wind speed is statistically significantly (p=0.00) larger compared to the observations. The RMSE in the wind direction is 5.18°, 5.37°, and 9.77°, for the YSU, MYNN3, and ACM2 simulations, respectively. The wind direction is statistically significantly different from observations in the YSU (p=0.03) and ACM2 (p=0.01) simulations.

Figure 5.9b shows the differences between the model and observations that are seen in the vertical profiles of temperature and dew point temperature for the TBW sounding for 1200 UTC 11 September. The temperature errors in the YSU simulation are around 0.5 $°C$ from near the surface to about 300 m. The temperature errors then decrease to near zero from 600–700 m in the YSU simulation before increasing to around 0.5 $°C$ from 1300–2300 m and then decreasing back to near zero error above 2300 m. The MYNN3 temperature errors are large as seen in the differences between observations and the simulation in Figure 5.9a. From near the surface to about 700 m, the MYNN3 simulation has a temperature error of around 2 $°C$. Above 700 m, the temperature errors in the MYNN3 simulation increase to a peak in error of around 3.25 $°C$ between 1100 and 1200 m, before decreasing back to temperature errors of 0.5 $°C$ at 2000 m. The temperature errors in the ACM2 simulation are around 1.5 $°C$ from near the surface to around 400 m, which slowly decrease through

3000 m to near zero error. The errors in the dew point temperatures are around -1.5 $^\circ C$, 0.5 $^\circ C$, and -0.5 $^\circ C$ for the YSU, MYNN3, and ACM2, respectively, near the surface. From 100–700 m, the YSU simulation has dew point temperature errors around 0.5 $^\circ C$, which then increase to around 1.5 $^\circ C$ between 1300 to 1700 m before dropping to near zero error closer to 3000 m. The MYNN3 dew point temperature errors range between 2–2.5 $^\circ C$ from 100–600 m. Above 600 m, the MYNN3 dew point temperature errors decrease to around 0.5 $^\circ C$ at 900 m before increasing again to 2 $^\circ C$ at 1700 m. From 1700–3000 m, the dew point temperature errors in the MYNN3 simulation decrease toward zero error. The ACM2 dew point temperature errors from 100–2500 m range between 1 and 1.5 $^\circ C$ before decreasing to near zero error around 3000 m.

The vertical profiles of temperature and dew point temperature at Miami (MFL) for 1200 UTC 11 September are shown in Figure 5.10a, which is well south of the tropical cyclone. This vertical profile offers a good comparison between profiles both close and far from the tropical cyclone center. The temperature profiles of the YSU and ACM2 simulations are very similar in the lowest 800 m and both simulations are warmer than observations. Below 800 m, the MYNN3 simulation temperatures are nearly identical to the observed sounding. In the YSU simulation, the temperatures are colder than observations from 1400–3000 m. The MYNN3 simulation becomes cooler than observations more rapidly at around 700 m through 3000 m. The ACM2 temperature profile is colder than observations from 900–3000 m. The dew point temperatures in the YSU and MYNN3 simulations are very similar to the observed dew point temperatures from near the surface to around 1300 m and, dew point temperatures diverge at this height. The ACM2 dew point temperatures are lower than observations near the surface to around 700 m. From 700–1400 m, all three simulations are very close to the observed dew point temperatures. Above 1400 m, the YSU and ACM2 dew point temperatures are very similar and are a bit higher than observations from about 1600 to 2200 m before becoming more similar to the observations above 2200 m. The MYNN3 simulation has a much higher dew point temperature above 1900 m compared to observations.

The RMSE over the lowest 3000 m in the temperature is 1.10 $°C$, 1.18 $°C$, and 1.29 $°C$ for the YSU, MYNN3, and ACM2 simulations, respectively. The dew point temperature RMSE is 0.59 $°C$, 1.17 $°C$, and 1.20 $°C$ for the YSU, MYNN3, and ACM2 simulations, respectively. The temperature and dew point temperatures from the simulations are not statistically significantly different from the observations.

The hodograph inset in Figure 5.10a shows that the model simulations have slightly higher wind speeds compared to the observations. The curvature in the hodographs are similar in the observations and models. The wind speed had a RMSE of 3.50 m/s in the YSU simulation, 2.58 m/s in the MYNN3 simulation, and 3.25 m/s in the ACM2 simulation. None of the simulation wind speeds are statistically significantly different from the observations. The RMSE in the wind direction is 12.75°, 11.02°, and 15.20°, for the YSU, MYNN3, and ACM2 simulations, respectively. The wind direction is statistically significantly different from the observations in the YSU (p=0.00) and ACM2 (p=0.00) simulations.

Figure 5.10b shows the differences between the model and observations that are seen in the vertical profiles of temperature and dew point temperature for the MFL sounding for 1200 UTC 11 September. The temperature errors in the YSU and ACM2 simulations are nearly identical from near the surface to around 800 m ranging from around 1.5 $°C$ and decreasing to around zero. From 800–1300 m, the YSU temperature errors are very close to zero, above which the YSU simulation error peaks at around -2 $°C$ between 1700–2100 m before dropping toward lower temperature errors aloft. The ACM2 simulation diverges from the YSU simulation at 800 m and continues to increase in error to around -2.5 $°C$ at 2000 m before dropping toward zero error above. The temperature errors of the MYNN3 simulation in the lowest 700 m are very low ranging from 0.25 to -0.25 $°C$. The MYNN3 simulation's temperature errors increase and peak at nearly -3 $°C$ at around 2000 m before decreasing toward zero above this level. The dew point temperature errors in the YSU and MYNN3 simulations range between -0.5 and 0.5 $°C$ in the lowest 1400 m. The YSU dew point temperature errors peak at 1.25 $°C$ at 1800 m before decreasing to -0.5 $°C$ above 2300

m. The MYNN3 simulation dew point temperature errors increase to almost 3.5 $^{\circ}C$ at 2700 m. The ACM2 dew point temperature in the lowest 500 m is around -1.75 $^{\circ}C$ and decreases to error around -0.25 $^{\circ}C$ from 700–1500 m. The dew point temperature errors peak in the ACM2 simulation at around 2000 m with a magnitude of around 1.25 $^{\circ}C$ before dropping off to near zero error above 2300 m.

The vertical profiles of temperature and dew point temperature at Jacksonville (JAX) for 1200 UTC 11 September are shown in Figure 5.11a, which is northeast of the center of circulation embedded within heavy tropical cyclone precipitation. The vertical profiles show the temperature and dew point temperature are very close to one another over the lowest 3000 m, indicating a very moist profile. The temperature profiles are very similar in all of the simulations in the lowest 3000 m. From the surface to about 500 m, the three simulations are all warmer than than the observed sounding, and from 500–600 m the temperature in the simulations is very close to observations. Above 600 m, the YSU simulation is warmer than the observed temperature through around 1300 m. From 1300–1800 m, all the simulations are slightly cooler than the observed temperature. Above 1800 m, the simulations are all warmer than observations. Since the profiles are so moist, the dew point temperature in the model simulations are all nearly identical to the temperature, except near the surface. From near the surface to 300 m, the YSU simulation has lower dew point temperatures than the observations. The ACM2 simulation also has lower dew point temperatures than observations from near the surface to about 600 m. The MYNN3 simulation had a very similar dew point temperature profile to the observations. The dew point temperatures in the simulations differ from the observations from 1600–1800 m where there is a brief divergence between the observed temperature and dew point temperature. The RMSE over the lowest 3000 m in the temperature is 0.46 $^{\circ}C$, 0.43 $^{\circ}C$, and 0.45 $^{\circ}C$ for the YSU, MYNN3, and ACM2 simulations, respectively. The dew point temperature RMSE is 0.37 $^{\circ}C$, 0.29 $^{\circ}C$, and 0.53 $^{\circ}C$ for the YSU, MYNN3, and ACM2 simulations, respectively. The temperatures and dew point temperatures from the simulations are not statistically significantly different from the observations.

The hodograph inset in Figure 5.11a shows that the model simulations have higher wind speeds compared to the observations as the hodograph is longer, especially in the MYNN3 simulation. The observed wind hodograph has similar curvature than the model simulations, with again the exception of the MYNN3 simulation which has more elongated curvature. The wind speed had a RMSE of 6.22 m/s in the YSU simulation, 10.93 m/s in the MYNN3 simulation, and 5.75 m/s in the ACM2 simulation. The RMSE in the wind direction is 6.38°, 10.89°, and 6.47°, for the YSU, MYNN3, and ACM2 simulations, respectively. Both the wind speed and direction is statistically significantly different in the MYNN3 (p=0.00) simulation compared to observations, reflective of the large differences pointed out on the hodograph (Fig. 5.11a, inset).

Figure 5.11b shows the differences between the model and observations that are seen in the vertical profiles of temperature and dew point temperature for the JAX sounding for 1200 UTC 11 September. The temperature errors are very similar in the model simulations from near the surface to around 200 m at around 0.5 $°C$. From 200–400 m, the temperature errors in the YSU and the MYNN3 simulations trend towards zero error, but the two simulations diverge at 400 m with the temperature errors in the YSU simulation increasing to 0.5 $°C$, while the MYNN3 simulation has near zero temperature errors from 400–1200 m. The temperature errors above 200 m in the ACM2 simulation are around 0.25 $°C$ through 1200 m. Above 1200 m, the model simulations all show similar temperature errors peaking around -1 $°C$ at 1400 m. The temperature errors at 1900 m in the simulations diverge with the YSU simulation showing a temperature error of around 0.25 $°C$, the MYNN3 simulation showing temperature errors of just over 0.5 $°C$, and the ACM2 simulation showing temperature errors of just under 0.5 $°C$ through 3000 m. The dew point temperature errors in the YSU and MYNN3 simulations are near zero from 100–400 m, after which the errors in the dew point temperatures in the YSU and MYNN3 simulations diverge with the MYNN3 simulation remaining near zero through 1500 m and with the YSU simulation error growing to just above 0.5 $°C$ from 700–1800 m. The ACM2 dew point temperature errors near the surface are around -1.25 $°C$, which reach zero error around 700 m before increasing to about 0.25 $°C$ error from 800–1500 m. As in the temperature errors, the dew point temperature errors peak around 1700 m at 0.75 $°C$ in all three simulations. Above 2000 m, the dew point temperature errors follow very closely to the temperature errors. The YSU dew point temperature errors are around 0.25 $°C$, just over 0.5 $°C$ in the MYNN3 simulation, and just under 0.5 $°C$ in the ACM2 simulation.

At the TBW sounding site at 1200 UTC 10 September, which is on the fringe of the tropical cyclone precipitation, the YSU simulation produced the lowest temperature and dew point temperature RMSEs over the lowest 3000 m (0.91 $°C$ and 1.26 $°C$, respectively). The simulations all showed a cold temperature bias from about 700–2100 m. At the TBW sounding site on 0000 UTC 11 September, which is within the tropical cyclone, the YSU simulation produced the lowest RMSEs in the lowest 3000 m for temperature, dew point temperature, and wind speed with RMSEs of 0.4 $°C$, 0.79 $°C$, and 8.64 m/s, respectively. All simulations show the largest temperature and dew point temperature profile errors occur in the lowest 100–200 m. The TBW sounding site at 1200 UTC 11 September, which is south of the tropical cyclone circulation, shows a warm bias in both the temperature and dew point temperature in all of the simulations in the lowest 3000 m. Like at TBW at 0000 UTC 11 September, the YSU simulation also produces the smallest RMSEs in temperature, dew point temperature, and wind speed with RMSEs of 0.55 $°C$, 1.04 $°C$, and 2.03 m/s, respectively. At the MFL sounding site at 1200 UTC 11 September, which is removed from the tropical cyclone circulation to the south, the YSU simulation produced the lowest RMSEs for the temperature (1.10 $°C$) and the dew point temperature (0.59 $°C$). The MYNN3 simulation produced the lowest RMSE with respect to the wind speed (2.58 m/s). In the low levels, all three simulations show a slight temperature warm bias in the low levels and they show a cold temperature bias aloft. The dew point temperatures in the three simulation show a slight cold bias in the low levels and generally a warm bias aloft. At the JAX sounding site at 1200

UTC 11 September, the MYNN3 simulation produces the lowest RMSEs in the temperature (0.43 °C) and dew point temperature (0.29 °C), and the ACM2 simulation showed the lowest RMSE in the wind speed (5.75 m/s).

The RMSEs for temperature and dew point temperature are summarized in Table 5.2. Across the sounding locations, the average RMSEs for temperature are 0.68 °C, 1.11 °C and 0.83 °C and the average RMSEs for dew point temperature are 0.81 °C, 1.24 °C and 1.22 °C for the YSU, MYNN3, and ACM2 simulations, respectively. As in the Harvey simulations, the 0–3-km temperature and dew point temperature profiles were not statistically significantly different from the observed soundings regardless of time or location. As shown in the soundings near and in the tropical cyclone precipitation, most of the PBL schemes were too cold in the lowest 200 m, but, again, these differences were not statistically significant from the observations. As cited in the Harvey sounding discussion, Hariprasad et al. (2014) and Banks et al. (2016) both noted systematic cold biases with RMSEs around 1 °C in various locations and under various weather flow regimes. Across the sounding locations in Hurricane Irma, the PBL simulations also showed statistically significant differences from one another, most notably at TBW at 0000 UTC 11 September and 1200 UTC 11 September (Figs. 5.8 and 5.9). The MYNN3 simulation showed statistically significantly different temperatures to both the YSU and ACM2 simulations. The YSU simulation showed statistically significantly different dew point temperatures to the MYNN3 simulation in the lowest 3 km at the 95% confidence interval. Differences across the PBL simulations are expected as each handles vertical mixing differently, as discussed in the previous chapter.

Summarized in Table 5.2 are the RMSEs for the wind speed and direction for the Irma simulations compared to the observed soundings. The average wind speed RMSEs are 5.58 m/s, 8.04 m/s, and 6.13 m/s and the average wind direction RMSEs are 20.52°, 19.46°, and 21.54° for the YSU, MYNN3 and ACM2 simulations, respectively. As in Harvey, the MYNN3 simulation produced statistically significantly faster wind speeds most frequently in the simulations of Hurricane Irma. Past literature suggests that the MYNN3 tends to more accurately predict wind speeds in a variety of situations and locations compared to many non-local PBL schemes (Hu et al. 2010; Misaki et al. 2019; Dzebre and Adaramola 2020). Recall that past literature has also suggested that the RMSE in the wind speed increases with increasing wind speed and the wind direction RMSE decreases with increasing wind speed (Surussavadee 2017). In the Irma soundings, the PBL scheme with the highest average wind speed RMSE (MYNN3) also has the lowest average wind direction RMSE, similar to Surussavadee (2017). Both the YSU and ACM2 schemes produced wind directions that were statistically significantly different most frequently across the observed soundings. The wind speeds showed larger RMSEs in the simulations of Hurricane Irma and smaller average wind direction RMSEs compared to what has been seen in past literature (Surussavadee 2017; Misaki et al. 2019; Dzebre and Adaramola 2020).

5.1.3 Harvey reconnaissance flight (USAF 305) dropsonde observations

Dropsonde observations from a reconnaissance flight (USAF 305) into Hurricane Harvey during landfall on 26 August released RD94 dropsondes from 0212–0419 UTC. There were no reconnaissance flights into Hurricane Irma within the analysis time. The dropsondes in Hurricane Harvey were released mainly in the eyewall and near the center of the tropical cyclone during landfall. Figures 5.12–5.17 show the vertical profiles (a) and associated error between the model and observations (b) from each dropsonde during this reconnaissance flight. The flight level at which these dropsondes were released ranges between about 2500 and 2700 m above the ground.

As seen in the model reflectivity loops [`http://www.atmos.albany.edu/student/dcard/files/Animation_Harvey_1km.html`] and in the reflectivity on the right side of Figures 5.1a–5.6a, the eye in the model simulations tends to be much larger than in observations. Thus, in order to align the observed and modeled vertical profiles, additional correction is needed due to the differences in the storm position. It is important to note that this location correction can result in cases where the dropsonde is supplying data over the ocean and the model profile is over land, such that it is important to discount the comparison within the PBL between the model and dropsonde observations, as the effects of the land surface can extend to the top of the PBL. The location of many of the dropsondes are near the eyewall and, as such, simply correcting the model profiles over the ocean would result in large errors in temperature, dew point temperature, and winds compared to the observations. Given the corrections and differences between land and ocean, little discussion will focus on the near surface values or the wind speed and direction. Additionally, the drift in the dropsondes was evaluated (not shown here) and they all showed little drift, most likely due to the fact that they are being dropped from a low altitude.

The first dropdsonde was released at around 0212 UTC 26 August near the eyewall of Hurricane Harvey at a height of around 2700 m (Fig. 5.12a). The vertical profile shows a very moist profile, which is not surprising given the location within the tropical cyclone eyewall. The temperature profile shows that, regardless of the simulation, the model is colder than the observations at nearly all levels above 200 m. The dew point temperatures in the simulations are actually very similar to the observed dew point temperatures, except above about 2000 m where the model dew point temperatures become lower than the observations. Over the drop distance, the temperature of the YSU simulation had an RMSE of 1.54 $^{\circ}C$. The MYNN3 simulation had a RMSE of 1.32 $^{\circ}C$ and the ACM2 simulation had a RMSE of 1.47 $^{\circ}C$. The dew point temperature has a RMSE of 0.49 $^{\circ}C$, 0.51 $^{\circ}C$, and 0.47 $^{\circ}C$ for the YSU, MYNN3, and ACM2 simulations, respectively.

The error between the model and observations in the temperatures and dew point temperatures are shown in Figure 5.12b. Ignoring the near surface, as stated previously, the model simulations show cold errors in the temperatures ranging from around -1 $^{\circ}C$ in the low levels to around -3 $^{\circ}C$ aloft. The dew point temperature error is small, ranging from 0.5 to -0.5 $^{\circ}C$ over the lowest 1800 m.

The hodograph shows that the winds in the model simulations are much weaker than the observations and also have less curvature than the winds observed from the dropsonde. As seen in the hodograph, there is a lot of error in the wind between the model and observations in the wind speed. The RMSEs in the wind speed for this dropsonde are 22.04 m/s, 19.07 m/s, and 22.91 m/s for the YSU, MYNN3, and ACM2 simulations, respectively.

The second dropdsonde was released at around 0218 UTC 26 August within the eye of Hurricane Harvey at a height of around 2600 m (Fig. 5.13a). The vertical profile, again, shows a very moist profile. The temperature profile shows that, regardless of the simulation, the model is slightly colder than the observations at all levels. The dew point temperatures in the simulation are very similar to the observed dew point temperatures. Over the total distance of the dropsonde, the YSU simulation has a temperature RMSE of 1.20 $°C$, the MYNN3 simulation has a RMSE of 1.06 $°C$ and the ACM2 simulation has a RMSE of 1.05 $°C$. The dew point temperature has a RMSE of 0.49 $°C$, 0.57 $°C$, and 0.37 $°C$ for the YSU, MYNN3, and ACM2 simulations, respectively.

The errors between the model and observations in the temperatures and dew point temperatures at each height are shown in Figure 5.13b. Ignoring the near surface, all the model simulations show cold errors in the temperature ranging from around -1 $°C$ in the low levels to around -2 $°C$ aloft. The dew point temperature error ranges from around 1 $°C$ to -0.5 $°C$ above 200 m.

The hodograph shows that the winds in the model simulations are slightly stronger than the observations, but, in both cases, the winds are very weak as they are located in the eye of the hurricane. As seen in the hodograph, the model and observations are in the eye of the simulation such that it does not make sense to discuss the errors in the wind speed or direction for this dropsonde.

The third dropdsonde was released at around 0222 UTC 26 August near the southwest eyewall of Hurricane Harvey at a height of around 2600 m (Fig. 5.14a). The temperature profile shows that the MYNN3 and ACM2 simulations are more similar to the observations than the YSU simulation, which is lower than observations from 400–1800 m. The dew point temperatures in the YSU and ACM2 simulations tend to be colder than observations starting from near the surface to around 1800 m, while the MYNN3 dew point temperatures are very similar to the observations. Over the distance of the dropsonde, the temperature in the YSU simulation has an RMSE of 1.63 $^{\circ}C$, the MYNN3 simulation has a RMSE of 0.62 $^{\circ}C$ and the ACM2 simulation has a RMSE of 1.01 $^{\circ}C$. The dew point temperatures have RMSEs of 1.48 $^{\circ}C$, 0.49 $^{\circ}C$, and 1.16 $^{\circ}C$ for the YSU, MYNN3, and ACM2 simulations, respectively.

The errors between the model and observations in the temperatures and dew point temperatures at each height are shown in Figure 5.14b. The YSU model simulation shows cold errors in the temperatures around -2 $^{\circ}C$ through most of the drop from 400–2000 m. The MYNN3 temperature errors are very low from 200–700 m and increase to about 0.5 $^{\circ}C$ from 900–1700m. The ACM2 temperature errors peak at -1.5 $^{\circ}C$ around 500 m, above which the temperature errors are reduced to near zero. All of the simulations showed large temperature errors near 3000 m as all the simulations failed to capture the increase in temperature in the observations around 2200 m. The dew point temperature errors in the YSU and ACM2 simulations are fairly similar in that both start with errors between -1.5 and -1 $^{\circ}C$, that diverge around 500 m, as the error in the ACM2 simulation decreases and the YSU error is about -1.25 $^{\circ}C$ through 1800 m where the YSU and ACM2 simulations meet again and tend towards zero above. The dew point temperature errors in the MYNN3 simulation are low over the whole drop, ranging between -0.5 and 0.5 $^{\circ}C$ everywhere below 2000 m.

The hodograph shows that the winds in the model simulations are, again, much weaker than the observations and also have less curvature. As seen in the hodograph, there is a lot of error in the wind between the model and observations in the wind speed. The RMSEs in the wind speeds for this dropsonde are 13.74 m/s, 24.94 m/s, and 17.46 m/s for the YSU, MYNN3, and ACM2 simulations, respectively.

The fourth dropdsonde was released at around 0307 UTC 26 August and, like Figure 5.13, was released in the eye of Hurricane Harvey at a height of around 2600 m (Fig. 5.15a). The temperature profile shows that, regardless of the simulation, the model, once again, is colder than the observations at all levels. The dew point temperatures in all of the simulations are very similar to the observed dew point temperatures, except above about 1500 m where the model dew point temperatures become lower than the observations. For temperature over the drop, the YSU simulation has a RMSE of 2.32 $°C$, the MYNN3 simulation has a RMSE of 1.97 $°C$ and the ACM2 simulation has a RMSE of 1.98 $°C$. The dew point temperatures have a RMSEs of 0.74 $°C$, 0.86 $°C$, and 0.71 $°C$ for the YSU, MYNN3, and ACM2 simulations, respectively.

The hodograph shows that the winds in the model simulations are slightly stronger than the observations, but, in both cases, the winds are very weak. As with the previous dropsonde within the eye, it does not make sense to discuss the errors in the wind speed or direction as, for weak winds, wind direction can have large errors. The errors between the models and observations in the temperatures and dew point temperatures at each height are shown in Figure 5.15b. The model simulations show cold errors in temperature ranging from around -3.5 $°C$ in upper levels to around -1.5 to -2 $°C$ in the lower levels in all the simulations. The dew point temperature errors are similar for all the model simulations and range from 0.5 to 0 $°C$ over the lowest 1300–1500 m, before the error in all the simulations grow to about -1.75 $°C$.

The fifth dropdsonde was released at around 0346 UTC 26 August in a rainband to the northeast of the tropical cyclone center at a height of around 2600 m (Fig. 5.16a). The temperature profile shows that, regardless of the simulation, the model is colder than the observations at all levels. The dew point temperatures in the simulations are all warmer than observations above 200 m. Over the drop distance, the YSU simulation temperature has a RMSE of 1.58 $°C$, the MYNN3 simulation has a RMSE of 1.24 $°C$ and the ACM2 simulation has RMSEs of 1.52 $°C$. The dew point temperatures have a RMSE of 1.40 $°C$, 1.15 $°C$, and 1.89 $°C$ for the YSU, MYNN3, and ACM2 simulations, respectively.

The errors between the model and observations in the temperatures and dew point temperatures at each height are shown in Figure 5.16b. Ignoring the near surface, the model simulations show cold errors in temperature ranging from around -1.5 $°C$ in the low levels to around -2.5 $^{\circ}C$ above 1400 m in the YSU and ACM2 simulations. The temperature errors in the low levels are similar in the MYNN3 simulation at around -1.5 $^{\circ}C$, which remains near that value over the entire drop. The dew point temperature errors have a much broader range than the temperature errors. The dew point temperature errors in the YSU simulation tend to increase with height from about 0.5 $^{\circ}C$ at 300 m to 1.5 $^{\circ}C$ near the drop height. The MYNN3 simulation errors stay around 1.5 $^{\circ}C$ through about 1300 m before decreasing to around 0.5 $^{\circ}C$ from 1500–2000 m.The ACM2 simulation dew point temperature errors are larger than the other simulations particularly from 300–1700 m where they range between 2 and 3 $^{\circ}C$.

The hodograph shows that the winds in the model simulations in both speed and curvature are very similar to observations. As seen in the hodograph, there is not a lot of error in the wind between the models and observations in both the wind speed and direction. The RMSEs in wind speed for this dropsonde are 5.60 m/s, 3.85 m/s, and 6.95 m/s for the YSU, MYNN3, and ACM2 simulations, respectively. All the RMSEs of temperature, dew point temperature, and wind are much more analogous to the sounding profiles compared to the other dropsondes, since this drop is not close to the center of Hurricane Harvey.

The sixth, and final, dropdsonde was released at around 0419 UTC 26 August within the eye of Hurricane Harvey at a height of around 2600 m (Fig. 5.17a). The temperature profiles show, regardless of the simulation, the model is slightly colder than the observations at all levels. The dew point temperatures in the simulations are very similar to the observed dew point temperatures, although the YSU simulation tends to be slightly higher than the observations. Over the depth of the drop, the temperature in the YSU simulation has an RMSE of 1.57 $^{\circ}C$, the MYNN3 simulation has a RMSE of 1.45 $^{\circ}C$ and the ACM2 simulation has a RMSE of 1.52 $^{\circ}C$. The dew point temperatures have a RMSE of 0.84 $^{\circ}C$, 0.81 $^{\circ}C$, and 0.63 $^{\circ}C$ for the YSU, MYNN3, and ACM2 simulations, respectively. The errors between the model and observations in the temperatures and dew point temperatures at each height are shown in Figure 5.17b. All the model simulations show a cold error in the temperatures ranging from around -2.5 $^{\circ}C$ around 300 m to between -1 and -0.5 $^{\circ}C$ at around 900 m. Above 1300 m, the temperature errors of all the simulations range from -1 to -2 $^{\circ}C$. The dew point temperature errors in the YSU simulation range from near 0 $^{\circ}C$ to 1 $^{\circ}C$ from 300–800 m, above which the errors remain about 1 $^{\circ}C$. The ACM2 simulation dew point temperature errors are similar, in that they start with near zero error around 300 m and increase to about 0.5 $^{\circ}C$ by about 600 m, where they remain through the rest of the profile. The MYNN3 dew point temperature errors have around zero error at 300 m and peak at about 1000 m at an error of around 1 $^{\circ}C$ before returning to near zero error aloft. The hodograph shows that the winds in the model simulations are slightly stronger than the observations, but, in both cases, the winds are very weak.

All of the dropsondes examined showed no statistically significant differences in the temperature and dew point temperature between the simulations and the observed values. It was also the case that the model simulations showed no statistically significant differences when compared to one another in terms of the temperatures and dew point temperature. With the exception of the dropsonde in the outer rainband (Fig. 5.16), all the dropsondes showed low-level winds that differed significantly between the observations and the simulations.

The MYNN3 and ACM2 simulations both showed the most similarities between the models and observations in the temperature and dew point temperature profiles of all of the dropsondes, producing the lowest RMSEs in the lowest 3 km. In the dropsonde observations within the tropical cyclone precipitation, the temperatures in the model tend to be colder than observations. A similar phenomenon was also seen in the soundings within the tropical cyclone, reinforcing the idea that the model has a cold bias compared to observations within the tropical cyclone precipitation. Cold biases in WRF simulations have been seen in precipitating and non-precipitating events in Europe during the summer months (García-Díez et al. 2013). Gunwani and Mohan (2017) showed similar results in India. Both García-Díez et al. (2013) and Gunwani and Mohan (2017) attribute this cold bias to the differences in the radiative balance and not the lack of entrainment in PBL schemes. In comparing individual PBL schemes, García-Díez et al. (2013) showed that the local PBL schemes tended to produce the strongest cold temperature biases compared to non-local schemes like the YSU (García-Díez et al. 2013; Cohen et al. 2017). This is attributed to the ability of non-local PBL schemes to promote relatively deeper PBLs compared to local schemes (García-Díez et al. 2013).

5.2 Depth of the tropical cyclone radial inflow

As in the previous chapter, the inflow depth is defined, as in Zhang et al. (2011c), as the height at which the inflow falls to 10% of its maximum value. Zhang et al. (2011c) ascertained that the inflow depth represents the top of the hurricane boundary layer better than the thermodynamic boundary layer depth and that methods to identify the depth of the boundary layer using a CRN may not produce the correct pattern of behavior of the PBL height in numerical models. The depth of the inflow in both hurricanes Harvey and Irma is examined and compared to observations from within the tropical cyclone. In Hurricane Irma, the TBW sounding site at 1200 UTC 10 September and 0000 UTC 11 September will be used to analyze the radial inflow (Figs. 5.7 and 5.8). For Hurricane Harvey, the sounding site at CRP at 0000 UTC 26 August will be used, along with the dropsonde from the rainband of Hurricane Harvey (Figs. 5.2 and 5.16). Additionally, the radial velocities from a mobile Doppler radar positioned to capture the landfall of Hurricane Harvey will also be used to diagnose the radial inflow. The particular soundings and dropsondes for each storm were chosen because they are close to the tropical cyclone, but not within the eye or eyewall. Locations within the eye and near the eyewall exhibit the largest gradients in wind spatially and, therefore, measurements are very sensitive to the location of the sounding or dropsonde in comparison to the model vertical profile location.

5.2.1 Radiosondes and dropsondes

The sounding for Hurricane Harvey from CRP at 0000 UTC 26 August is located just outside the eyewall as seen in Figure 5.2a. Figure 5.18 (left) shows that the observed radial inflow at the CRP sounding site is very similar to the YSU and ACM2 simulations over the lowest 3000 m. The observations show a maximum radial inflow of about -14 m/s at around 300 m. The YSU and ACM2 simulations show that the radial inflow peaks between 100 and 200 m at -12 and -13 m/s, respectively. The MYNN3 simulation has a much stronger radial inflow compared to the observations around -20 m/s between 100–200 m. The simulations switch from radial inflow to radial outflow between 850 and 1000 m, with the observations switching at around 800 m. The model simulations show PBL heights of around 1450 m, 500 m, and 1300 m in the YSU, MYNN3, and ACM2 simulations, respectively. The inflow depths for the model simulations are around 950 m, 900 m, and 800 m in the YSU, MYNN3, and ACM2 simulations, respectively. The model inflow depths are all very similar to each other and are about 200–300 m higher than the observations, which showed an inflow height of around 650 m. The modeled PBL height in the MYNN3 simulation was the closest to the observed inflow height from CRP at 0000 UTC 26 August.

A dropsonde released into Hurricane Harvey around 0346 UTC 26 August in a rainband northeast of the tropical cyclone center is seen in Figure 5.16a. Figure 5.18 (right) shows the observed radial inflow at the dropsonde location is weaker than all of the model radial inflows through the depth of the dropsonde. The observations show a maximum in radial inflow of around 10 m/s that extends from near the surface to about 400 m. The YSU simulation shows a maximum in the radial inflow around -16 m/s, and the MYNN3 simulation shows a maximum in the radial inflow around -13 m/s, with both simulations peaking from 100–300 m. The maximum in radial inflow for the ACM2 simulation is around -12 m/s and peaks much higher than the observations or other models between 400 and 700 m. Both the simulations and the observations tend to weaken in radial inflow with height (Fig. 5.18). The model simulations show PBL heights of around 1550 m, 500 m, and 1000 m in the YSU, MYNN3, and ACM2 simulations, respectively. The inflow depths for the model simulations were around 1400 m in the YSU, 2900 m in the MYNN3, and 1850 m in the ACM2. The model inflow depth in the MYNN3 simulation is so high because the radial inflow does not drop off very rapidly. Similarly, because the maximum in the radial inflow in the ACM2 simulation is higher than the other simulations, the inflow depth is also shifted upward. The observed inflow depth is around 1600 m. Both the model PBL height and inflow depth for the YSU simulation were very close to the observed inflow depth from this dropsonde in Hurricane Harvey.

The sounding for Hurricane Irma from TBW at 1200 UTC 10 September is located on the fringes of the tropical cyclone precipitation, as seen in Figure 5.7a. Figure 5.19 (left) shows that the observed radial inflow at the TBW sounding site is very similar to the YSU simulation over the lowest 300 m. The observations show a maximum radial inflow of about -9 m/s at around 300 m and again at around 1200 m. The YSU and ACM2 simulations show that the radial inflow peaks between 100 and 200 m at -8.5 and -6.5 m/s, respectively. The MYNN3 simulation has a much weaker radial inflow compared to the observations and the other simulations at around -3.5 m/s peaking between 100–200 m. The model simulations show PBL heights of around 800 m, 500 m, and 1150 m in the YSU, MYNN3, and ACM2 simulations, respectively. The inflow depths for the model simulations were around 700 m, 400 m, and 900 m in the YSU, MYNN3, and ACM2 simulations, respectively. The observations showed an inflow height of around 1350 m, due to the very deep radial inflow observed in the sounding. The modeled PBL height in the ACM2 simulation was the closest to the observed inflow height from TBW at 1200 UTC 10 September.

The sounding for Hurricane Irma from TBW at 0000 UTC 11 September is located within the tropical cyclone precipitation, as seen in Figure 5.8a. Figure 5.19 (right) shows that the observed radial inflow at the TBW sounding site is very similar to the YSU and ACM2 simulations through the lowest 600 m. The observations showed a maximum radial inflow of around -24 m/s at 500 m. The YSU simulation shows a maximum in radial inflow of around -23.5 m/s between 400–600 m. The ACM2 simulation has a maximum in radial inflow around -24 m/s between 200–500 m. The MYNN3 simulation has the most shallow radial inflow that reaches a maximum of around -22 m/s between 100–200 m, before quickly becoming radial outflow. The model simulations show PBL heights of around 1400 m, 400 m, and 1400 m in the YSU, MYNN3, and ACM2 simulations, respectively. The inflow depths for the model simulations are around 2050 m in the YSU, 400 m in the MYNN3, and 1300 m in the ACM2. The observed model inflow depth is around 1100 m. The YSU simulation has such a high inflow height due to the fact the radial inflow does not drop off as rapidly with height as seen in the ACM2 and MYNN3 simulations. The MYNN3 inflow height is the most similar to the observations, even though the radial inflow was more shallow by about 200 m. The YSU and ACM2 simulations show the modeled PBL height most similar to the observed inflow depth with a difference of around 300 m.

5.2.2 Mobile radar inflow observations

The mobile Doppler radar observations allow for the the examination of the radial winds using the radial velocities, which show the components of the wind toward (blue) and away from (red) the radar. This wind information is used to study the depth of the boundary layer as done in Alford et al. (2020) for Hurricane Irene (2011).

Both Figures 5.20 and 5.21 show cross sections of Hurricane Harvey's boundary layer prior to landfall across the coastline. The cross section in Figure 5.20 at 2349 UTC 25 August shows that the center of Harvey is about 80 km to the southeast of the radar site, with the eyewall (RMW) located at about 22 km. From 44–80 km from the center, or from two to three-and-a-half times the RMW, the inflow depth increases from about 900 to 1200 m. The cross section in Figure 5.21 at 0004 UTC 26 August shows the center of Harvey about 76 km to the southeast of the radar site, with the eyewall (RMW) located at about 20 km. From 50–76 km from the center, or from two-and-a-half to almost four times the RMW, the inflow depth increases rapidly from about 400 m to about 1200 m at three times the RMW, before decreasing back to around 900 m at just less than four times the RMW. In Figure 5.21, the coast line of Texas is at approximately 50 km from the radar site. At about 30 km from the radar site, the approximated inflow depth decreases to below the lowest observation angle of the model radar going toward the center of Harvey. A similar decrease in the approximate inflow height is seen in Figure 5.20 going across the coastline and in towards the center of the storm.

Both Figures 5.22 and 5.23 show cross sections of Hurricane Harvey's boundary layer after landfall when the center of the storm is over Texas. The cross section in Figure 5.22 at 1025 UTC 26 August shows that the center of Harvey is located at about 46 km north of the radar site, with the eyewall (RMW) located at about 8 km. The inflow depth is very consistent from 20–44 km or from about two-and-a-half to about five-and-a-half times the RMW at about 700 m. The cross section in Figure 5.23 at 1154 UTC 26 August shows that the center of Harvey is about 60 km north of the radar site, with the eyewall (RMW) at about 14 km from Harvey's center. Similar to Figure 5.22, the inflow depth is very consistent from 28–60 km from the center of Harvey or from two to four times the RMW at about 700 m. The inflow depth over land shows a much more consistent pattern than along the coastline.

Across the coast, Figure 4.11 showed the model reflectivity and cross section radial wind at 0000 UTC 26 August, similar to the mobile Doppler radar observation time. The cross sections show that over the land the inflow depth is deepest in the YSU and ACM2 simulations by about 200–400 m compared to the MYNN3 simulation. Both the YSU and ACM2 simulations showed PBL heights that are decoupled from this inflow height, unlike the MYNN3 simulations. The YSU and ACM2 simulations also had a large discontinuity in the PBL height near the coastline of the model simulations. In the YSU PBL scheme, where the PBL transitions from the land to ocean, the CRN changes as described in the previous chapter and the PBL height responds to this change in CRN by abruptly dropping from 1800 m in depth to around 300 m. A similar discontinuity is found in the ACM2 simulation where, although the CRN does not change, the stability changes from the land to the ocean

(Fig. 4.8) resulting in a drop in the PBL height from around 1600 m to 500 m.

Over the ocean prior to landfall, the inflow depth in Harvey was less than that observed over land at the same time (Figs. 5.20 and 5.21). Once the hurricane was fully over land, the inflow depth proved to be very consistent around 700 m in both the inflow cross sections (Figs. 5.22 and 5.23). Similar findings were found in Alford et al. (2020), particularly at the land–ocean interface, that there is a transition from the hurricane boundary layer over the ocean to the internal boundary layer over land, of which the hurricane boundary layer was generally lower in height compared to the internal boundary layer. In general, the strength of the inflow observed in all the velocity cross sections ranged from 15 to over 20 m/s (Figs. 5.20, 5.21, 5.22, and 5.23).

5.3 Observations of cell reflectivity in Hurricane Harvey

The mobile Doppler radar also allows for examination of the vertical reflectivity profiles of rotating and non-rotating convection to compare to the model reflectivity presented in the cell composites from Chapter 3 (Figs. 3.32, 3.33, 3.34, and 3.35) and structures seen in past literature (Hence and Houze 2008; Li and Wang 2012; Card 2019). In Chapter 3, the vertical reflectivity structures showed the most difference between the non-rotating and rotating cell composites. Since the tilt in the reflectivity cross section is with respect to the mobile radar location, it is important to note that the direction of the tilt will be different with respect to the center of Harvey. The non-rotating cell composites showed reflectivity had no tilt with height (Fig. 3.45), while the rotating cell composites showed that the reflectivity was generally shallower than the non-rotating composites and tilted with height (Fig. 3.44). These structures were also seen in past literature in cross sections of tropical cyclone rainbands (Hence and Houze 2008; Li and Wang 2012; Card 2019) dependent on if the cross section is taken in the mature or non-mature parts of the principal rainband.

Figures 5.24, 5.25, and 5.26 show the planar and cross section reflectivity, and velocity, from three rotating cells identified in the mobile Doppler radar velocity. The cell at 2207

UTC 25 August is located at about 97°W and 28.4°N in the planar plots of Figure 5.24. The planar velocity shows that this particular convective cell is rotating (Fig. 5.24b). The radar reflectivity cross section shows the cell, located at about 43 km from the radar location, is only slightly tilted away from the radar with height at this time, which is analogous to tilting radially outward with height from the center of Harvey. The maximum in reflectivity for this rotating cell is located in the lowest sweep at about 500 m extending to about 2000 m in height with a magnitude of about 45 dBZ. The second rotating cell was observed in the same line as the first cell at 2216 UTC 25 August and is located at about 97°W and 28.4°N in the planar plots in Figure 5.25. The planar plot of velocity shows this particular cell is rotating (Fig. 5.25b). The reflectivity cross section shows that this cell is located about 52–60 km away from the mobile radar location and is tilted away from the radar with height. A tilt away from the radar at this location is analogous to a tilt radially outward from the center of Harvey. In this cell, the 45 dBZ isodop extends upward from the lowest radar elevation to about 750–2500 m. The final rotating cell in this analysis was at 2225 UTC 25 August at about 97°W and 28.2°N in the planar plots in Figure 5.26. The planar plot of velocity again shows this particular cell is rotating (Fig. 5.26b). The reflectivity cross section shows that this cell is about 49 km from the radar and has a clear tilt toward the radar with height. At this location, a tilt toward the radar is analogous to a tilt radially outward from the center of Harvey. The depth of the 45 dBZ reflectivity extends from the lowest radar angle around 500 m to about 4000 m in height.

The mobile radar was able to intersect many non-rotating cells at once. The first cross section at 0954 UTC 26 August intersected three convective cells that were not rotating in the radar velocity (Fig. 5.27b). The first cell is located about 22 km away from the radar site along a very prominent rainband moving away from the center of Harvey. The second cell is located about 56 km away from the radar site along a more scattered rainband, as is the third cell that is located about 86 km away from the radar site (Fig. 5.27a). The reflectivity in all three cells lacks any tilt with height, especially the first cell (located at 22 km), which has the appearance in reflectivity of a mushroom. With exception of the second cell, the first and third non-rotating cells extend to about 5500 m in height. In the first cell, which is a part of the principal rainband, the maximum in reflectivity extends from the lowest radar angle at about 250 m to about 5500 m with a reflectivity of about 45 dBZ. In the second cell, the 45 dBz isodop extends from the bottom of the radar sweep to about 2500–3000 m, and the third cell extends to about 5500 m. The second cross section at 1101 UTC 26 August shows a cross section containing two non-rotating cells (Fig. 5.28). The first cell is located about 25 km from the radar site in scattered rainband convection. The first cell is a bit more shallow than the second cell, only extending to about 4000 m in height with the highest reflectivity of around 40 dBZ extending from about 250 m to 2500 m, and does not show any tilt with height. The second non-rotating cell is located about 46 km from the radar site and extends from about 500–5500 m with the maximum in reflectivity around 45 dBZ removed from the surface from about 4500–5500 m in height. Again, this second cell doesn't show any tilt with height and, like the first cell in Figure 5.27, seems somewhat mushroom shaped.

5.4 Summary and discussion

The vertical profiles of temperature and dew point temperature in the simulations of hurricanes Harvey and Irma both tended to preform best in the areas of the tropical cyclone with high moisture content. In the simulations of both Harvey and Irma, the YSU and ACM2 simulations produced the least RMSEs of temperature and dew point temperature in the lowest 3000 m; however, almost every profile within the tropical cyclone precipitation exhibited a cold bias near the surface in each PBL scheme. These results echo the findings of García-Díez et al. (2013) that the diurnal, seasonal, and geographical sensitivities of PBL schemes over Europe showed cold biases in surface temperatures throughout the summer both in precipitating and clear sky situations. Gunwani and Mohan (2017) echoed the results of García-Díez et al. (2013) for regions over India. Specifically, the local PBL schemes tended to produce the strongest cold temperature biases compared to the YSU and ACM2 schemes (García-Díez et al. 2013; Cohen et al. 2017). The YSU and ACM2 simulations typically present the warmest temperatures in the PBL, which García-Díez et al. (2013) attribute to the ability of non-local PBL schemes to promote relatively deeper PBLs compared to local schemes. These cold biases present an interesting problem for the YSU PBL scheme, in particular. As discussed in Chapter 3, the YSU scheme CRN is dependent on the near surface stability. As shown in Figure 4.6, the first model level virtual potential temperature in the YSU simulations is only about 1–3K colder than the surface, which is cool enough to support the stable boundary layer revision for the YSU scheme from Hong (2010). As mentioned previously, the stable boundary layer revision (Hong 2010) alters the CRN from zero to 0.25. The cold temperature biases observed in both the soundings and dropsondes ranged from 1–2K near the surface in the YSU scheme, which may incorrectly define the state of the PBL as stable when it is closer to moist neutral or weakly unstable, as seen in the vertical profiles and by the amount of CAPE in the boundary layer. As discussed previously, the variation of CRN can drastically alter other mechanisms within the PBL such as the PBL height and the vertical mixing; thus, making a mistake in assigning the CRN to 0.25 could alter the mechanisms in the PBL for the wrong reasons in the YSU scheme, particularly in the landfalling hurricane environment. This result continues to echo the findings of Kepert (2012), that although non-local KPP closure PBL schemes can preform satisfactorily in some situations (Nolan et al. 2009a,b), KPP schemes, specifically the YSU, should be used with caution. This caution is particularly relevant to the case here where, although the YSU simulations are preforming well compared to the observations of temperature and dew point temperature, it may be the result of incorrect assumptions.

The composite radial inflow in Harvey (Fig. 5.18) showed that both observations are located within the tropical cyclone precipitation and the sounding is located over land (Fig. 5.2) and the dropsonde is located over the ocean in a distant rainband (Fig. 5.16). In the previous chapter, the differences between the ocean and land vertical profiles were noted comprehensively with the PBL height shown to be deeper over land (Fig. 4.4) and inflow depth shown to be deeper over the ocean. Overall, the PBL height in the MYNN3 simulation was the closest to the inflow depth of the observed vertical profile over land. The YSU and ACM2 simulations produced PBL heights that were about 650–800 m too deep, although the inflow depth was very similar between the YSU, MYNN3 and ACM2 simulations and the observations. The results of the land vertical profile (Fig. 5.18) inflow depth were very similar to the dropsonde observation composite from Zhang et al. (2011c). In the ocean vertical profile, the YSU simulation produced both the inflow depth and PBL height most similar to the observed inflow height. There was a large discrepancy between the MYNN3 and ACM2 simulated PBL heights and the inflow depths. Compared to the dropsonde observation composite from Zhang et al. (2011c), the observed inflow depth of the dropsonde in the distant rainband was higher by 300–400 m.

The composite radial inflow in Irma (Fig. 5.19) showed that for both times at TBW the soundings are located near and within the tropical cyclone precipitation (Figs. 5.7 and 5.8). Both vertical profiles were located over land and, thus, as seen in the previous chapter, differences between the ocean and land vertical profiles were noted in depth with the PBL height shown to be deeper over land (Fig. 4.5). Over both sounding sites, the ACM2 simulation preformed best producing the closest PBL height to the observed inflow depth; however, the MYNN3 simulation in the second observation (Fig. 5.19, right) showed the inflow depth that was closest to the observed inflow depth. The composite radial inflow from the dropsonde composite from Zhang et al. (2011c) peaked at about 1200 m, which is within 100–200 m of the observed at both of the TBW sounding sites.

The inflow depth measured by the mobile Doppler radar observations showed (Figs. 5.20 and 5.21) the existence of an internal boundary layer over land and a hurricane boundary layer over the ocean, similar to the results seen in radar observations of the landfall of Hurricane Irene (2011) (Alford et al. 2020). The approximate inflow depth in the 2349 UTC 25 August cross section (Fig. 5.20) increased from 900–1200 m from two to three-and-a-half times the RMW. In comparison, the dropsonde composite of Zhang et al. (2011c) showed an increase in the inflow depth from 1000–1200 m from two to three-and-a-half times the RMW. The inflow depth in the 0004 UTC cross section (Fig. 5.21) showed an increase from about 400 to 1200 m from about two-and-a-half to three-and-a-half times the RMW before decreasing back to around 900 m at four times the RMW. Again, comparing to the dropsonde composites of Zhang et al. (2011c), the inflow depth increases from just over 1000 to 1200 m at three-and-a-half times the RMW, where it peaks before dropping back to around 1000 m at four times the RMW, which is a similar peak and drop off to what is seen in the observed inflow.

The modeled inflow depth and reflectivity at 0000 UTC 26 August across the coast (Fig. 4.11) were presented in the previous chapter. The YSU simulation showed an inflow depth that increases from about 600 m near the RMW to a peak around two times the RMW at 1100 m, before decreasing back to around 600 m. In the MYNN3 simulation, the inflow depth increases from around 200 m at the RMW and plateaus at about 700 m. The ACM2 simulation showed a rapid increase in the inflow depth near the RMW, increasing from about 300–700 m before decreasing to about 600 m at two times the RMW. Beyond two times the RMW, the inflow depth quickly increases to around 1100 m before slowly falling off at larger multiples of the RMW. Although there was a discontinuity in the PBL heights present at the coasts in the YSU and ACM2 simulations, they performed well in terms of the inflow depth observed beyond two times the RMW in the mobile Doppler radar cross sections.

The inflow depths of the cross sections at 1025 UTC and 1154 UTC 26 August (Figs. 5.22 and 5.23) were consistent at around 700 m in depth from two-and-a-half to five times the RMW. Over land, the observed inflow height is much different than what was observed in the dropsondes from Zhang et al. (2011c). Over land, the inflow depths were constant with multiples of the RMW in the model simulation cross sections from the previous chapter (Fig. 4.13) at 1000 UTC 26 August. Over land, the MYNN3 simulation preformed best in comparison to the mobile Doppler radar cross sections, while the YSU and ACM2 simulations produced inflow that was generally deeper than observed by about 100–400 m. The static nature of the inflow depth over land is more characteristic of the internal boundary layer observed during the landfall of Hurricane Irene, which was fairly consistently around 1000 m in depth (Alford et al. 2020).

The mobile Doppler radar also allowed for the examination of the reflectivity structure of rotating and non-rotating cells during the landfall of Hurricane Harvey. All of the observed rotating cells in the radar reflectivity cross section showed some degree of tilt with height radially outward from the center of Harvey (Figs. 5.24, 5.25, and 5.26). This tilt radially outward with height was analogous to the tilt in the reflectivity seen in the rotating cell composites of Harvey (Figs. 3.34 and 3.35) and has been seen in observational and modeling studies (Barnes et al. 1983; Hence and Houze 2008; Yu and Tsai 2013; Moon and Nolan 2015a; Tang et al. 2018b; Card 2019). The maximum in reflectivity (around 45 dBZ) of the observed rotating cells was concentrated near the lowest radar angle and extended to about 2000–4000 m, which aligns well with the vertical extent seen in past literature (Eastin and Link 2009; Card 2019), as well as the vertical extent seen in the composites in the previous chapter (Figs. 3.34 and 3.35). Overall, the structure of both the rotating cell composites (Figs. 3.34 and 3.35) and past observational studies of convection in tropical cyclones (Hence and Houze 2008; Eastin and Link 2009; Card 2019) showed very similar features.

The observed non-rotating cells in the radar reflectivity cross sections did not show any tilt with height, which is similar to the non-rotating cell composites in Hurricane Harvey (Figs. 3.32 and 3.33). The maximum in reflectivity in the observed non-rotating cells was typically between 40 and 45 dBZ, and extended from the lowest radar angle, which varied between 250 and 500 m to approximately 4000–5000 m in height. The non-rotating cell composites from the model simulations of Harvey (Figs. 3.32 and 3.33) showed that the 45-dBZ model reflectivity generally extended to about 6000 m in height, which is a bit higher than the observed cells in the cross sections (Figs. 5.27 and 5.28), although both show a mushroom like shape to the reflectivity, very similar to the non-rotating cell composites.

Overall, the structure of both the non-rotating cell composites (Figs. 3.32 and 3.33) and past observational studies of convection in tropical cyclones (Hence and Houze 2008; Li and Wang 2012) showed very similar features.

5.5 Tables and figures

Table 5.1: The RMSE for the temperature (°C), dew point temperature (°C), wind speed (m/s), and wind direction (°) of the simulations compared to the observed soundings for Hurricane Harvey. An asterisks indicates that the value is statistically significantly different from the observations at the 95% confidence interval (p≤0.05)

Harvey Sounding RMSE						
Date	**Site**	**Simulation**	**Temperature (°C)**	**Dew Point Temperature (°C)**	**Wind Speed (m/s)**	**Wind Direction (°)**
0000 UTC 26 August	BRO	YSU	2.05	0.55	1.04	7.02
		MYNN3	2.31	0.68	3.52*	4.60
		ACM2	1.09	0.94	2.08	13.55*
	CRP	YSU	0.70	1.48	2.99	7.73
		MYNN3	1.43	1.23	7.15*	12.04
		ACM2	1.04	1.08	3.13	6.71
1200 UTC 26 August	BRO	YSU	1.60	1.07	1.94	18.37
		MYNN3	2.21	0.78	1.45	23.46
		ACM2	2.10	1.13	1.53	13.78
	LCH	YSU	1.03	1.63	2.51	137.25
		MYNN3	0.74	2.56	2.16	147.76*
		ACM2	0.55	1.10	1.89	160.86*
0000 UTC 27 August	BRO	YSU	1.28	1.27	4.86*	28.03
		MYNN3	1.94	2.03	3.89*	20.16
		ACM2	2.19	1.02	4.75*	18.09
	CRP	YSU	1.49	1.02	6.91*	10.09*
		MYNN3	1.32	0.76	2.81	8.85*
		ACM2	1.27	1.29	6.04*	15.43*
Average		**YSU**	**1.36**	**1.17**	**3.38**	**34.75**
		MYNN3	**1.66**	**1.34**	**3.50**	**36.15**
		ACM2	**1.37**	**1.09**	**3.24**	**38.07**

Table 5.2: The RMSE for the temperature ($^{\circ}C$), dew point temperature ($^{\circ}C$), wind speed (m/s), and wind direction ($^{\circ}$) of the simulations compared to the observed soundings for Hurricane Irma. An asterisks indicates that the value is statistically significantly different from the observations at the 95% confidence interval (p$\leq$0.05)

Irma Sounding RMSE						
Date	**Site**	**Simulation**	**Temperature (° C)**	**Dew Point Temperature (°C)**	**Wind Speed (m/s)**	**Wind Direction (°)**
1200 UTC 10 September	TBW	YSU	0.91	1.26	7.51*	65.46
		MYNN3	1.15	2.09	6.87	65.44
		ACM2	0.94	2.01	8.44*	65.75
0000 UTC 11 September	TBW	YSU	0.40	0.79	8.64	12.83
		MYNN3	0.66	0.88	11.99*	4.59
		ACM2	0.51	1.01	11.09*	10.50
1200 UTC 11 September	TBW	YSU	0.55	1.04	2.03	5.18*
		MYNN3	2.14	1.77	7.85*	5.37
		ACM2	0.98	1.37	2.12	9.77*
	MFL	YSU	1.10	0.59	3.50	12.75*
		MYNN3	1.18	1.17	2.58	11.02
		ACM2	1.29	1.20	3.25	15.20*
	JAX	YSU	0.46	0.37	6.22	6.38
		MYNN3	0.43	0.29	10.93*	10.89*
		ACM2	0.45	0.53	5.75	6.47
Average		**YSU**	**0.68**	**0.81**	**5.58**	**20.52**
		MYNN3	**1.11**	**1.24**	**8.04**	**19.46**
		ACM2	**0.83**	**1.22**	**6.13**	**21.54**

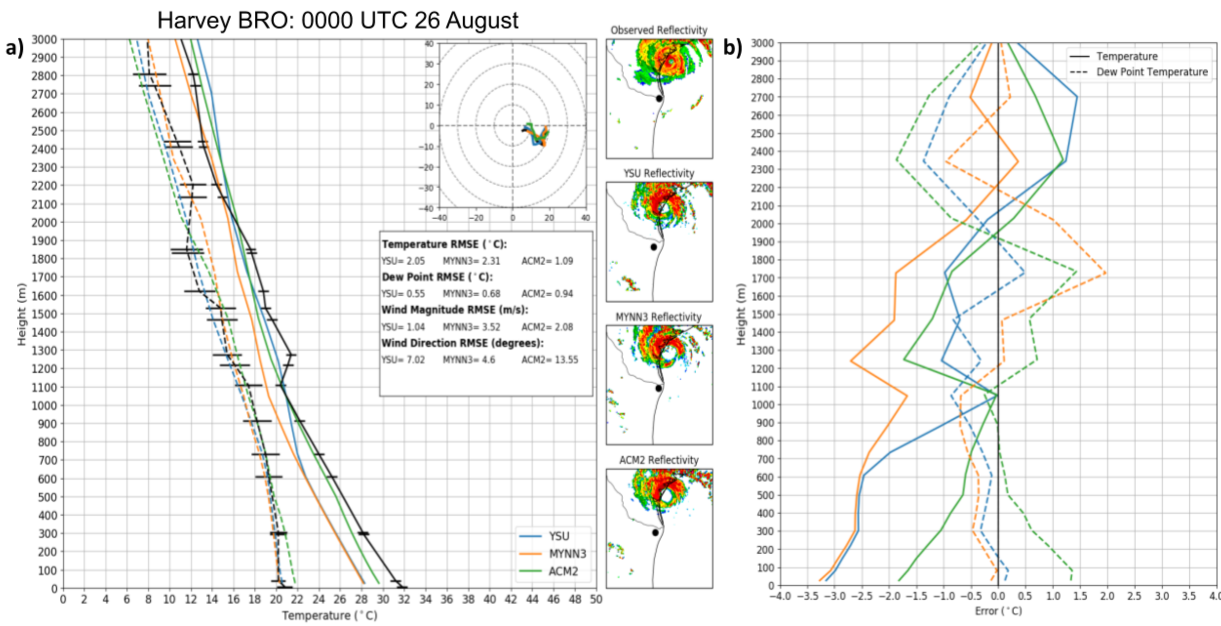

Figure 5.1: Harvey BRO 0000 UTC 26 August a) vertical profile of temperature ($^{\circ}C$, solid), dew point temperature ($^{\circ}C$, dashed), hodograph (m/s, inset), and RMSE of the temperature, dew point, wind speed, and wind direction over the lowest 3 km (inset). The uncertainty in the temperature and dew point temperature measurements for the observations are shown in the horizontal error bars. Located to the right of the vertical profiles are reflectivity plots from the observed Hurricane Harvey and the model with the location of the vertical profiles (black dot). Error of the temperature and dew point with respect to height (b).

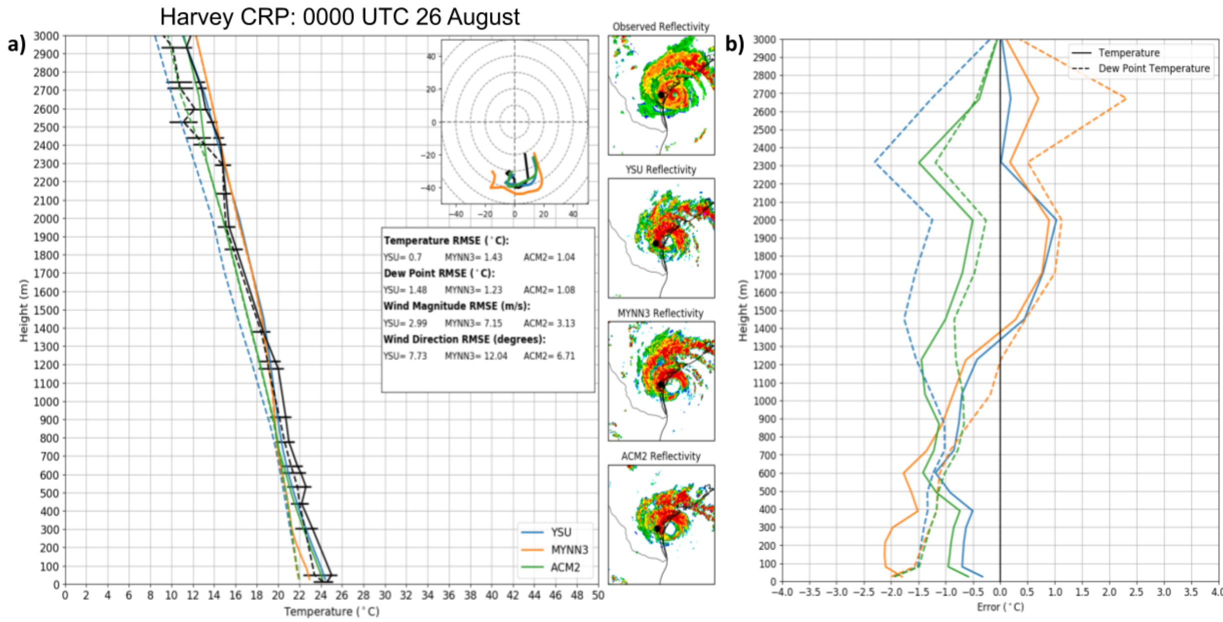

Figure 5.2: Same as Figure 5.1, but for CRP at 0000 UTC 26 August.

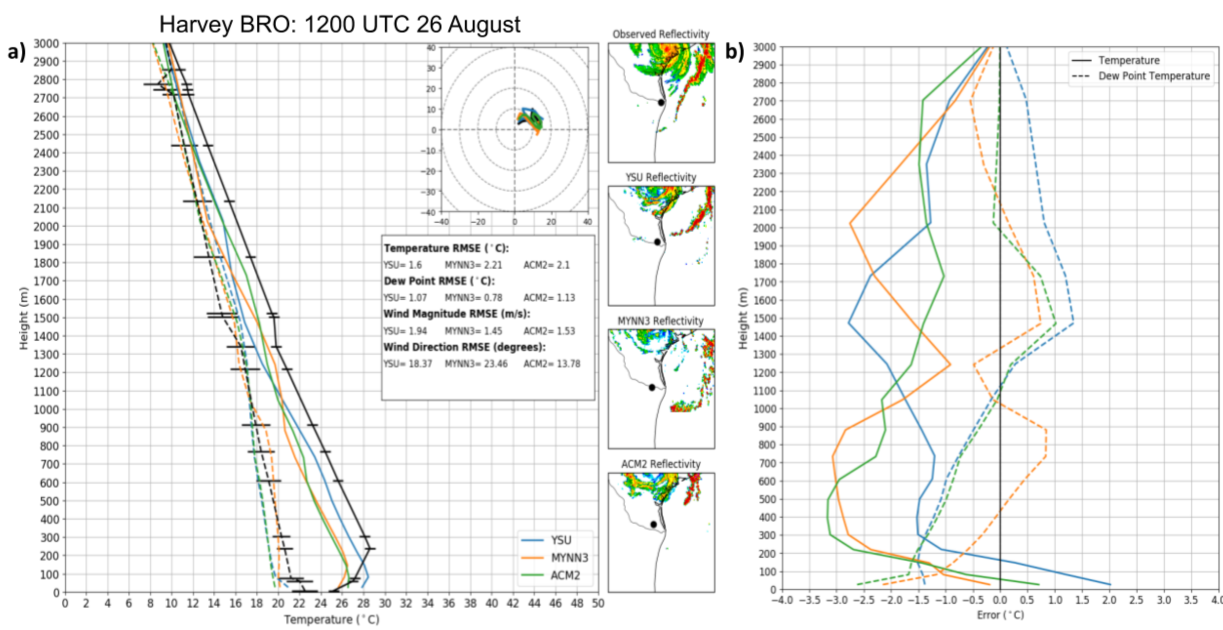

Figure 5.3: Same as Figure 5.1, but for BRO at 1200 UTC 26 August.

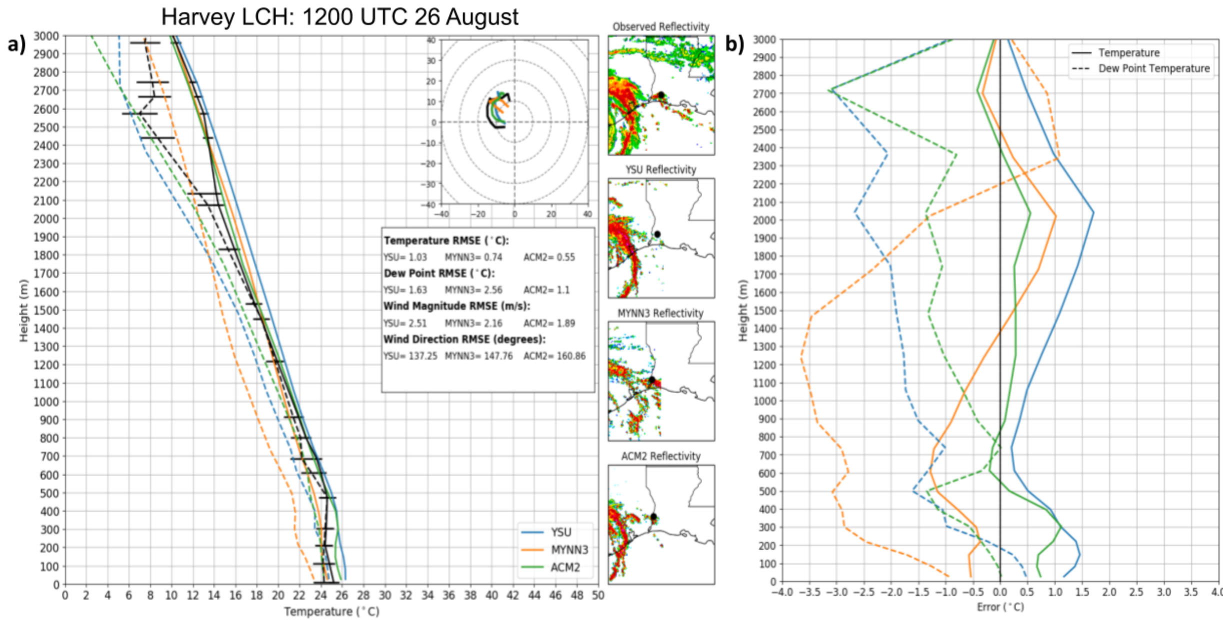

Figure 5.4: Same as Figure 5.1, but for LCH at 1200 UTC 26 August.

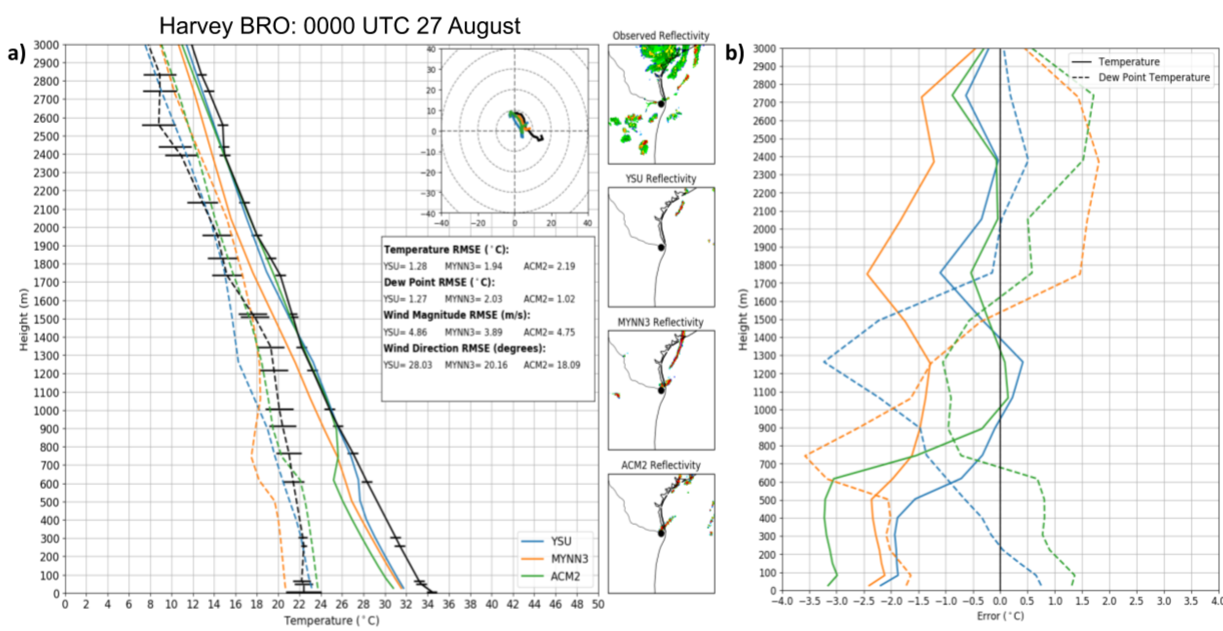

Figure 5.5: Same as Figure 5.1, but for BRO at 0000 UTC 27 August.

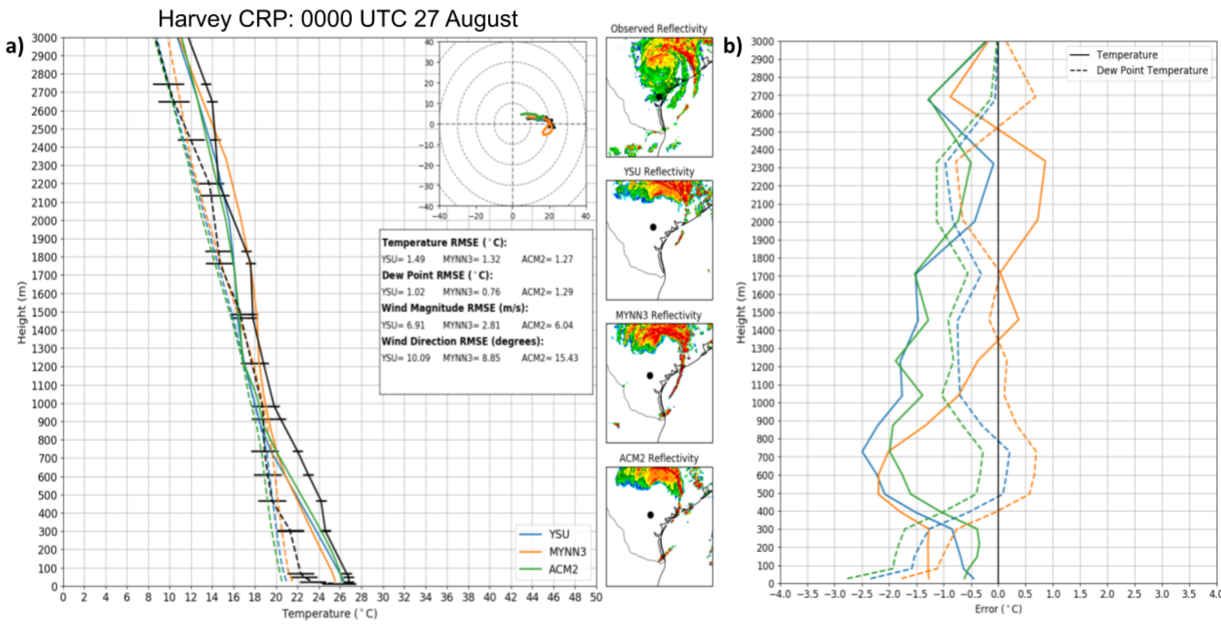

Figure 5.6: Same as Figure 5.1, but for CRP at 0000 UTC 27 August.

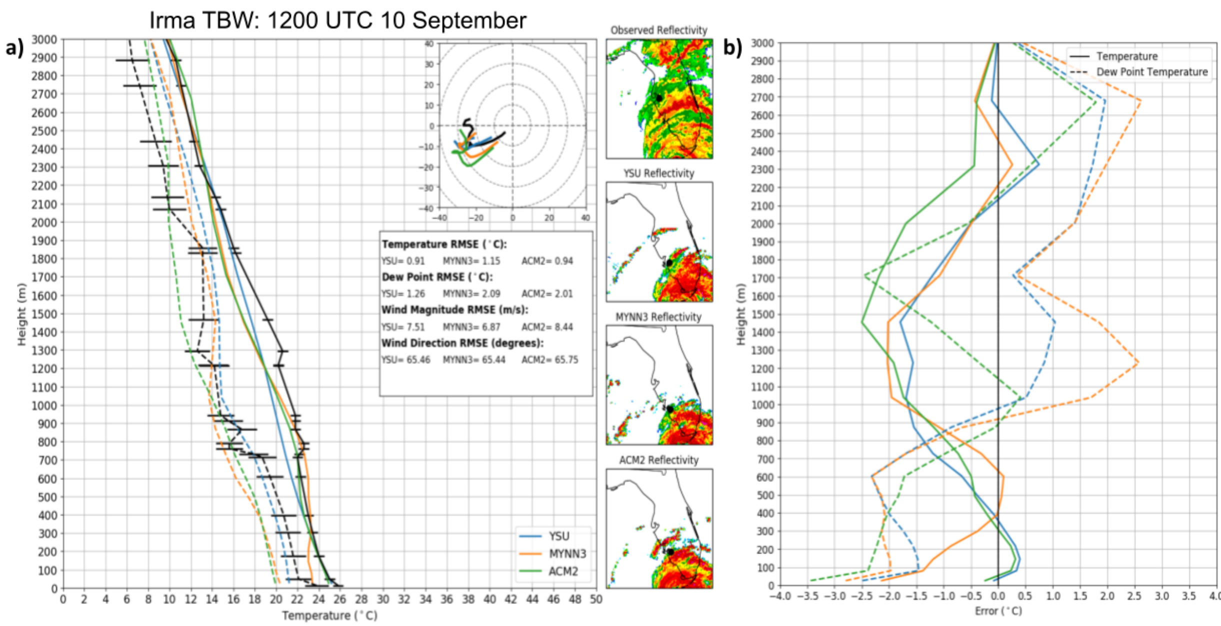

Figure 5.7: Irma TBW 1200 UTC 10 September a) vertical profile of temperature ($^{\circ}C$, solid), dew point temperature ($^{\circ}C$, dashed), hodograph (m/s, inset), and RMSE of the temperature, dew point, wind speed, and wind direction over the lowest 3 km (inset). The uncertainty in the temperature and dew point temperature measurements for the observations are shown in the horizontal error bars. Located to the right of the vertical profiles are reflectivity plots from the observed Hurricane Irma and the model with the location of the vertical profiles (black dot). Error of the temperature and dew point with respect to height (b).

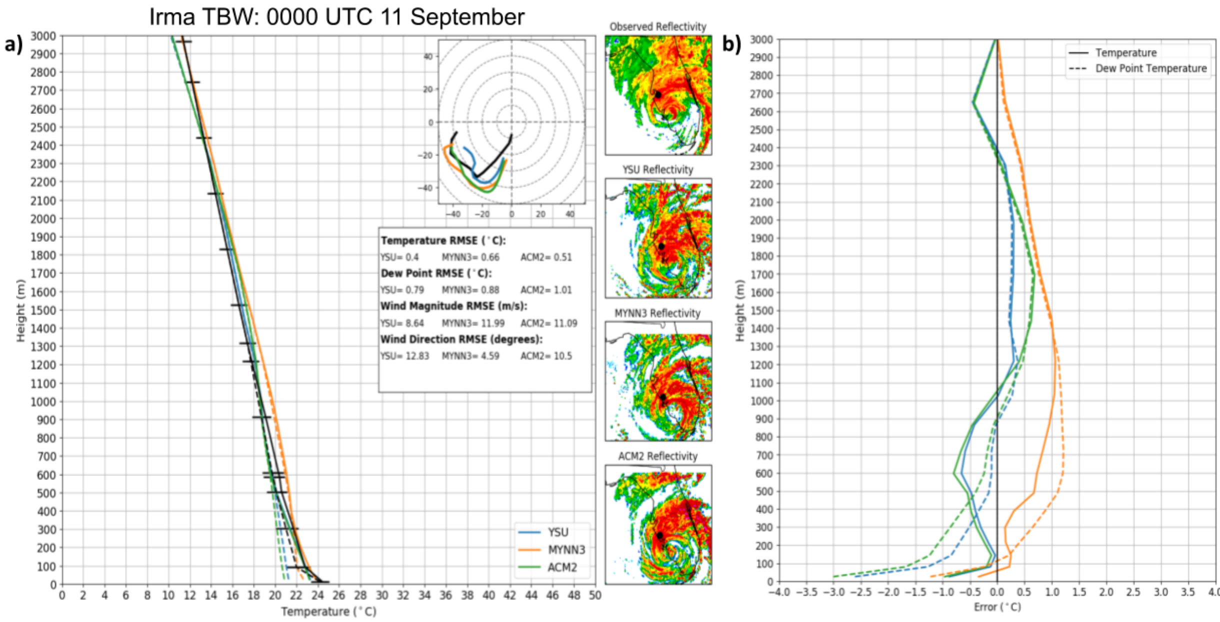

Figure 5.8: Same as Figure 5.7, but for TBW at 0000 UTC 11 September.

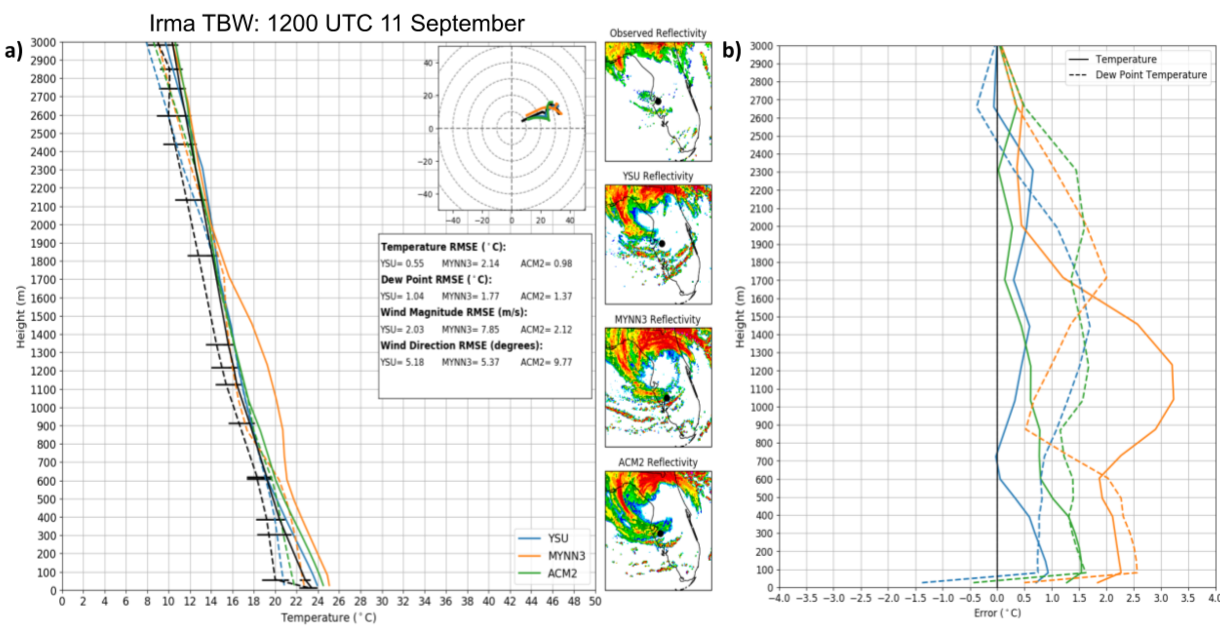

Figure 5.9: Same as Figure 5.7, but for TBW at 1200 UTC 11 September.

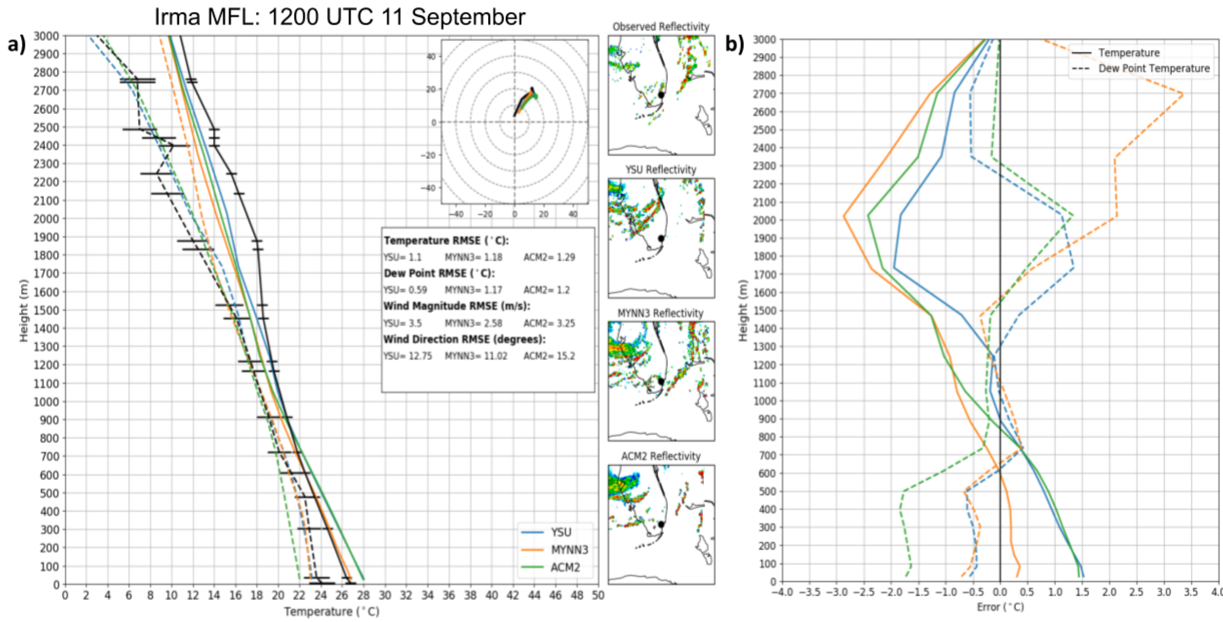

Figure 5.10: Same as Figure 5.7, but for MFL at 1200 UTC 11 September.

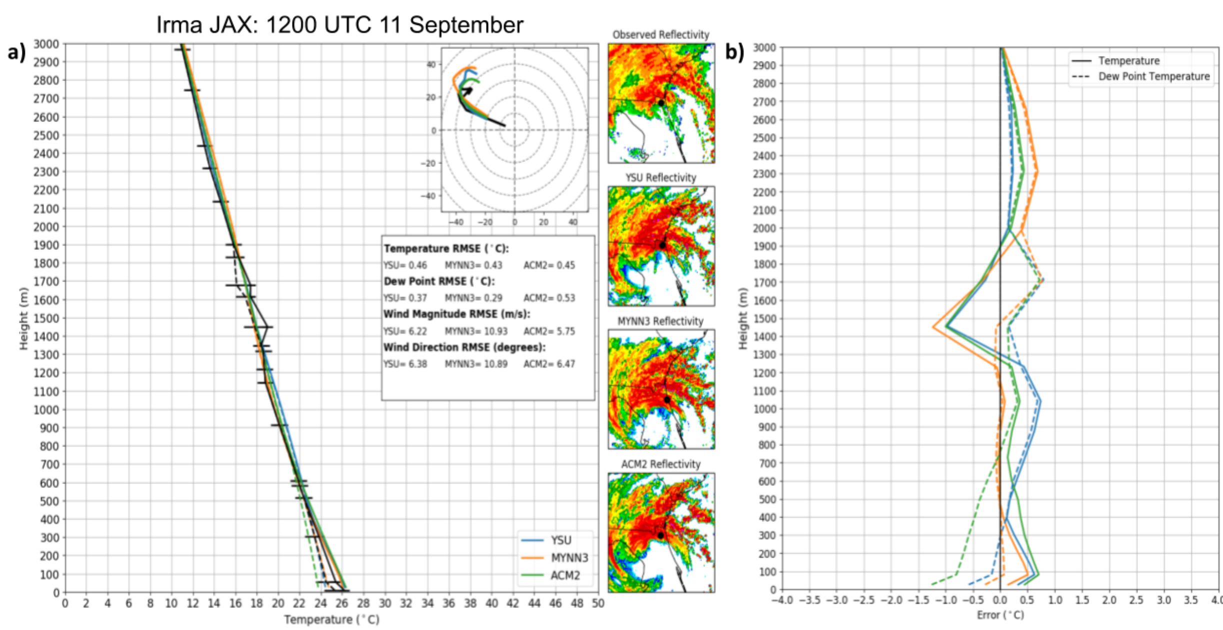

Figure 5.11: Same as Figure 5.7, but for JAX at 1200 UTC 11 September.

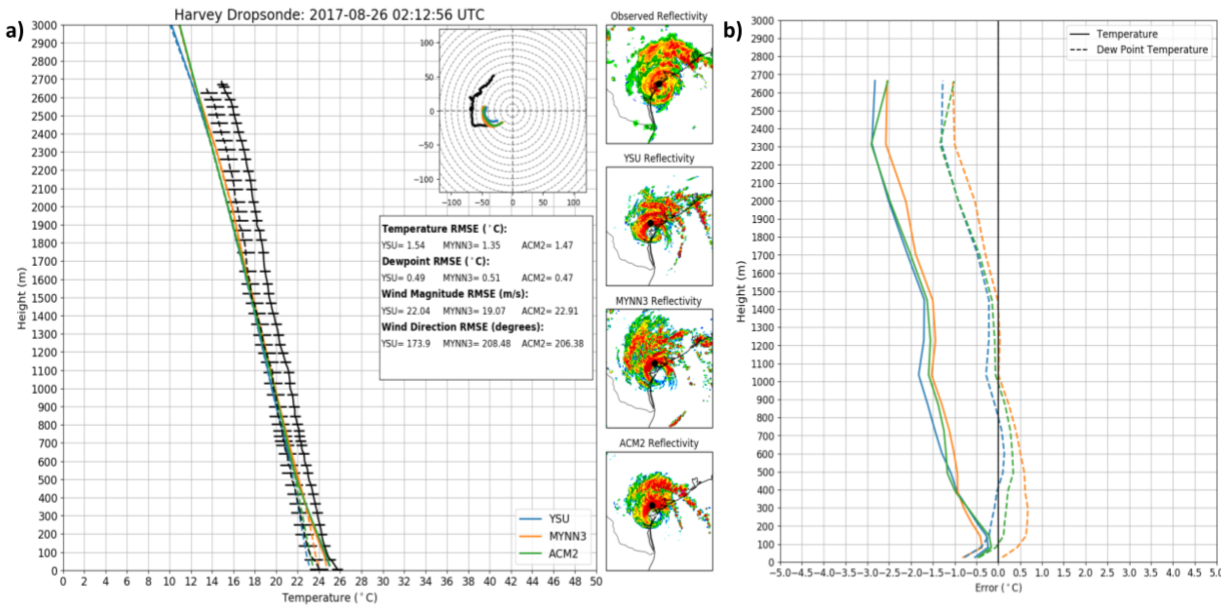

Figure 5.12: Harvey dropsonde from 0212 UTC 26 August: a) vertical profile of temperature ($^{\circ}C$, solid), dew point temperature ($^{\circ}C$, dashed), hodograph (m/s, inset), and RMSE of the temperature, dew point, wind speed, and wind direction over the lowest 3 km (inset). The uncertainty in the temperature and dew point temperature measurements for the observations are shown in the horizontal error bars. Located to the right of the vertical profiles are reflectivity plots from the observed Hurricane Harvey and the model with the location of the vertical profiles (black dot). Error of the temperature and dew point with respect to the vertical height (b).

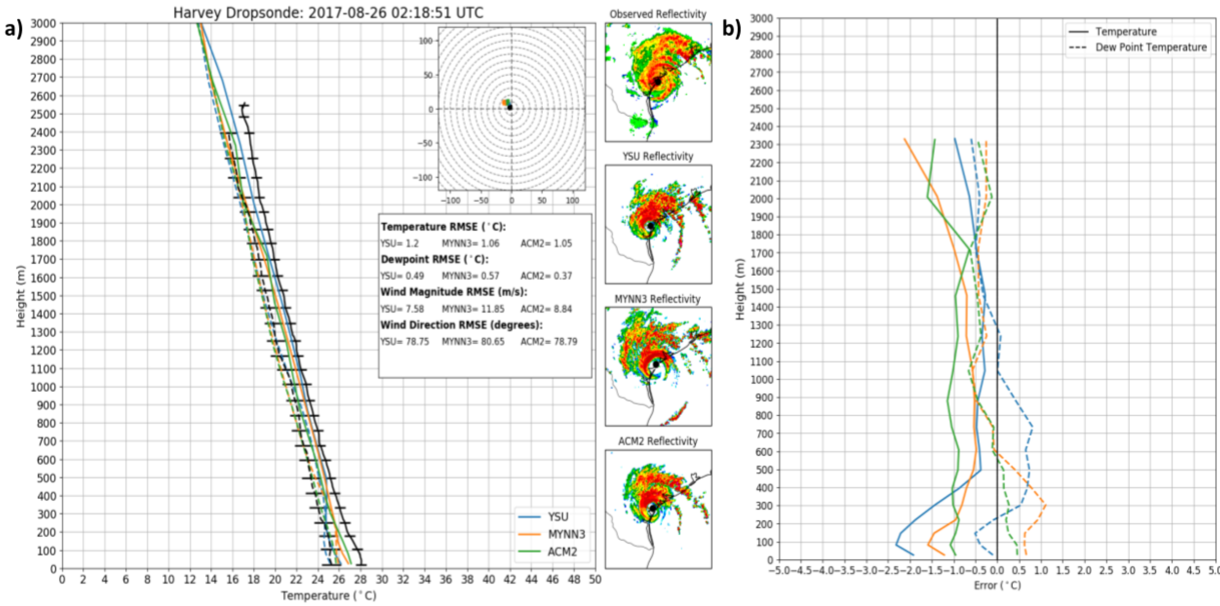

Figure 5.13: Same as Figure 5.12, but for a dropsonde at 0218 UTC 26 August

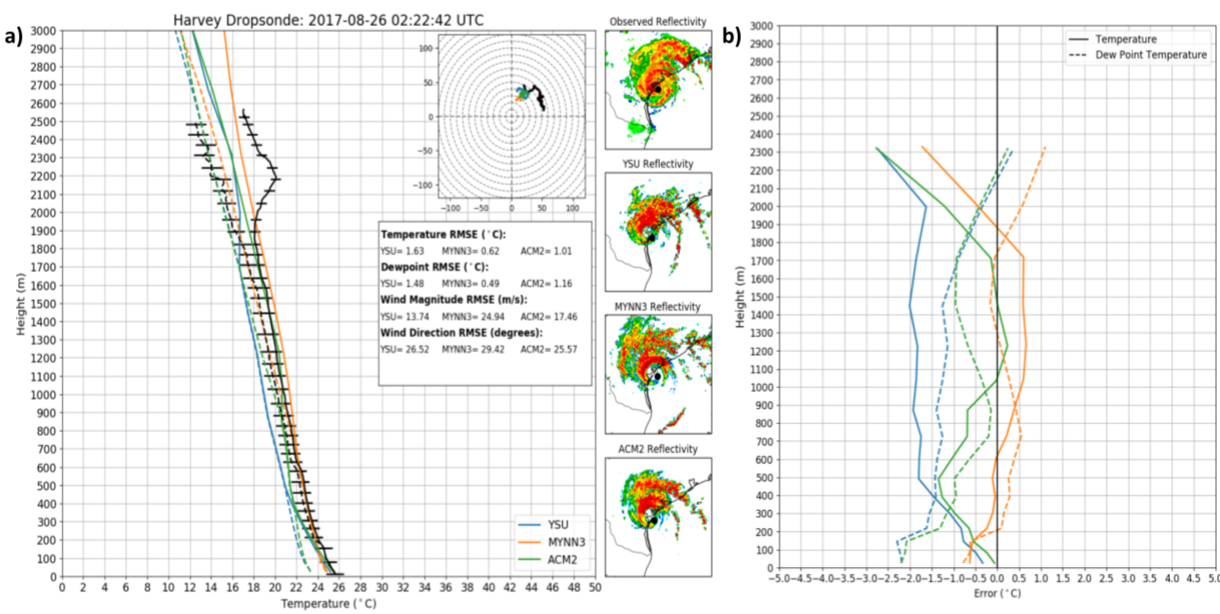

Figure 5.14: Same as Figure 5.12, but for a dropsonde at 0222 UTC 26 August

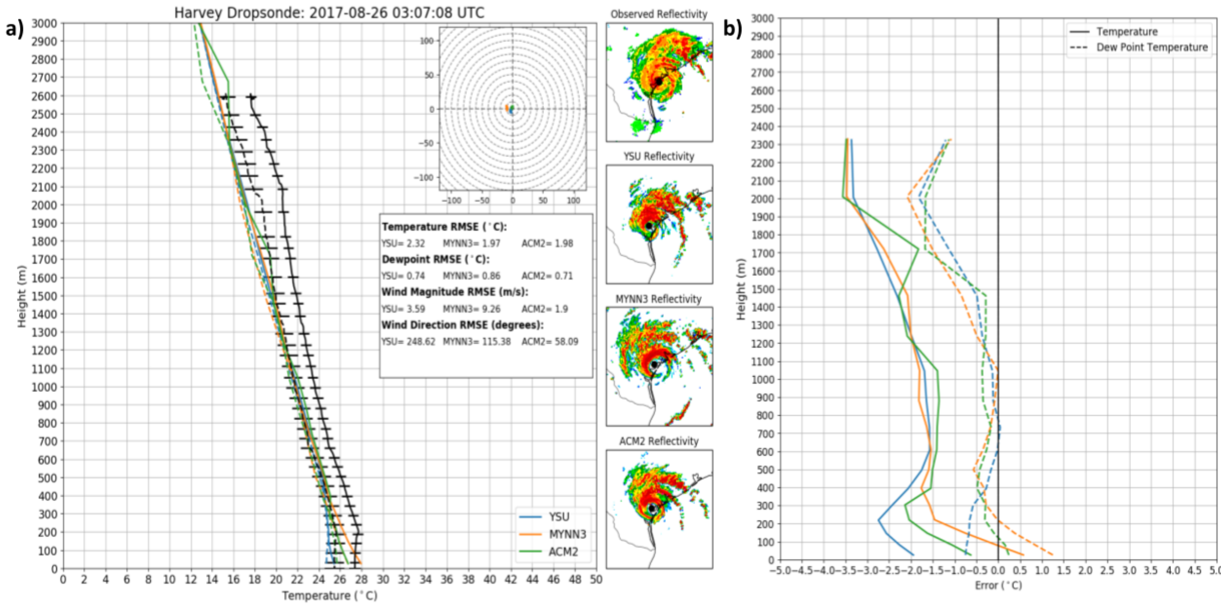

Figure 5.15: Same as Figure 5.12, but for a dropsonde at 0307 UTC 26 August

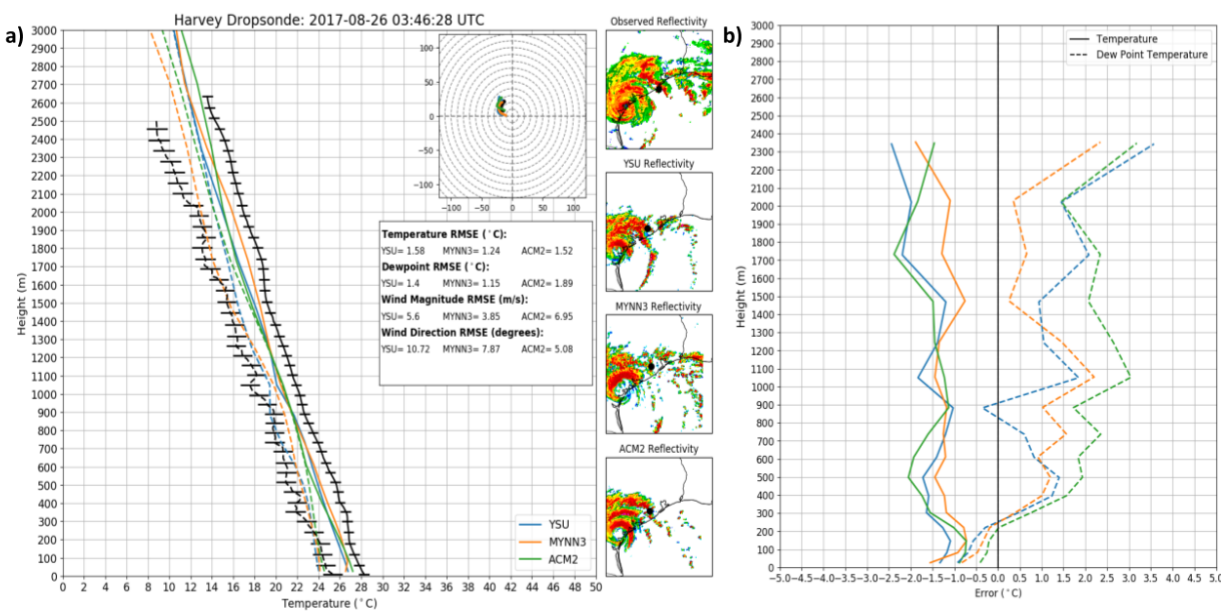

Figure 5.16: Same as Figure 5.12, but for a dropsonde at 0346 UTC 26 August

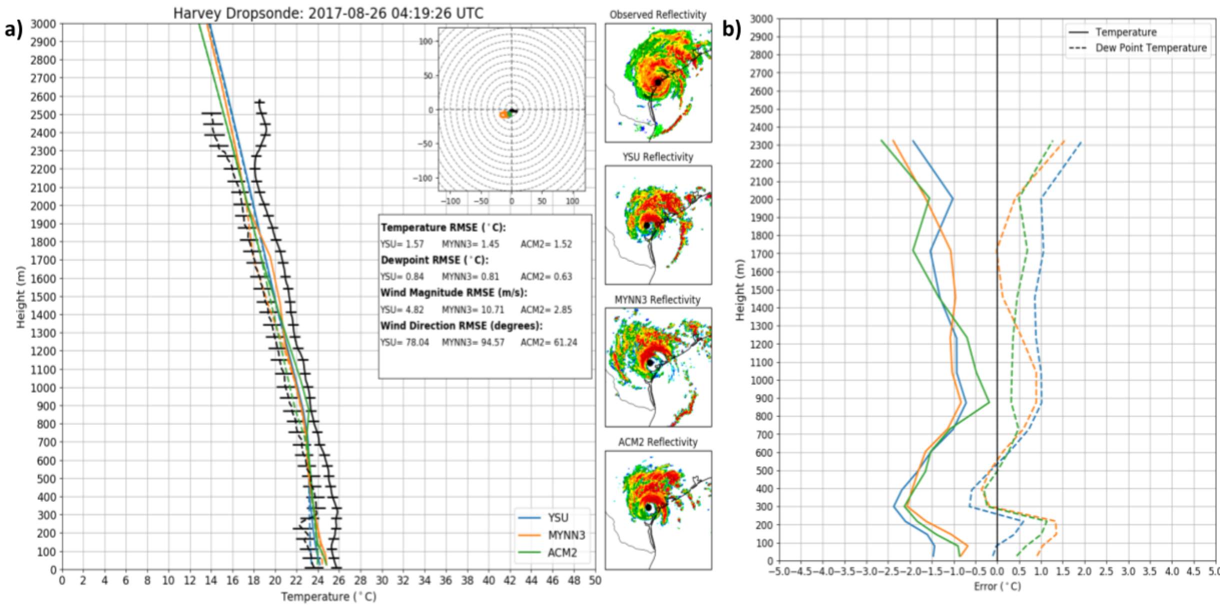

Figure 5.17: Same as Figure 5.12, but for a dropsonde at 0419 UTC 26 August

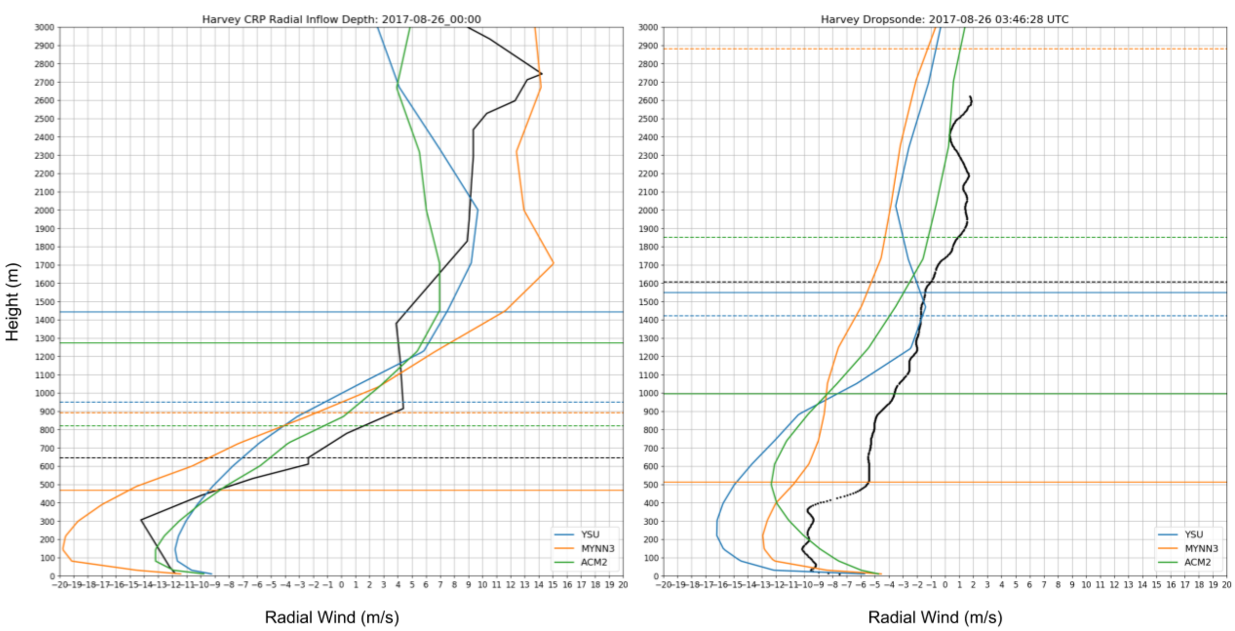

Figure 5.18: The radial inflow (m/s, solid), inflow depth (horizontal, dashed), and the model PBL height (horizontal, solid) for CRP at 0000 UTC 26 August as presented in Figure 5.2a (left) and the dropsonde released at 0346 UTC 26 August as presented in Figure 5.16a (right).

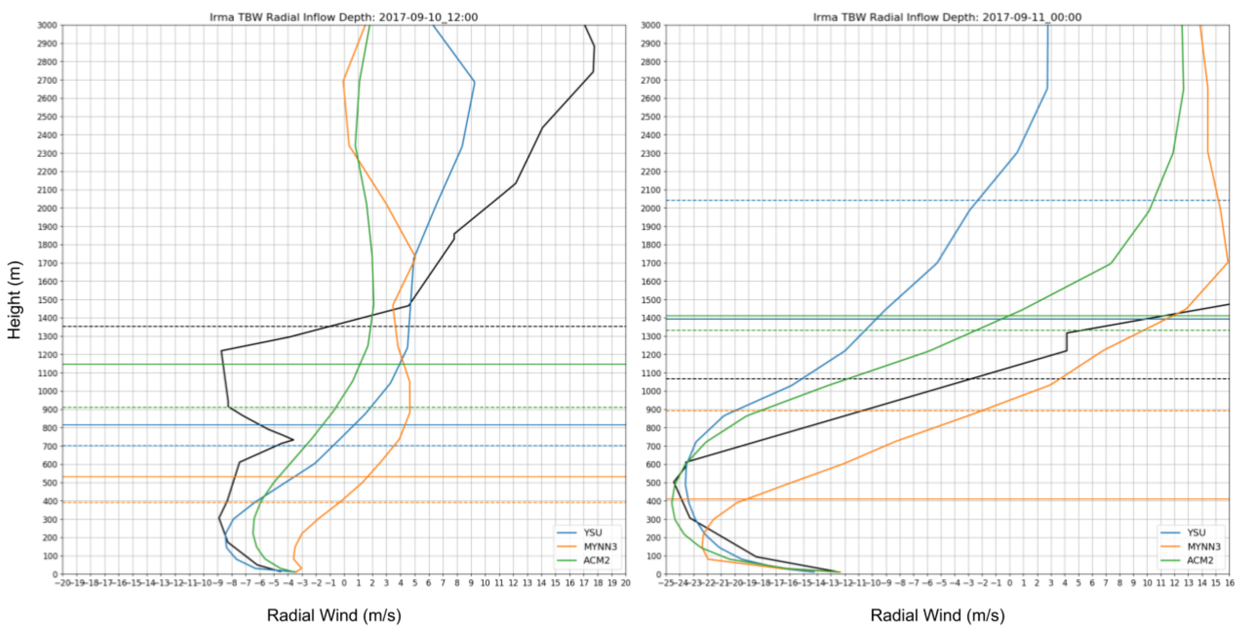

Figure 5.19: The radial inflow (m/s, solid), inflow depth (horizontal, dashed), and the model PBL height (horizontal, solid) for TBW at 1200 UTC 10 September as presented in Figure 5.7a (left) and at 0000 UTC 11 September as presented in Figure 5.8a (right).

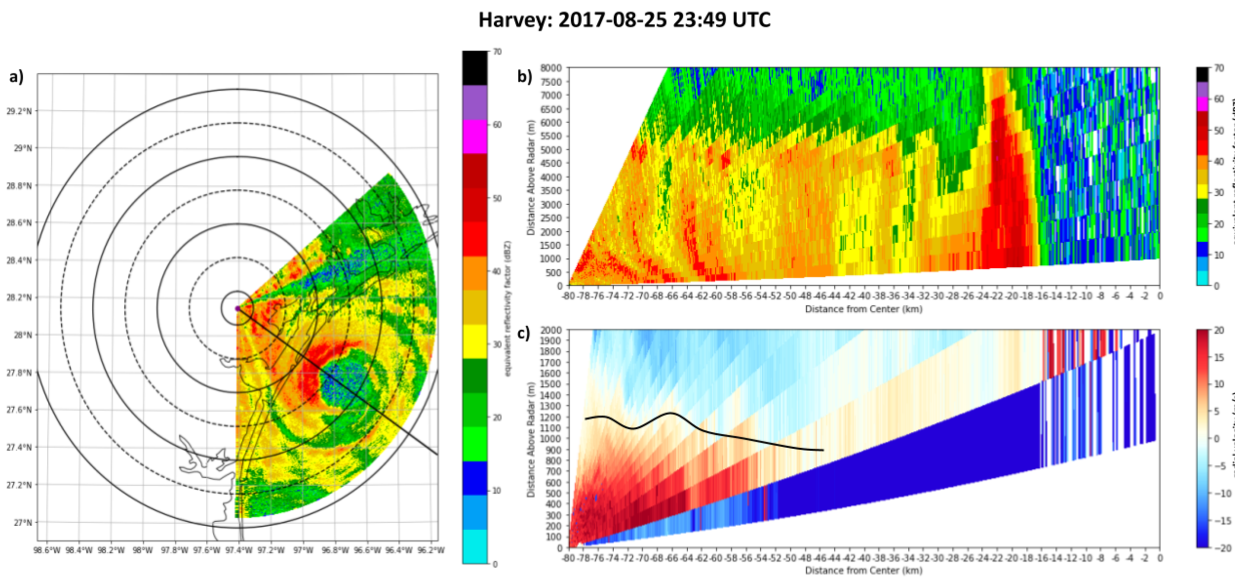

Figure 5.20: Mobile Doppler radar observations of Hurricane Harvey at 2349 UTC 25 August: a) planar plot of the equivalent reflectivity (dBZ, shaded), with range rings from 10–130 km every 20 km and cross section line (black), b) cross section of reflectivity (dBZ, shaded), and c) cross section of radar velocity (m/s), and line showing the approximate inflow depth.

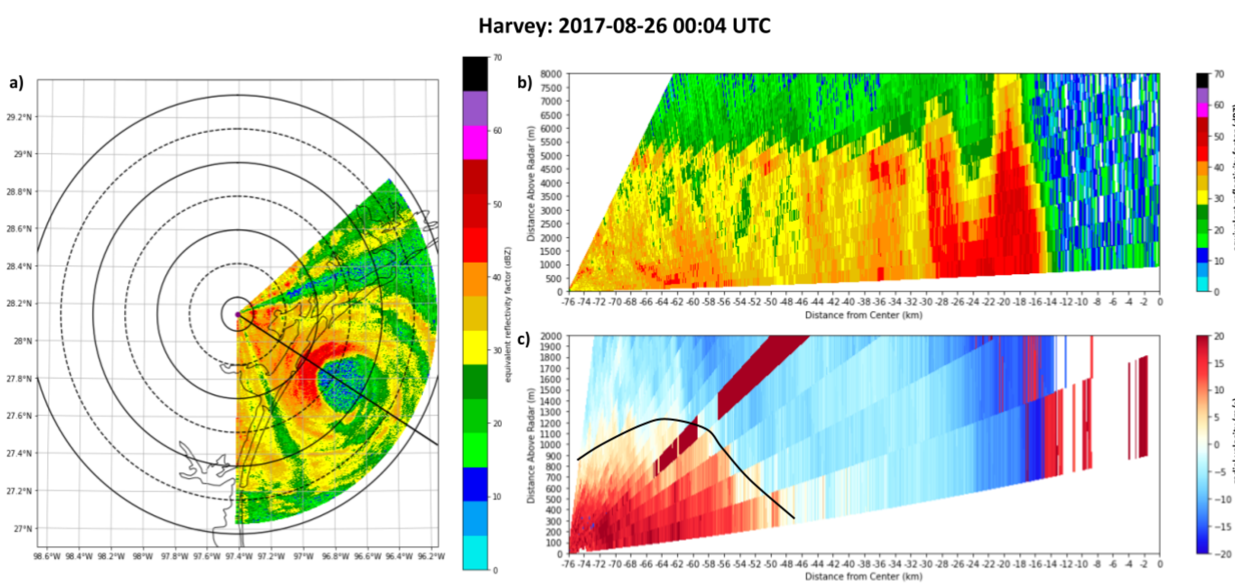

Figure 5.21: Same as Figure 5.20, but for 0004 UTC 26 August.

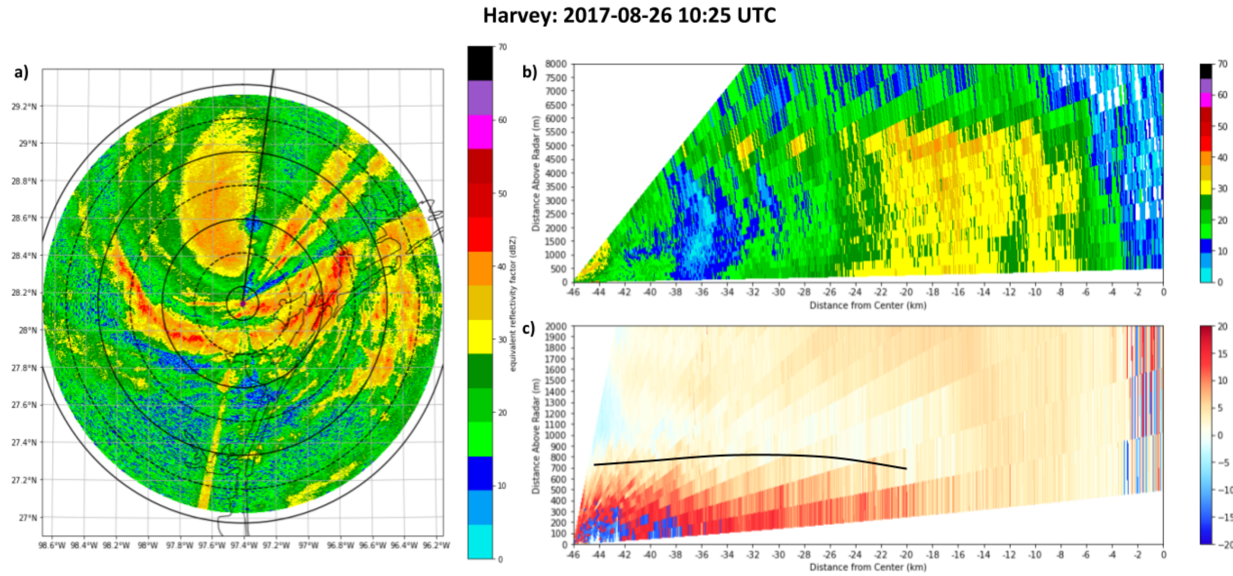

Figure 5.22: Same as Figure 5.20, but for 1025 UTC 26 August.

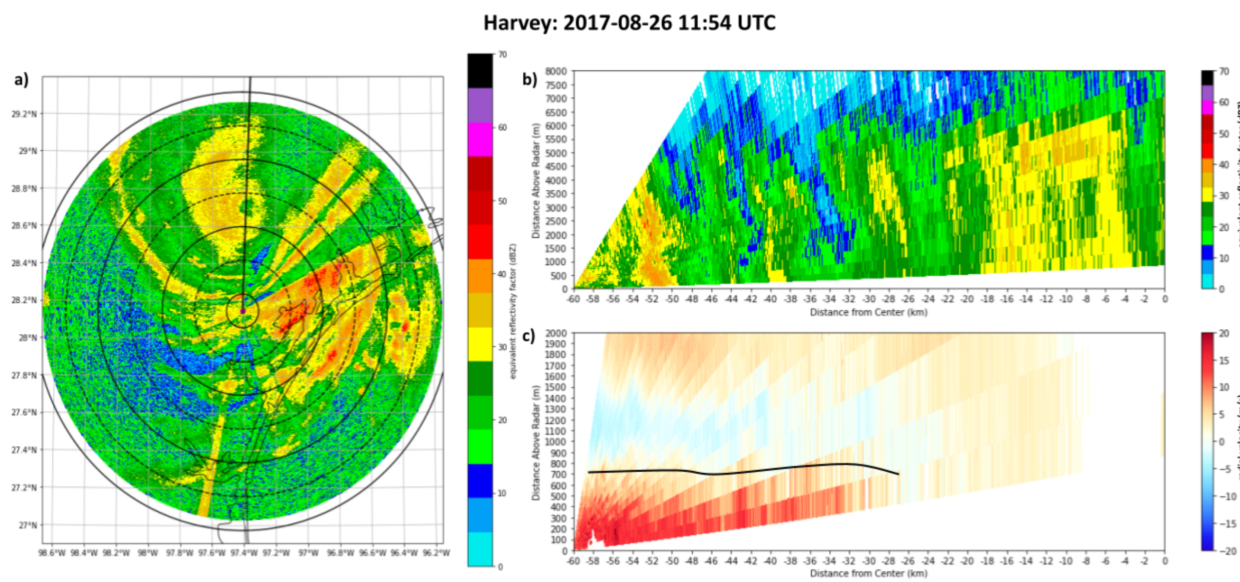

Figure 5.23: Same as Figure 5.20, but for 1154 UTC 26 August.

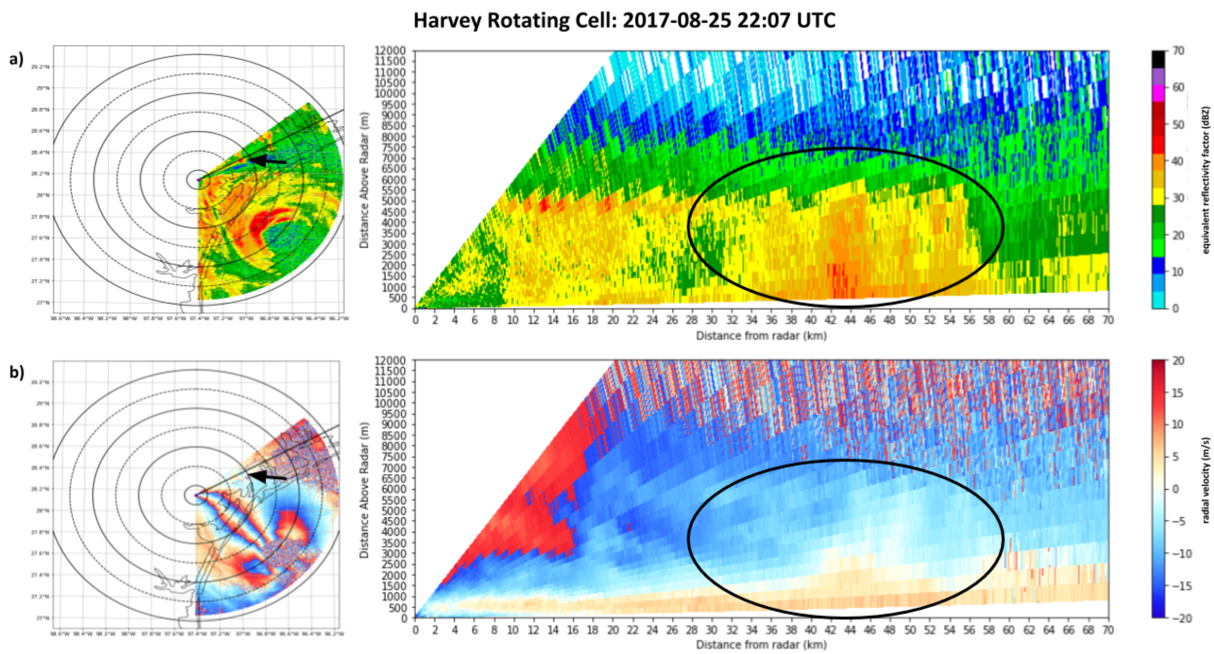

Figure 5.24: Mobile Doppler radar observations of a rotating cell in Hurricane Harvey at 2207 25 August: a) planar (left) and cross section (right) of the equivalent reflectivity (shaded, dBZ) and b) planar (left) and cross section (right) of the radar velocity (shaded, m/s). Both planar plots show range rings from 10–130 km every 20 km.

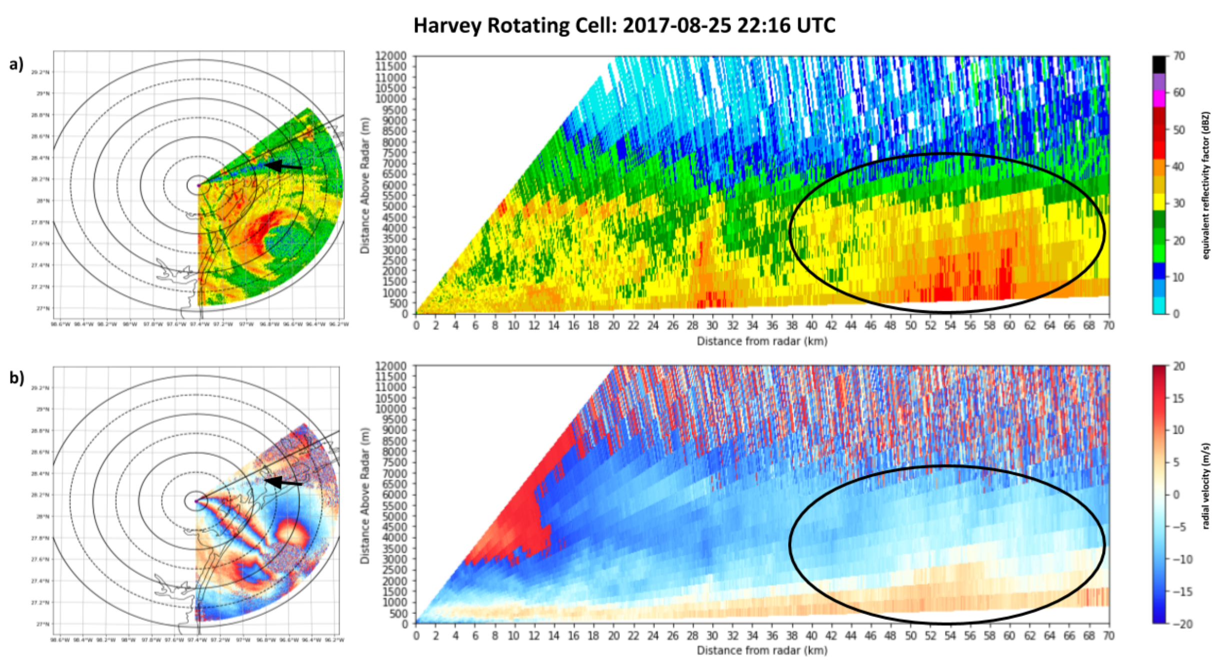

Figure 5.25: Same as Figure 5.24, but for a rotating cell at 2216 UTC 25 August.

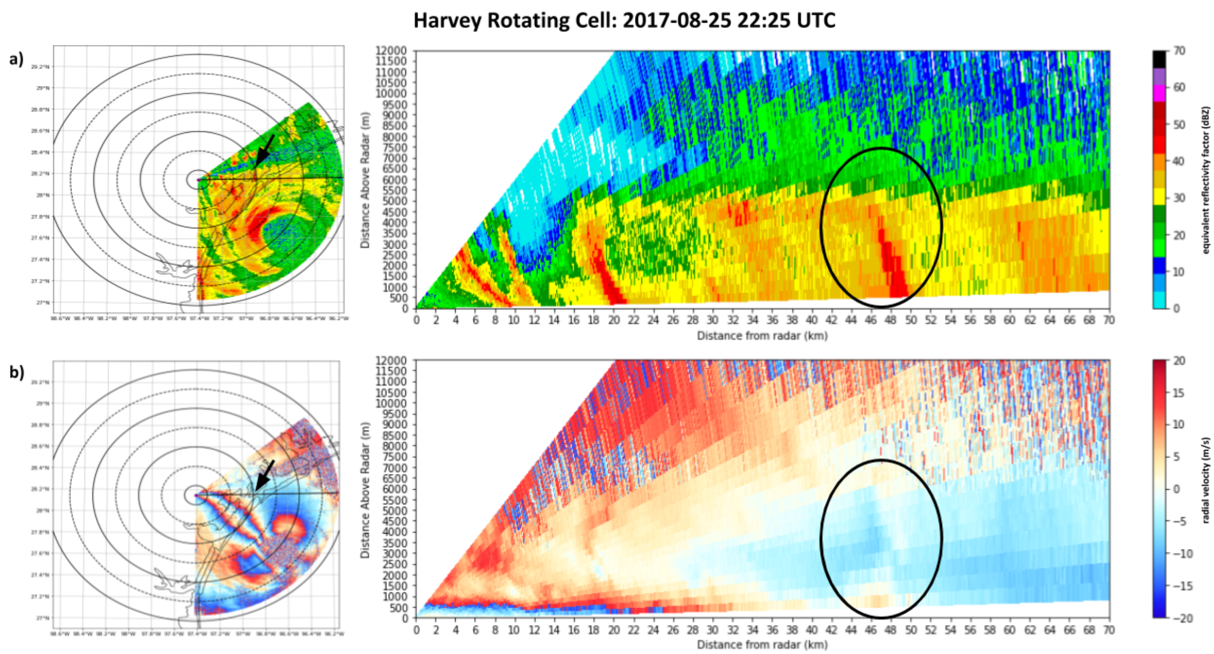

Figure 5.26: Same as Figure 5.24, but for a rotating cell at 2225 UTC 25 August.

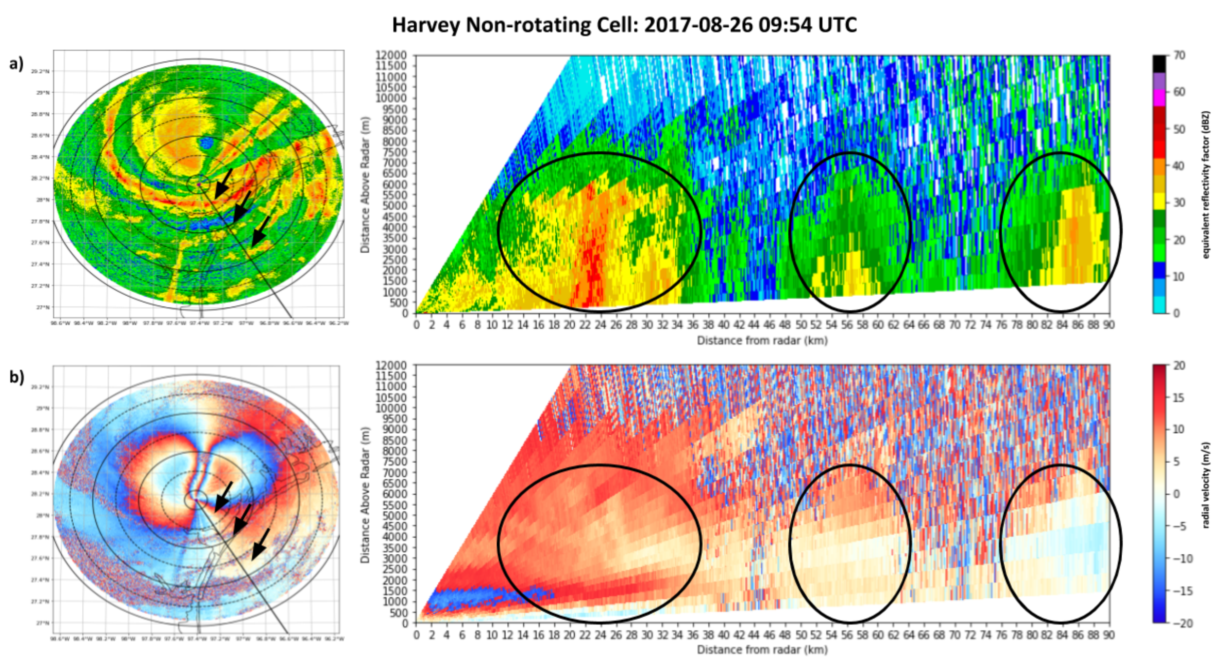

Figure 5.27: Same as Figure 5.24, but for non-rotating cells at 0954 UTC 26 August.

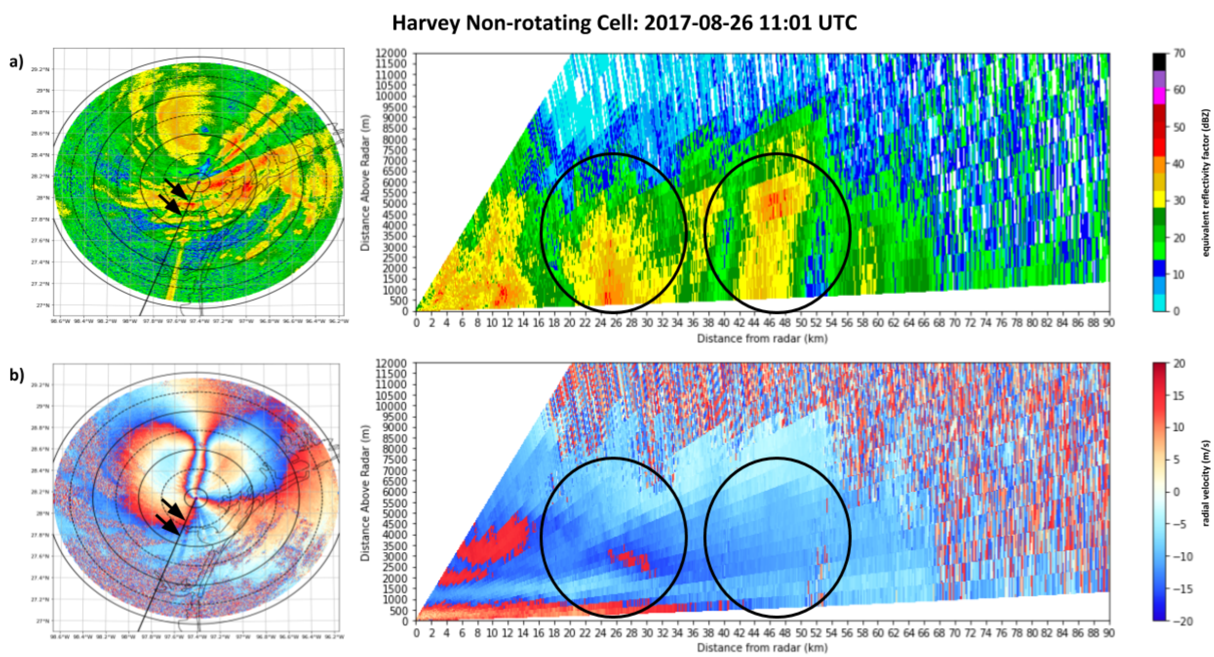

Figure 5.28: Same as Figure 5.24, but for non-rotating cells at 1101 UTC 26 August.

6. Conclusions and future work

6.1 Questions and conclusions

The overarching goal of this dissertation was to further understand tropical cyclone supercells and how PBL parameterization my affect the ability to model them. Carroll-Smith et al. (2019) used tropical cyclone tornado surrogates in high-resolution model simulations of Hurricane Ivan, noting that further research should work to understand how model parameterizations, such as PBL schemes, might impact convection. This dissertation investigated the convective environments of rotating convection, and the three-dimensional structure of convection in the rainbands of tropical cyclones Harvey and Irma, with emphasis being drawn to the differences in the environments across the PBL schemes and the mechanisms within the PBL schemes that cause these differences.

The first goal was to discuss the spatial and temporal distribution of rotating and non-rotating convection in modeled tropical cyclones Harvey and Irma (2017), as well as their convective environments. The second goal was to discuss the mechanisms of the PBL schemes and how they result in the differences seen in the simulations of tropical cyclones Harvey and Irma (2017). This dissertation investigated differences in the PBL and inflow layer heights, as well as transport of moisture, heat, and momentum in the boundary layer. Lastly, this dissertation discussed the verification of the PBL simulations using radiosonde, dropsonde, and mobile Doppler radar observations from hurricanes Harvey and Irma (2017).

Presented in Chapter 3 was the spatial and temporal distribution of convective cells, the effects of geography on the convective cell location, the differences in the convective environments, the structure of the rotating and non-rotating cells, and the overall differences in the PBL schemes. In Chapter 3 the questions to answer were: Do the spatial and temporal distributions of rotating convection align with previous studies of tornadoes in tropical cyclones? What effect(s) does the coastline have on convective cells and convective cell types? What are the differences in the convective environments that are affected by the choice of PBL scheme? How do the modeled rotating and non-rotating cells differ in structure from one another? What is the typical structure of the modeled rotating and non-rotating convective cells, both over the land and over the ocean?

6.1.1 Question 1: Do the spatial and temporal distributions of rotating convection align with previous studies of tornadoes in tropical cyclones?

It was hypothesised that rotating cells would be most frequent in the northeast quadrant (wrt geographic North) and downshear/downshear-left (wrt vertical wind shear) in the tropical cyclone simulations mirroring what has been seen in observations and other modeling studies looking at rotating convection in tropical cyclones (McCaul 1991; Schultz and Cecil 2009; Edwards 2012; Carroll-Smith et al. 2019; Card 2019). The spatial distributions of the rotating convection seen in Figures 3.1 and 3.5 align very well with the findings of McCaul (1991), Schultz and Cecil (2009), and Edwards (2012), who found tropical cyclone tornado reports are favored in the northeast quadrant of the tropical cyclone. The tropical cyclone tornado surrogates (Carroll-Smith et al. 2019; Card 2019) in the simulations of Harvey and Irma also showed an affinity to be located northeast of the storms' centers with respect to geographic north and downshear to downshear-left with respect to vertical wind shear, as was also shown in the NCAR Ensemble in Card (2019).

In Card (2019) the total number of rotating cells outnumbered the total number of non-rotating cells by a factor of 2–3 times in the NCAR ensemble, which was a much larger differential than in the WRF simulations of Harvey and Irma. The NCAR ensemble has 3-km horizontal grid spacing and thus like Carroll-Smith et al. (2019) uses a lower 0–3-km updraft helicity threshold to identify the rotating cells, which could result in over estimating the number of rotating cells. In the Harvey WRF simulations, the number of identified non-rotating cells was about 22% greater than the number of identified rotating cells (Fig. 3.1). The number of identified non-rotating cells was 14%, 36%, and 8% more than the number of identified rotating cells for the YSU, MYNN3, and ACM2 simulations, respectively (Fig. 3.3). In the Irma WRF simulations, the number of identified non-rotating cells was about 18% less than the number of identified rotating cells (Fig. 3.5). The number of identified non-rotating cells was 46% and 16% less than the number of identified rotating cells for the YSU and MYNN3 simulations, respectively (Fig. 3.7). The Irma ACM2 simulations show 18% more identified non-rotating cells compared to identified rotating cells, which aligns well with the results from the Harvey simulations (Fig. 3.7). Overall, the MYNN3 simulations of both Harvey and Irma showed the largest number of identified rotating cells (n=1183 and n=685, respectively). The number of rotating cells were highest in the MYNN3 simulations because the 0–3-km updraft helicity 99.95^{th} percentile was the lowest amongst the tested PBL schemes (Tables 5.1 and 5.2). It was found that the 0–3-km vertical wind shear was weaker in the MYNN3 simulations reducing the 0–3-km updraft helicity.

In terms of the temporal distribution, it was hypothesized tropical cyclone tornado activity would peak in the early-mid afternoon (McCaul 1991; Schultz and Cecil 2009; Edwards 2012). It was expected that the peak in rotating cell activity in hurricanes Harvey and Irma will align best with the observed peak in tornado reports (Figs. 1.4 and 1.5) from 0400–1000 UTC for Harvey and 1700–2300 UTC for Irma.

The temporal distribution of the rotating convection was noticeably different from observational studies such as McCaul (1991), which showed that 57% of tropical cyclone tornadoes occur between 1400–2300 UTC (corresponding roughly to 0900–1800 local time in the southeastern U.S.). Schultz and Cecil (2009) concurred with this, and found a pronounced peak in tropical cyclone tornado reports in the early- to mid-afternoon, with similar findings in Edwards (2012). In the simulations of hurricanes Harvey and Irma, the peaks in identified rotating convective cells tended to be in the late afternoon and into the early morning hours (Figs. 3.11 and 3.13). To compare to the observed tornado reports (Figs. 1.4 and 1.5, right), Harvey showed a peak between 0400–1000 UTC and Irma showed a peak between 1700–2300 UTC, aligning very well with the peak in rotating cell activity in the

Harvey simulations, but earlier than the increased activity in the rotating cell activity in the Irma simulations. As noted previously, there are two factors which may result in differences between observations and the simulations. First, although Carroll-Smith et al. (2019) showed that for Hurricane Ivan (2004) the tropical cyclone tornado surrogates successfully identified where tornado reports were likely to occur, the tropical cyclone tornado surrogates may not be so representative of tornado reports in Harvey or Irma. Second, many biases in observed tornado reports may affect the temporal distribution due to the daytime tornado reporting bias, evacuations limiting population, and/or the difficulty of verifying reports in areas of post-storm damage.

The differences in the temporal distribution of tropical cyclone tornado reports and the model surrogates suggest that tropical cyclones can produce tornadoes at almost all times as neither the Harvey or Irma simulations aligned with the expected peak in tropical cyclone tornadoes from climotologies (McCaul 1991; Schultz and Cecil 2009; Edwards 2012). Other factors may impact the temporal distribution of tropical cyclone tornadoes such as landfall time.

6.1.2 Question 2: What effect(s) does the coastline have on convective cells and convective cell types?

Past observational studies have shown that non- or weakly-rotating cells begin to rotate more rapidly as they approach the coastline (Baker et al. 2009; Eastin and Link 2009). As such, it was hypothesized that the rotating cells would be located closer to the coastline compared to non-rotating cells (Baker et al. 2009; Eastin and Link 2009).

The coastline had an impact on the location of the rotating and non-rotating convection observed in the simulations of hurricanes Harvey and Irma. Figures 3.2 and 3.6 showed that the rotating cells tend to be located closer to the coast and tend to penetrate further inland compared to the non-rotating cells. The rotating cells in all the simulations were statistically significantly closer to the coast compared to the non-rotating cells (Figs. 3.16 and 3.17).

The distances from the coast of the rotating and non-rotating cells are in large agreement with observations of convective cells in Hurricane Ivan (Baker et al. 2009; Eastin and Link 2009), in which it was shown that non- or weakly-rotating convection typically exists offshore and begins to rotate more vigorously once the cells approached and made landfall. Cross sections across the coastline of the rainbands in Harvey and Irma (Figs. 3.25 and 3.26) showed that the hodographs became elongated over and approaching the land due to friction that drives higher 0–3-km vertical wind shear over land compared to the ocean. As mentioned previously, the 0–3-km vertical wind shear plays an important role in the development of rotating convection in tropical cyclones (McCaul and Weisman 1996).

6.1.3 Question 3: What are the differences in the convective environments that are affected by the choice of PBL scheme?

It was hypothesized that the sub-grid scale mixing in the boundary layer in each PBL scheme would result in differences in the convective environments including the 0–3-km helicity, low-level relative humidity, and low-level CAPE. These environmental variables have been shown to be important to tropical cyclone supercell development.

It was expected that the 0–3-km helicity (vertical shear) would be higher over the land compared to the ocean, with this low-level helicity being important in the development of rotating convection in tropical cyclones (McCaul and Weisman 1996). The different PBL schemes showed substantial differences in the 0–3-km updraft helicity, low-level relative humidity, and low-level CAPE. The YSU and ACM2 simulations produced statistically significantly more 0–3-km updraft helicity (Figs. 3.18 and 3.19), which was mainly driven by large-scale differences in the 0–3-km helicity (0–3-km shear) between the PBL schemes. The cross sections of the coastline in the simulations of Harvey and Irma showed a statistically significant increase in the the 0–3-km vertical wind shear from ocean to land, induced by surface friction (Figs. 3.25 and 3.26). The 0–3-km vertical wind shear was 76–216% and 24–36% higher over land compared to over the ocean in the cross sections of Harvey and

Irma, respectively (Figs. 3.25 and 3.26). Baker et al. (2009) showed that in observations of Hurricane Ivan the 0–1-km vertical wind shear was 37% higher over land compared to over the ocean. The 0–3-km vertical shear was weakest in MYNN3 simulations, which was attributed to strong and shallow vertical eddy mixing over the ocean (Fig. 4.15), confined just below the PBLH. This strong mixing leads to large negative wind tendencies in the boundary layer (Figs. 4.19 and 4.22). As noted previously, the strong low-level mixing and resulting large negative wind tendencies acts to decrease the 0–3-km vertical wind shear.

The tropical cyclone environment is known for high moisture content. Past literature suggests that PBL schemes with strong and deep vertical mixing produce warming and drying at low levels of the PBL, which is particularly true for non-local PBL schemes (Braun and Tao 2000; Bright and Mullen 2002; Kain et al. 2005; Hill and Lackmann 2009; Hu et al. 2010). As such, it was hypothesized that the scheme with shallow and weak vertical mixing would result in the highest relative humidity in the low levels of the PBL.

The relative humidity CAFDs showed that the MYNN3 simulations had higher frequencies of high relative humidity in the low levels (below 500 m) compared to the YSU and ACM2 simulations (Fig. 3.28). Strong and shallow mixing over the ocean near the surface in the MYNN3 simulations of both hurricanes Harvey and Irma (Fig. 4.15) drove positive tendencies in water vapor in the lowest 500 m (Figs. 4.18, 4.19, 4.20, 4.21, 4.22, and 4.23), leading to higher values of RH. The YSU and ACM2 simulations showed deeper mixing than the MYNN3 simulations.

It was hypothesized that the simulation which produced the most vertical eddy mixing would produce the largest values of CAPE. Zhang et al. (2017) showed in model simulations of landfalling tropical cyclones that larger vertical eddy mixing resulted in an increase in CAPE in the boundary layer. The CFADs of CAPE (Fig. 3.29) showed that the CAPE was concentrated below 3 km in all the simulations. The MYNN3 PBL scheme tend to have high values of CAPE, although the high values of CAPE lacked depth, while the YSU and ACM2 simulations showed more moderate values of CAPE but over a larger depth than the

MYNN3 simulations (Fig. 3.29). In the composites of the rotating and non-rotating cells, the CAPE was largest in the ACM2 simulation (Figs. 3.30 and 3.31), attributed to the stronger and deeper mixing in the ACM2 scheme compared to the other PBL schemes (Fig. 4.15). As seen in the ACM2 cell composites, the high CAPE results in the strongest vertical motions across all of the PBL simulations. The maximum CAPE in the cell composites was generally 20% and 130% larger over the ocean compared to over land in the non-rotating and rotating cells, respectively (Figs. 3.40, 3.41, 3.42, and 3.43). This result aligns well with observations of Hurricane Ivan from Baker et al. (2009) which showed the 0–3-km CAPE was about 35% higher over the ocean compared to over the land.

6.1.4 Questions 4 and 5: How do the modeled rotating and non-rotating cells differ in structure from one another? What is the typical structure of the modeled rotating and non-rotating convective cells, both over the land and over the ocean?

The schematics of the rotating and non-rotating composite cells show the main features of these cells in the tropical cyclones (Figs. 3.44 and 3.45). It was hypothesized that the rotating cells would show characteristics similar to the mature cells embedded within principal rainbands. Rotating cells are located closer to the tropical cyclone center northeast of the storms' centers coinciding with the mature region of the principal rainband (Hence and Houze 2008; Card 2019). It was also expected that many similar features between the schematic of rotating cells and the observations in Hurricane Ivan of rotating cells (Eastin and Link 2009) would be seen. The non-rotating cells were hypothesized to take on the structure of the non-mature principal rainband cells near the begining of the rainband (Hence and Houze 2008; Li and Wang 2012), further from the tropical cyclone center, which was seen in the identified non-rotating cells.

The rotating cell schematic (Fig. 3.44) was very similar to the schematics of a cross section through the mature cell embedded within a principal rainband presented in Hence and Houze (2008) and Card (2019), as the reflectivity signature tends to tilt radially outward with height (extending to approximately 8 km) and a strong maximum in the tangential wind appears on the radially outward side about 1–2 km from the composite center at about 2–4 km in height. While the non-rotating cell schematic (Fig. 3.45), with vertically-erect reflectivity signature, strong updraft positioned in the mid-levels, and weak tangential wind maximum further radially outward from the center of the composite compared to the rotating cells. The non-rotating cell composite is similar to what is expected in the non-mature cells embedded within the principle rainband from Hence and Houze (2008) and Li and Wang (2012).

The biggest difference seen between land and ocean cells was the extent of dry air in the upper levels. The ocean cell composites consistently had more dry air in the upper levels compared to the land cells, with many composites showing some areas of relative humidity less than 50% (Figs. 3.33b, 3.35b, 3.37b and 3.39b). The oceanic principal rainbands from Hurricane Katrina in Hence and Houze (2008) showed that the radially inward side of the rainband (closer to the tropical cyclone center) tended to be drier and have less reflectivity in the upper levels, which was seen in both the non-rotating and rotating ocean cell composites. The PBL heights in the land cell composites showed much more variation than the oceanic cell composites, generally ranging between 500 and 1500 m in depth (Figs. 3.32, 3.33, 3.34, 3.35, 3.36, 3.37, 3.38, and 3.39)

Presented in Chapter 4, the differences in the PBL schemes seen in Chapter 3 were investigated to determine the mechanisms within the PBL schemes that could cause these differences. Chapter 4 attempted to answer the questions: Why does the PBL height differ between land and ocean identified cells? What mechanisms of the PBL schemes contribute to the differences seen in the environment including, why did the MYNN3 simulations produce less 0–3-km shear compared to the YSU and ACM2 simulations (Figs. 3.22 and 3.23), why is the relative humidity concentrated in the low levels in the MYNN3 simulations (Fig. 3.28), and why do the ACM2 cell composites produce more low-level CAPE compared to the other PBL schemes?

6.1.5 Question 6 and 7: Why does the PBL height differ between land and ocean identified cells? How does the CRN affect the vertical eddy mixing?

The key mechanism that resulted in the large differences in the PBL schemes over land and over the ocean (Figs. 4.4 and 4.5) was tied to the use of a CRN to calculate the PBLH. The stable boundary layer revision (Hong 2010) is applied to the YSU scheme when the model surface virtual potential temperature is cooler than the first model level virtual potential temperature, which was the case in the simulations of hurricanes Harvey and Irma, particularly in land areas within the tropical cyclone precipitation (Figs. 4.6, 4.7, and 4.8). In the unstable boundary layer, the CRN is set to a fixed value of zero in the YSU scheme and 0.25 in the ACM2 scheme, whereas in the stable boundary layer the CRN in the YSU scheme over land is set to 0.25 (Hong 2010). Since the CRN for the stable boundary layer over land in both the YSU and ACM2 schemes is the same, it is not surprising that the PBLH is very similar. The differences seen in the PBLH over land between the YSU and ACM2 schemes can be attributed to the entrainment term in the YSU PBL scheme that acts to modify the PBLH over time, which is not present in the ACM2 PBL scheme. Over the ocean, the ACM2 scheme had the deepest PBLH due to the CRN being 0.25, compared to the CRN of zero for the YSU scheme. Depending on the stability conditions, the ACM2 PBL scheme alters the mixing from pure local mixing for stable conditions to pure non-local mixing for unstable conditions. The differences in the CRN between the land and ocean in the YSU simulations drives a discontinuity in the PBL height seen in the coastal cross sections (Figs. 4.11 and 4.12). The ACM2 simulation also showed a similar discontinuity in the PBL height at the coastline to the one seen in the YSU simulations. In this case, the discontinuity in the ACM2 PBL height is not driven by a change in the CRN across the coast, but rather the difference in stability between the land and ocean driving the abrupt change from mostly local mixing to mostly non-local mixing altering the PBL height calculation. Similar discontinuities are not seen at the coastline in the MYN3 simulations.

Kepert (2012) noted that although non-local KPP closure PBL schemes can preform satisfactorily in some situations (Nolan et al. 2009a,b), KPP schemes should be used with caution. The results of the simulations of hurricanes Harvey and Irma would suggest much of the same issuance of caution. The YSU scheme preformed well compared to observations at some locations in the hurricanes, but, like all the other PBL schemes, showed a cold bias, which could impact the regions that would and should be using the stable boundary revision (Hong 2010).

The non-local PBL schemes that utilize KPP closure have diagnosed PBLHs that are very different over land compared to PBL schemes which use other methods, mainly because of the use of a CRN to determine the PBL depth. The CRN is not only responsible for the PBLH in KPP schemes, but is also responsible for the magnitude and depth of the eddy mixing (Bu et al. 2017). Gopalakrishnan et al. (2021) showed that in the next-generation, FV3-based, Hurricane Analysis and Forecast System (HAFS) the uncertainty in variables used to define the eddy diffusivity leads to diverse model solutions in model forecasts and that two diverse PBL schemes can create converging forecast results when eddy diffusivity or mixing length are adjusted based on observations. The ACM2 simulation had the highest CRN over both land and ocean in both simulations. It was expected that the ACM2 simulation would show the strongest and deepest mixing due to the higher CRN. This result was seen in both the eddy mixing over the land and ocean (Fig. 4.15) and in the tendencies (Figs. 4.20 and 4.23). The PBLH is used in further calculations within the YSU and ACM2 PBL schemes such that misrepresentations of the depth of the PBL can affect other mechanisms within the boundary layer, such as the vertical mixing profile. In TKE PBL schemes, the PBLH is a calculated variable that does not feed back into subsequent calculations within the MYNN3 PBL scheme.

6.1.6 *Question 8: What mechanisms of the PBL schemes contribute to the differences seen in the environment?*

The eddy vertical mixing and the resulting tendencies show how the mechanisms within the PBL schemes affect the environment. Recall that the ACM2 simulations showed the largest and deepest vertical eddy mixing, while the MYNN3 simulations showed the most shallow mixing (Fig. 4.15). The MYNN3 vertical eddy mixing was confined to below 1500 m beyond the RMW (Fig. 4.16), with much of the eddy mixing going to zero between 1700 and 2200 m in Harvey and Irma. This eddy mixing concentrated in the low levels leads to the tendencies in water vapor, temperature, and wind being confined to the lowest 2–3 km (Figs. 4.19 and 4.22). The positive tendencies in water vapor confined to the low levels acts to increase the moisture and, hence, the relative humidity in the low levels in the MYNN3 simulations (Fig. 3.28). The low-level confinement and strength of the wind tendencies (Figs. 4.19 and 4.22) in the MYNN3 simulations acts to limit the 0–3-km shear seen in the Harvey and Irma simulations (Figs. 3.25 and 3.26). The 0–3-km updraft helicity is reduced as a consequence of this lower 0–3-km vertical shear in the MYNN3 simulations. Chapter 3 also showed that the ACM2 cell composites had stronger vertical motion and more CAPE in the low levels (Figs. 3.30 and 3.31) compared to the other PBL schemes in the convective cell composites. The increased CAPE in the PBL was the result of the increased vertical mixing seen in the ACM2 simulations (Fig. 4.15), which has been noted by Zhang et al. (2017) to increase CAPE in the boundary layer in simulations of landfalling tropical cyclones.

Presented in Chapter 5 are the model comparison to observations. First, the vertical profiles of temperature, dew point temperature, and wind from soundings and dropsondes in hurricanes Harvey and Irma were investigated to answer the questions: Which PBL schemes preform best in different locations around the storms? How do inflow depths in observations from soundings, dropsondes, and mobile radar compare to the model simulations? The mobile Doppler radar reflectivity was also used to compare the reflectivity in observed rotating and non-rotating cells to the composite cells from Chapter 3.

6.1.7 Question 9: Which PBL schemes preform best in different locations around the storms compared to observations?

It was expected that the YSU and ACM2 simulations were likely to show the warmest temperatures in the PBL (García-Díez et al. 2013; Cohen et al. 2017). Although not explicitly shown in tropical cyclones, past literature such as Hariprasad et al. (2014) and Banks et al. (2016) suggest that over a wide variety of locations and weather conditions it is likely that the model simulations will show a cold bias in the low levels. Misaki et al. (2019) and Dzebre and Adaramola (2020) suggest that the MYNN3 simulation would more accurately predict the wind speeds compared to non-local PBL schemes (YSU and ACM2). Gunwani and Mohan (2017) argued that over India the ACM2 scheme has the most consistent accuracy as it uses a combination of both local and non-local mixing. Local schemes should be more suitable for stable conditions and non-local schemes should be better suited for unstable conditions. During stable and neutral conditions ACM2 scheme shuts off non-local transport and uses local closure and can represent both the super-grid-scale and sub-grid-scale mixing most realistically (Pleim 2007b). As, such it is expected that the ACM2 simulations should preform well in a verity of situations in the tropical cyclone environment.

All the PBL schemes did exhibit a cold temperature bias, specifically near the surface. Of the three PBL schemes tested, the YSU and ACM2 simulations showed the warmest temperatures in the PBL. García-Díez et al. (2013) attributed this to the ability of non-local PBL schemes to promote deeper PBL heights and more vertical mixing, which is certainly true examining the vertical profiles of vertically eddy mixing in the YSU and ACM2 simulations compared to the MYNN3 simulation (Fig. 4.15). As noted previously, the near surface temperature can affect the stability in the boundary layer resulting in the use of different assumptions in the YSU and ACM2 schemes.

The cold bias over land in the simulations ranged from 1–3 K, which provided enough of a difference in between the surface and first model level to support the stable boundary revison in the YSU scheme (Hong 2010). The simulations showed a cold bias with respect to the soundings and dropsondes with observed temperatures 1–2 K warmer than in the simulations putting into question if the boundary layer is in reality stable. This result again echoes that KPP PBL schemes should be with caution in tropical cyclone simulations as they are very sensitive to the near surface stability (Kepert 2012).

Past literature suggested that the MYNN3 would more accurately predict wind speeds in a variety of situations and locations compared to many non-local PBL schemes (Misaki et al. 2019; Dzebre and Adaramola 2020), contradictory to what is observed in the simulations of hurricanes Harvey and Irma. Other past studies, that focused on the daytime coastal Texas environment, have shown that the YSU and ACM2 PBL schemes tend to produce less bias in wind speed profiles in the PBL compared to local PBL schemes for slower wind speeds (Hu et al. 2010). The MYNN3 simulations of both Harvey and Irma produced the largest average RMSE (3.50 m/s and 8.05 m/s) and faster wind speeds at the observation sites. The ACM2 simulation produced the smallest average RMSE in Harvey (3.24 m/s) and the YSU simulation produced the smallest average RMSE in Irma (5.58 m/s) for wind speed.

The ACM2 simulations of Harvey and Irma produced wind directions that were statistically significantly different most frequently across the observed soundings. It is also important to note that the RMSE in the wind speed increases with increasing wind speed and the wind direction RMSE decreases with increasing wind speed (Surussavadee 2017). For example, stronger winds should have generally less error in the wind direction and that weaker winds should have generally more error in the wind direction. Stronger winds should generally have more error compared to weaker winds.

The wind speeds in the simulations of Harvey and Irma showed larger RMSEs compared to past literature, which aligns well with the past statement on how RMSE generally varies with wind speed. The tropical cyclone winds are generally faster compared to winds typically observed in a variety of situations and locations typically used to test PBL schemes (Misaki et al. 2019; Dzebre and Adaramola 2020). The wind direction RMSEs were lower compared to the past literature (Surussavadee 2017; Misaki et al. 2019; Dzebre and Adaramola 2020), again in agreement with the past statement on how RMSE wind direction varies with wind speed. The fast winds within the tropical cyclone results in generally less RMSE in the wind direction compared to the typically observed wind direction RMSEs in the variety of situations and locations typically used to test PBL schemes (Misaki et al. 2019; Dzebre and Adaramola 2020).

6.1.8 Question 10: How do inflow depths in observations from soundings, dropsondes, and mobile radar compare to the model simulations?

Alford et al. (2020) showed the boundary layer flow in observations of Hurricane Irene (2011) were different between the land and over the ocean. The inflow depth was expected to change across the coastline as observed in Hurricane Irene (Alford et al. 2020), while the inflow depth was expected to be consistent over the land. It was noted previously that the PBL heights in both the Harvey and Irma simulations differed drastically between the land and ocean, such that it was also expected that the depth of the tropical cyclone inflow (a good measure for the actual depth of the PBL; (Zhang et al. 2011c)) to differ between the land and ocean. In particular, it was expected that the YSU and ACM2 simulations of both Harvey and Irma would show the deepest inflow depths. It was expected that the simulations of Harvey and Irma would align well with the dropsonde observations of Zhang et al. (2011c), the caveat being that the results of Zhang et al. (2011c) looked at dropsondes of oceanic tropical cyclones, but this research is looking at landfalling tropical cyclones with a mix of land and ocean points creating the azimuthal averages.

The PBL heights of the MYNN3 simulations of Harvey at CRP were around 500 m and the closest model PBL heights to the observed inflow depth. All of the inflow depths of the simulations were clustered between 800–950 m, but the model PBL heights in the YSU and ACM2 simulations were much higher than the inflow depths at 1450 and 1300 m, respectively. The dropsonde in a distant rainband northeast of the center of Harvey (Fig. 5.18, right) had an observed inflow depth of around 1600 m, which was a bit higher than the dropsonde observations from Zhang et al. (2011c). The inflow depth and model PBL height in the YSU simulation were the most similar to the observed inflow depth at 1400 and 1550 m, respectively. There was a large discrepancy between the MYNN3 and ACM2 simulated PBL height and the inflow depths. The observations at TBW at 0000 UTC 11 September in Irma (Fig. 5.19, right) showed an observed inflow depth around 1100 m near the outside of the eyewall. This inflow depth was very similar to the dropsonde composites of Zhang et al. (2011c). The modeled PBL heights in both the YSU and ACM2 simulations were the closest to the observed inflow height with both around 1400 m. The inflow depth in the MYNN3 simulations were about 200 m less than the observed inflow depth and the model PBL height was much lower at around 400 m corresponding to the shallow inflow depth in the MYNN3 simulation compared to the YSU and ACM2 simulations, as well as the observations.

The inflow depth measured by the mobile Doppler radar observations showed (Figs. 5.20 and 5.21) an internal boundary layer over land and a hurricane boundary layer over the ocean, similar to the results seen in radar observations of the landfall of Hurricane Irene (Alford et al. 2020). The modeled PBL depth and reflectivity at 0000 UTC 26 August for Hurricane Harvey (Fig. 4.11) were presented in the previous chapter along with similar cross sections from Hurricane Irma (Fig. 4.12). There was a discontinuity in the PBL heights present at the coasts in the YSU and ACM2 simulations of Harvey and Irma, the transition across the coastline was expected to be more gradual. The sharpness of the discontinuity may be affected by the horizontal grid spacing. Given this discontinuity in the PBL height at the coastline, both the YSU and ACM2 simulations performed well in terms of the inflow depth observed beyond two times the RMW in the mobile Doppler radar cross sections.

The inflow depths of the mobile radar cross sections at 1025 UTC and 1154 UTC 26 August (Figs. 5.22 and 5.23) were consistent with multiples of the RMW at around 700 m in depth from two-and-a-half to five times the RMW. Over land, the observed inflow height was much different than what was observed in the dropsondes from Zhang et al. (2011c). Over land, the inflow depths were also very stable with multiples of the RMW in the model simulation cross sections from the previous chapter (Fig. 4.13) at 1000 UTC 26 August. The static nature of the inflow depth over land was more characteristic of the internal boundary layer observed during the landfall of Hurricane Irene, which was fairly consistently around 1000 m in depth (Alford et al. 2020).

6.1.9 *Question 11: How do the reflectivity cross sections from rotating and non-rotating cells observed by the mobile Doppler radar compare to the model rotating and non-rotating cell composites?*

As stated previously, it was hypothesized that the rotating cells would take on characteristics of the mature principal rainband cells (Hence and Houze 2008; Card 2019) and that the non-rotating cells would take on the characteristics of the non-mature principal rainband cells at the start of the rainband (Hence and Houze 2008; Li and Wang 2012). It was also hypothesized that observed rotating and non-rotating cells will exhibit similar characteristics, in terms of the height and structure of the reflectivity, to both the composites and the past literature (Hence and Houze 2008; Li and Wang 2012; Card 2019).

All of the observed rotating cells in the radar reflectivity cross sections showed some degree of tilt with height radially outward from the center of Harvey. This general tilt radially outward with height was analogous to the tilt in the reflectivity seen in the rotating cell composites of Harvey (Figs. 3.34 and 3.35). The maximum in reflectivity of the observed rotating cells was concentrated near the lowest radar angle and extended to about 2000–2500 m in the cells at 2207 and 2216 UTC 25 August. This depth was extremely similar to the extent of the reflectivity in the rotating cell composites of Harvey (Figs. 3.34 and 3.35) that show that the high reflectivity around 45 dBZ only extends to about 2500–3000 m in height.

The observed non-rotating cells in the radar reflectivity cross sections did not show any tilt with height, similar to the non-rotating cell composites in Hurricane Harvey (Figs. 3.32 and 3.33). The maximum in reflectivity in the observed non-rotating cell cross sections was typically between 40 and 45 dBZ and extended from the lowest radar angle, which varied between 250 and 500 m to approximately 4000–5000 m in height. The non-rotating cell composites from the model simulation of Harvey (Figs. 3.32 and 3.33) showed that the 45-dBZ model reflectivity generally extended to about 6000 m in height, which was a bit higher than the observed cells in the cross sections (Figs. 5.27 and 5.28), although both show a mushroom-like shape to the reflectivity, very similar to the non-rotating cell composites.

6.2 Future work

Future work should focus on three key categories highlighted in this dissertation. First, future work should further investigate the temporal cycle of tropical cyclone tornado reports. Second, future work should focus on better ways of representing the boundary layer in tropical cyclones, particularly at the coastline. Lastly, future work should include a comprehensive field campaign to directly observe rotating cells in tropical cyclones during landfall. This would allow for a more direct comparisons between tropical cyclone tornado surrogates in high-resolution model simulations and intensively observed cells.

First, more work is needed to investigate the diurnal cycle of tropical cyclone tornado reports in observations and in models of a variety of different tropical cyclones. This work could utilize tropical cyclone tornado surrogates as in Carroll-Smith et al. (2019), Card (2019), and this dissertation to compare to more detailed observations of tornadoes during tropical cyclone landfall. This research and many previous studies show that it would be most judicious to monitor for tornado activity near the coastline on the northeast- or downshear-quadrants of the landfalling tropical cyclone to observe tropical cyclone tornadoes. This work, along with the work of Carroll-Smith et al. (2019) and Card (2019), shows that tropical cyclone tornado surrogates could be used in model simulations of landfalling tropical cyclones to determine the highest risk areas for tornadoes. The temporal distribution of tropical cyclone tornado surrogates in the model simulations also aligned well with the tornado reports from Harvey and Irma, but do not align well with the climotologies of tropical cyclone tornado reports (McCaul 1991; Schultz and Cecil 2009; Edwards 2012). This suggests there is still more to learn about the temporal frequency of tropical cyclone tornadoes and how this may be impacted by differences in landfall times. Tropical cyclone tornado surrogates in model simulations are a useful tool to identify where strong rotating cells are likely to be in the landfalling tropical cyclone. Tornado surrogates should be used to help forecasters identify areas of potentially high tornado risk hours to days in advance of a landfalling tropical cyclone helping to reduce false alarm rates.

Second, future research should focus on better depictions of the boundary layer for landfalling tropical cyclones as the coastline can act to create sharp differences in PBLH and vertical eddy mixing in non-local and hybrid PBL schemes. It is possible that the horizontal grid spacing may affect the sharpness of the transition from the land to ocean. Both non-local and hybrid PBL schemes are dependent on stability that can differ between the land and ocean (YSU and ACM2). As highlighted in this dissertation, the YSU and ACM2 simulations did well in depictions of some aspects of the tropical storm environment; however, it is possible these schemes produced good results for the wrong reasons, particularly considering the large differences in the CRN of both simulations and the effects on the vertical mixing and PBL depth. Smoother transitions from the land to ocean surfaces are almost necessary to further improve these PBL schemes in landfalling tropical cyclones, and may be improved by increases to horizontal grid spacing in model simulations. Further research should focus on how other PBL schemes differ across the coastline in landfalling tropical cyclones, and why. This dissertation identified the stability as the driving mechanisms that resulted in the differences between the local PBL scheme (MYNN3) and the YSU and ACM2 schemes. Future research could alter the mechanisms of the YSU and ACM2 PBL schemes in terms of the CRN and stability to more accurately reproduce the environment of landfalling tropical cyclones. As Gopalakrishnan et al. (2021) showed, the next-generation, FV3-based, HAFS can create diverse model solutions based on the uncertainty in variables used to define the eddy diffusivity (i.e., CRN and mixing length) and that two diverse PBL schemes can create converging forecast results when eddy diffusivity or mixing length are adjusted based on observations. The results of Gopalakrishnan et al. (2021) highlight that even in the next-generation forecast models uncertainties within the PBL scheme eddy diffusivity needs to continue to be studied and improved.

Lastly, future work should incorporate a comprehensive field campaign to address the limited number of direct observations of tropical cyclone tornadoes in landfalling storms using a combination of soundings, dropsondes, and both land-based and aircraft radars. Such assets should be positioned to capture high-resolution observations of rotating thunderstorms embedded within tropical cyclone rainbands. Such a study would help to build the knowledge of observed tropical cyclone tornadoes, the local-scale environment, and allow for more direct comparisons with high-resolution models to improve forecasts of tropical cyclone tornadoes. This future work could drastically improve the forecasts to tropical cyclone tornadoes and possibly help reduce the high tornado warning false alarm rates in landfalling tropical cyclones.

APPENDIX A

American Meteorological Society (AMS) Copyright Notice

BIBLIOGRAPHY

Alford, A. A., M. I. Biggerstaff, and G. D. Carrie, 2019: Mobile ground-based SMART radar observations and wind retrievals during the landfall of Hurricane Harvey (2017). *Geo. Data J.*, **6**, 205–213.

Alford, A. A., J. A. Zhang, M. I. Biggerstaff, P. Dodge, F. D. Marks, and D. J. Bodine, 2020: Transition of the hurricane boundary layer during the landfall of Hurricane Irene (2011). *J. Atmos. Sci.*, **77**, 3509–3531.

Anthes, R. A., and S. W. Chang, 1978: Response of the hurricane boundary layer to changes of sea surface temperature in a numerical model. *J. Atmos. Sci.*, **35**, 1240–1255.

Bai, L., Z. Meng, K. Sueki, G. Chen, and R. Zhou, 2019: Climatology of tropical cyclone tornadoes in china from 2006 to 2018. *Sci. China Earth Sci.*, **63**, 1–15.

Baker, A. K., M. D. Parker, and M. D. Eastin, 2009: Environmental ingredients for supercells and tornadoes within Hurricane Ivan. *Wea. Forecasting*, **24**, 223–224.

Banks, R. F., J. Tiana-Alsina, J. M. Baldasano, F. Rocadenbosch, A. Papayannis, S. Solomos, and C. G. Tzanis, 2016: Sensitivity of boundary-layer variables to pbl schemes in the wrf model based on surface meteorological observations, lidar, and radiosondes during the hygra-cd campaign. *Atmos. Res.*, **176**, 185–201.

Barnes, G. M., E. J. Zipser, D. Jorgensen, and F. Marks, 1983: Mesoscale and Convective Structure of a Hurricane Rainband. *J. Atmos. Sci.*, **40**, 2125–2137.

Braun, S. A., and W.-K. Tao, 2000: Sensitivity of high-resolution simulations of Hurricane Bob (1991) to planetary boundary layer parameterizations. *Mon. Wea. Rev.*, **128**, 3941–3961.

Bright, D. R., and S. L. Mullen, 2002: Short-range ensemble forecasts of precipitation during the southwest monsoon. *Wea. Forecasting*, **17**, 1080–1100.

Brotzge, J., S. Erickson, and H. Brooks, 2011: A 5-yr climatology of tornado false alarms. *Wea. Forecasting*, **26**, 534–544.

Bu, Y. P., R. G. Fovell, and K. L. Corbosiero, 2017: The influences of boundary layer mixing and cloud-radiative forcing on tropical cyclone size. *J. Atmos. Sci.*, **74**, 1273–1292.

Card, D., 2019: A multiscale analysis of the rainband and cellular structure in hurricanes Harvey and Irma (2017) using the NCAR Ensemble. M.S. thesis, Department of Atmospheric and Environmental Science, University at Albany, 127 pp., URL https://search.proquest.com/docview/2318188203?accountid=14166.

Carroll-Smith, D. L., 2018: "If it happened in. . . " a pseudo-global warming assessment of tropical cyclone tornadoes. Ph.D. thesis, University of Illinois at Urbana-Champaign, URL https://www.ideals.illinois.edu/handle/2142/101477.

Carroll-Smith, D. L., L. C. Dawson, and R. J. Trapp, 2019: High-resolution real-data WRF modeling and verification of tropical cyclone tornadoes associated with Hurricane Ivan (2004). *Electronic J. Severe Storms Meteor.*, **14**, 1–36.

Chen, F., and J. Dudhia, 2001: Coupling an advanced land surface– hydrology model with the Penn State–NCAR MM5 modeling system. Part I: Model description and implementation. *Mon. Wea. Rev.*, **129**, 569–585.

Cohen, A. E., S. M. Cavallo, M. C. Coniglio, and H. E. Brooks, 2015: A review of planetary boundary layer parameterization schemes and their sensitivity in simulating southeastern us cold season severe weather environments. *Wea. Forecasting*, **30**, 591–612.

Cohen, A. E., S. M. Cavallo, M. C. Coniglio, H. E. Brooks, and I. L. Jirak, 2017: Evaluation of multiple planetary boundary layer parameterization schemes in southeast us cold season severe thunderstorm environments. *Wea. Forecasting*, **32**, 1857–1884.

Coniglio, M. C., J. Correia Jr, P. T. Marsh, and F. Kong, 2013: Verification of convection-allowing wrf model forecasts of the planetary boundary layer using sounding observations. *Wea. Forecasting*, **28**, 842–862.

Copernicus Climate Change Service (C3S), 2019: ERA5: Fifth generation of ecmwf atmospheric reanalyses of the global climate. Copernicus Climate Change Service Climate Data Store (CDS), URL https://cds.climate.copernicus.eu/cdsapp#!/home.

Corbosiero, K. L., and J. Molinari, 2003: The relationship between storm motion, vertical wind shear, and convective asymmetries in tropical cyclones. *J. Atmos. Sci.*, **60**, 366–376.

Cruz, F. T., and G. T. Narisma, 2016: WRF simulation of the heavy rainfall over metropolitan manila, Philippines during tropical cyclone Ketsana: a sensitivity study. *Meteorol. Atmos. Phys.*, **128**, 415–428.

Curtis, L., 2004: Midlevel dry intrusions as a factor in tornado outbreaks associated with landfalling tropical cyclones from the Atlantic and Gulf of Mexico. *Wea. Forecasting*, **19**, 411–427.

DeHart, J. C., R. A. Houze Jr, and R. F. Rogers, 2014: Quadrant distribution of tropical cyclone inner-core kinematics in relation to environmental shear. *J. Atmos. Sci.*, **71**, 2713–2732.

Didlake, A. C., and R. A. Houze, 2009: Convective-scale downdrafts in the principal rainband of Hurricane Katrina (2005). *Mon. Wea. Rev.*, **137**, 3269–3293.

Donelan, M., B. K. Haus, N. Reul, W. Plant, M. Stiassnie, H. C. Graber, O. Brown, and E. Saltzman, 2004: On the limiting aerodynamic roughness of the ocean in very strong winds. *Geophys. Res. Lett.*, **31**.

Dzebre, D. E., and M. S. Adaramola, 2020: A preliminary sensitivity study of planetary boundary layer parameterisation schemes in the weather research and forecasting model to surface winds in coastal ghana. *Renew. Energy*, **146**, 66–86.

Eastin, M. D., and M. C. Link, 2009: Miniature supercells in an offshore outer rainband of Hurricane Ivan (2004). *Mon. Wea. Rev.*, **137**, 2081–2104.

Edwards, R., 2010: Tropical cyclone tornado records for the modernized national weather service era. *Preprints, 25th Conf. on Severe Local Storms, Denver, CO, Amer. Meteor. Soc. P*, Vol. 2.

Edwards, R., 2012: Tropical cyclone tornadoes: A review of knowledge in research and prediction. *Electronic J. Severe Storms Meteor.*, **7**, 1–61.

Edwards, R., A. R. Dean, R. L. Thompson, and B. T. Smith, 2012: Convective modes for significant severe thunderstorms in the contiguous United States. Part III: Tropical cyclone tornadoes. *Wea. Forecasting*, **27**, 1507–1519.

Edwards, R., and A. E. Pietrycha, 2006: Archetypes for surface baroclinic boundaries influencing tropical cyclone tornado occurrence. *AMS 23nd Conf. Severe Local Storms*, St. Louis MO, Storm Prediction Center, URL https://www.spc.ncep.noaa.gov/publications/edwards/tcfronts.pdf.

Fovell, R. G., K. L. Corbosiero, and H.-C. Kuo, 2009: Cloud microphysics impact on hurricane track as revealed in idealized experiments. *J. Atmos. Sci.*, **66**, 1764–1778.

Fovell, R. G., and H. Su, 2007: Impact of cloud microphysics on hurricane track forecasts. *Geophys. Res. Lett.*, **34**.

García-Díez, M., J. Fernández, L. Fita, and C. Yagüe, 2013: Seasonal dependence of wrf model biases and sensitivity to pbl schemes over europe. *Quart. J. Roy. Meteor. Soc.*, **139**, 501–514.

Garratt, J., 1977: Review of drag coefficients over oceans and continents. *Mon. Wea. Rev.*, **105**, 915–929.

Garratt, J., 1990: The internal boundary layer — a review. *Bound.-Layer Meteor.*, **50**, 171–203.

Gentry, M. S., and G. M. Lackmann, 2010: Sensitivity of simulated tropical cyclone structure and intensity to horizontal resolution. *Mon. Wea. Rev.*, **138**, 688–704.

Gentry, R. C., 1983: Genesis of tornadoes associated with hurricanes. *Mon. Wea. Rev.*, **111**, 1793–1805.

Giammanco, I. M., J. L. Schroeder, and M. D. Powell, 2013: GPS dropwindsonde and wsr-

88d observations of tropical cyclone vertical wind profiles and their characteristics. *Wea. Forecasting*, **28**, 77–99.

Gopalakrishnan, S., A. Hazelton, and J. A. Zhang, 2021: Improving hurricane boundary layer parameterization scheme based on observations. *Earth and Space Sci.*, **8**, e2020EA001 422.

Gopalakrishnan, S. G., F. Marks Jr, J. A. Zhang, X. Zhang, J.-W. Bao, and V. Tallapragada, 2013: A study of the impacts of vertical diffusion on the structure and intensity of the tropical cyclones using the high-resolution hwrf system. *J. Atmos. Sci.*, **70**, 524–541.

Green, B. W., F. Zhang, and P. Markowski, 2011: Multiscale processes leading to supercells in the landfalling outer rainbands of Hurricane Katrina (2005). *Wea. Forecasting*, **26**, 828–847.

Gunwani, P., and M. Mohan, 2017: Sensitivity of wrf model estimates to various pbl parameterizations in different climatic zones over india. *Atmos. Research*, **194**, 43–65.

Hariprasad, K., C. V. Srinivas, A. B. Singh, S. V. B. Rao, R. Baskaran, and B. Venkatraman, 2014: Numerical simulation and intercomparison of boundary layer structure with different PBL schemes in WRF using experimental observations at a tropical site. *Atmos. Research*, **145**, 27–44.

Hence, D. A., and R. A. Houze, 2008: Kinematic structure of convective-scale elements in the rainbands of hurricanes Katrina and Rita (2005). *J. Geophys. Res.*, **113**, D15 108.

Hill, K. A., and G. M. Lackmann, 2009: Analysis of idealized tropical cyclone simulations using the weather research and forecasting model: Sensitivity to turbulence parameterization and grid spacing. *Mon. Wea. Rev.*, **137**, 745–765.

Hirth, B. D., J. L. Schroeder, C. C. Weiss, D. A. Smith, and M. I. Biggerstaff, 2012: Research radar analyses of the internal boundary layer over Cape Canaveral, Florida, during the landfall of Hurricane Frances (2004). *Wea. Forecasting*, **27**, 1349–1372.

Hock, T. F., and J. L. Franklin, 1999: The NCAR GPS dropwindsonde. *Bull. Amer. Meteor. Soc.*, **80**, 407–420.

Hong, S.-Y., 2010: A new stable boundary-layer mixing scheme and its impact on the simulated east asian summer monsoon. *Quart. J. Roy. Meteor. Soc.*, **136**, 1481–1496.

Hong, S.-Y., and J.-O. J. Lim, 2006: The WRF single-moment 6-class microphysics scheme (wsm6). *J. Kor. Meteor. Soc.*, **42**, 129–151.

Hong, S.-Y., Y. Noh, and J. Dudhia, 2006: A new vertical diffusion package with an explicit treatment of entrainment processes. *Mon. Wea. Rev.*, **134**, 2318–2341.

Hong, S.-Y., and H.-L. Pan, 1996: Nonlocal boundary layer vertical diffusion in a medium-range forecast model. *Mon. Wea. Rev.*, **124**, 2322–2339.

Houze, R. A., 2010: Clouds in tropical cyclones. *Mon. Wea. Rev.*, **138**, 293–344.

Hu, X.-M., J. W. Nielsen-Gammon, and F. Zhang, 2010: Evaluation of three planetary boundary layer schemes in the wrf model. *J. Appl. Meteor. Climatol.*, **49**, 1831–1844.

Iacono, M. J., J. S. Delamere, E. J. Mlawer, M. W. Shephard, S. A. Clough, and W. D. Collins, 2008: Radiative forcing by long-lived greenhouse gases: Calculations with the aer radiative transfer models. *Geophys. Res. Lett.*, **113**, D13 103.

Ingleby, B., 2017: *An assessment of different radiosonde types 2015/2016*. European Centre for Medium Range Weather Forecasts.

Jankov, I., W. A. Gallus Jr, M. Segal, B. Shaw, and S. E. Koch, 2005: The impact of different WRF model physical parameterizations and their interactions on warm season MCS rainfall. *Wea. Forecasting*, **20**, 1048–1060.

Jiménez, P. A., J. Dudhia, J. F. González-Rouco, J. Navarro, J. P. Montávez, and E. García-Bustamante, 2012: A revised scheme for the WRF surface layer formulation. *Mon. Wea. Rev.*, **140**, 898–918.

Kain, J. S., S. Weiss, M. Baldwin, G. Carbin, D. Bright, J. Levit, and J. Hart, 2005: Evaluating high-resolution configurations of the WRF model that are used to forecast severe convective weather: The 2005 SPC/NSSL spring program. *Preprints, 21st Conf. on Weather Analysis and Forecasting/17th Conf. on Numerical Weather Prediction, Washington, DC, Amer. Meteor. Soc. A*, Vol. 2.

Kepert, J. D., 2012: Choosing a boundary layer parameterization for tropical cyclone modeling. *Mon. Wea. Rev.*, **140**, 1427–1445.

Lackmann, G. M., 2015: Hurricane Sandy before 1900 and after 2100. *Bull. Amer. Meteor. Soc.*, **96**, 547–560.

Landsea, C. W., and J. L. Franklin, 2013: Atlantic hurricane database uncertainty and presentation of a new database format. *Mon. Wea. Rev.*, **141**, 3576–3592.

Li, Q., and Q. Fang, 2018: A numerical study of convective-scale structures in the outer cores of sheared tropical cyclones. Part I: Updraft traits in different vertical wind shear magnitudes. *J. Geophys. Res. Atmos.*, **123**, 12–097.

Li, Q., and Y. Wang, 2012: A comparison of inner and outer spiral rainbands in a numerically simulated tropical cyclone. *Mon. Wea. Rev.*, **140**, 2782–2805.

Lim, K.-S. S., and S.-Y. Hong, 2010: Development of an effective double-moment cloud microphysics scheme with prognostic cloud condensation nuclei (CCN) for weather and climate models. *Mon. Wea. Rev.*, **138**, 1587–1612.

Liu, S., and X.-Z. Liang, 2010: Observed diurnal cycle climatology of planetary boundary layer height. *J. Climate*, **23**, 5790–5809.

Lorente-Plazas, R., P. A. Jiménez, J. Dudhia, and J. P. Montávez, 2016: Evaluating and improving the impact of the atmospheric stability and orography on surface winds in the WRF model. *Mon. Wea. Rev.*, **144**, 2685–2693.

Markowski, P., C. Hannon, J. Frame, E. Lancaster, A. Pietrycha, R. Edwards, and R. L. Thompson, 2003: Characteristics of vertical wind profiles near supercells obtained from the rapid update cycle. *Wea. Forecasting*, **18**, 1262–1272.

Martinaitis, S. M., 2017: Radar observations of tornado-warned convection associated with tropical cyclones over Florida. *Wea. Forecasting*, **32**, 165–186.

McCaul, E., 1987: Observations of the Hurricane Danny tornado outbreak of 16 August 1985. *Mon. Wea. Rev.*, **115**, 1206–1223.

McCaul, E., 1991: Buoyancy and shear characteristics of hurricane tornado. *Mon. Wea. Rev.*, **119**, 1954–1978.

McCaul, E., 1993: Observations and simulations of hurricane-spawned tornadic storms. *Washington DC American Geophysical Union Geophysical Monograph Series*, **79**, 119–142.

McCaul, E., and M. Weisman, 1996: Simulations of shallow supercell storms in landfalling hurricane environments. *Mon. Wea. Rev.*, **124**, 408–429.

McCaul, E. W., and M. L. Weisman, 2001: The sensitivity of simulated supercell structure and intensity to variations in the shapes of environmental buoyancy and shear profiles. *Mon. Wea. Rev.*, **129**, 664–687.

Mellor, G. L., and T. Y. Yamada, 1982: Development of a turbulence closure model for geophysical fluid problems. *Rev. Geophys. Space Phys.*, **20**, 851–875.

Misaki, T., T. Ohsawa, M. Konagaya, S. Shimada, Y. Takeyama, and S. Nakamura, 2019: Accuracy comparison of coastal wind speeds between WRF simulations using different input datasets in Japan. *Energies*, **12**, 2754.

Molinari, J., D. M. Romps, D. Vollaro, and L. Nguyen, 2012: Cape in tropical cyclones. *J. Atmos. Sci.*, **69**, 2452–2463.

Molinari, J., and D. Vollaro, 2008: Extreme helicity and intense convective towers in Hurricane Bonnie. *Mon. Wea. Rev.*, **136**, 4355–4372.

Molinari, J., and D. Vollaro, 2010: Distribution of helicity, CAPE, and shear in tropical cyclones. *J. Atmos. Sci.*, **67**, 274–284.

Moon, Y., and D. S. Nolan, 2015a: Spiral rainbands in a numerical simulation of Hurricane Bill (2009). Part I: Structures and comparison to observations. *J. Atmos. Sci.*, **72**, 164–190.

Moon, Y., and D. S. Nolan, 2015b: Spiral rainbands in a numerical simulation of Hurricane Bill (2009). Part II: Propagation of inner rainbands. *J. Atmos. Sci.*, **72**, 191–215.

Nakanishi, M., and H. Niino, 2006: An improved Mellor–Yamada level-3 model: Its numerical stability and application to a regional prediction of advection fog. *Bound.-Lay. Meteorol.*, **119**, 397–407.

Nakanishi, M., and H. Niino, 2009: Development of an improved turbulence closure model for the atmospheric boundary layer. *J. Meteor. Soc. of Japan. Ser. II*, **87**, 895–912.

Nielsen-Gammon, J. W., X.-M. Hu, F. Zhang, and J. E. Pleim, 2010: Evaluation of planetary boundary layer scheme sensitivities for the purpose of parameter estimation. *Mon. Wea. Rev.*, **138**, 3400–3417.

Nolan, D. S., J. A. Zhang, and D. P. Stern, 2009a: Evaluation of planetary boundary layer parameterizations in tropical cyclones by comparison of in situ observations and high-resolution simulations of Hurricane Isabel (2003). Part I: Initialization, maximum winds, and the outer-core boundary layer. *Mon. Wea. Rev.*, **137**, 3651–3674.

Nolan, D. S., J. A. Zhang, and D. P. Stern, 2009b: Evaluation of planetary boundary layer parameterizations in tropical cyclones by comparison of in situ observations and high-resolution simulations of Hurricane Isabel (2003). Part II: Inner-core boundary layer and eyewall structure. *Mon. Wea. Rev.*, **137**, 3675–3698.

Novlan, D., and W. Gray, 1974: Hurricane-spawned tornadoes. *Mon. Wea. Rev.*, **102**, 476–488.

NWS, 2012: Hurricane Irene, August 21-30, 2011. Tech. rep., NOAA/NWS Service Assessment, 129 pp. URL https://www.weather.gov/media/publications/assessments/Irene2012.pdf.

Pleim, J. E., 2007a: A combined local and nonlocal closure model for the atmospheric boundary layer. Part I: Model description and testing. *J. Appl. Meteor. Climatol.*, **46**, 1383–1395.

Pleim, J. E., 2007b: A combined local and nonlocal closure model for the atmospheric boundary layer. Part II: Application and evaluation in a mesoscale meteorological model. *J. Appl. Meteor. Climatol.*, **46**, 1396–1409.

Powell, M. D., and S. H. Houston, 1998: Surface wind fields of 1995 hurricanes Erin, Opal, Luis, Marilyn, and Roxanne at landfall. *Mon. Wea. Rev.*, **126**, 1259–1273.

Rai, D., and S. Pattnaik, 2018: Sensitivity of tropical cyclone intensity and structure to planetary boundary layer parameterization. *Asia-Pacific J. Atmos. Sci.*, **54**, 473–488.

Rasmussen, E. N., 2003: Refined supercell and tornado forecast parameters. *Wea. Forecasting*, **18**, 530–535.

Rasmussen, E. N., and D. O. Blanchard, 1998: A baseline climatology of sounding-derived supercell andtornado forecast parameters. *Wea. Forecasting*, **13**, 1148–1164.

Rogers, R., S. Lorsolo, P. Reasor, J. Gamache, and F. Marks, 2012: Multiscale analysis of tropical cyclone kinematic structure from airborne doppler radar composites. *Mon. Wea. Rev.*, **140**, 77–99.

Rogers, R. F., M. L. Black, S. S. Chen, and R. A. Black, 2007: An evaluation of microphysics fields from mesoscale model simulations of tropical cyclones. Part I: Comparisons with observations. *J. Atmos. Sci.*, **64**, 1811–1834.

Schultz, L. A., and D. J. Cecil, 2009: Tropical cyclone tornadoes, 1950–2007. *Mon. Wea. Rev.*, **137**, 3471–3484.

Stensrud, D. J., 2007: *Parameterization schemes: keys to understanding numerical weather prediction models*. Cambridge University Press.

Stull, R. B., 1988: *An introduction to boundary layer meteorology*, Vol. 13. Springer Science & Business Media.

Sun, X., and A. P. Barros, 2012: The impact of forcing datasets on the high-resolution simulation of Tropical Storm Ivan (2004) in the Southern Appalachians. *Mon. Wea. Rev.*, **140**, 3300–3326.

Sun, X., and A. P. Barros, 2014: High resolution simulation of Tropical Storm Ivan (2004) in the Southern Appalachians: role of planetary boundary-layer schemes and cumulus parametrization. *Quart. J. Roy. Meteor. Soc.*, **140**, 1847–1865.

Surussavadee, C., 2017: Evaluation of WRF near-surface wind simulations in tropics employing different planetary boundary layer schemes. *2017 8th International Renewable Energy Congress (IREC)*, IEEE, 1–4.

Tang, J., J. A. Zhang, S. D. Aberson, F. D. Marks, and X. Lei, 2018a: Multilevel tower observations of vertical eddy diffusivity and mixing length in the tropical cyclone boundary layer during landfalls. *J. Atmos. Sci.*, **75**, 3159–3168.

Tang, X., W.-C. Lee, and M. Bell, 2018b: Subrainband structure and dynamic characteristics in the principal rainband of Typhoon Hagupit (2008). *Mon. Wea. Rev.*, **146**, 157–173.

Tang, X., and Z. Tan, 2006: Boundary-layer wind structure in a landfalling tropical cyclone. *Adv. Atmos. Sci.*, **23**, 737–749.

Torn, R. D., G. J. Hakim, and C. Snyder, 2006: Boundary conditions for limited-area ensemble kalman filters. *Mon. Wea. Rev.*, **134**, 2490–2502.

Tyagi, B., and Coauthors, 2018: Performance analysis of planetary boundary layer parameterization schemes in WRF modeling set up over Southern Italy. *Atmosphere*, **9**, 272.

Vaisala, 2014: Vaisala dropsone RD94. Vaisala Rep., URL https://www.vaisala.com/sites/default/files/documents/RD94-Dropsonde-Datasheet-B210936EN-A-LoRes.pdf.

Vaughan, M. T., and R. G. Fovell, 2020: The influence of boundary layer mixing strength on the evolution of a baroclinic cyclone. *Manuscript submitted for publication.*

Verbout, S. M., D. M. Schultz, L. M. Leslie, H. E. Brooks, D. J. Karoly, and K. L. Elmore, 2007: Tornado outbreaks associated with landfalling hurricanes in the North Atlantic Basin: 1954–2004. *Meteor. Atmos. Phys.*, **97**, 255–271.

Vescio, M. D., S. J. Weiss, and F. P. Ostby, 1996: Tornadoes associated with Tropical Storm Beryl. *Natl. Wea. Dig.*, **21**, 2–10.

Wang, Y., 2007: A multiply nested, movable mesh, fully compressible, nonhydrostatic tropical cyclone model–TCM4: Model description and development of asymmetries without explicit asymmetric forcing. *Meteorol. Atmos. Phys.*, **97**, 93–116.

Warner, T. T., 2010: *Numerical weather and climate prediction.* Cambridge University Press.

Weiss, S., 1987: Some climatological aspects of forecasting tornadoes associated with tropical cyclones. *Preprints, 17th Conf. on Hurricanes and Tropical Meteorology*, Amer. Meteor. Soc., Miami, FL, 160–163.

Williams, G. J., 2019: Idealized simulations of the inner core boundary layer structure in a landfalling tropical cyclone. Part I: Kinematic structure. *Trop. Cyclone Res. Rev.*, **8**, 47–67.

Wong, M. L., and J. C. Chan, 2007: Modeling the effects of land–sea roughness contrast on tropical cyclone winds. *J. Atmos. Sci.*, **64**, 3249–3264.

Xie, B., J. C. Fung, A. Chan, and A. Lau, 2012: Evaluation of nonlocal and local planetary boundary layer schemes in the WRF model. *J. Geophys. Res.*, **117**, D12 103.

Yu, C.-K., and C.-L. Tsai, 2013: Structural and surface features of arc-shaped radar echoes along an outer tropical cyclone rainband. *J. Atmos. Sci.*, **70**, 56–72.

Zhang, C., Y. Wang, and K. Hamilton, 2011a: Improved representation of boundary layer clouds over the southeast Pacific in ARW-WRF using a modified Tiedtke cumulus parameterization scheme. *Mon. Wea. Rev.*, **139**, 3489–3513.

Zhang, F., Z. Pu, and C. Wang, 2017: Effects of boundary layer vertical mixing on the evolution of hurricanes over land. *Mon. Wea. Rev.*, **145**, 2343–2361.

Zhang, J. A., F. D. Marks, M. T. Montgomery, and S. Lorsolo, 2011b: An estimation of turbulent characteristics in the low-level region of intense hurricanes Allen (1980) and Hugo (1989). *Mon. Wea. Rev.*, **139**, 1447–1462.

Zhang, J. A., D. S. Nolan, R. F. Rogers, and V. Tallapragada, 2015: Evaluating the impact of improvements in the boundary layer parameterization on hurricane intensity and structure forecasts in HWRF. *Mon. Wea. Rev.*, **143**, 3136–3155.

Zhang, J. A., R. F. Rogers, D. S. Nolan, and F. D. Marks Jr, 2011c: On the characteristic height scales of the hurricane boundary layer. *Mon. Wea. Rev.*, **139**, 2523–2535.